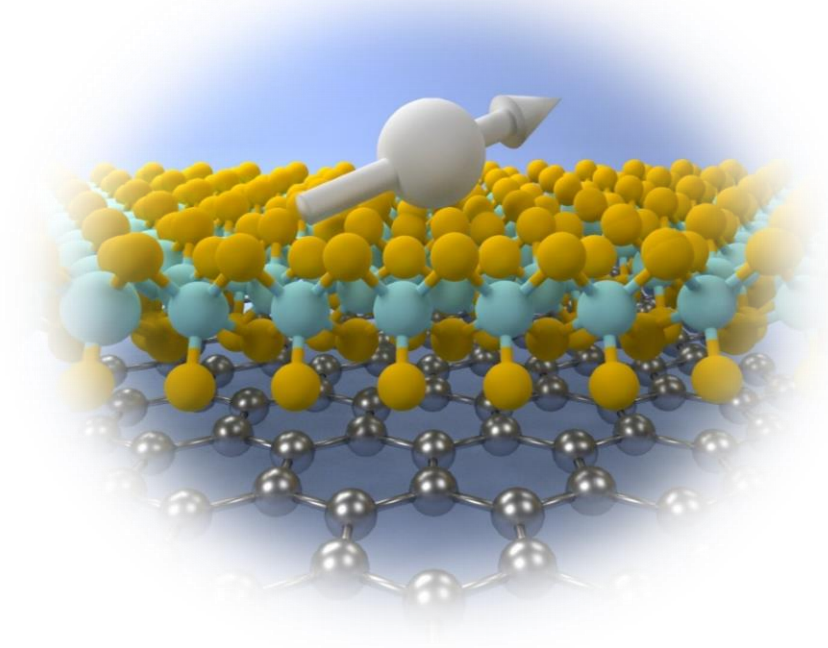


Spin-orbit proximity in van der Waals heterostructures



Franz Herling

PhD Thesis

Supervisor: Prof. Fèlix Casanova and Prof. Luis E. Hueso

2022



Laburpena

Informazio teknologiarren garapen azkarrak eguneroko bizitzako aspektu guztietan du eragina. Gizarteko alor denetan ari da eragiten eta aldaketa iraultzaile bat gertatzeko aukera infinitua da. Honen iturburua orain dela mende erdiko asmakuntza da: zirkuitu integratua. Zirkuitu hauek transistorea dute oinarri, elektrikoki kontrolatu daitekeen etengailua. Mota honetako billoika elementu aurkitzen dira siliziozko txip batean, erdieroaleen industriak daukan miniaturizazio gaitasunari esker. Dena den, material zientziaren aurrerapen teknologiko hau energia kontsumo eta txikiagotzearen limite fisikora iristen ari da, oinarrizko aldaketa bat ezinbestekoa bilakatuz.

Elektroiaren kargaren orde, spina, bere mekanika kuantikako propietatea, memoria aplikazioetarako erabiltzea ohikoa bilakatu da eta hainbat proposamen ere egin dira zirkuitu logikoak garatzeko spintronikan oinarrituz. Hala ere, material arruntek ingurugiro temperaturan ez daukate halako gailuentarako beharrezkoa den spin difuzio luzera. Zientzialari ugari uste dute grafenoak – material bikaina denak spina distantzia luzean garraiatzeko – eta beste bi-dimentsiotako (2D) material batzuek arazoa konpondu dezaketela. Gainera, gertutasun efektuak atek irekitzen ditu 2D material batetik beste batera propietateak transferitzeko. Van der Waals heteroegituretan (vdW) trantsizio metal dikalkogenuroak (TMDC) erabili daitezke grafenoko spin-orbita akoplamendua handitzeko, honek spin fenomeno harrigarriak eragiten dituelarik.

Tesi honetan, grafeno/TMDC vdW heteroegiturak erabili dira, Hall egitura eta elektrodo ferromagnetikoak dituen gailu bat garatzeko. Gailu hau erabiliz, spin Hall efektua erakutsi da grafenoan, spin-orbita akoplamenduak (ingelesez spin-orbit coupling, SOC), MoS_2 -rekiko gertutasuna dela medio, eragindakoa. Erresistentzia ez lokalaren Hanle prezesioak ebidentzia esperimental sinesgarria emateaz gain, spin garraio eta spin karga konbertsioak kuantifikatzea ahalbidetzen du. Biak material berdinen zati ezberdinetan gertatzeak eraginkortasun handia izatea eragiten du spin-karga korrante (ingelesez spin-to-charge conversion, SCC) irteera boltaian ingurugiro temperaturan. Horrez gain, SCC-aren kontrola bermatu da eremu elektriko bat aplikatuz, efizientzia errekorra neurtu delarik WSe_2 grafeno gertutasunean, SCC luzera 40nm izanik.

Gertutasunak induzitutako SOC-ak spin biziraupen denboraren anisotropia handia eragiten du, eta honekin batera, 2D materialen egoera elektronikoen aran izaerak kontrol aginte paregabea eskaintzen du. Grafeno/ WSe_2 spin balbula lateral batean, spin prezesio koherentea lortu da kanpo eremu magnetikorik aplikatu gabe, baita erregimen difusiboan ere. Nabarmenezkoa da prezesio spin polarizazioaren zeinua aldatua izan daitekeela eremu elektriko eta drift korrante bidez, era honetan, spin transistore bat lortuz ingurugiro temperaturan zuzen funtzionatzen duena.

Emaitza hauek, 2D materialen gaitasuna erakusten dute spinean oinarritutako gailu berriak inplementatzeko, energia eraginkorrak diren spinean oinarritutako logika gailuetan eta etorkizuneko beste aplikazioetan.

Abstract

The rapid progress of modern information technology influences all aspects of everyday life. More and more, it is transforming every part of society and the possibilities for revolutionary changes seem endless. At its core, this is fueled by one, half a century old invention: the integrated circuit. It uses the simple concept of the transistor, an electrically controllable switch, but fabricates it by the billion on a small silicon chip through the miniaturization capabilities of the semiconductor industry. However, the technological advancements and developments in material science are reaching the physical limits of size reduction and energy consumption. A fundamental paradigm change is needed.

Using the quantum mechanical property of spin instead of the charge of the electron is already established for memory applications and multiple proposals exist to also use such a spintronic idea in logic circuits. However, conventional materials lack the long spin diffusion lengths at room temperature necessary for such devices. Many scientists believe that the discovery of graphene – an excellent material for long-distance spin transport – and other two-dimensional (2D) materials could solve this problem. Additionally, the proximity effect opens ways to transfer properties from one 2D material into another. In van der Waals (vdW) heterostructures, transition metal dichalcogenides (TMDCs) can be used to enhance the spin-orbit coupling (SOC) of graphene, leading to fascinating spin phenomena.

In this thesis, such graphene/TMDC vdW heterostructures were used to develop a device that combines Hall probes with ferromagnetic electrodes. With it, the spin Hall effect in graphene induced by SOC proximity with MoS₂ could unambiguously be demonstrated. The Hanle precession of the non-local resistance not only gives convincing experimental proof but also allows the quantification of the spin transport and the spin-to-charge conversion (SCC). The fact that both occur in different parts of the same material gives rise to a high efficiency for the SCC voltage output up to room temperature. Additionally, the control of the SCC by applying a gate voltage was shown in graphene proximitized with WSe₂, enabling a record efficiency measured with an SCC length of around 40 nm.

The proximity-induced SOC also leads to strong spin lifetime anisotropy and, together with the valley character of the electronic states in 2D materials, provides unique control knobs. In a graphene/WSe₂ lateral spin valve, coherent spin precession in the absence of an external magnetic field was achieved, even in the diffusive regime. Remarkably, the sign of the precessing spin polarization can be tuned by a gate voltage and by a drift current, realizing a spin transistor working up to room temperature.

These results show the capability of 2D materials to advance toward the implementation of novel spin-based devices for energy-efficient spin-based logic and other future applications.

Table of Contents

Laburpena	i
Abstract	iii
1 Introduction	1
1.1 Christmas 1947: The invention of the transistor	1
1.2 The race between PRL and PRB: The birth of spintronics	2
1.3 Friday night experiments: The discovery of graphene	3
1.4 This thesis: The combination of the abovementioned	4
2 Spin	7
2.1 ...-orbit coupling	7
2.2 ... transport and relaxation	11
2.3 ... injection and detection	14
2.4 ... precession	16
2.5 ...-to-charge conversion	19
3 Two-dimensional materials	27
3.1 Graphene	27
3.1.1 Early history, discovery, and Nobel prize	27
3.1.2 Recent scientific developments	29
3.1.3 Steps towards industrial application	30
3.2 Transition metal dichalcogenides	31
3.3 Other members of the 2D material family	34
3.4 Van der Waals heterostructures and proximity effects	35

4	Experimental techniques	41
4.1	Exfoliation and deterministic transfer	41
4.2	Clean room fabrication	43
4.2.1	Electron-beam lithography	43
4.2.2	Reactive ion etching	45
4.2.3	Metal deposition	45
4.3	Characterization techniques	46
4.3.1	X-ray reflectivity	46
4.3.2	Atomic force microscopy	46
4.3.3	Laser Raman microscopy	47
4.3.4	Scanning electron microscopy	48
4.3.5	Electronic measurements	49
5	Spin-to-charge conversion in graphene proximitized with MoS₂	53
5.1	Early experimental claims and theoretical predictions	53
5.2	Device characterization and spin transport	55
5.3	Experimental observation of spin-to-charge conversion in graphene/MoS ₂	61
6	Record spin-to-charge conversion efficiency by electrical control in graphene proximitized with WSe₂	71
6.1	Theoretical prediction of Fermi energy dependence	71
6.2	Device characterization, spin transport, and spin-charge interconversion	73
6.3	Temperature and gate dependence of the spin-to-charge conversion in graphene/WSe ₂	80
6.4	Comparison to other spin-to-charge conversion systems	87
7	Coherent spin precession in graphene proximitized with WSe₂	93
7.1	Spin polarization in the strong spin-orbit coupling regime	93
7.2	Gate-controlled anisotropic spin transport in graphene/WSe ₂	96
7.3	Drift-current-guided anisotropic spin transport in graphene/WSe ₂	102
7.4	Magnetic-field-free control of spin polarization in graphene/WSe ₂ at room temperature	106
7.5	Spin field-effect transistor and Datta-Das proposal	108

8	Local device as a step towards spintronic application	111
8.1	Introduction to the device proposal by Intel	111
8.2	2D material local SCC device	112
8.3	Device design iterations	115
9	Conclusion and outlook	119
	Appendix A Contact pulling in Hanle precession measurements	123
	Appendix B Fitting of the Hanle precession data in Python	125
	Bibliography	127
	List of publications	153
	List of acronyms and symbols	155
	Acknowledgments	159

1 Introduction

1.1 Christmas 1947: The invention of the transistor

There are two ways to tell the following story: one is a Christmas miracle, in which the skilled experimentalist Walter Brattain (1902-1987) and the genius theoretician John Bardeen (1908-1991), guided by a visionary supervisor William Shockley (1910-1989), invented the first transistor on 23rd December 1947. The other is the dirty side of science: two overworked scientists, spending the day before Christmas Eve alone in the lab, trying to overcome the challenges of insufficient material and sensitive equipment – their first prototypes stopped working by the mere closing of an adjacent lab door – just to almost lose the affiliated patent to their autocratic supervisor [1].

But no matter how the story is told, the result is the same: Originally working on a way to amplify signals for telephone lines, that fateful day the work of these three scientists led to the first working transistor and they shared the Nobel prize in Physics of 1956 for it. After their initial publication [2], it would need another eight years of progress in material technology before the first practical field-effect transistor based on silicon appeared. It gave the starting signal for the advances of microelectronics in integrated circuits, the rise of Silicon Valley, and the accompanying transformation of society. Nowadays, there are one million times more transistors produced each year worldwide than grains of wheat and rice combined. But the end of this success story is on the horizon: the miniaturization is hitting the physical limits when device dimensions reach the nanometer scale [3].

Another maybe even bigger problem comes from the fact that, forty years later, the fundamental principle of electronic devices is still the same: the movement of charges – electrons or holes – enables most of the modern processing power. An inevitable consequence of this charge flow (besides in a superconductor) is Joule heating, a problem that gets even worse for devices on the micro- and nanometer scale. Today, more than half of the power in a commercial processor is lost due to leakage currents and data centers use 50% of their energy consumption for cooling [4]. By 2030, some authors predict that information and communication technology could account for a fifth of the worldwide electricity demand [5] – a dooming economic and environmental crisis.

The solution to it may lay in a paradigm shift towards a technology that is already used in most data storage and memory applications in modern computers: spintronics.

1.2 The race between PRL and PRB: The birth of spintronics

The origin of this new idea shines a light on another aspect of science: the race to publish and patent. In 1988, two scientists, Albert Fert (1938) in France and Peter Grünberg (1939-2018) in Germany, were working separately from each other on the resistance of an epitaxially grown sandwich structure of two ferromagnetic (FM) and a non-magnetic metallic layer. They discovered that the electrical resistance would change in a magnetic field and therefore depend on the direction of the magnetizations, being higher for antiparallel alignment than for the parallel case.

The origin for this giant magnetoresistance lies in spin-dependent scattering. While an electron travels through such a system, it will scatter less when its spin is antiparallel to the magnetization of the ferromagnets. In the parallel case, this is true for all layers, in the antiparallel alignment only for every second one, which increases the resistance.

While the German team was first to submit these results to Physical Review B, they only measured a 10% change in resistance at low temperatures and it took till the next year until the paper was published [6]. The French group was able to observe a 50% magnetoresistance due to their superlattice structure and with a three-month delay sent their findings to Physical Review Letters, a high-impact journal that published the article the same year, seemingly getting the scoop and coining the new term along the way [7]. However, while writing up the draft for publication, Grünberg, seeing the potential applications, had also written a patent for a magnetic field sensor based on this effect that went on to earn his home institution, the Research Centre Jülich, an eight-figure income [8]. Consequently, it is hard to say who in the end won the race and the story has a happy end anyway, as both scientists were honored jointly with the Nobel prize in 2007.

As mentioned, giant magnetoresistance can be used as a sensor and, under the leadership of Stuart Parkin at IBM, the epitaxial growth of the films was replaced by cheaper sputtering deposition to commercialize it in read-heads for hard drives. The first products were introduced at the end of the 90s and in 2020 the market had a volume of roughly 60 billion dollars [9]. As this new technology was utilizing the spin of the electrons and its interaction with a magnetization of a ferromagnet or a magnetic field, it started a new field called spintronics, which dominates the memory and data storage sector till nowadays. Hard drives are still the cheapest way to store information permanently but the read heads are now based on the similar tunnel magnetoresistance, where the mid-layer is changed for an insulator [10]. Other spintronic effects such as spin-orbit torque or spin-transfer torque have led to the development and mass production of magnetoresistive random-access memory, a non-volatile memory concept that uses less energy and switches faster than other embedded or cache memories [11].

Obviously, the question arises if using spin could also solve the aforementioned problems of logic devices. However, it would require coherent spin transport over longer length scales, which requires the epitaxial growth of ultra-clean systems. Since the discovery of

the giant magnetoresistance, this presents a complicated material science challenge – one that potentially has been solved with a piece of adhesive tape.

1.3 Friday night experiments: The discovery of graphene

The two Russian scientists Andre Geim (1958) and Konstantin Novoselov (1974) had an interesting rule in their lab: They used Friday afternoons (and evenings) to conduct experiments without rules just following curiosity, trying out things that the German word *Schnapsidee* describes pretty well. In their Dutch lab in Nijmegen, where Novoselov did his Ph.D. under Geim, that led to levitating a living frog, demonstrating that the diamagnetic moment of water can have a stable energy minimum in a static magnetic field [12], earning Geim together with Michael Berry the Ig Nobel prize in 2000.

This tradition was kept when both of them moved to Manchester. One topic they got interested in was graphite, a material known to everybody from the tip of pencils. They were asking themselves if it would be possible to extract a single sheet of the crystal, a hypothetical atomically thin layer called graphene, which was theoretically studied but believed to be impossible to exist under real-world conditions. Following the maxim of making the best of the tools available, and perhaps inspired by the Gecko-like tape they invented previously, they started to peel off flakes of graphite from a larger crystal with commercial adhesive tape. Repeating that process, they were able to thin down the material but did not manage to dissolve the tape without losing those fragments. However, when pressing it on a standard SiO₂ wafer, the flakes not only stuck to the substrate but also showed different optical contrast, dependent on the number of graphene layers.

Subsequently, they studied the electrical transport properties of mono-, bi-, and few-layer flakes and were able to show interesting properties and clear indications for the two-dimensional (2D) nature of the samples [13, 14]. This not only started a boom in research with roughly 120,000 papers about graphene published until today but also won them the Nobel prize in Physics in 2010. The main achievement was however not just the new and intricate physics that graphene opened the door to, but also replacing molecular beam epitaxy equipment worth millions of dollars with an office supply and sharing their recipes freely with other research groups. Due to this, graphene was intensively studied and other 2D materials, such as insulating hexagonal boron nitride (h-BN), semiconducting transition metal dichalcogenides (TMDC), or even ferromagnets, were discovered [15, 16]. They could form the material platform on which the next generation of electronic and spintronic devices is built [17, 18].

1.4 This thesis: The combination of the abovementioned

This thesis explores how the extraordinary properties of the recently discovered 2D materials and their proximity effects in van der Waals (vdW) heterostructures can be exploited to realize spintronic device ideas to solve the current problems of transistor logic in complementary metal-oxide-semiconductor (CMOS) technology. The optimistic dream is that an all-2D-material spin-field effect transistor could break the current barriers of further miniaturization of integrated circuits and massively reduce the energy consumption by minimizing waste heat. Additionally, for the integration into existing electronic infrastructure, efficient spin-to-charge conversion (SCC) will play a critical role. The results of this work demonstrate both concepts on a laboratory, single-device level.

After the (historical) introduction has been given in this chapter, the following chapter starts with the theory necessary to understand the spin phenomena in Condensed Matter. Starting from the basic principle of spin-orbit coupling (SOC), the diffusive transport with its exponential decay and oscillatory precession of spin polarization is explained as well as the essential requirement of spin injection from an FM electrode. Finally, the main topic of this thesis, SCC is introduced, paying attention to the two underlying physical phenomena of spin Hall effect (SHE) and Rashba-Edelstein effect (REE).

Chapter 3 will give a broad overview of the progress in graphene and its use in spintronics. Starting from the discovery and the Nobel prize, important milestones and the most recent reports benchmarking values such as electron mobility and spin diffusion length will be referenced. The results are also compared to graphene grown by chemical vapor deposition (CVD) as a step towards industrial application. The chapter will include an overview of other 2D materials, mainly TMDCs, and finish with summarizing the effects in graphene-based vdW heterostructures, namely the proximity-induced SOC.

In Chapter 4, the main experimental techniques that were used during the preparation of this thesis are presented. Nanofabrication and the characterization of the samples required the usage of complex equipment such as electron-beam lithography and low-noise electronic measurements in a cryostat that can only be mentioned and summarized and not explained in detail. Where it is necessary, further pedagogical literature is referenced.

The following three chapters will present the results of the main publications of this Ph.D. (see the list of publications for full references). Firstly, the breakthrough of the experimental observation of SCC directly in graphene by non-local magnetotransport experiments. Secondly, building up on those findings, the electrical control of the proximity-induced SHE, tuning the conversion efficiency to one of the largest values reported so far. Thirdly, using the proximity effect to achieve the strong SOC regime and realize the long-awaited milestone of the Datta-Das transistor at room temperature.

Chapter 8 will take a look at how to use the scientific results presented here in a device design proposed by Intel. This requires taking the step from the non-local measurements suitable for studying fundamental physical effects to a local design, where outputs sufficient for real-world applications can be achieved.

The last chapter will provide a summary of the thesis and an outlook on future possible research topics. As typical in science, this thesis answers a few, small questions in the world of Condensed Matter Physics and at the same time opens up a lot of new ones for the next generation of students. Additionally, as every Ph.D. comes with its own special set of mistakes and regrets, I will also try to describe the encountered and (partially) resolved obstacles in this experimental work.

2 Spin

2.1 ...-orbit coupling

Electronics and spintronics are based on two fundamental properties of the electron: charge and spin. And while the first one is easily accessible to everybody who owns a balloon and a full head of hair, it took till the formulation of quantum mechanics in the first half of the 20th century to grasp the second one. Though much could be said about the electron's third property, mass, like the interesting concept of effective mass that allows the study of the electronic motion in crystals by band theory, it will play no role in the rest of this thesis.

Spin is an intrinsic angular momentum of the electron or rather any elementary particle. For electrons as fermions, it is quantized along an axis into the two distinctive values $\pm \frac{1}{2} \hbar$ or spin up and down, where \hbar is the reduced Planck constant, a fundamental value in quantum mechanics with the unit of eVs [19]. The classical interpretation of the spin as an angular momentum due to the electron spinning around its own axis can explain some of the experimental observations but falls short to describe the full concept of this quantum mechanical property.

Nevertheless, the interplay of spin and charge leads to a magnetic moment similar to the classical Ampère-Maxwell law. The spin magnetic moment of the electron m_s is given by

$$m_s = \pm \frac{1}{2} \hbar g \frac{e}{2m_e} \cong \pm m_B \quad (1)$$

where e and m_e are the charge and mass of the electron and m_B is the Bohr magneton, the magnetic moment due to the orbital angular momentum of an electron in its ground state [19]. This simple correlation between the two magnetic moments arrives from g , a dimensionless quantity with an approximate value of 2 in the case of electrons that can be derived from the Dirac equation, a milestone in theoretical physics, connecting quantum mechanics to special relativity.

m_s not only couples the spin to magnetic fields but also leads to the magnetization of ferromagnets, materials that have an imbalance between spin up and down electrons. This difference arises from the exchange interaction, originating in unpaired electrons and

Pauli repulsion for fermions, a quantum mechanical effect that again has no classical analog.

In contrast, there is a classical picture for the interaction between spin and orbital momentum called spin-orbit coupling: When moving through the electrical field of the atomic nucleus, or more generally any electric potential gradient, the electron sees in its rest frame an effective magnetic field – the spin-orbit field (SOF) – that interacts with the spin magnetic moment. This is an important concept for spintronics as it connects the motion of the electron caused often by its charge to its spin that can interact with ferromagnets or magnetic fields.

As mentioned, spin dynamics will be studied in graphene in this thesis, and while it and other 2D materials will be introduced in the next chapter, two fundamental properties are necessary for the following theoretical treatment of SOC: Firstly, due to its thickness of down to one atomic layer, the motion of the electron is limited to the x - y -plane. However, other materials such as TMDCs can be stacked on top along the z -axis, leading to a potential difference along that axis and a mixing of properties between the two materials called the proximity effect, further explained in Section 3.4. Secondly, due to its honeycomb crystal structure with two sublattices, graphene has two sets of points in its Brillouin zone called K and K' valley [20]. That is where the Dirac points of the band structure can be found, and their difference is important in the interpretation of most of the experimental results of this thesis.

The full Hamiltonian of this system has to consider all the different SOC terms that can occur [21]:

$$H = H_O + H_I + H_R + H_{VZ} + H_{PIA} \quad (2)$$

The first term describes the orbital part of the Hamiltonian:

$$H_O = \pm \hbar v_F (\sigma_x k_x + \sigma_y k_y) + \Delta \sigma_z \quad (3)$$

where v_F is the Fermi velocity, $\vec{\sigma}$ is the pseudospin Pauli operator for the vector space of the graphene sublattices and \vec{k} is the momentum vector. The \pm comes from the opposite sign for graphene's K and K' valleys. The last part opens up a gap Δ in the band structure due to a staggered potential if the two sublattices of graphene have different on-site energies, for example, due to wrinkles or varying proximity with the TMDC.

The following terms of Equation 2 describe the spin dynamics with the Pauli spin operator \vec{s} , with the next one giving the intrinsic SOC of graphene with the parameter λ_I :

$$H_I = \pm \lambda_I \sigma_z s_z \quad (4)$$

As carbon with an atomic number of 6 is a relatively light atom, the intrinsic SOC in graphene due to the nuclei is small and long spin coherence times are expected as the following SOC contributions mainly appear in proximitized graphene.

The third term is the Rashba SOC that has been originally studied in III-V semiconductor-based 2D electron gases (2DEG) but also applies to potential differences across interfaces or synthetic Rashba systems:

$$H_R = \pm\lambda_R(\sigma_x s_y - \sigma_y s_x) \quad (5)$$

Here, λ_R gives the strength of the SOC, which originates from the asymmetry across the interface of the graphene and TMDC flakes. The spin splitting due to the Rashba SOC leads to a unique spin texture for the in-plane momenta as seen in Figure 2.1a, which enables the Rashba-Edelstein effect for the interconversion of charge and spin as discussed in Section 2.5.

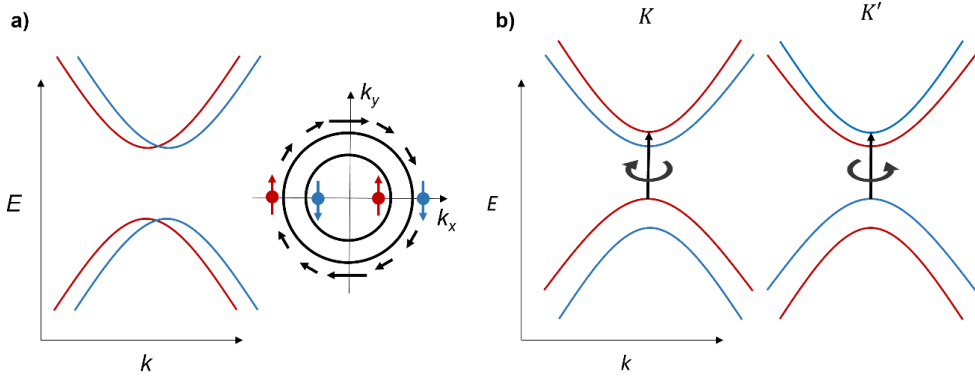


Figure 2.1: Effect of SOC on a general, parabolic energy dispersion. a) Rashba SOC splits bands into spin up (red) and down (blue). The typical spin texture is visible in the cut along the in-plane momentum axes through the conduction band. **b)** Spin-split bands for VZ SOC with different signs for K and K' valley. The selection rules for optical excitations with circularly polarized light (black arrows) are due to the spin-valley locking spin-sensitive. Images adapted from Ref. [22] and [23].

The fourth term describes the valley-Zeeman (VZ) SOC with the amplitude λ_{VZ} that is imprinted into graphene from the TMDCs due to the proximity:

$$H_{VZ} = \pm\lambda_{VZ}s_z \quad (6)$$

The origin of the VZ term is the broken inversion symmetry in the plane due to the three-layer hexagonal crystal structure that is based on the 1:2 atomic ratio of transition metals and chalcogenides in TMDCs [24]. Like in graphene, this leads to two inequivalent valleys, K and K' . Additionally, the heavy transition metal atoms have high atomic numbers and therefore a large intrinsic SOC. It leads to an energy splitting of the spin subbands, similar to the effect of a magnetic field, normally called the Zeeman effect – hence the name. Due to the time-reversal symmetry between the K and K' valleys, the sign of the SOF is opposite for the two valleys as seen in Figure 2.1b.

In general, the valley index can be used as a pseudospin, which could theoretically be used in a future field of valleytronics [24, 25]. This pseudospin also exists in graphene, but there it only stems from the broken inversion symmetry and no band splitting occurs due to SOC. In TMDCs, the imbalance of the spin texture by the VZ term leads to spin-valley locking, where the population of one valley is connected to one spin polarization, which makes experiments connecting valley and spin possible. So far, valleytronics has mainly seen optical experiments exploiting the selection rules, where the valley polarization has been measured [26] and pumped [27, 28] or, using the spin-valley locking, used for generating spin currents inside the TMDC [29] or injecting spins into graphene [23]. This also stems from the difficulty of electrically contacting the semiconducting TMDCs [30].

The last term in Equation 2, H_{PIA} for the pseudospin inversion asymmetry contribution, describes local effects of, for example, adatoms [31]:

$$H_{PIA} = \alpha(\Sigma_{PIA}\sigma_z + \Delta_{PIA})(k_x s_y - k_y s_x) \quad (7)$$

where α is the lattice constant of graphene and Σ and Δ are defined as the sum and the difference of the SOCs in the two sublattices. It was introduced to explain a series of experimental results discussed in Section 5.1 that finally were shown not to have a spin origin. Additionally, as it depends linearly on the momentum, it should lead to an electron-hole asymmetry that has not been observed in any spin lifetime anisotropy experiments [32]. As there are no experimental signs of this SOC part, it will be neglected for the rest of this thesis.

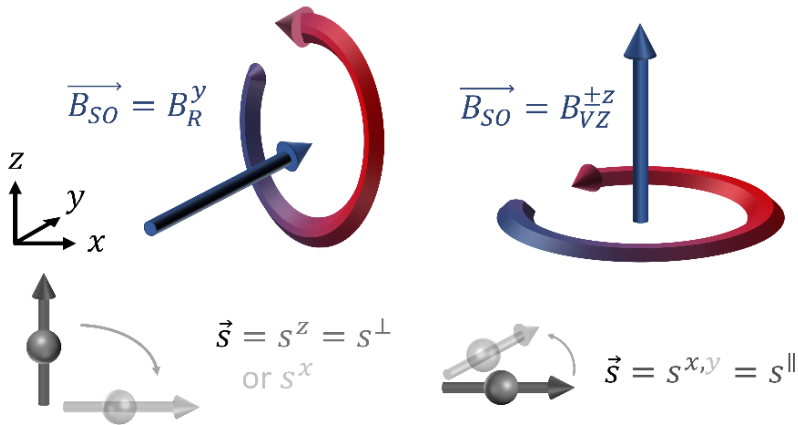


Figure 2.2: SOC and spin relaxation. The Rashba SOF \vec{B}_R points perpendicular to the momentum k_x along the y -axis in case of a potential difference along z . It therefore interacts with the magnetic moment of electrons with spins out-of-plane and along x shown in grey below. The resulting spin precession is shown in the circular red and blue arrows. The VZ SOF is parallel to the z -axis with opposite signs for K and K' valley and induces precession of the in-plane spins.

An overview of typical values for the individual SOC parameters for different TMDCs can be found in Ref. [24] or for proximitized graphene in Ref. [33], where the contributions vary by an order of magnitude across different TMDCs. However, for all of them, the important contributions are Rashba and VZ SOC, especially because they are also leading to the later discussed SCC effects. It should be noted that these two SOC and their SOFs have distinctive directions. Their symmetries will play a significant role in this thesis and are pictured in Figure 2.2. They lead to the precession of spins pointing along different axes and therefore govern independent spin relaxations. Both of these points will be discussed further in the next section, where the diffusion of the electrons and the spins through the crystal will be the topic, as, so far, the motion of the electron was only considered in terms of interaction of its spin with an effective magnetic field.

2.2 ... transport and relaxation

The Drude model explains the diffusive transport of an electron through a periodic, ionic crystal as a straight path that changes direction after elastic collisions similar to how an untalented billiard player gets his ball closer to the pocket. It connects the phenomenological values of resistance R , voltage V and current I of Ohm's law $R = V/I$ to the underlying crystal structure and the motion of the electron in an electrical field.

To include the spin into this picture, the two-channel model by Mott [34] splits up the charge carriers into two separated channels for spin up and down. As seen in Figure 2.3, this makes it possible to define a charge current I_c as net movement of charge without net accumulation of spins (panel a). Vice versa, a spin current I_s as spin transport without net movement of charges (panel c). Finally, a spin-polarized current is defined as movement of spins and charges (panel b), like it occurs in an FM due to its spin imbalance introduced by the exchange interaction.

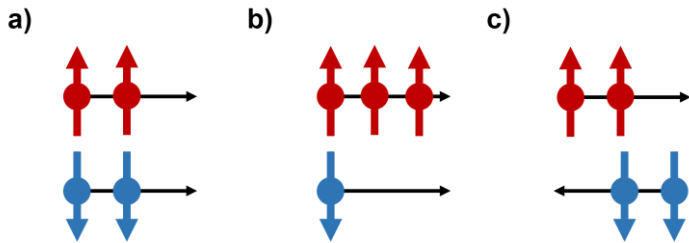


Figure 2.3: Charge and spin currents. a) Pure charge current, with the same amount of spin up and down electrons traveling in the same direction. b) Spin-polarized charge current, with an excess of one spin population. c) Pure spin current, with a balance of spin-polarized electrons traveling in opposite directions.

From the graphical definition, it is easily seen that $I_c = I_\uparrow + I_\downarrow$ as the sum of the currents for spin up and down and $I_s = I_\uparrow - I_\downarrow$ for the difference. This description of spin currents requires coherent spin polarization of the electrons through an imbalance between the

two channels up and down. Outside of ferromagnets, however, this separation will weaken over time towards an equilibrium. To understand spin transport via spin currents, it is therefore important to know the two main spin relaxation mechanisms that lead to a mixing of the carriers in the two channels. Conveniently, the underlying cause is in these two cases the already discussed phenomenon of spin-orbit coupling.

The first one is called Elliott-Yafet (EY) mechanism [35, 36] and is pictured in Figure 2.4a. Here, the SOC, associated with defects and impurities in the crystal structure, leads to a slight mixture of Pauli spin up and down states so that an electron state for spin up is also made up of a small portion of spin down. Normal scattering events caused by impurity atoms or defects now have a chance to flip the electron state from spin up to spin down. The spin relaxation time τ_s is therefore directly proportional to the momentum scattering time τ_p . EY is the dominant mechanism in non-magnetic metals and semiconductors with inversion symmetry such as Si or Ge. In graphene, the spin-flip requires typically a million scattering events before it occurs [17].

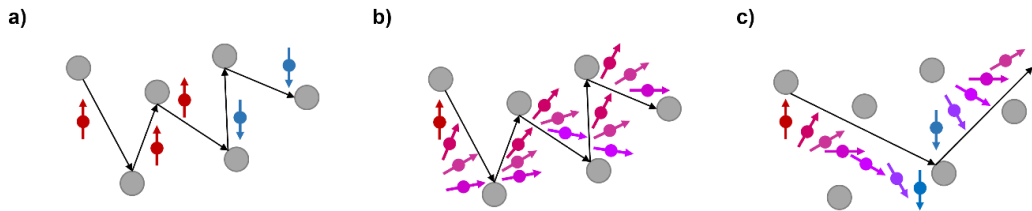


Figure 2.4: Spin relaxation mechanisms. **a)** For the Elliott-Yafet mechanism, spin relaxation is induced by certain scattering events as they can flip the spin polarization. **b)** In the Dyakonov-Perel mechanism, the spin precession due to SOC leads to spin relaxation and is restarted by scattering. **c)** If the SOF is large enough and the time between scattering events is sufficiently long, the spin polarization can be flipped by precession. This is called the strong spin-orbit coupling regime.

The second mechanism is called Dyakonov-Perel (DP) [37] and is shown in Figure 2.4b. It is present in systems without inversion symmetry, so, for example, non-centrosymmetric crystals such as GaAs. In that case, the SOFs due to inversion symmetry breaking lead to the precession of the direction of the spin polarization as they act on the spin magnetic momentum as described in Figure 2.3. Every scattering event now changes the direction of \vec{k} and therefore \vec{B}_{SO} , resetting the precession. As a consequence, τ_s is proportional to $1/\tau_p$.

It should be noted that, for the DP mechanism, it is possible to reach coherent spin precession from spin up to down only due to the SOF as illustrated in Figure 2.4c. This strong SOC regime can be achieved when the momentum scattering time is long enough and the SOF is strong enough so that the spin polarization fully rotates between scattering events [38]. If one could control this internal precession electrically, it would mean the realization of the spin field-effect transistor that was proposed by Datta and Das over 30

years ago [39]. Since then, it has been a long-sought-after milestone in spintronics to realize this modulation of the spin polarization in a diffusive channel at room temperature. Chapter 7 will not only present other concepts for this device and recent realizations at low temperatures in other material systems, but also demonstrate a Datta-Das transistor made up of a graphene/TMDC heterostructure.

An early theoretical work showed that the DP mechanism should be larger in graphene than EY [40], while a later work came to the conclusion that depending on the carrier density the EY mechanism should be dominating the spin relaxation [41]. Additionally, the type of defects would play a role: In CVD-grown graphene, grain boundaries and on exfoliated flakes, impurities should lead to scattering events interacting with the spin.

Experimentally, the dependence of τ_s on the mean free path and therefore τ_p showed that in monolayer graphene the EY mechanism is largest [42], which was later confirmed with the addition that DP is dominating in bilayer graphene [43], as there, it is an order of magnitude larger than in the case of monolayers [44]. The most probable cause for this is the influence of adatoms on the spin transport as defects and impurities on the surface are more and more shielded with an increasing number of layers, suppressing the EY mechanism. Convincingly, the same interplay between the two mechanisms was found for CVD-grown graphene [45]. Additionally, the spin relaxation due to EY is weaker when increasing the number of layers in a few-layers flake of graphene [46] and comparable to the DY mechanism when encapsulating monolayer graphene in h-BN [47].

Mathematically, the spin relaxation can be described in the framework of a diffusion equation – coming from the Drude model – with two different chemical potentials for spin up and down – stemming from Mott’s two-channel picture – giving the chemical potential for spin:

$$\mu_s = \frac{\mu_\uparrow - \mu_\downarrow}{2} \quad (8)$$

and charge:

$$\mu_c = \frac{\mu_\uparrow + \mu_\downarrow}{2} \quad (9)$$

They can be translated to carrier densities by multiplying with the density of states at the Fermi level:

$$n_{s/c} = \mu_{s/c} e \nu(E_F) \quad (10)$$

and their spatial change, together with the width w and square resistance R_{sq} of the channel, gives the currents defined above:

$$I_{s/c} = - \frac{w}{e R_{sq}} \frac{d\mu_{s/c}}{dx} \quad (11)$$

The evolution in time is now given by the diffusion and relaxation of the spin that so far should account for all spin dynamics and therefore result in a steady-state:

$$\frac{\partial \mu_s}{\partial t} = D_s \frac{\partial^2 \mu_s}{\partial x^2} - \frac{\mu_s}{\tau_s} = 0 \quad (12)$$

where D_s as the spin diffusion constant was introduced. The product of the two spin transport parameters gives the spin diffusion length $\lambda_s = \sqrt{D_s \tau_s}$, fully characterizing the spin transport. Before adding a magnetic and electric field to this description, the next section is going to discuss how to create the spin imbalance $\mu_\uparrow \neq \mu_\downarrow$ (so that $\mu_s \neq 0$) through spin injection.

2.3 ... injection and detection

As already mentioned, ferromagnets have an intrinsic imbalance between spin up and down due to the exchange interaction. A charge current flowing in an FM electrode is, therefore, spin-polarized [48]. At the interface between the FM and a non-magnetic metal, this coupling between charge and spin leads to a spin accumulation at either side [49]. In the case of a tunnel barrier, the spin polarization of the charge current flowing through the interface is now given by the polarization $P = I_s/I_c$ and the resulting total chemical potential by:

$$\mu = \frac{P(\mu_\uparrow - \mu_\downarrow)}{2} + \frac{(\mu_\uparrow + \mu_\downarrow)}{2} \quad (13)$$

As the channel is connected to the electrical ground, the second term for the charge will be zero. The first term gives the amount of injected spins that will diffuse in the non-magnetic metal side as a spin current. The direction of the spin polarization is given by the magnetization direction of the FM.

In a lateral spin valve (LSV), a second FM electrode is used to detect this spin current, shown in Figure 2.5a. Depending on the magnetization, a different chemical potential μ_\uparrow or μ_\downarrow is probed as seen in Figure 2.5b. The resulting voltage is picked up as a non-local voltage with:

$$V_{NL} = \pm \frac{P \mu_s}{e} \quad (14)$$

where μ_s is multiplied by the spin polarization of the FM detector P that should be equal to the reciprocal case of injection [50]. The sign of the voltage depends on the magnetization direction of the detection electrode.

As in Figure 2.5c, the experimental data is often plotted as $R_{NL} = V_{NL}/I_c$ against the magnetic field that switches the magnetization of the FM electrodes. As they have different widths, the two electrodes have distinct coercive fields that lead to an observable antiparallel state. The advantage of the non-locality of the measurement is the reduction of non-spin-related signals. Theoretically, the two values for parallel and antiparallel states should be centered around zero but, experimentally, a background is often unavoidable due to spurious currents [52, 53] or inhomogeneous current flow through the

tunnel barrier [54]. They can be removed by taking the difference between the two values to obtain the spin signal $\Delta R_{NL} = (R_{NL}^P - R_{NL}^{AP})/2$ [55].

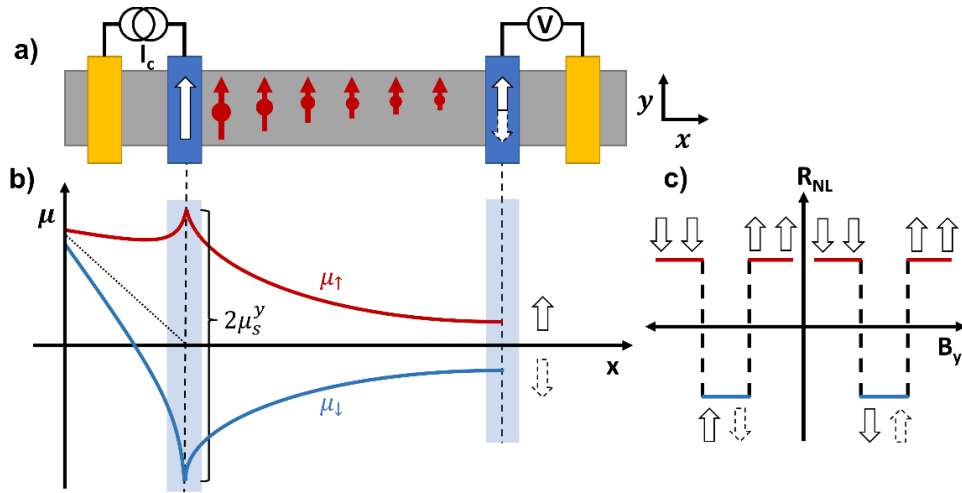


Figure 2.5: Schematic of the non-local lateral spin valve measurement. **a)** The setup with two FM electrodes (blue), their magnetization (white arrows) and non-magnetic channel and electrodes (grey and gold). The non-local measurement scheme (see Figure 4.7 for explanation) leads to a diffusion of spin (red). **b)** Chemical potential inside the channel between the FM electrodes (shaded blue around the dashed lines). The difference between μ_{\uparrow} and μ_{\downarrow} is shown for the injector. The detector probes a positive or negative value of this quantity depending on the magnetization orientation. The dotted line indicates the chemical potential of the electrons in the absence of spin injection. **c)** The resulting non-local resistance when sweeping the magnetic field to flip the magnetization of the FM electrodes. Images adapted from Ref. [51].

The principle of spin injection from a ferromagnet was first theoretically proposed by Aronov in 1977 [56] and experimentally demonstrated by Johnson and Silsbee eight years later together with the non-local measurement scheme [57]. The LSV design and ΔR_{NL} signal was presented in 2001 by the van Wees group, where the devices were made up of permalloy as FM electrode and a non-magnetic metal for the channel [55]. One year later, a tunnel barrier between the FM electrode, in this case Co, and the metallic channel was introduced [51]. By varying the distance between the electrodes over different devices, the spin diffusion length of the channel materials, Cu and Al, was determined. It was shown that λ_s strongly decreases up to room temperature, a longstanding problem for spintronic applications that can be seen across most non-magnetic metals [58]. This can be solved with the introduction of graphene as an almost temperature-independent spin transport channel.

The first, rather crude local LSV measurements with graphene were already done in 2006 [59]. In the next year, the van Wees group again added tunnel barriers and the non-local measurement protocol to extract a spin diffusion length of around $2 \mu\text{m}$ at room temperature [60]. By optimizing the device design and tunnel barriers, non-local LSV signals of $\Delta R_{NL} \approx 130 \Omega$ have been measured in graphene at room temperature [61].

Tunnel barriers between the FM and the channel are necessary [62] due to the conductivity mismatch between the two materials [63]. Especially in the case of graphene, the FM has a lower spin resistance, which leads to backflow of the injected spins, suppressing the signal across the channel. A Schottky barrier would also increase the resistance but destroy the spin polarization P of the interface that characterizes the amount of spin injected into the channel as a percentage of the charge current. The precise control of the contact, barrier thickness, and resistance is therefore extremely important.

In the already mentioned experiments [51, 60, 61], Al_2O_3 and MgO have been used as a resistive oxide layer, while in this thesis TiO_2 is utilized. However, it is known in the graphene community that all of these materials do not grow epitaxially on graphene, but rather in islands with pinholes. It is probable that those spatially inhomogeneous layers result in additional spin relaxation and hinder spin transport [54]. However, there have been reports of successfully using pre-patterned contacts for spin injection into graphene flakes stamped onto them after fabrication to avoid this issue [64]. Other solutions are the use of bilayer h-BN as a tunnel barrier with up to 100% spin polarization [65] or SrO to allow for higher current densities [66].

The LSV measurements with FM electrodes are the basis for most of the experimental data presented in this thesis. Besides this electrical scheme, it is also possible to inject and detect spins thermally from a ferromagnet with the spin-dependent Seebeck [67] and spin-dependent Peltier effects [68], respectively. Spin injection is also possible with electromagnetic radiation through ferromagnetic resonance by spin pumping [69] and its reciprocal effect, spin-transfer torque, can be used for detecting spin currents [70]. A third way are the spin-to-charge conversion mechanisms explained in Section 2.5.

2.4 ... precession

The non-local LSV measurement scheme described so far in this section only included the application of a magnetic field along the easy axis of the FM electrode (y) to switch the magnetization, measuring the step-like shape of the change in R_{NL} as the spin signal. But, since the first reports [57], experimentalists have also recorded the response of the system to a magnetic field perpendicular to the easy axis, for example, along the channel (x) or out-of-plane (z).

The external magnetic field interacts with the spin momentum and, like the SOFs, leads to precession, named – after the same response of light – Hanle precession. The resulting Larmor frequency can be calculated with:

$$\vec{\omega} = \frac{g\mu_B}{\hbar} \vec{B} \quad (15)$$

The term for the precession has to be added to Equation 12, where the spin chemical potential now is a vector $\vec{\mu}_s$, which refers to the spin polarization:

$$D_s \frac{\partial^2 \vec{\mu}_s}{\partial x^2} - \frac{\vec{\mu}_s}{\tau_s} + \vec{\omega} \times \vec{\mu}_s = 0 \quad (16)$$

As seen here and illustrated in Figure 2.2, the magnetic field, spin polarization, and precession direction are orthogonal to each other. Spins pointing in one direction will therefore be transformed and rotate into another direction. For example, for a field along x , $\vec{B} = (B, 0, 0)$ and $\vec{\omega} = (\omega, 0, 0)$, this leads to a coupling between the spin accumulations along the y and z axes:

$$D_s \frac{\partial^2 \mu_s^y}{\partial x^2} - \frac{\mu_s^y}{\tau_s} - \omega \mu_s^z = 0 \quad (17)$$

$$D_s \frac{\partial^2 \mu_s^z}{\partial x^2} - \frac{\mu_s^z}{\tau_s} + \omega \mu_s^y = 0 \quad (18)$$

$$D_s \frac{\partial^2 \mu_s^x}{\partial x^2} - \frac{\mu_s^x}{\tau_s} = 0 \quad (19)$$

Due to the isotropic spin transport in graphene, for other magnetic field directions, the indices can be permuted. As the detector electrode only probes the spin pointing in-plane along y , only the solution for μ_s^y to Equation 17 and 18 has to be analyzed. Those diffusion equations can be solved by a set of Bloch equations, known from nuclear magnetic resonance. To solve these equations analytically, a set of boundary conditions has to be assumed:

- For both sides of the channel, the spin accumulation has to go to zero: $\lim_{x \rightarrow \pm\infty} \mu_s = 0$.
- Between those two minima, μ_s is continuous, even below the injector or over boundaries between regions with different spin transport parameters.
- Also, the spin current I_s is continuous, except at the injector, where it changes due to the injected spin current by PI_c .

The solution can then be expressed in terms of non-local resistance, as the applied charge current will be the input and the measured voltage the output for the measurement. As in the LSV signal, there is a parallel and antiparallel state, plotted exemplary in Figure 2.6a. However, the data now includes the oscillatory precession and exponentially decaying spin relaxation, so when looking at it as a function of B , the spin transport parameters can be extracted.

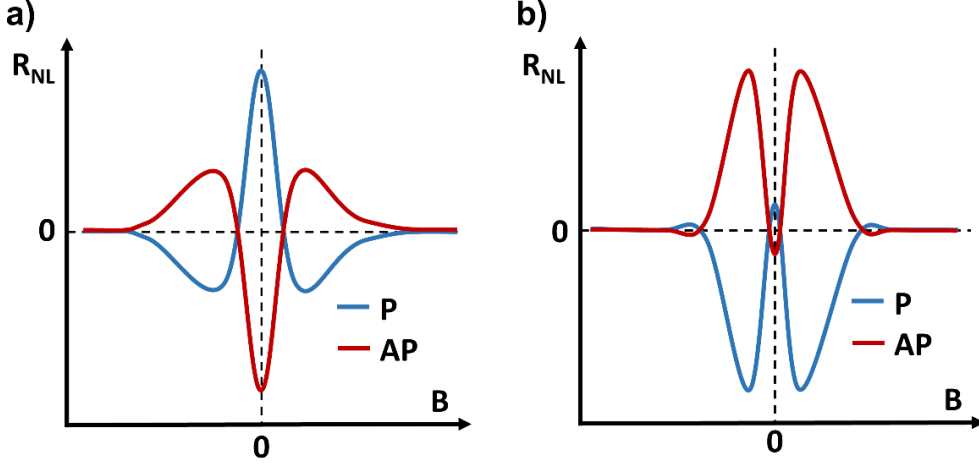


Figure 2.6: Symmetric Hanle precession. a) The resulting non-local resistance when sweeping the magnetic field perpendicular to the easy axis of the FM electrode for the isotropic ($\tau_{\parallel} = \tau_{\perp}$) and b) anisotropic ($\tau_{\parallel} < \tau_{\perp}$) case. The blue and red curves indicate the initial state of the injector and detector magnetizations, parallel and antiparallel, and only differ in sign. Images adapted from Ref. [71].

This is done by taking the following equation as the solution to the Bloch equations and fitting it to the difference between the two symmetric Hanle curves to remove any non-spin-related background [51]:

$$\begin{aligned} \Delta R_{NL} &= \frac{R_{NL}^P - R_{NL}^{AP}}{2} \\ &= \frac{P^2 \cos^2(\beta) R_{sq} \lambda_s}{w} \operatorname{Re} \left\{ \frac{e^{-\frac{L}{\lambda_s} \sqrt{1-i(\omega)\tau_s}}}{\sqrt{1-i(\omega)\tau_s}} \right\} \end{aligned} \quad (20)$$

where β is the angle between magnetization direction and easy axis of the FM electrode, R_{sq} , w and L is the square resistance, width, and length of the spin transport channel. The fit parameters are the spin diffusion length λ_s and spin relaxation time τ_s (that as a reminder are connected to the spin diffusion constant D_s by $\lambda_s = \sqrt{\tau_s D_s}$) and the product of the polarization of the injector (P_i) and detector (P_d) interface $P^2 = P_i P_d$. The resulting polarization $P = \sqrt{P_i P_d}$ is an effective polarization for the LSV.

As the magnetic field interacts not only with the spin magnetic moment of the electrons in the channel but with the FM electrode, the direction of the effective magnetization will depend on \vec{B} . The angle β can be extracted from the experimental data or theoretically from the Stoner-Wohlfarth model as explained in Appendix A. The spin transport parameters obtained from distance-dependent LSV measurements are very similar to the

ones extracted from the fits of Hanle precession data [51, 72]. More details on the computational realization of the fits with Python can be found in Appendix B.

So far, only the isotropic case has been discussed. To introduce anisotropy between in-plane and out-of-plane spins, the uniform spin lifetime τ_s in Equation 17 and 18 has to be replaced with an in-plane and out-of-plane lifetimes τ_{\parallel} and τ_{\perp} [42]:

$$D_s \frac{\partial^2 \mu_s^y}{\partial x^2} - \frac{\mu_s^y}{\tau_{\parallel}} - \omega \mu_s^z = 0 \quad (21)$$

$$D_s \frac{\partial^2 \mu_s^z}{\partial x^2} - \frac{\mu_s^z}{\tau_{\perp}} + \omega \mu_s^y = 0 \quad (22)$$

For the case of $\tau_{\parallel} < \tau_{\perp}$, as can be found due to VZ SOC in TMDCs or proximitized graphene, the resulting symmetric Hanle precession curve is plotted in Figure 2.6b. Due to the decreased lifetime for the spins point along y , $\Delta R_{NL}(B = 0)$ as the distance between parallel and antiparallel curves at zero field is reduced. However, due to the enhanced out-of-plane lifetime when the spins precess towards z , the shoulders for the mid-field range are pronounced.

The last step for a full description of the spin dynamics in the lateral spin valve is the addition of electron drift due to an external electric field, for example, via an applied dc current. The updated Equation 12 then includes the drift velocity v_d :

$$D_s \frac{\partial^2 \mu_s}{\partial x^2} - \frac{\mu_s}{\tau_s} - v_d \frac{\partial \mu_s}{\partial x} = 0 \quad (23)$$

It is apparent from the formula that the spin drift can extend the spin transport over distances longer than allowed by the spin relaxation [73]. The physical explanation is that – opposite to the situation in Figure 2.3c – a net movement of electrons along the direction of the current also transports spin, additionally to the spin diffusion. This directed spin transport is faster than diffusion and asymmetric in the direction of the current, so that both acceleration and slowdown of the spin transport are possible. Experimentally, those two cases can be realized by changing the sign of the applied dc current, hence offering increased control over the spin transport in the channel. A similar effect for the spin signal has been achieved by introducing a thermal gradient across the graphene channel but, as with other spin-dependent thermal effects, this is outside of the scope of this thesis [74].

2.5 ...-to-charge conversion

The effect that a longitudinal current produces a transverse voltage in an out-of-plane magnetic field due to deflection of electrons by the Lorentz force was discovered by Hall in 1879 [75] and is used until today to measure the carrier density in planar samples. However, he also found that the linear dependence between transverse voltage and magnetic field did not hold true for ferromagnets, where an additional zero-field contribution could be measured, the accordingly named anomalous Hall effect. The

origin for it was later found to be again SOC, as the effective magnetic field deflects electrons depending on their spin polarization [76].

Dyakonov and Perel [77] concluded that this deflection for moving electrons in a non-magnetic material should lead to an observable spin separation, essentially giving a mechanism to convert charge currents into spin currents, named spin Hall effect by Hirsch in 1999 [78]. As seen in Figure 2.7a, spin up and down electrons of an unpolarized charge current are deflected to opposite sides due to the different sign of the spin magnetic moment and a spin accumulation is created on the sides of the channel, leading to a perpendicular spin current.

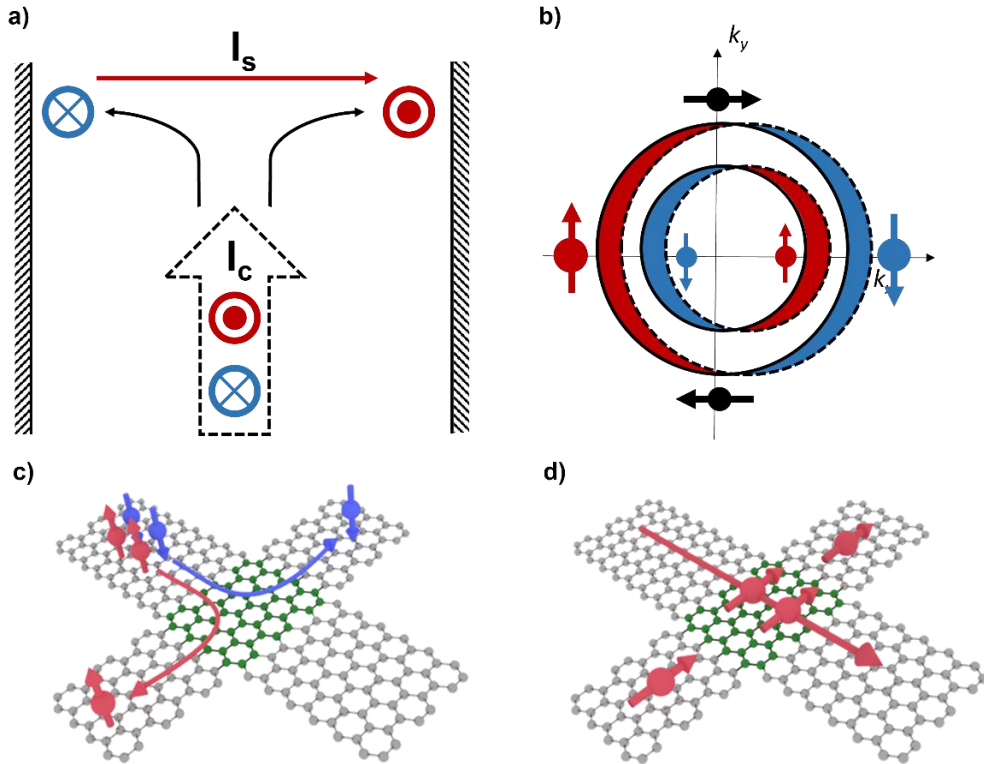


Figure 2.7: SCC mechanisms. **a)** SHE, where a deflection of spin up and down electrons of a charge current into opposite directions leads to a transverse spin separation and accumulation on the sides. **b)** Rashba spin texture, where a circular spin-polarized Fermi contour for the in-plane momentum leads to a spin-polarized current when shifted along one axis due to an applied electric field and therefore a spin accumulation. **c)** For the SHE in proximitized graphene, a charge current is converted below the TMDC (area in green) to a transverse out-of-plane-polarized spin current that diffuses into the etched Hall bar. **d)** For the REE, a charge current leads to an in-plane spin accumulation below the TMDC that diffuses into all directions, while here only the spin current along the graphene Hall leads is pictured.

In three-dimensional materials, a spin accumulation will also appear on the top and bottom surfaces. To generalize, the directions of charge and spin current have to be considered now. Together with the direction of the spin polarization, they follow:

$$\vec{I}_s = \frac{\hbar}{e} \theta_{SH} \vec{I}_c \times \vec{s} \quad (24)$$

where θ_{SH} is the spin Hall angle, which gives the efficiency of the interconversion between the two currents as a dimensionless parameter. A longstanding endeavor in the field of spintronics is to find materials with large θ_{SH} to use them in the next generation of spintronic devices.

In the case of this thesis, where the SHE occurs in proximitized graphene, only the spin current with out-of-plane polarization is picked up in a structured Hall bar with a TMDC flake in the center as illustrated in Figure 2.7c. A spin current along z can be neglected due to the 2D charge and spin transport in graphene. However, it is possible that a charge current flows into the TMDC flake and leads to SHE in the bulk there.

Besides the intrinsic mechanism explained so far, that nowadays is formulated with a more general motivation from topology via the Berry curvature [79], there are extrinsic mechanisms such as skew scattering and side jump that lead to the same spin separation. They are also contributing to the SHE as well as to the anomalous Hall effect. Disentangling those different contributions is an ongoing research topic in the field of spintronics [80].

Additionally, the Onsager reciprocity [81], coming from the time reversibility of the microscopic dynamics of spin diffusion, dictates that the inverse spin Hall effect (ISHE) as spin-to-charge conversion works as well: a spin current will lead to a transverse charge current that can be measured as a voltage across two leads in a Hall bar structure. Also, in this case, charge and spin current directions and spin polarization will adhere to the orthogonality rule.

The first experimental observation of the SHE was done by Kerr rotation microscopy, with which the current-induced spin accumulation on the edges of a semiconductor channel could be detected [82]. For the ISHE, a spin current was created by spin pumping from an FM and injected into Pt, generating a measurable voltage that, as predicted, depends on the polarization of the spin current [83]. Valenzuela and Tinkham then measured the same effect electrically with an LSV in the same year [84]. They injected a spin current with an FM into the channel of a Hall bar made of Al. Due to the ISHE, a voltage can be measured across the Hall arms, similar to the detection of spins with an FM electrode. The polarization P of the detector (or injector for the SHE) is hereby replaced with the factor between I_c and I_s , the spin Hall angle θ_{SH} . As this non-local setup to measure SCC will be used in most experiments of this thesis, it is shown separately in Figure 2.8, but is fundamentally not very different to the LSV shown before.

Similar to the anisotropic transport, the polarization of the spin current plays now an important role. Due to the orthogonality of the (I)SHE in Equation 24, only spins pointing

out-of-plane will be converted. In the original report [84], this is achieved experimentally by applying a magnetic field out-of-plane that pulls the magnetization of the FM electrode out-of-plane. Consequently, the injected spin current has an out-of-plane magnetization. However, in the case of graphene, an out-of-plane magnetic field can also lead to large magnetoresistance that can hide the SCC contribution to the signal, so that a different approach is chosen here. While injecting a spin current with a polarization along y , a magnetic field along x will precess those spins towards the z direction. Depending on the strength of the magnetic field and the parameters of the spin transport, a certain amount of spins will be converted in the area with ISHE.

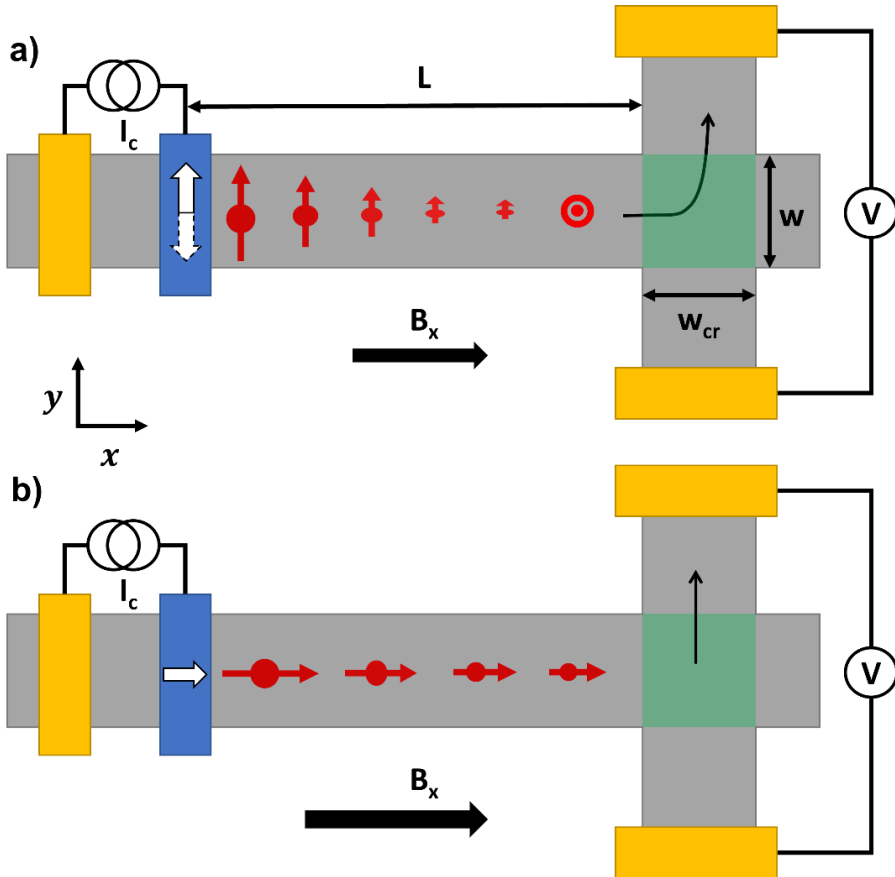


Figure 2.8: Schematic of the non-local SCC measurement. a) A spin current with a polarization depending on the magnetization direction of the injector electrode is injected into the channel and precesses due to the applied magnetic field B_x . The spin current is converted via the ISHE inside of the green shaded area that represents the proximitized graphene with TMDC on top. The resulting voltage can be picked up across the Hall bar arms. **b)** In the case of the IREE, a stronger magnetic field leads to a pulling of the magnetization of the injector electrode and the injection of an in-plane-polarized spin current. According to the symmetry of the SCC mechanisms, it will be converted along the graphene/TMDC interface to a transverse charge current.

Accordingly, in the mathematical treatment, P_d of the detector in Equation 20 has to be replaced by θ_{SH} and the solution for μ_s^z to Equation 17 and 18 will give the contributing amount of spin current. Also, the spins are only converted in the area with SOC, where the graphene channel is proximitized, so that just the width of the Hall cross w_{cr} (the green shaded areas in Figure 2.8) has to be used. The following equation, using the two non-local resistances $R_{NL}^{\uparrow/\downarrow}$ for up and down magnetization along y of the injector electrode, describes the dependence on the magnetic field:

$$R_{SCC} = \frac{R_{NL}^{\uparrow} - R_{NL}^{\downarrow}}{2} = \frac{P\theta_{SH} \cos^2(\beta) R_{sq} \lambda_s}{w_{cr}} \text{Im} \left\{ \frac{e^{-\frac{L}{\lambda_s} \sqrt{1-i(\omega)\tau_s}}}{\sqrt{1-i(\omega)\tau_s}} - \frac{e^{-\frac{L+w_{cr}}{\lambda_s} \sqrt{1-i(\omega)\tau_s}}}{\sqrt{1-i(\omega)\tau_s}} \right\} \quad (25)$$

The resulting antisymmetric Hanle curves are plotted in Figure 2.9a. The two different curves are now not for the parallel and antiparallel state of the FM electrodes but only for the initial magnetization direction of the injector (or detector in the case of SHE). As for the symmetric Hanle, the difference R_{SCC} between the two curves is used to remove any spurious effects in the measurement that lead to a non-zero background in the non-local measurement. A fit of Equation 25 to the experimental data allows the calculation of the SCC parameters θ_{SH} and λ_s , assuming an injector polarization P , for example, the one from the symmetric Hanle curves.

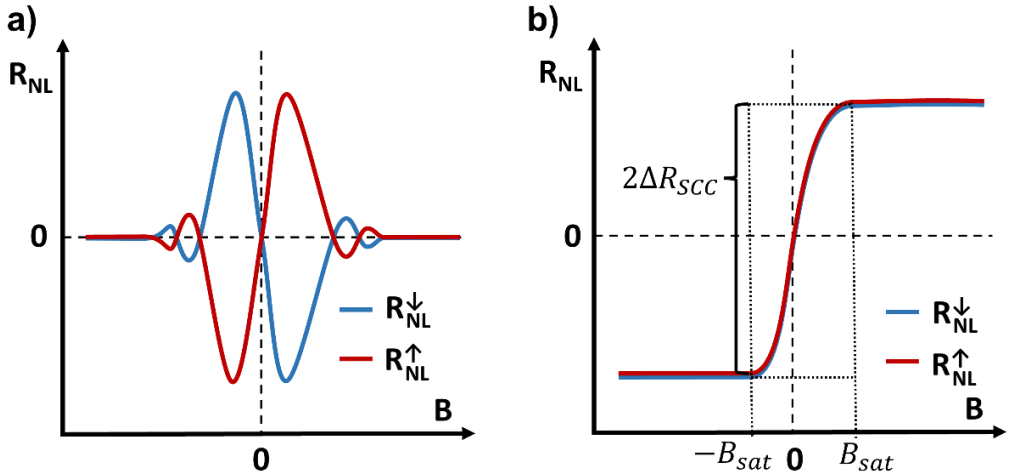


Figure 2.9: Measured signal for SCC experiments. **a)** Antisymmetric Hanle curves for a magnetic field perpendicular to the spin polarization that is converted as for the ISHE in the LSV in Figure 2.8a. **b)** S-shaped signal for a magnetic field parallel to the converted spins as for the IREE in the LSV in Figure 2.8b. In both panels, the blue and red curves indicate the initial state of the injector magnetization, along $\pm y$. In a) they only differ in sign, in b) they are identical.

In the same way Dyakonov and Perel deduced spin separation and therefore spin-charge interconversion from the basic principle of SOC, Edelstein looked at the Rashba spin texture in a 2DEG. It is a direct result of the above-defined Rashba SOC spin splitting the bands as depicted in Figure 2.1a, sometimes called Rashba or Bychkov–Rashba effect [85]. Edelstein proposed that the combination of this momentum-dependent spin polarization together with an electric current induces a spin accumulation [86]. The applied electric field, in this case $\vec{E} = (E, 0, 0)$, shifts the Fermi contours, which produces a nonequilibrium spin density as illustrated in Figure 2.7b. The reason for this is the larger density of states with spin down for electrons travelling in the direction of $+k_x$. The resulting spin accumulation has a perpendicular, in-plane polarization and can diffuse as a spin current as shown in Figure 2.7d for the case of proximitized graphene in a Hall bar shape. From an experimental point of view, a system with REE therefore converts a charge current into a spin current with in-plane spin polarization.

Reciprocally, the inverse Rashba-Edelstein effect (IREE) converts a spin accumulation with an in-plane polarization at an interface or in a 2D channel into a perpendicular charge current. For the first experimental observation of the IREE, the spin accumulation was created by circularly polarized light, so that the effect is also known as the spin galvanic effect [87]. On the other hand, for the REE, the in-plane polarization can also be probed optically as it introduces a degree of circular polarization to the photoluminescence spectrum and changes sign when reversing current direction [88]. Subsequently, the SCC via the IREE has also been observed with an electrically induced spin current by spin pumping [22] or in the LSV design used here [89]. The Onsager reciprocity between the direct and inverse can also be observed electrically in the same LSV [90, 91].

In the latter case, one can apply an out-of-plane magnetic field to generate the spin polarization along x by precession that would be converted by the IREE in the Hall bar cross. As for the ISHE, an antisymmetric Hanle curve would then be measured. However, one can run into the same magnetoresistance problems as mentioned above. Alternatively, applying $\vec{B} \parallel x$ will, for strong enough fields, pull the magnetization of the FM electrode into the in-plane hard axis and lead to the injection of the required spins. This LSV measurement is sketched in Figure 2.8b. Figure 2.9b shows the resulting S-shaped signal in essentially the same measurement setup as for the ISHE. If both mechanisms are present, the signal will be a convolution of the curves in panels a) and b). To distinguish the two effects, $R_{NL}^{\uparrow/\downarrow}$ and $R_{NL}^{\downarrow/\uparrow}$ have to be subtracted (ISHE) and added (IREE) as the two effects depend differently on the initial magnetization direction of the injector.

The conversion due to the IREE can be mathematically analyzed in a 2D system by:

$$\Delta R_{SCC} = \frac{R_{NL}^{\uparrow/\downarrow}(+B_{sat}) - R_{NL}^{\uparrow/\downarrow}(-B_{sat})}{2} = \frac{P\alpha_{REE}R_{sq}\lambda_s}{w_{cr}} \left(e^{-\frac{L}{\lambda_s}} - e^{-\frac{L+w_{cr}}{\lambda_s}} \right) \quad (26)$$

Different from Equation 25, there is no precession in the spin signal and therefore no difference between the two curves for different initial magnetization alignments. Rather,

the spin signal is extracted from the difference in non-local resistance for a large positive and negative magnetic field, higher than the saturation field of the signal B_{sat} , indicated in Figure 2.9b. Above this saturation, the spins are injected in-plane along x , as shown in Figure 2.8b.

The Rashba-Edelstein efficiency was introduced above as dimensionless efficiency between the spin current and resulting charge current $\alpha_{REE} = I_s^y / I_c^x$, analog to the spin Hall angle θ_{SH} . However, in most experimental cases such as the ones that use spin pumping to create a spin current [22, 92, 93], the efficiency is given by $\lambda_{IREE} = I_c^{2D} / I_s^{3D}$, where a three-dimensional spin current from an FM is converted to a 2D charge current at an interface, 2DEG or in a surface state. Consequently, this efficiency now has the unit of length. As in the case of the ISHE, this figure of merit is comparable across different materials systems and therefore advantageous to α_{REE} , for which the amount of spin current reaching the conversion area has to be calculated. But similar to the case of the ISHE, the conversion happens across the spin diffusion length, just now here along an interface of two materials and for the in-plane spin polarization, so that $\lambda_{IREE} = \alpha_{REE} \lambda_s^{\parallel}$.

It can be theoretically shown that for the ISHE, the product of $\theta_{SH} \lambda_s$ is equivalent to λ_{IREE} [94], making it possible to compare the efficiencies of the two effects. The spin diffusion length takes the spin transport across the conversion area into account and gives the maximum amount of spin that can be converted, a figure of merit that is important for device application [95]. For example, there has been recently a device proposal by Intel for a scalable spintronic logic, combining SOC for read-out and magnetoelectric switching for writing [96]. While the advantages in energy consumption and size are obvious – the switching energy is reduced by a factor of up to 30, the switching voltage and the area for a logic component by a factor of 5 – the current SCC materials are not efficient enough to deliver the required voltage output. For resistive materials, a lower boundary of $\theta_{SH} \lambda_s$ or $\lambda_{IREE} > 5$ nm is expected [96].

For prototypical ISHE materials such as the heavy metals Pt or Ta, $\theta_{SH} \lambda_s$ is 0.1-0.3 nm [80, 97], very similar to the results for the IREE from the well-known Bi/Ag Rashba interface [22]. However, there are theoretical predictions of SCC in graphene proximitized with a TMDC, where the efficiency is one or two orders of magnitude larger [98, 99]. This could clear the path to application for a new generation of spintronic devices as a beyond-CMOS technology [100]. The necessary information to understand this novel and interesting material system will be given in the next section.

3 Two-dimensional materials

3.1 Graphene

3.1.1 Early history, discovery, and Nobel prize

Graphene is a 2D sheet of carbon atoms arranged in a honeycomb lattice. The early history of it starts with the study of naturally occurring graphite, where the layers are stacked to form a three-dimensional crystal weakly coupled by van der Waals forces. While it was initially regarded as niche basic research, the technological advances that followed World War II spurred the search for new materials and the more applied field of material science became increasingly important. This rush brought the discovery of buckyballs and carbon nanotubes as the first member of the family of fullerenes, of which graphene can be seen as the most extreme archetype (see Figure 3.1) and works on graphene in bulk graphite through transmission electron microscopy [101].

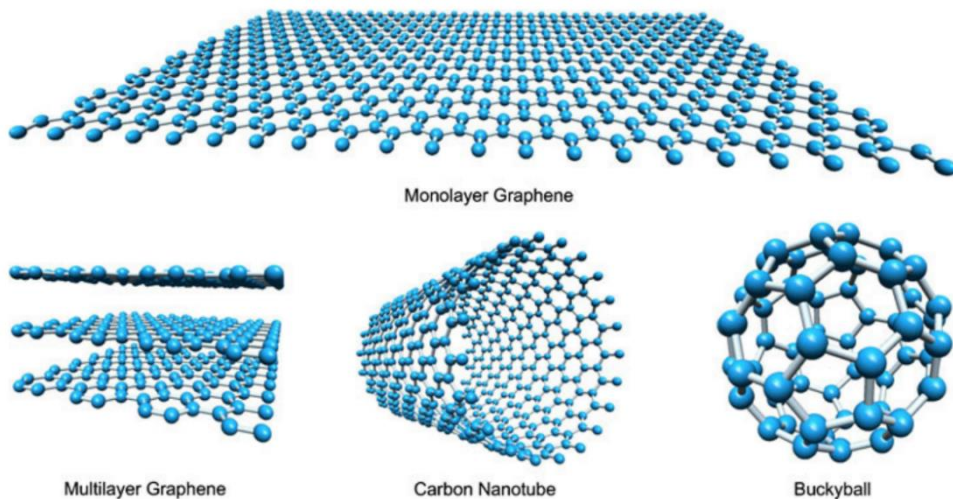


Figure 3.1: Crystal structure of carbon-based fullerenes. The hexagonal structure of monolayer and multilayer graphene, carbon nanotubes, and buckyballs. Images taken from Ref. [102].

At the center of these efforts and influential for the theoretical developments in the area of graphene was Mildred Dresselhaus, the so-called “queen of carbon”, who together with her husband, Gene, wrote the principal textbook on fullerenes. Not surprisingly, as

he discovered the SOC now named after him, they also published the first paper on SOC in graphite [103]. The theoretical exploration of graphene led on the one hand to predictions of interesting physics and on the other hand to doubt about the possibility of the realization of such a truly 2D system [104, 105].

These findings again inspired more experimental research into graphene with different approaches such as separating the layers of graphite by inserting ions through chemical or applied electrical potential – intercalation – but also with the help of tape – exfoliation [106]. The latter method was finally the breakthrough in 2004 for achieving few-layer down to monolayer flakes as reported in the seminal Science and Nature papers [13, 14]. Besides this surprisingly easy-to-reproduce method to create atomically thin films in micrometer size and of high quality, in which electrons are confined to a truly 2D channel, the main highlight in these first articles was the electronic properties of graphene. Figure 3.2a shows the unique band structure, where the linear dispersion for electrons and holes leads to a Dirac cone for conduction and valence band that only have a small overlap in the Dirac point. This results in a strong ambipolar electric field effect, where conductivity (Figure 3.2b) and carrier density can be tuned electrically (Figure 3.2c) across a charge neutrality point (CNP). It should be noted that, for bilayer graphene, this band structure is slightly distorted and a bandgap can open up around the Dirac point for an electrical field across [107].

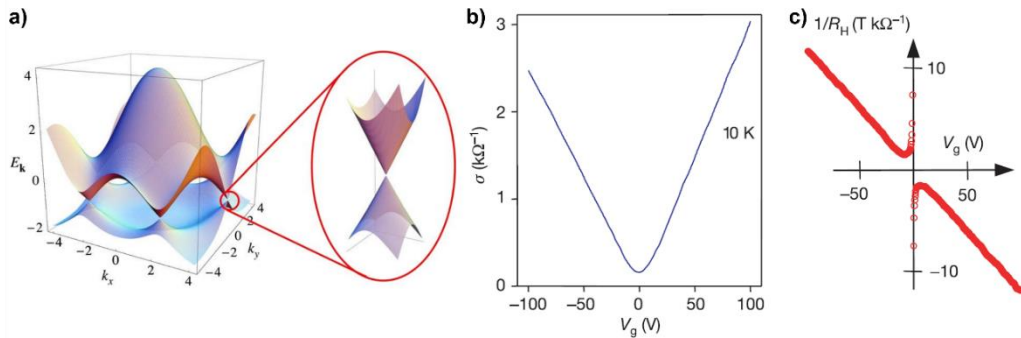


Figure 3.2: Electronic properties of graphene. **a)** Band structure of graphene, showing the six Dirac cones for electrons and holes for the three pairs of K and K' valleys and zoomed in one of the Dirac points in detail. **b)** Conductivity of graphene as a function of gate voltage, effectively sweeping the band structure in a) from bottom to top, so that the Dirac point coincides with the point of minimum conductivity. **c)** Hall coefficient of the same sample as a function of gate voltage, indicating the transition from hole to electron regime across the CNP. Images taken from Ref. [108] and [14].

While these results paved the way to current applications such as graphene field-effect transistors as highly sensitive sensors [109], graphene is also an excellent material to study fundamental physics. Early on, it was shown that, due to the linear dispersion, carriers behave as massless Dirac fermions evidenced by a half-integer quantum Hall

effect at low temperatures [14]. Shortly after, the quantum Hall effect was observed even at room temperature – a first for any material system [110].

3.1.2 Recent scientific developments

The abovementioned discoveries of fundamental research, as well as future electronic applications, rely on the high carrier mobility in graphene devices. It is almost temperature-independent and roughly the same for electrons and holes, with initial room temperature values of around $10,000 \text{ cm}^2/\text{Vs}$ [13]. While this is still an order of magnitude lower than the theoretical limit due to intrinsic phonon scattering at around $200,000 \text{ cm}^2/\text{Vs}$, it is close to the maximum value of around $40,000 \text{ cm}^2/\text{Vs}$ due to the interactions with the standard SiO_2 substrate [111]. An insulating substrate can induce charge puddles in the graphene and its surface roughness leads to wrinkles in the 2D material, hindering the electrical transport.

To overcome these limitations, experimentalists have suspended graphene in air or vacuum [112], reaching mobilities of up to $200,000 \text{ cm}^2/\text{Vs}$ but only at low temperatures [113] and after current annealing that detaches any residue from the fabrication process from the flake [114]. However, the complicated nanofabrication necessary for the suspended devices makes future exploration difficult. Additionally, the intrinsic wrinkling of graphene, one of the reasons the 2D crystal is actually thermodynamically stable, prevents reaching higher values at room temperature.

Accordingly, for improving the electrical transport, graphene should be straightened out by providing an atomically flat substrate and should also be shielded from any fabrication residue that leads to unwanted, intrinsic doping and scattering. This can be achieved by sheathing it with another 2D material, preferably an insulating one such as h-BN. Essentially a sandwich with graphene in the middle, these encapsulated devices have shown mobilities and carrier inhomogeneities that are almost an order of magnitude better than bare devices on SiO_2 [115–117]. Besides the abovementioned advantages, stacks of 2D materials also show self-cleansing at the interface. In van der Waals heterostructures, any remaining contamination tends to aggregate in larger clusters, leaving the rest of the area atomically clean [117, 118]. This behavior is not observed for other substrates and is one of the reasons why combining 2D materials is an interesting research avenue.

Furthermore, encapsulating with 2D materials also encases the inner flake and protects it against reacting with oxygen as the top and bottom layer seal airtight. Only this shielding allows studying sensitive materials such as the 2D ferromagnets mentioned in Section 3.3.

However, to electrically contact the flake, the cover of the top or bottom insulating layer has to be broken. This area of direct exposure to the deposited metal will weaken most of the advantages inherent to vdW heterostructures. One way to circumvent this problem is using a metallic 2D material embedded in the stack as an electrode. Another one is to etch the sides of the three-dimensional stack to create one-dimensional contacts for the

graphene two-dimensional flakes. These edge contacts are minimally invasive and have improved the recorded mobility values, reaching $140,000 \text{ cm}^2/\text{Vs}$ at room temperature [119]. It is possible to extend this method for more complex geometries by using graphene as an etch stop and accessing layers inside the stack with one-dimensional contacts [120].

Achieving these high charge carrier mobilities in more complex vdW heterostructures has been also a cornerstone for the study of the spin transport in graphene. Following the same advances in device design and fabrication process, the spin diffusion length λ_s has been increased step-by-step in recent years.

Initially, theoretical calculations based on the Dyakonov-Perel and Elliot-Yafet mechanisms for spin relaxation estimated an upper limit of around $20 \mu\text{m}$ [40]. Although the first experiments for exfoliated graphene on SiO_2 only reported λ_s of $\sim 2 \mu\text{m}$ in LSVs measured via spin precession [60], these results were almost temperature-independent and already impressive at 300 K, since comparable metallic systems need liquid helium temperatures to reach such values [51, 55, 58].

Pre-patterning the complicated contacts necessary for spin injection on a substrate and stamping a top-capped graphene flake increased λ_s up to $10 \mu\text{m}$ [64] and fully encapsulating it with h-BN up to $12 \mu\text{m}$ [121]. At low temperatures, values even larger than $20 \mu\text{m}$ have been reported [122], additionally suggesting that the spin transport is mainly limited by the graphene regions outside of the LSV and, by increasing the encapsulated region, spin information could be transported over even longer distances. By paying attention to the full coverage of exfoliated graphene by h-BN to prevent any contact with fabrication residue and wrinkles that are inherent to smaller capping layer flakes, it was possible to reach $\lambda_s = 30 \mu\text{m}$ in exfoliated graphene in channels of a few micrometer length [123].

So far, this value could only be improved by using a directional drift current to accelerate the diffusive spins over distances of $90 \mu\text{m}$ at room temperature [73]. This method is also used in the results of Chapter 7. However, non-local spin transport over $45 \mu\text{m}$ channel length was reported in large-scale devices, even with a λ_s of just $13 \mu\text{m}$ [124, 125]. To realize such channel lengths, exfoliated flakes are inadequate, so that they are replaced by grown graphene, which is the topic of the next section.

3.1.3 Steps towards industrial application

From the beginning of the graphene “hype”, it was clear that the realization of applied graphene devices will hinge on an industrial-scale production method. Exfoliation is not a deterministic process and flakes are randomly placed on the substrate and as mentioned above, their area is small, preventing any automated process for subsequent fabrication.

The most studied epitaxial process is chemical vapor deposition, where gases supply the elemental reactants to assemble the target material and form a solid on a heated substrate. In the case of graphene, the gases are normally methane or ethane providing the necessary

carbon atoms and metal single or large-grain crystals can be used as substrates due to their smooth surfaces and catalytic role.

The current industry standard hereby is Cu foil as it is a relatively inexpensive material and shows low solubility for carbon, which self-limits the growth process to a monolayer. After the growth at temperatures of up to 1000 °C that also anneal the copper to increase grain size, the graphene has to be detached from the Cu foil and transferred to a substrate. In the beginning, this meant wet etching the metal film completely [126] or dry-releasing it with the help of a polymer membrane, which reduces the process residue and increases the mobility of the synthetic graphene by an order of magnitude [127]. In both cases, the copper cannot be used again, which increases the production cost noticeably. However, it is now also possible to pick up the CVD-grown graphene directly from the Cu foil, which then can be used again, and together with encapsulation in h-BN this method achieves mobilities of up to 100,000 cm²/Vs at room temperature [128].

The high-quality, large-area flakes of graphene synthesized in that way allow 2D spintronic circuit architectures on a large scale [129] that could be used in more complex devices and logic circuits. Additionally, theoretical calculations show that spin transport is not affected strongly by grain boundaries, the main drawback of CVD graphene compared to exfoliated flakes in electrical applications [130]. Fine-tuning the growth process also enables studying the spin transport in mono-, bi- and trilayer graphene in a more controlled way than exfoliation can provide [45].

With the further maturation of graphene, other production methods have been introduced, for example, roll-to-roll techniques for flexible and transparent electrodes in commercial products such as touchscreens or wearable electronics, where sizes up to 30 inches have been reported [131]. However, neither in the field of electronics nor spintronics has graphene found its full industrial potential yet, despite large multinational efforts such as the European Union-funded Graphene Flagship [132].

Another quite different approach for synthesizing graphene, that should be mentioned here, is to bake out the silicon from SiC single-crystal surfaces, leaving patches of multilayer graphene [133]. Interesting results and large signals in LSVs have been achieved with this material [134], but the necessary substrates are prohibitively expensive for commercial purposes. However, they are used in the epitaxial growth of other 2D materials such as transition metal dichalcogenides.

3.2 Transition metal dichalcogenides

The fundamental structural principle of graphite that allows the exfoliation of graphene, strong covalent bonds in the plane and only weaker van der Waals forces between the layers, also applies to other materials, generally called vdW materials. Hence, since the discovery of graphene, the family of 2D materials has been growing steadily [15, 16].

One prominent sub-group of these layered materials are TMDCs. Chemically, they are made up of a transition metal with a partially filled d-shell, found in the d-block of the

periodic table, prominently Mo^{4+} and W^{4+} , and two chalcogenides as a dianion, mainly S^{2-} , Se^{2-} or Te^{2-} . Electrically, they are mainly semiconducting with large bandgaps interesting for optoelectronic applications [135, 136].

Opposite to graphene, the monolayers of TMDCs are made up of two elements and the crystal structure is different as seen in Figure 3.3a. As every transition metal ion is connected to six chalcogenides in a trigonal prismatic geometry, the trilayer sandwich structure breaks the inversion symmetry of the crystal in the plane.

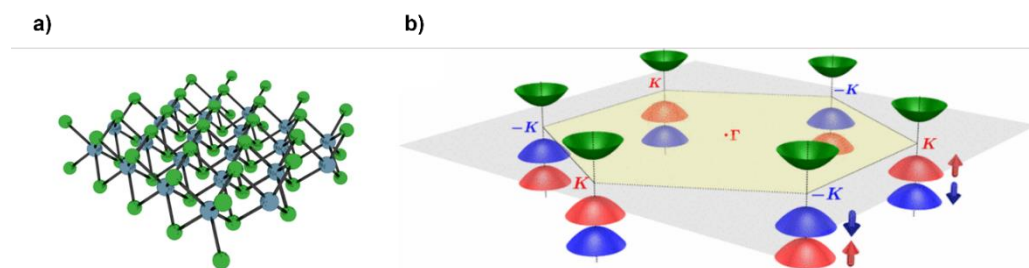


Figure 3.3: Crystal and band structure of TMDCs. a) Monolayer of a TMDC with a layer of transition metal ions sandwiched between chalcogenides. b) Band structure of a TMDC monolayer with the spin-split bands located at the K points. Image taken from Ref. [24].

This missing symmetry leads to an asymmetric potential and together with the spin-orbit coupling originating from the d-orbitals of the heavy metal atoms lifts the spin degeneracy of the conduction and valence band [137]. In TMDCs, the spin splitting has been theoretically predicted to be in the range of 100s of meV [138] and has been observed experimentally with angle-resolved photoemission spectroscopy in the bulk and mono-layer [139, 140]. Additionally, inversion symmetry breaking creates valley polarization, where low energy carriers are located in two inequivalent valleys in momentum space, specifically the K and K' points given by the location of the band edges around the direct band gap (shown in Figure 3.3b). The time-reversal symmetry couples the binary valley index to the spin, leading to spin-valley locking [24] and also to the prediction of valley and SHE in TMDCs [24]. While the valley Hall effect has been confirmed experimentally [141], a direct measurement of the SHE in TMDCs remains an open challenge. Finally, the additional valley degree of freedom has been reported to cause magnetoelectricity [142].

Depending on the symmetry between the upper and lower three chalcogenides connected to one transition metal ion, TMDCs can be divided into two different phases: H phase (prominently MoS_2 , MoSe_2 , WS_2 , and WSe_2) that are mainly semiconducting and T phase (such as MoTe_2 and WTe_2) that are mainly semimetallic [143]. Figure 3.4 compares the two cases graphically. A number before the letter for the phase indicates the stacking of the neighboring layers, where 1 stands for AA and 2 for AB stacking, and so on.

Experimentally, contacting semiconducting TMDCs electrically has proven to be difficult. Routinely used metal contacts such as Au form a Schottky barrier with the 2D

materials and their atomically flat surfaces have no dangling bonds, creating a high-resistive interface. Additionally, in contrast to bulk material, the interface governs most of the electrical properties, making the contact resistance sensitive to growth conditions and prevents for instance using doping, a common strategy to reduce barrier height. However, these obstacles can be overcome when using another metallic 2D material as an electrode, most frequently graphene [30].

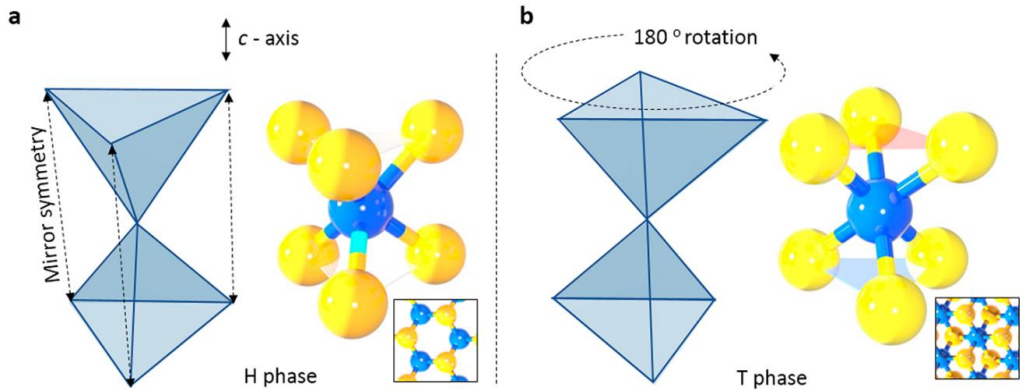


Figure 3.4: Crystal phases of TMDCs. a) H phase, where the mirror symmetry between the two layers of chalcogenides is preserved. **b)** T phase, where the two tetrahedrons are rotated to each other. Images taken from Ref. [143].

Besides members of the three normal groups of electrical conductivity – metals, semiconductors, and insulators – there are also layered TMDCs that show superconductivity such as NbSe₂ that can be studied in 2D devices [144, 145]. For example, the vdW interface between exfoliated samples has been used to construct a Josephson junction [146].

In spintronics, TMDCs are mainly exploited for their strong SOC and have been used passively as spin sink layer in non-local lateral spin valve [147, 148] and spin torque measurements [149] or also actively as spin current source [150–152]. Interestingly, the lower symmetry of TMDCs in the 1T phase allows couplings between spin and charge that are prohibited in high symmetry crystals, for example, additional directions in the SHE [153, 154]. However, the mirror symmetry in 2H TMDCs, together with the valley-dependent SOF due to VZ SOC, will stabilize spins pointing out-of-plane as for them intravalley scattering will not lead to dephasing [155, 156]. The result is a long spin lifetime τ_S^\perp that has been observed optically at low temperatures with values of up to 5 ns [157].

Similar to graphene, TMDCs can be grown by CVD [158] and, recently, even wafer-sized synthetic heterostructures with graphene have been reported [159]. This progress is especially important as all the advantages of vdW heterostructures such as self-cleansing interfaces also apply for TMDCs and, for example, the electron mobility can be improved by encapsulation [160].

3.3 Other members of the 2D material family

In general, the material of choice for encapsulation is in most cases h-BN providing an atomically flat substrate [115]. Like graphene, it can be exfoliated down to the monolayer from a bulk crystal [161], as every layer is made up of a honeycomb crystal of boron and nitrogen atoms. Additionally, as both materials have similar lattice constants, they can be easily combined in vdW heterostructures. However, h-BN has a set of complimentary properties: as an insulator with a large bandgap of almost 6 eV, it can be used where the electrical or thermal conductivity of graphene would be a problem or where photoluminescence is needed [162].

The key role h-BN plays in the study of 2D materials can maybe be best seen in publication statistics: Takashi Taniguchi and Kenji Watanabe of the National Institute of Materials Science in Japan grow the high-quality h-BN crystals used by most research teams worldwide, in a high-temperature, extreme-pressure anvil. With almost 1000 papers and 100,000 citations, they are now some of the most published researchers.

Not so widely studied, but, nevertheless, interesting, is another monoatomic 2D material, black phosphorus that shows a wrinkled honeycomb lattice. Similar to graphene, it hosts a 2DEG with high carrier mobility that can be tuned electrically but also has a semiconducting bandgap that is strongly dependent on the number of layers [163, 164]. An LSV experiment with large changes in the non-local resistance has been realized in black phosphorus [165]. However, it has not seen many applications outside of initial academic research, especially due to its high sensitivity to air.

Finally, also ferromagnetic materials have been added to the 2D family recently [166] that show stable magnetization down to the monolayer, such as Fe_3GeTe_2 [167], or bilayer, such as $\text{Cr}_2\text{Ge}_2\text{Te}_6$ [168]. Even the transitions from ferromagnet to antiferromagnet and back for varying the thickness from mono-, to bi- to trilayer have been observed [169]. 2D FM candidates now include transition metal dichalcogenides such as CrSe_2 , VSe_2 , or CrTe_2 , transition metal trihalides with CrI_3 and CrCl_3 as examples, and transition metal phosphorous trichalcogenides, for instance, MnPS_3 and NiPS_3 [170, 171].

What most of those materials have in common is that they are extremely sensitive to air or humidity – sometimes the atomic thin films disappear in seconds under ambient atmosphere. They are therefore exfoliated in gloveboxes and encapsulated for further measurements.

Switching the magnetization of a 2D FM with the spin-orbit torque of another 2D material [172–174] or using them to inject spin into graphene [175] are ongoing research challenges and solving them will pave the way for spintronic devices embedded fully into vdW heterostructures.

3.4 Van der Waals heterostructures and proximity effects

Besides exfoliating different materials reliably in μm -sized flakes with a detectable number of layers, deterministic transfer methods are the basis for creating vdW heterostructures. While the exact processes are described in Section 4.1, the basic steps are stamping and picking up, where a flake or a whole stack is placed in a specific spot or is removed from a substrate to transfer it to another one via a membrane. This essentially enables control on an atomic level and, due to the wide variety of 2D materials, designing the properties of a crystal layer by layer is possible.

Multilayer stacks enable the realization of more complex electronic devices such as a vertical p-n junction fabricated only from 2D semiconductors, metals, and insulators [176] or light-emitting diodes in vdW heterostructures with tens of layers [177]. For spintronic applications, vertical spin filters and magnetic tunnel junctions have been realized completely or partly with vdW heterostructures [178].

But vdW heterostructures are not only remarkable because the sequence of the different materials can be controlled down to the monolayer, but also because their order influences the properties of every layer, generally known as the proximity effect [179]. This opens up a plethora of different combinations and new physics to explore. The reason lays in the atomical thinness of 2D materials: in adjacent layers the electronic orbitals hybridize, transferring properties between them. Physically, this interlayer coupling is due to the quantum tunneling through the barrier of the vdW gaps and even though the vdW interactions are weak, this proximity effect can drastically change the electronic band structure or the spin texture. It should be noted that, on a fundamental level, this is different from other ways of changing or combining properties of materials such as doping or functionalizing with adatoms, where the addition often comes with the disadvantages of impurities or defects leading to, for example, low mobility [179].

Historically, the proximity effect has been mainly explored for superconductivity, where the properties of a superconductor are transferred to an adjacent material [180] and initially this was also a topic of interest for graphene, studying the proximity effect in graphene-based Josephson junctions [181].

After the discovery of further 2D materials and graphene's prominent role as spintronic material, the focus shifted towards enhancing SOC in graphene, mainly by combining it with TMDCs that have an inherently strong SOC. Figure 3.5 shows the resulting band structure due to the proximity effect of such vdW heterostructures, where a large spin splitting can be imprinted into graphene and, in the case of WSe_2 , even band inversion can be observed. As expected for the hexagonal lattice, the minima in the energy-momentum dispersion are around the corners of the Brillouin zone, the K and K' points [25].

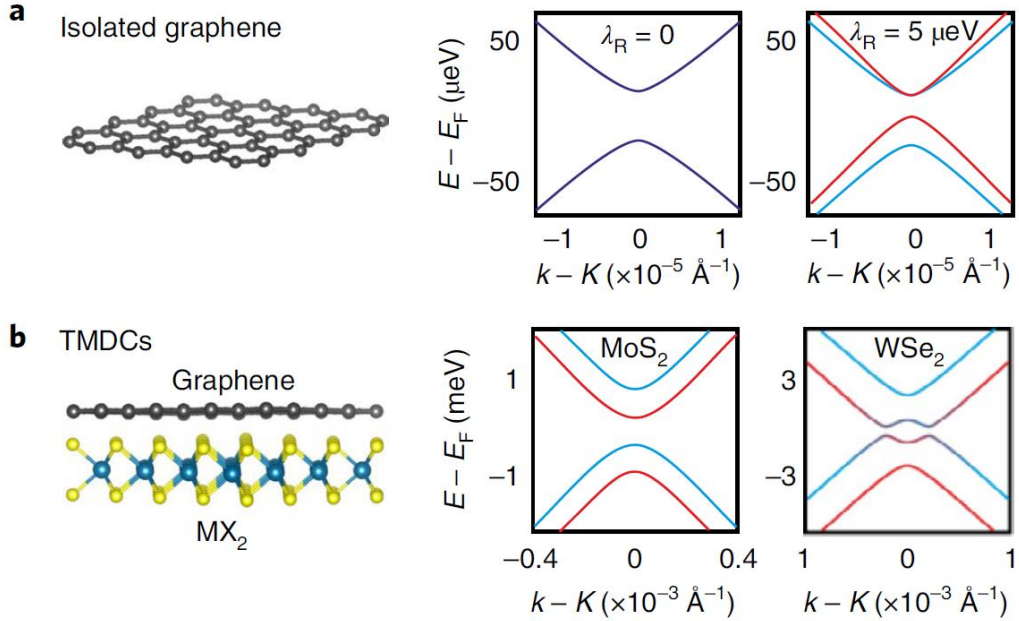


Figure 3.5: Effect of an adjacent TMDC on the band structure of graphene calculated from first principles. a) The band structure of pristine graphene around the K point in momentum space with a small band gap opening up between conduction and valence band due to intrinsic SOC ($\lambda_I = 12 \mu\text{eV}$). The same on the right with a Rashba strength of $5 \mu\text{eV}$, where blue and red show the energy of spins up and down, respectively. **b)** Band structure of a graphene-based heterostructure with MoS_2 as TMDC on the left and WSe_2 on the right. In both cases the proximity-induced valley-Zeeman SOC leads to spin-split bands, but, only in the second case, band inversion is also predicted. Images taken from Ref. [21].

One important finding of the theoretical first-principles calculations of these bilayer systems is the preservation of the Dirac cone in the bandgap of the TMDC [182]. The proximity effect, therefore, is not detrimental to the electrical transport properties of graphene. This allows the combination of the intrinsic high mobility and long spin diffusion length with the imprinted strong SOC, which is in the range of a few meV [21].

As explained in Section 2.1, there are two main parts to the SOC in graphene proximitized by a TMDC. Due to the potential difference at the interface, a sizable Rashba field arises, that points in the plane, perpendicular to the momentum direction. It mainly governs the spin relaxation of the out-of-plane spins. The effective field associated with the VZ SOC of the TMDC, on the other hand, points out of the plane with opposite signs for the K and K' valleys. It leads to spin precession of the spins with polarization in the plane. The resulting spin texture and anisotropic spin transport depend on the effective SOFs composed of those two contributions. In general, the strength of the SOC is determined by the choice of the TMDC, besides parameters of the interface such as distance of the vdW gaps, roughness and wrinkles of the flakes, and contamination between the layers.

Looking at the calculated band structure of graphene/TMDC (Figure 3.5b), it can be seen that, in the case of WSe₂, the enhancement of the SOC is so strong that the valence and conduction band form an anti-crossing for spin up and down. This band inversion is one of the precursors to the quantum spin Hall effect [33]. Similarly, pseudo-helical edge states that are topologically trivial, but, nevertheless, protected against perturbations have been theoretically predicted [183] and experimentally observed by capacitance measurements [184]. These findings have driven the search for emergent topological phenomena in proximitized materials.

Prominently, the proximity-induced SOC also leads theoretically to anisotropic spin transport as the spin-valley locking of the TMDC is imprinted into graphene. The out-of-plane lifetime τ_s^\perp is then stabilized by the VZ SOF and the in-plane spin lifetime τ_s^\parallel is tied to the much shorter intravalley scattering. The anisotropy, given by the ratio $\tau_s^\perp/\tau_s^\parallel$, is predicted to reach values of tens to hundreds [185].

In comparison, τ_s^\perp is around 20% smaller than τ_s^\parallel in pristine graphene [42] and while this value can be increased to 35% by electrically gating [121], in agreement with the EY mechanism in monolayers, these measurements require a large, out-of-plane magnetic field, so that the real value is probably between 0 and 10% [186]. In bilayer graphene, the small out-of-plane SOC of 12 μeV leads to a $\tau_s^\perp/\tau_s^\parallel$ ratio of 8 at low temperatures and only close to the Dirac point. These results also support the argument for the DP mechanism in bilayer graphene. However at room temperature, the spin transport is, similar to the case of monolayer graphene, almost isotropic [187].

For graphene/TMDC heterostructures, an anisotropy factor of ~ 11 with $\tau_s^\perp \approx 40$ ps and $\tau_s^\parallel \approx 3.5$ ps at 75 K has been found experimentally [71], with similar results reported up to room temperature [188]. This large anisotropy of the spin transport is a clear sign for the enhanced SOC by proximity effect.

Another consequence of the induced SOC is the occurrence of weak antilocalization [98]. This quantum mechanical correction of the resistance is based on the self-interference of electrons in different paths due to scattering. When the precession times due to SOFs are similar to the momentum scattering time τ_p , the spin state can influence this interference and change it from destructive to constructive. This change can be reverted, when applying a magnetic field, aligning the spins, hence measuring a cusp-like feature in the resistance for low fields. The spin transport parameters can be extracted from this data, making it a useful tool to study spin dynamics in electronic measurements.

A large set of such graphene/TMDC experiments has been conducted, using MoS₂ [189–191], WSe₂ [189–193] and WS₂ [189, 191, 192, 194–196]. The reported strengths of the resulting SOC ranges from 1 to 10 meV and there is no clear consensus on the type, with some authors claiming Rashba and others VZ SOC. However, all of them show short spin relaxation times in the range of picoseconds, which can only be explained by an enhanced SOC, for which the most likely reason is the proximity effect.

The most interesting consequence of the SOC in graphene induced by a TMDC via proximity for this thesis is however the theoretical prediction of SHE [98, 197] and REE [32, 99] in those heterostructures. The imprinted SOFs lead to these SCC effects as described in Section 2.5. However, the connection between them is not as straightforward as naively assumed. Both SOC types are necessary to observe the SHE and while the REE can be seen if only Rashba SOC is presented, it is enhanced for an additional VZ SOC contribution [32, 197].

While the abovementioned weak antilocalization needs a certain amount of intervalley scattering and has been mainly observed in samples with lower mobility, the spin Hall angle is significantly suppressed for disorder. Here, it leads to a fluctuating effective magnetic field that reduces the SHE [98]. This means that relatively clean graphene samples are needed to observe this effect. Interestingly, this also means long spin diffusion lengths as listed above, which would mean record-value efficiencies shown by the product $\theta_{SH}\lambda_s$ even for the predicted modest spin Hall angles of around 1% [32]. For the REE, the theoretical calculations are even more optimistic, giving an efficiency close to unity [99].

The observation of SCC directly in graphene due to the proximity effect by a TMDC is one of the main goals of this thesis and the experimental results are presented in Chapter 5. The following chapter will also show the electrical control of the SHE that is one of the features of the Fermi-level-dependent enhancement of the SOC [33, 98, 182]. Similar results have been reported since by other groups [198, 199].

Another interesting application of the proximity effect, especially for spintronics, is the imprinting of magnetism into graphene. Theoretical studies have calculated a transferred exchange interaction from metallic FMs that could even be tuned by an applied gate voltage [200, 201]. The resulting large spin splitting could be used for the creation of polarized spin currents or to utilize graphene as an ultra-thin spin filter. Experimentally, to separate the contribution of the FM source and the proximitized graphene, the focus has been on studying graphene on ferromagnetic insulators such as yttrium iron garnet or EuS. While early transport experiments lacked an unequivocal sign of induced magnetic moments [202–204], later reports have shown clear proofs of enhanced exchange interaction [205] or by antiferromagnets in quantum [206] or spin magnetotransport measurements [207]. Recently, the effect has also been studied for other 2D materials such as TMDCs, where the spin and valley splitting can be increased. This has been realized for WSe₂ on EuS [208] or CrI₃ in a fully 2D materials stack [209]. But the application is not limited to changing the properties of the proximitized material and can also be used to experimentally study the source layer, like in the case of the 2D insulating FM Cr₂Ge₂Te₆ probed by its proximity effect into Pt [210].

When studying the proximity effect in vdW heterostructures, it is important to note that the effect comes mainly from directly adjacent layers due to the exponential decay of the tunneling probability with distance. On one hand, this means that the thickness of the source material plays almost no role. On the other hand, the thickness of the proximitized

layer has to be controlled precisely. For example, in bilayer graphene, this means that mainly the layer of carbon atoms adjacent to the second material will feel the proximity effect [21].

Another key parameter is the twist angle between the two flakes, graphically defined in Figure 3.6a. One prominent example is the case of “magic angle” graphene, where in a vdW multilayer of two [211] or three [212] graphene layers the transport becomes superconducting for twist angles slightly above 1° due to the strong interlayer coupling. Such precision is currently only experimentally doable in homojunctions, where the different layers are ripped off from one single flake and then stacked on top of each other with a slight rotation before stamping [121]. For even smaller twist angles, atomic reconstruction is expected to lead to interlayer commensurability, flattening out the intralayer lattice rotation.

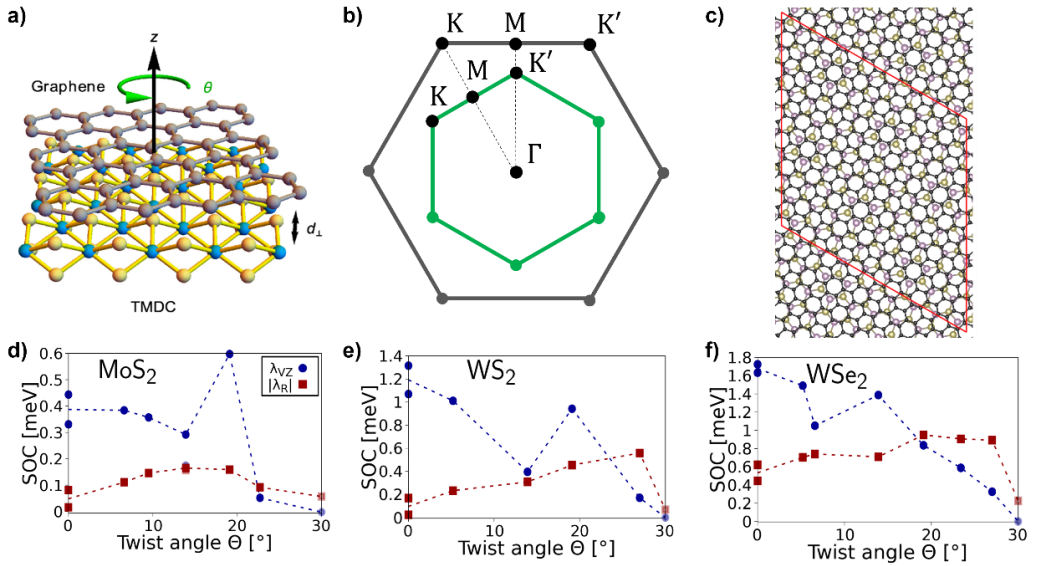


Figure 3.6: Twist angle in a graphene/TMDC bilayer heterostructure. **a)** The twist angle θ is defined as rotation around the out-of-plane axis z between graphene and the TMDC flake. The distance d_{\perp} between the two layers in that direction is given from the vdW gap. Image taken from Ref. [213]. **b)** Brillouin zone of graphene (grey) and a TMDC (green) with an angle of $\theta = 30^\circ$. The alignment of the high symmetry points of the two reciprocal lattices is shown by dashed lines. Image adapted from Ref. [214]. **c)** For the same twist angle, the two Bravais lattices seen in top view form a Moiré supercell. The red parallelogram shows the resulting supercell. Image taken from Ref. [215]. **d)** The Rashba SOC parameter λ_R (red squares) and the VZ SOC parameter λ_{VZ} (blue dots) as a function of the twist angle θ for the heterostructures of graphene with the 2H TMDCs MoS₂, **e)** WS₂, and **f)** WSe₂. Images taken from Ref. [216].

In the case of induced SOC, the twist angle between TMDC and graphene controls the amplitude of the in-plane Rashba and out-of-plane VZ contribution [213, 214, 217, 218]. Here, the significant rotation angles are given by the symmetry of the two lattices as seen in Figure 3.6b and are calculated to be around 20° . In that range, the strength of the different SOC contributions can amount to a multiple of their 0° values as seen in Figure 3.6d-f. Hence, the dominating contribution to the SOC can be tuned by the alignment of the two flakes. The next sets of experiments in the field of proximitized materials will surely study the influence of twist angle on effects such as spin lifetime anisotropy or spin-charge interconversion.

Opposite to graphene homojunctions originating from the same flake, in heterostructures with TMDCs the rotational displacement between the two layers cannot be controlled during the transfer process. However, it can still be imaged in the stamped bilayer as the TMDCs have a smaller but also hexagonal Wigner-Seitz cell. The resulting Moiré pattern as seen in Figure 3.6c can be observed by scanning tunneling microscopy and the twist angle can be deduced from it [219].

Additionally, the proximity effect is not limited to one property in bilayer structures. In a trilayer, the sandwiched monolayer will feel contributions from the top and bottom layers. Zollner et al. propose to use this case to imprint magnetic exchange coupling and SOC at the same time into graphene to create a material, where those two couplings can be swapped by an applied gate voltage [220].

As the hybridization of the electronic orbitals due to the proximity effect depends strongly on the spatial overlap, a recent study applied hydrostatic pressure to a graphene/TMDC heterostructure to reduce the size of the vdW gap. They saw a change in magnetotransport measurements of the sample in an anvil, suggesting increasingly stronger SOC coupling with applied pressure [221].

Finally, also the strain in-plane in one material and out-of-plane or laterally between the two layers will play a role in the results of the proximity effect, especially in graphene/TMDC heterostructures, where a sizable lattice mismatch exists [216]. Even though experimentally it will be challenging to control these parameters reliably in samples, certain properties could be engineered via strain [222].

4 Experimental techniques

4.1 Exfoliation and deterministic transfer

Since the initial discovery of graphene, the basic method of exfoliation has not undergone substantial changes. It still relies on adhesive tape, bulk crystals, and SiO₂ substrates. Firstly, industrial wafer dicing support such as Nitto tape has replaced standard Scotch tape as it is available in larger dimensions. Secondly, the bulk crystals of the materials used in this thesis (graphene and TMDCs) can be ordered from companies such as HQ graphene or NGS Naturgraphit in high quality. Finally, the substrates were cut from commercially available n-doped Si wafers with thermally grown SiO₂ and cleaned with plasma ashing, acetone, and isopropanol.

The flakes of 2D materials are peeled off the bulk crystal with the tape (see Figure 4.1a), cleaved multiple times, and then pressed on the substrate. Appropriate flakes are chosen manually under an optical microscope (see Figure 4.1b), while there are reports of using automated microscope stages and machine-learning-based image recognition to ease that task [223–225]. Additionally, newer exfoliation methods relying on a combination of polymer and thin, flat metal films have been shown to yield monolayers with macroscopic dimensions limited only by the sizes of the bulk crystals, which would make this step redundant [226].

Due to the optical contrast of graphene on SiO₂, the number of layers can be estimated initially [227]. Here, the best visibility can be achieved at an oxide thickness of 300 nm that was used for all the samples [228]. However, a reliable determination can only be realized by combining those optical images with other experimental methods mentioned below.

For creating bilayers of 2D materials (see Figure 4.1c), the exfoliation on PDMS as a substrate is necessary [116, 229]. Fixed on a glass slide, flakes can so easily be stamped on other flakes on SiO₂ substrates. While earlier processes required a hydrophobic polymer [230] or a stack with a water-soluble layer [115] both in combination with water, PDMS substrates enable the dry, deterministic transfer that is also solvent-free. However, they limit the quality and size of achievable flakes due to surface roughness and hinder the optical identification of monolayer flakes.

To create multi-layer stacks, a polycarbonate (PC) membrane is added on top of the PDMS stamp [116, 119]. Due to the temperature-dependent viscoelasticity of this

material, flakes can be picked up from SiO₂ substrates at a certain temperature when they adhere more to the polymer than to the oxide and stamped onto other flakes at higher temperatures when the van der Waals forces are stronger than the adhesion to the membrane. Therefore, it is possible to create stacks of different 2D materials attached to the PC, that are in a final step transferred onto a substrate by melting the membrane. The remaining polymer is then dissolved in dichloromethane. While other methods work with the same principle but use poly(vinyl alcohol) as a membrane [231], completely solvent-free stacking that relies only on the difference in thermal expansion between polymers and the 2D materials, is also reported [232]. An overview and comparison of the different, available techniques for deterministic transfer can be found in the review in Ref. [233].

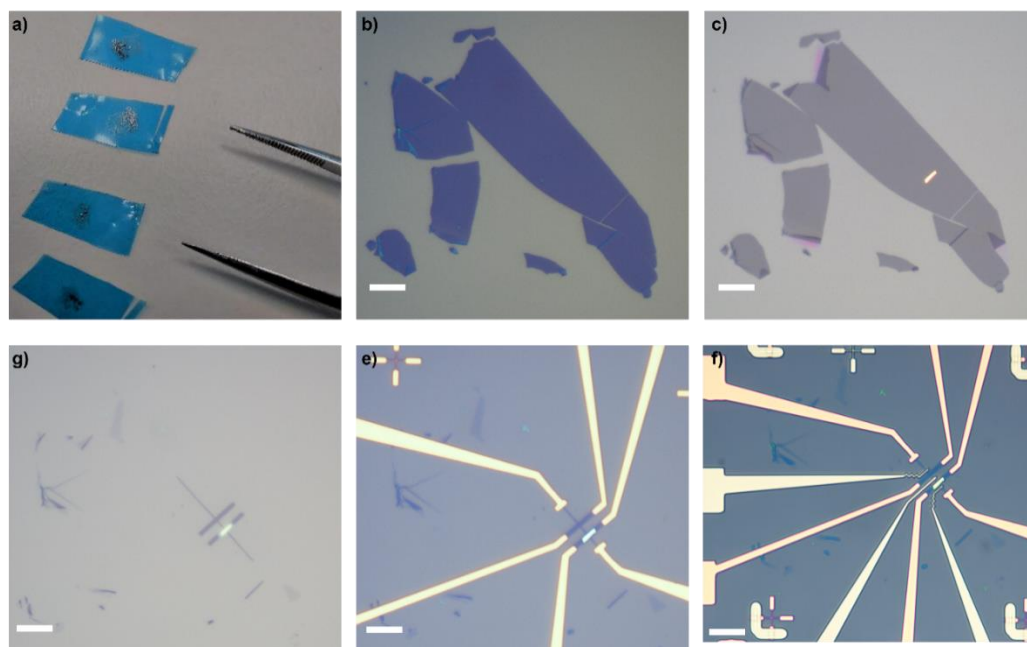


Figure 4.1: Fabrication process of a graphene-based vdW heterostructure. **a)** Nitto tape with cleaved flakes from a graphite crystal. **b)** Exfoliated flake of graphene on SiO₂ substrate. **c)** TMDC (yellow) stamped on top of the graphene flake. **d)** Heterostructure etched into a Hall bar. Thicker, folded areas due to the transfers visibly remain after the etching. **e)** Au contacts deposited. **f)** Finished device after Co deposition, ready to be wire bonded. The white scale bars are 10 μm long.

For 2D materials, the different thicknesses in vdW heterostructures can in that way be controlled down to the atomic layer, but the lateral precision of the materials is given by the resolution of the optical microscope and the control of the glass slide holder. The machine used in the context of this thesis for stamping is shown in Figure 4.2 and offered micrometer precision.

The quality of the interfaces in vdW heterostructures depends on the residue of the stacking process, where the PC method is preferable to the PDMS technique. It can

further be improved by exfoliation and stacking in a glovebox with an inert atmosphere (in the case here Ar) [234].



Figure 4.2: Transfer system and optical microscope. On the left and right of the microscope with large working distance objectives, two motor-controlled arms for holding the glass slide and micromanipulator can be seen. The stage has an integrated hotplate and can be rotated.

In a final step, the heterostructures are annealed at 400 °C in an ultra-high vacuum, which relaxes any stress and wrinkles in the 2D materials and clusters any contamination in bubbles [232]. Here, also mechanical cleaning with an atomic force microscope (see Section 4.3.1) can be used [235].

4.2 Clean room fabrication

4.2.1 Electron-beam lithography

After the 2D material flakes or stacks are prepared on the substrate, they need to be structured and contacted. In scientific and commercial applications, this is done by lithography processes. They fundamentally consist of three steps: coating the sample with a resist, exposure to transfer the design, and development to structure the resist layer.

As the lateral size of the devices is limited by material parameters like the spin diffusion length, they are normally in the sub-micron range below the resolution of optical lithography processes that use light for the exposure. They can however be used for initially writing a grid of numerical markers on the substrates (via an optical mask in a mask aligner with ultraviolet light) or larger bond pads for wire bonding (via the mask-less laser writing).

To achieve the details necessary for the subsequent steps of etching and thin film deposition, the short wavelengths of electrons are needed for the exposure. They are provided by an electron-beam of a scanning electron microscope (see Section 4.3.4). Together with appropriate resists that are sensitive to the energy of electrons, the resolution is improved to the nanometer range. Electron-beam lithography is used since the 1980s and is now a standard process in nanofabrication. Information about the fundamental steps is widely available in the literature, for example, in Ref. [236].

The resist is drop casted and spin coated on the substrate. For almost all samples in this thesis a double layer of electron-beam sensitive resist, poly(methyl methacrylate) (PMMA), dissolved in anisole, was used. A double layer of two different concentrations of PMMA helps in the final lift-off step after the deposition, as it creates an undercut when the lower layer is more sensitive to the exposure. The sensitivity to the electron-beam can be controlled by the molecular weight (given in thousands), the thickness of the layers by the concentration of anisole (given in percent with A indicating the solvent). Here, PMMA 495 A4 was used as the bottom and PMMA 950 A2 as the top layer.

The desired pattern is written onto the resist by exposing it controlled to an electron-beam. The design is normally broken down into quadratic write fields of μm -size and the beam deflected inside those to write the structure. The fabrication recipes have to consider the acceleration voltage of the electron-beam, exposure time and therefore dose, the aperture, and the write field and step size to achieve optimal results. Alignment with the flake, overlaying with previously written elements, and stitching of the write fields can also lead to errors and must be taken into account.

After the writing of the structure, the resist is developed by washing away the exposed, broken-down parts of the resist, which leaves a gap for etching or deposition as PMMA is a positive resist. Methyl isobutyl ketone dissolved in isopropanol was used as a developer. After subsequent steps, the remaining resist can be dissolved in acetone, which also removes any material on top after a thin film deposition leaving only the designed metallic contacts.

Electron-beam lithography, as well as the following steps, is done in a clean room facility, where the ambient air is controlled and filtered, to prevent any contamination of the nanostructures.

4.2.2 Reactive ion etching

Already in the initial Science paper, dry etching in oxygen plasma was used to structure the graphene flakes into Hall bar shapes [13], as it was an industry standard at the time [237]. Till now, it is still the go-to method for graphene-based samples due to its wide availability and reproducibility, while new approaches such as nanocutting with nanoparticles [238] or probe tips [239] have been reported.

In a reactive ion etcher, a plasma is created by introducing a gas (often oxygen) into a vacuum chamber and applying a strong, oscillating electromagnetic field to it. In that way, the electrons are separated from the gas molecules, so that the remaining ions can be accelerated towards the sample. There, they will remove material due to their kinetic energy like in a sputter target or via chemical reactions. The rate of etching can be controlled by the composition, flow and pressure of the used gases and the applied bias. An exemplary result can be seen in Figure 4.1d.

A similar machine called a plasma asher is used to clean the substrates before the exfoliation process. It works with the same principle but is less aggressive, as the ions are not accelerated and therefore no physical process happens. However, it can remove organic residues like photoresist chemically.

4.2.3 Metal deposition

The thin film deposition of metals in this thesis is based on the evaporation of metal atoms from a source or target in a vacuum chamber and the transfer of that gas to the sample, where it will re-condensate as deposited layer, hence the name physical vapor deposition. There are basically two methods to provide the necessary energy for the first step: heat or a concentrated electron-beam.

In this thesis, thermal deposition was mainly used to deposit Au in high quality and purity for electrical contacts (see Figure 4.1e). The raw material, cut from an Au wire, is placed on a holder made of W, which is heated up by running a current through it. Subsequently, the Au will melt and evaporate. The sample is placed over the W crucible on a rotating plate to ensure homogeneous deposition. As Au does not grow epitaxially on graphene and has low adhesion to the SiO₂ substrate, a wetting layer has to be inserted. Typically, a thin film of Ti is used for this, but also other metals such as Cr are possible.

In electron-beam deposition, free electrons are created by heating a W filament and are then accelerated into the target by applying a voltage in the kV range and focused by a magnetic field. They are energetic enough to directly melt the raw material in the crucible. The choice of materials that can be evaporated is therefore only limited by the available voltage and not by the melting point of the heating element like in thermal evaporations. This method was used to deposit thin films of Ti, Cr, and Co (see Figure 4.1e).

The thickness of the deposited film during the process can be controlled via a quartz crystal monitor that is calibrated by test runs and subsequent X-ray reflectivity measurements.

4.3 Characterization techniques

4.3.1 X-ray reflectivity

The thickness of thin metal films that are deposited on a substrate (for example, to control a deposition process) can be measured by X-ray reflectivity. As the name suggests, an X-ray beam is reflected from the surface and measured in the specular direction, so that the incidence angle is equal to the reflected angle. Due to the multiple interfaces between air, the films, and the substrates, multiple reflections interfere with each other and when scanning the incidence angle an oscillating signal can be measured. The period of these oscillations gives information about the layer thicknesses, the decay of the signal allows to draw conclusions about the interlayer roughness. As the beam spot size is a few 100 μm , the deposition after nanofabrication cannot be controlled by this method.

4.3.2 Atomic force microscopy

To characterize the sample topography after the (successful) fabrication process, atomic force microscopy is the standard method in most labs. Invented like its predecessor, the scanning tunneling microscope, at IBM in the 1980s [240], commercial versions nowadays fit in a small suitcase and can give images with nanometer resolution in lateral and vertical direction in a few minutes.

The main component is a cantilever that raster scans the topography by either touching the sample directly (contact mode) or tailing its contour with a distance while vibrating with a small amplitude. In this non-contact mode, the vibration frequency of the cantilever is measured by a laser reflected from its back. The resonance frequency of the cantilever will change due to the atomic forces between its atomically sharp tip and the sample – hence the name. The oscillation and the movement in all three directions are controlled by piezoelectric elements and enable micrometer-sized images with nanometer resolution like the one shown in Figure 4.3. This method was used in this thesis to check the thickness of metal electrodes and measure thick TMDC flakes.

However, atomic force microscopy gives unreliable results when measuring the thickness of few-layer graphene flakes as the apparent thickness measured includes the van der Waals gap and the distance between graphene and SiO_2 , which is unknown even for atomically smooth surfaces and can be quite large on rough substrates. Therefore, only a qualitative comparison between flakes with different numbers of layers is possible and the number of layers cannot be determined from the measured thickness alone.

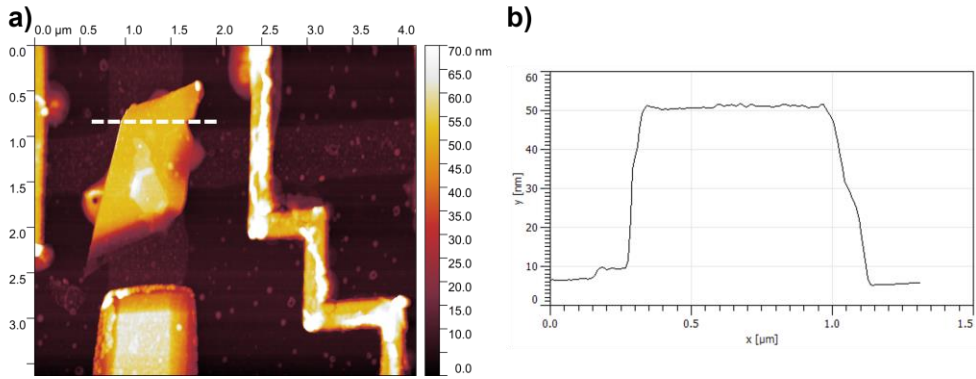


Figure 4.3: Atomic force microscopy characterization of a typical device after the electronic measurements. a) Area scan in tapping mode showing the topography of the device (the same as in Figure 4.5). The oxidation of the Co electrodes is visible as well as some contamination across the graphene flake and the substrate. **b)** Line profile taken along the marked line across the WSe₂ flake.

4.3.3 Laser Raman microscopy

After the first discovery of graphene, the question arose, how to reliably determine the number of layers of (exfoliated) flakes. Optical methods such as Raman spectroscopy were shown to be definite in characterizing the number of layers in flakes [241, 242] not just for graphene but for other 2D materials as well [243].

The basic working principle is the Raman or Stokes scattering of light, where the inelastic scattering leads to a shift in the wavenumber of the reflected light in regard to a monochromatic incidence – normally a laser is used here. In the total spectrum of this Raman shift, certain peaks in intensity correspond to unique vibrational modes of molecules that absorb energy, which enables the chemical identification of the sample.

For graphene, the interesting peak is located around a shift of 2700 cm^{-1} , which is historically called G' (as it appears together with a stronger G peak at roughly 1600 cm^{-1} in graphite) or more correctly 2D. The number of layers can be extracted by fitting a certain number of Lorentzian functions to it. Due to the valley degeneracy of graphene in the K and K' point, it originates from a double resonant process and two Lorentzian functions have to be used per layer. Therefore, for more than five layers, the spectra become hardly distinguishable from the one of graphite [242]. Figure 4.4 shows the spectrum of a graphene flake with three layers used in a device.

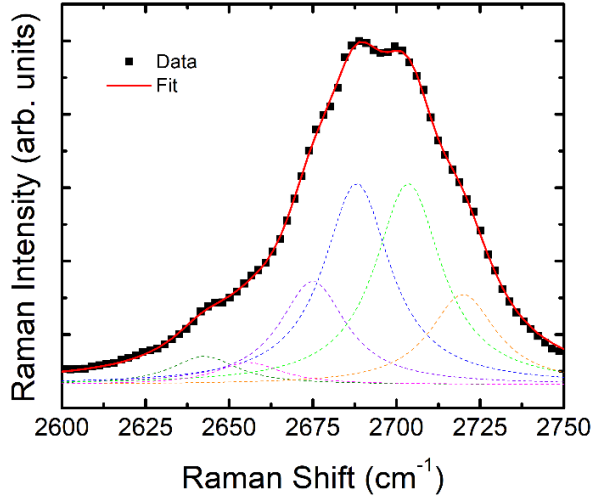


Figure 4.4: Raman spectroscopy of a graphene flake. Measured with a confocal microscope using a green, polarized laser (wavelength 532 nm), the shift in wavenumber of the reflected light due to inelastic scattering is plotted. The Raman intensity profile can be fitted with 6 Lorentzian functions, which gives a thickness of three layers for the graphene flake.

4.3.4 Scanning electron microscopy

Optical microscopy has the same limitations when imaging a device as the optical methods during the fabrication process with the wavelength of the visible light limiting the spatial resolution.

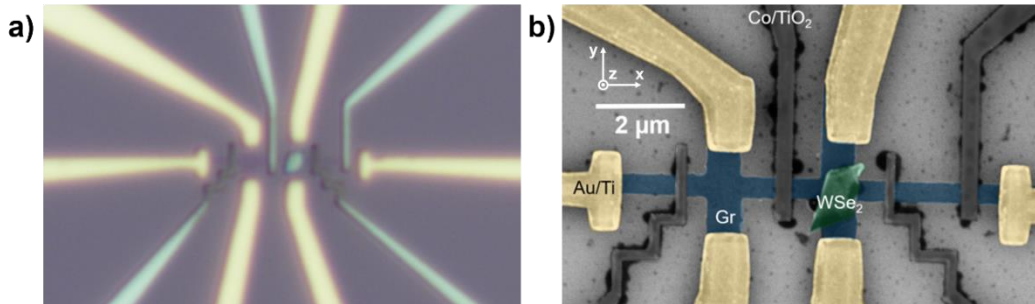


Figure 4.5: Microscope images of a typical device. **a)** Optical image with 100x magnification before electronic measurements. **b)** False-colored scanning electron microscopy of the same device after electronic measurements. The different parts of the sample are labeled to make it possible to visualize the results of the different nanofabrication steps described above.

While using an electron-beam in a scanning electron microscope solves this problem, this method is also more destructive to the sample and cannot be used during the fabrication

process. For one, the electrons used there have more energy than the photons, so that they damage the surface of the sample. On the other hand, when protected by a spin coated photoresist, the imaging will expose the whole area of view. Hence, it is only used after the electronic measurements. Figure 4.5 compares both results.

4.3.5 Electronic measurements

The electrical characterization of all the samples presented in this thesis has been performed in two, almost identical cryostats by Quantum Design, one of them can be seen in Figure 4.6. In both, liquid helium is used to cool the sample between 350 K down to 2 K and re-liquefied in a closed-loop system. Such low temperatures also enable the use of a superconducting solenoid magnet, so that an external magnetic field of up to 9 T can be applied in a fixed direction. However, as the sample holder inside of the cryostat can be rotated 360° around one axis, the magnetic field can be applied in one plane, which depends on the mounting of the sample.



Figure 4.6: Physical properties measurement system. On the left, the Dewar of the cryostat is visible, in which vacuum shields the liquid helium that cools the sample. The temperature and the field of the superconducting magnets are controlled with the rack on the right. In the middle, the switch box for electrical contacts and the nanovoltmeter, the current source, and the source measure unit can be seen.

The system offers eight electrical contacts that can be connected via a switch box to a variety of ac and dc electronic measurement equipment. In this thesis, low-noise measurements were performed with a Keithley current source combined with a

nanovoltmeter, while drift currents and gate voltages were applied with a source measure unit by the same company. The dc current was applied in a reversal technique known as delta mode that mimics an ac current and removes thermoelectric effects [244].

Figure 4.7 shows the four different configurations of electronic measurements that are mentioned throughout this thesis. The easiest way to characterize the resistance of a sample is by applying current and measuring the resulting voltage with the same pair of electrodes (Figure 4.7a). However, the calculated resistance $R = V/I = R_{sample} + R_{contact}$ also includes the contact resistance, which in case of tunnel barriers or Schottky barriers can be larger than the actual resistance of the sample. To exclude this contribution, the four-point measurement setup can be used (Figure 4.7b). Here, the current-injecting and voltage-sensing electrodes are separated and therefore contact or lead resistances are eliminated from the measurement. The contact resistance itself can be measured in three-point (Figure 4.7c), where the contribution of the shared lead itself can in the case of metallic electrodes often be neglected against the resistance of the interface between the sample and the electrode.

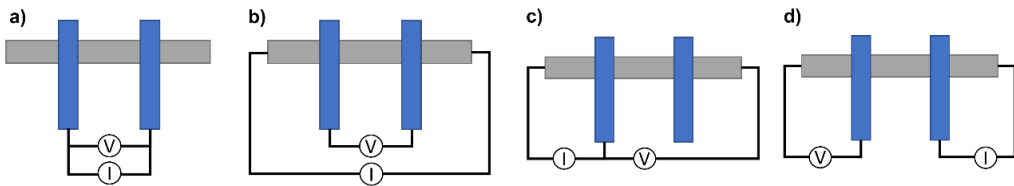


Figure 4.7: Electronic measurement configurations. **a)** Two-point measurement by applying the current and measuring the voltage with the same pair of electrodes. **b)** Four-point measurement, for which independent voltage and current probes are necessary. **c)** Three-point measurement, where one electrode is shared. **d)** Non-local setup, where the current and voltage loops are separated.

The previously mentioned configurations can be grouped as longitudinal, as they measure the voltage in the same direction as applying the current. For measuring the transverse Hall resistance, the four-point setup is used but the voltage and current leads are perpendicular to each other, on opposite arms of a Hall bar. So far, these setups have been local measurements as the voltage is picked up across an area intersecting the charge current path. In the case of the non-local setup, the current path is spatially separated from the voltage electrodes (Figure 4.7d). As described in Section 2.2, it is used for quantifying spin effects across the channel that can easily be covered by a charge current flowing along the same path. Due to spurious effects, they will however contribute in most samples to the non-local resistance so that a magnetic field dependence is necessary most of the time to extract the pure spin signal. The final case is the experiment for SCC measurements (Figure 2.8), using a non-local, transverse setup to detect, for example, SHE.

This gives a good overview of most of the experimental methods used in this thesis. Together with the theoretical background from Chapter 2 and the information about 2D materials in Chapter 3, the reader should be able to understand the results presented in the following chapters, starting with the observation of SCC directly in graphene.

5 Spin-to-charge conversion in graphene proximitized with MoS₂

5.1 Early experimental claims and theoretical predictions

As explained in Section 3.1, graphene is an ideal material for spin transport due to its long spin relaxation length even at room temperature. The underlying reason is the low intrinsic SOC. However, the generation and tuning of spin currents need strong SOC, so that they are out of reach for graphene, limiting the capability for active spintronic device functionalities and related applications.

This explains the experimental interest from early on to detect enhanced SOC in graphene, most prominently in a series of reports from a research group in Singapore showing the resulting SHE in hydrogenated graphene [245], CVD-grown graphene with Cu adatoms [246], and in graphene/WS₂ heterostructure devices [247]. While these studies had some theoretical backing of SOC induced by hydrogenation [31] and extrinsic effects such as skew scattering by adatoms [248], they relied on a fundamentally flawed double Hall bar design [249].

Instead of the SCC configuration in an LSV with an FM electrode shown, for example, in Figure 2.8, a device with two Hall bars was used. While, in one bar, the SHE is supposed to convert the applied charge current into a transverse spin current that flows to the main channel, in the other bar, the ISHE detects this spin current. This eliminates spurious effects associated with the use of FM electrodes such as stray fields but does not guarantee a spin contribution in the measured signal. While a signal change with the switching of the magnetization of an FM suggests spin injection and transport and the precession of the signal for an applied magnetic field proves the spin character of the results, the double Hall bar design leads to a multitude of spin-unrelated non-local contributions. Spin injection, transport and detection can therefore not be concluded from the data. Furthermore, the main reason for the presented Hanle-like curves in an external magnetic field is most probably magnetoresistance. Consequently, this experiment design has widely been rebutted by experimental and theoretical works collected in the review in Ref. [249].

Noticeably, other spin-unrelated contributions have been identified for graphene with adatoms [250] and no further experimental proof for SCC in hydrogenated graphene has been found [251]. However, the body of theoretical work regarding spin-orbit proximity in graphene/TMDC bilayers grew, with further theoretical predictions of SHE [98, 197] and REE [99] in such heterostructures due to the enhanced SOC.

Some of those calculations report the spin Hall conductivity σ_{xy} , that is related to the already known spin Hall angle θ_{SH} via the longitudinal conductivity σ_{xx} :

$$\theta_{SH} = \frac{\sigma_{xy}}{\sigma_{xx}} \quad (27)$$

In the case of graphene and TMDCs, a substantial VZ SOC is imprinted into graphene [33, 182] and due to the symmetries discussed in Section 2.1 and 2.5, only spins pointing along z are converted, so the spin Hall conductivity σ_{xy}^z for this spin polarization has to be considered. For the transport in 2D materials here, the conductivity has units of conductance, similarly to how the inverse of the square resistance R_{sq} is taken for σ_{xx} .

One of the results for σ_{xy}^z is exemplary plotted in Figure 5.1. For clean samples, a sizable spin Hall conductivity is predicted, reaching $1.4 \times 10^{-7} \Omega^{-1}$ or a spin Hall angle of 4% [32]. However, it also shows that strong intervalley scattering should give rise to a suppression of the SHE. And while TMDCs will also transfer their spin-valley locking into graphene and therefore reduce exactly this type of scattering, experiments to observe the SHE in such heterostructures have to be carefully designed. Care should be taken that the interfaces between the two materials are clean and flat, as wrinkles, impurities, and defects will lead to scattering, reducing the amplitude of the measured SCC signal [32].

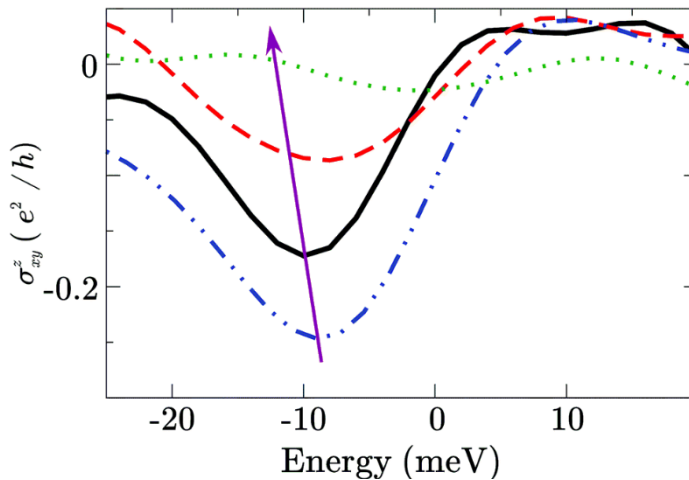


Figure 5.1: SHE and scattering. The spin Hall conductivity of a graphene/TMDC heterostructure (in this example WS_2) for different intervalley scattering strengths starting from none, increasing for the purple arrow direction. The effect is suppressed for stronger intervalley scattering. Image adapted from Ref. [32].

Early experimental results showed via photoemission that the theoretical band alignment of MoS₂ and graphene can actually be observed in real-world samples [252]. In a next step, a spin field-effect switch using graphene as transport channel and MoS₂ as spin sink layer was reported [147, 148], meaning that the spins are either absorbed into the TMDC flake and possibly converted into charge or the same happens directly in the proximitized graphene. Hinting the first option of SHE directly in the TMDC, Luo et al. were able to use a MoS₂ flake to optically inject spins into graphene across the TMDC/graphene interface by exciting them with circularly polarized light and detecting the resulting spin current with an FM electrode [23]. In the case of electrical spin-injection in an LSV, one could assume that the SCC also occurs in the TMDC flake. To pick up the resulting voltage, the electrical contacting of TMDC would then be necessary, something that proves to be experimentally difficult [30].

To overcome this obstacle, graphene can also be used to contact the TMDC. One possible option is the graphene Hall bar structure with TMDC flake on top that has been shown so far as configuration for SCC measurements. Before measuring SCC in this device, spin injection into graphene has to be achieved. The spin transport has to be fully characterized in a pristine graphene part and compared to the proximitized region, where absorption or anisotropy has to be observed. The realization of these measurements is shown in the next section.

5.2 Device characterization and spin transport

The following two sections will present results from the first main paper of this thesis [253]. The data is based on two identically fabricated samples – A and B – of which the first one is shown in Figure 5.2.

The experimental techniques used are explained in Chapter 4, but the main steps and some of the details are given hereinafter. The graphene/MoS₂ vdW heterostructures were fabricated by mechanical exfoliation followed by dry viscoelastic stamping. First, graphene was exfoliated from bulk graphite crystals using a Nitto tape (Nitto SPV 224P) onto Si substrate with 300 nm SiO₂. Few-layer graphene flakes were identified by optical contrast under an optical microscope. Then, a MoS₂ crystal was exfoliated using the Nitto tape and transferred onto a piece of PDMS (Gelpak PF film with a retention level of 4 and 17-mm thickness). After identifying a short and narrow MoS₂ flake using an optical microscope, it was stamped on top of graphene using a visco-elastic stamping tool, where a three-axis micrometer stage was used to accurately position the two flakes. The flake was then structured into a graphene double Hall bar using electron-beam lithography followed by reactive ion etching. After etching, the sample was annealed for 1 h at 400 °C in an ultra-high vacuum (10⁻⁹ torr) to possibly remove any contamination from the exfoliation and transfer process and relax the strain between the two flakes.

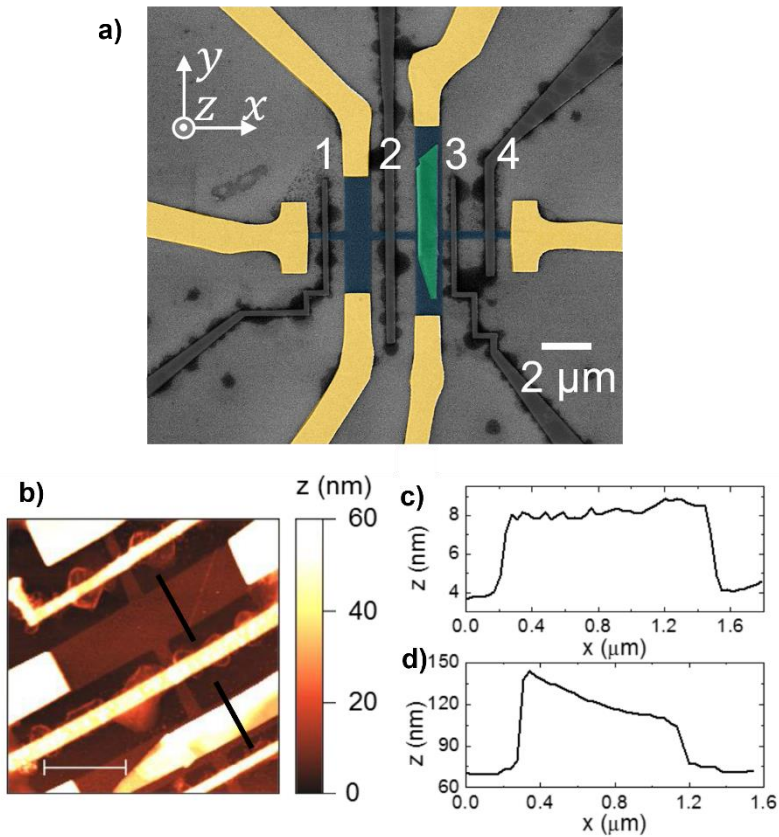


Figure 5.2: Device characterization. **a)** False-colored scanning electron microscopy image of the device. The width of the horizontal graphene (in blue) channel is 350 nm. The width of the MoS₂ flake (in green) and the two vertical graphene channels are 0.9 μm and 1.2 μm, respectively. **b)** Area scan with atomic force microscopy showing the topography of the device. The white scale bar is 2 μm long. **c)** Line profile taken along the top black line in **b)** across the graphene flake, where the thickness of the graphene flake is extracted to be roughly 5 nm, equivalent to around ten layers. **d)** Line profile taken along the bottom black line in **b)** across the MoS₂ flake, where the thickness of the MoS₂ flake is between 35 and 75 nm.

The remaining graphene structure was then contacted with 3-nm-thick Ti as wetting layer and 40-nm-thick Au as electrical contacts, fabricated using electron-beam lithography followed by electron-beam deposition in ultra-high vacuum (10^{-9} mbar) and lift-off. Using the same procedure, the 35-nm-thick Co electrodes were fabricated on top of the graphene channel. Before this deposition, a TiO_x resistive layer to overcome the conductivity mismatch was fabricated by depositing 3 Å of Ti and subsequent natural oxidation in air. The widths of the Co electrodes vary between 250 nm to 400 nm, leading to different coercive fields for each electrode.

The four Co electrodes (see Figure 5.2a for numbering) enable the measurement of different LSVs and SCC configurations, which are shown in Figure 5.3: In panel a) an

LSV with FM electrodes and pristine graphene (between electrodes 1 and 2) with a Hall bar in between. The standard LSV without this Hall bar (between electrodes 3 and 4) is not shown as during the measurement the graphene flake broke between those two contacts. Both of them can be used to characterize the charge and spin transport in the pristine graphene area. In panel c) the LSV with a TMDC flake on top of the graphene channel (between electrodes 2 and 3) is shown, making it possible to see the effect of the proximity effect by comparison. Finally, panels b) and d) show the SCC configuration of those LSVs, replacing the detector electrode by measuring the voltage with the Au contacts on the top and bottom of each Hall bar. This allows again to study the change from pristine graphene to graphene proximitized with MoS₂.

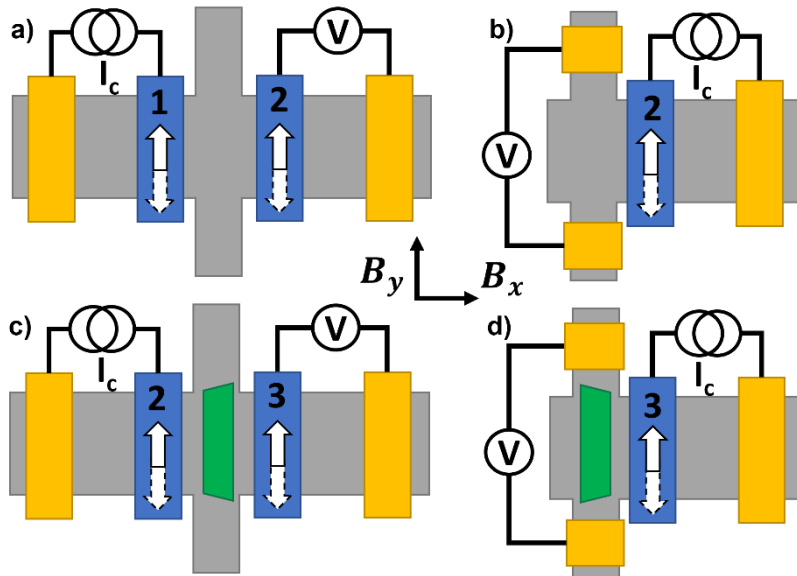


Figure 5.3: Different LSV and SCC configurations. a) LSV of pristine graphene between two FM electrodes with a Hall bar in between. The standard LSV without Hall bar between electrodes 3 and 4 is not shown. b) SCC configuration of the pristine graphene Hall bar in a). c) LSV with a TMDC flake proximitizing the cross area. d) SCC configuration of the LSV in c).

As a first step, spin transport was confirmed and studied in the two LSVs while the SCC measurements are shown in the next section. For that, the non-local resistance was measured across each LSV in sample A at room temperature while applying a magnetic field along y . This leads to the observation of a visible parallel and antiparallel magnetization state as the electrodes have different coercive fields and the magnetization switches for different B_y values (here up to 50 mT). Figure 5.4 shows the results for the two LSVs at room temperature.

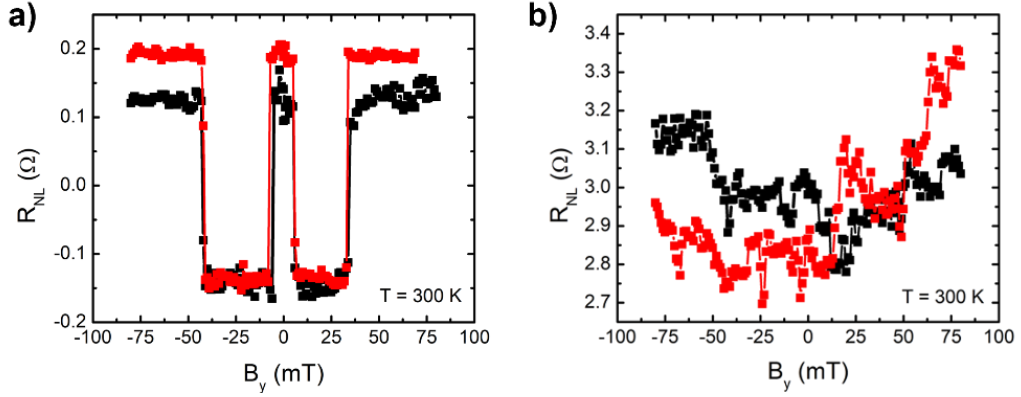


Figure 5.4: LSV signals at room temperature in sample A. **a)** LSV with a bare Hall bar in the middle (Figure 5.3a), **b)** LSV with a Hall bar in the middle and MoS₂ flake on top (Figure 5.3c). For the red curves, the voltage and current leads are interchanged.

The first observation is that the spin signal ΔR_{NL} – the difference between the two resistance states – is clearly visible in Figure 5.4a. Additionally, it is apparent that the signal across the LSV with the TMDC in Figure 5.4b is suppressed. Both electrodes 2 and 3 are included in the reference LSVs on the right and on the left and show a signal (not plotted for the LSV between electrodes 3 and 4), therefore, missing spin injection or detection cannot be the reason – the spin current seems to disappear or rather the spin imbalance seems to relax in the Hall bar region. This is in line with the two options mentioned above, where the spin current is either absorbed into the MoS₂ or converted in the proximitized graphene.

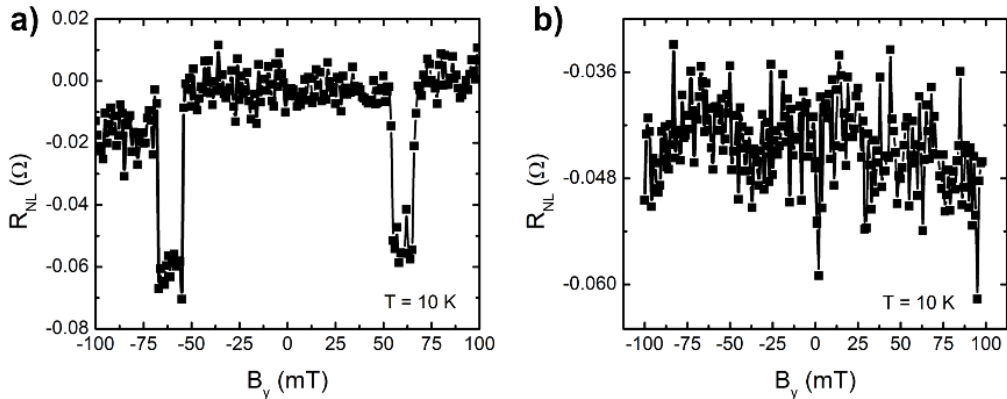


Figure 5.5: LSV signals at 10 K in sample A. **a)** LSV with bare Hall bar in the middle (same as Figure 5.4a) and **b)** with a MoS₂ flake on top (same as Figure 5.4b).

However, it should be noted that the noise is larger in this measurement compared to the one in the reference LSV and a small spin signal would probably be hidden by the

background fluctuation. Hence, a measurement at low temperatures will be more significant as the noise level should be reduced. Subsequently, Figure 5.5 shows the same data as in Figure 5.4 for 10 K. Unfortunately, it was not possible to measure the standard LSV due to a breakage of the graphene channel between electrodes 3 and 4 while cooling down that could later be observed in the scanning electron microscopy image.

In Figure 5.5a, a few details can be noticed: The coercive fields are higher than at room temperature, in line with the expected behavior of the magnetization dynamics of an FM. The background noise level is smaller than in the measurement before, due to the reduced thermal fluctuation of the electrons. Finally, the spin signal ΔR_{NL} is smaller, which can be explained in the following when looking at the temperature dependence of the spin transport parameters.

The measurement across MoS_2 in Figure 5.5b can give a better upper limit for the observable spin signal: Compared to the other LSV, ΔR_{NL} is reduced from 60 m Ω to less than the noise level of 5 m Ω . This means a sizable amount of spin current is either absorbed or converted, achieving the first preliminary goal in this study. It means that the interface between the two vdW materials is clean enough to allow substantial spin transport across or even the enhancement of SOC by proximity effect.

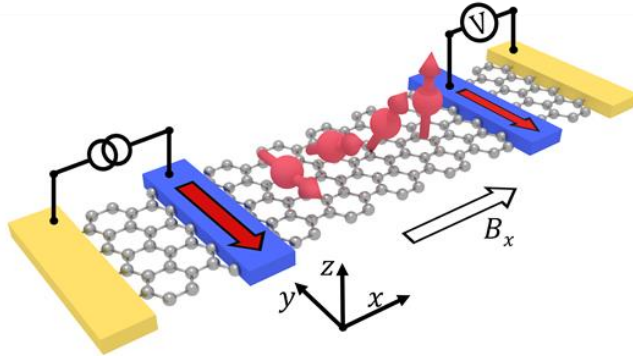


Figure 5.6: Sketch of the configuration used in the LSV precession measurement. The magnetic field along x leads to a rotation of the spin polarization resulting in a Hanle curve for the non-local resistance. The Hall bar arms of graphene between the FM electrodes have been omitted.

To further characterize the spin transport parameters in the LSVs, Hanle precession measurements were conducted between room temperature and 10 K. The setup for the non-local measurement as a function of the magnetic field, along x now, is shown in Figure 5.6. As pictured, the injected spin will now precess around B_x , following an in-plane/out-of-plane oscillation that will have different starting points of the rotation for parallel and antiparallel states. For higher fields, the magnetization of the FM electrodes will be pulled along the x -axis. Consequently, the injected spins will point in the same

direction and no precession will occur, leading to a saturation of the resistance value that is the same for the two initial magnetization configurations.

Figure 5.7 shows the results for room temperature, 100 K, and 10 K for this measurement across the pristine graphene LSVs. In all three cases, some resistance spikes for the mid-field range can be observed. While other experiments have linked smaller jumps to the pinning of domain walls in the FM electrode [254], the origin of those outlier values is not clear and they are disregarded in the subsequent analysis as a probable measurement artifact.

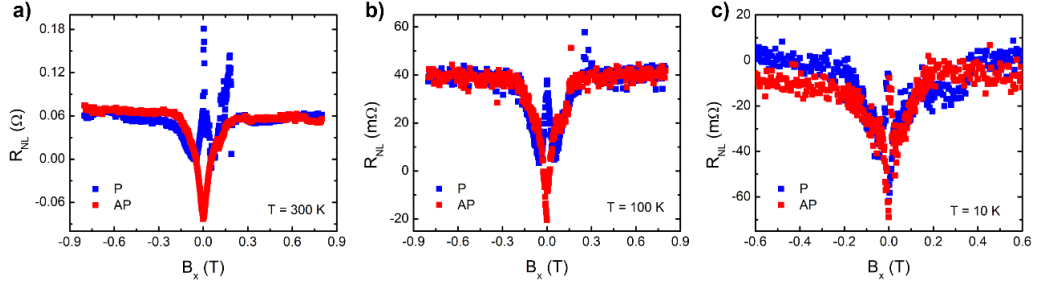


Figure 5.7: Symmetric Hanle precession across the reference LSV in sample A for a) 300 K, b) 100 K and c) 10 K. The blue and red curves indicate the initial state of the injector and detector magnetizations, parallel and antiparallel.

As in the B_y -measurements, ΔR_{NL} at zero field is reduced when decreasing the temperature. This is not surprising, as both measurements probe the same value. However, this reduction seems to be less intense when going from 100 K to the lowest temperature of 10 K that shows almost the same amplitude. However, the amplitude ΔR_{NL} at zero field for room temperature in Figure 5.7a is reduced compared to the LSV signal in Figure 5.4a. As the Hanle data was obtained after cooling down and warming up the sample, the tunnel barrier was probably degraded and spin injection or detection weaker compared to the initial LSV measurement.

10 K is also the temperature where the full analysis and fit of the experimental data for one exemplary curve is shown in Figure 5.8. The angle between the magnetization of the FM electrode and the applied magnetic field is plotted in Figure 5.8a. This value can be calculated from $\bar{R}_{NL} = (R_P + R_{AP})/2$, with the exact calculation given in Appendix A. It shows that the magnetization is fully saturated above a saturation field B_{sat} of roughly 240 mT, coinciding with the field value above which the parallel and antiparallel curve correspond.

Figure 5.8b shows $\Delta R_{NL} = (R_P - R_{AP})/2$, giving the symmetric Hanle curve with spin-unrelated background removed. From it, the spin transport parameters can be extracted as described in Section 2.3. The results of the fits to all symmetric Hanle curves for the different samples and temperatures are listed in Table 1. This completely describes the spin transport in the pristine graphene, the second preliminary goal of this study.

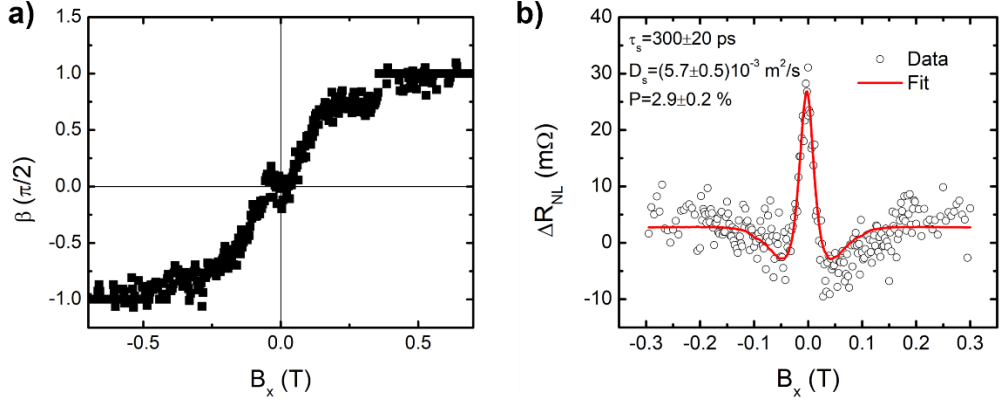


Figure 5.8: Analysis of the symmetric Hanle curve of the reference LSV at 10 K in sample A. a) Angle between the magnetization of the FM electrode and the applied magnetic field extracted from the data in Figure 5.7c. It shows that the pulling of the magnetization that is fully aligned parallel above 240 mT. b) Fit of the data in Figure 5.7c to Equation 20 with the spin transport parameters of the fit given.

A general trend can be observed in both samples: The spin diffusion constant D_s^{gr} is strongly reduced with decreasing temperature, while the spin lifetime τ_s^{gr} is doubled. This means that the spin diffusion length λ_s^{gr} is constant between 10 K and room temperature. One conclusion is that, therefore, P is playing a larger role in the amplitude of the LSV signal in this device. This also explains why the reduction of ΔR_{NL} is smaller for the lowest temperature step from 100 to 10 K.

As no spin signal was observed across the graphene/TMDC region, the third target – demonstrating anisotropic spin transport due to SOC by proximity effect – was not achieved. This leads now finally to the measurement of the SCC, the last and main objective.

5.3 Experimental observation of spin-to-charge conversion in graphene/MoS₂

To measure the conversion of an injected spin current into a charge current across the graphene Hall bar, the measurement setup in Figure 5.9 was used.

As described in Section 2.5, one of the FM electrodes of the LSV is essentially replaced by the graphene Hall bar. It can pick up the SCC-related voltage and the dependence of the resulting non-local resistance on a magnetic field along x can shed light on the underlying mechanism as B_x leads to the same precession of the spin polarization as for the symmetric Hanle curve.

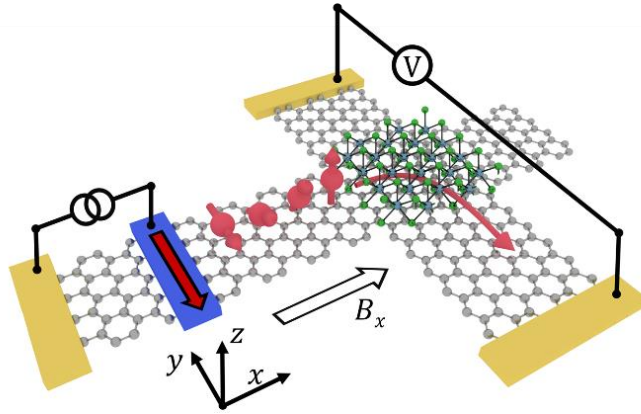


Figure 5.9: Sketch of the configuration used in the SCC measurement. The magnetic field along x leads to a rotation of the spin polarization resulting in out-of-plane spins that are converted by ISHE in the proximitized graphene underneath the TMDC flake. For higher fields, the magnetization of the FM electrode and therefore the polarization of the injected spin current is aligned along x (not pictured).

Figure 5.10a shows the resulting data for the graphene Hall bar with MoS₂ on top at 10 K. Two, clear antisymmetric Hanle curves can be observed for the different magnetization directions of the FM injector electrode. This initial state has to be set by applying a magnetic field along y before the measurement. The further analysis of this data is shown in Figure 5.10b and Figure 5.10c, where the difference $R_{SCC} = (R_{NL}^{\uparrow} - R_{NL}^{\downarrow})/2$ and the sum $\bar{R}_{SCC} = (R_{NL}^{\uparrow} + R_{NL}^{\downarrow})/2$ of those two curves are plotted, respectively.

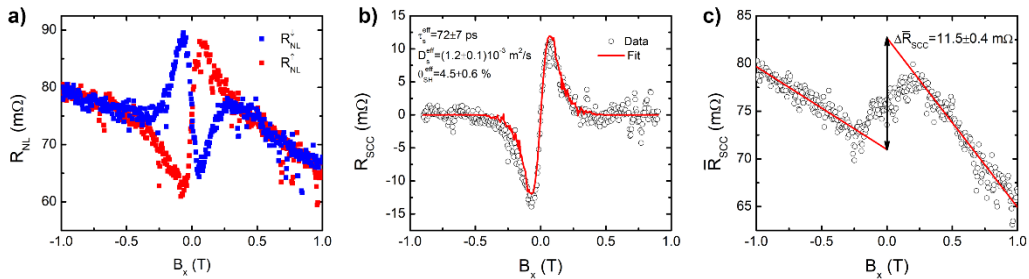


Figure 5.10: Analysis of the antisymmetric Hanle curve at 10 K for sample A. **a)** Raw data of the SCC measurement. The blue and red scatter plots indicate the initial state of the injector magnetization **b)** Fit curve in red to the data in **a)** with $R_{SCC} = (R_{NL}^{\uparrow} - R_{NL}^{\downarrow})/2$ as black circles to Equation 25 with the SCC parameters of the fit given. **c)** Arithmetic mean of the data in **a)** with $\bar{R}_{SCC} = (R_{NL}^{\uparrow} + R_{NL}^{\downarrow})/2$ as black circles and the in-plane SCC signal ΔR_{SCC} given. The red lines are linear fits to the background on either side of the switching fields of $B_x \approx \pm 240$ mT.

In Figure 5.10a, the change of the non-local resistance in a magnetic field – the clear Hanle precession – and the difference for the two injector directions are unambiguous proofs that SCC occurs in sample A.

As discussed in Section 2.5, this SCC can have three distinct sources: First, proximity-induced ISHE in graphene; second, proximity-induced IREE at the graphene/TMDC interface and thirdly, ISHE in MoS₂. For the first case, considering the symmetry of the SHE, an electrical voltage can be picked up along the graphene/MoS₂ Hall bar (y -direction) if a spin current along the graphene channel (x -direction) with out-of-plane spin polarization (z -direction) is converted. For the second case, spins with an in-plane polarization parallel to the spin current direction (x -direction) result in electrons with a k -vector in an in-plane but perpendicular direction that can be picked up as voltage difference (y -direction). The same spins will be converted in the third case, as they are absorbed into the MoS₂ (z -direction), again leading to a measurable electrical current along the Hall bar (y -direction).

Considering the behavior of the magnetization direction of the FM injector electrode shown earlier, it is clear which effects are probed for which field region: For zero field, no SCC signal is expected as spins with a polarization along y are not converted. No difference for R_{NL}^\uparrow and R_{NL}^\downarrow is therefore seen there in Figure 5.10a. Increasing B_x rotates the spin out of plane, exposing the ISHE contribution of the proximitized graphene. Two distinct shoulders in the Hanle curves with opposite sign can be seen for this field range, clearly visible in Figure 5.10b. Finally, when the magnetization is pulled and only spins point along x are injected, the contribution of the IREE and the ISHE in the TMDC can be seen in the difference for high positive and negative magnetic fields in Figure 5.10c. The amplitude of this SCC signal $\Delta\bar{R}_{SCC}$ is quantified by calculating the zero-field extrapolation using linear fittings to the background at high positive and negative fields.

The conclusion is that the observance of an antisymmetric Hanle curve is unambiguous proof that SCC occurs in graphene due to the proximity-enhanced SOC giving rise to ISHE, an unprecedented experimental demonstration. The SCC parameter of the ISHE can therefore be extracted by fitting Equation 25 in Section 2.5 to the data and Figure 5.10b shows the results. An effective spin Hall angle $\theta_{SH}^{eff} \approx 4.5\%$ can be extracted as well as an effective spin diffusion length $\lambda_s^{eff} \approx 300$ nm. This is an order of magnitude larger than the maximum theoretically predicted value of $\theta_{SH} \approx 0.1\%$ for graphene/MoS₂ using the square resistance R_{sq} as the inverse of graphene conductivity σ_{xx} [98]. λ_s^{eff} is an average of the value for the pristine graphene channel λ_s^{gr} between injector and Hall bar and the $\lambda_s^{gr/TMDC}$ of the proximitized Hall bar. The SOC imprinted by the TMDC into graphene will reduce the spin diffusion length significantly, so that it is safe to assume that $\lambda_s^{gr} > \lambda_s^{eff} > \lambda_s^{gr/TMDC}$. This approximation is necessary, as no spin signal could be measured across the graphene/TMDC LSV to extract the spin transport parameters separately. As shown in the next chapter, the approximation can introduce an uncertainty into the determination of the effective SCC parameters.

The second SCC contribution can either be assigned to proximity-induced IREE in the graphene or ISHE in the TMDC, but the experiment does not allow to disentangle between them. Interestingly, this S-shaped background signal was not observed in sample B for any temperature. The linear background, which is approximated with two linear fits as shown in Figure 5.10c, changes slope at magnetic field $B_x \approx \pm 240$ mT, the same field that saturates the magnetization of the Co electrodes (Figure 5.8a). This confirms that the signal is due to an in-plane SCC in graphene/MoS₂.

Assuming the signal is completely due to IREE, Equation 26 can be used to extract the efficiency $\alpha_{REE} \approx 0.85\%$ and it is therefore significantly smaller than the ISHE contribution. On the other hand, if the in-plane SCC occurs due to ISHE in MoS₂, it requires spin absorption from graphene into the TMDC, which depends on the resistivities and spin diffusion lengths of both materials and their interface resistance. As both flakes are stamped together into one heterostructure in the devices and the TMDC is not electrically contacted, it is not possible to separately quantify the resistivity of MoS₂. However, the SCC signal measured across the graphene/MoS₂ channel depends on two competing contributions that vary in opposite way with this resistivity: First, an increase in resistivity decreases the spin absorption and, thus, the SCC signal. Second, it also increases the effective resistance of the graphene/MoS₂ region and, thus, increases the SCC voltage until it saturates due to the shunting effect of the graphene channel. In the optimal resistivity value ($\approx 7 \times 10^{-4}$ Ωm) to maximize the resulting SCC signal, a minimum spin Hall angle of MoS₂, $\theta_{SH}^{MoS_2} \approx 3.3\%$, is required to obtain the $\Delta\bar{R}_{SCC}$ signal of 11.5 m Ω . This lower bound is very similar to the efficiency of the ISHE in the proximitized graphene and a reasonable value for the TMDC [255].

One control experiment for the ISHE in proximitized graphene is the injection from the two directions along the graphene channel into the proximitized area. This was not possible in sample A due to the already mentioned breakage of the graphene channel, but in Sample B this test was conducted, and the results are plotted in Figure 5.11. Injecting from different sides leads to opposite directions of the spin current. Hence, due to the orthogonality of the ISHE, similar curves but with opposite sign were measured. This fully rules out that the ISHE in MoS₂ plays a role here. If the spin current would be absorbed into the TMDC flake along z , the initial spin current direction would play no role and the data from the two injectors should have the same sign.

Noticeably, the spin Hall angle for the right electrode ($\theta_{SH}^{right} = 4.8\%$) is three times larger than for the left ($\theta_{SH}^{left} = 1.5\%$), while the spin transport parameters are very similar (see Table 2). While the latter is expected due to the contribution of the pristine graphene part, the former could have a physical reason. The width of the MoS₂ flake is larger than the expected $\lambda_s^{gr/TMDC}$, so that injection from the right and the left probe essentially different proximitized regions that could be heterogeneous. However, it should also be noted that θ_{SH}^{eff} is calculated from the fit parameter $P\theta_{SH}^{eff}$, the product of injection polarization and spin Hall angle, by assuming $P = \sqrt{P_i P_d}$ from the product of

injection (P_i) and detection polarization (P_d) of the symmetric Hanle precession of the reference graphene LSV. Very different polarizations for the injector and detector will therefore lead to a larger error in the estimation of θ_{SH}^{eff} . Additionally, this is also the reason why only the absolute value of the spin Hall angle can be reported, as the sign cannot be extracted from this product. Furthermore, in the case of injecting spin current from both sides, only P of the LSV on the right is known (see Table 2) and was used to calculate both spin Hall angles. This introduces an additional uncertainty to the result.

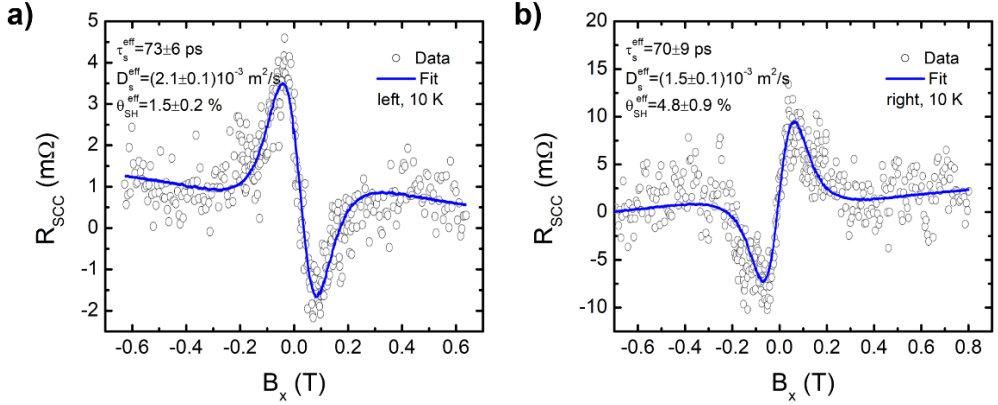


Figure 5.11: Antisymmetric Hanle curves for both sides in Sample B. a) Data and fit for using the electrode on the left and **b)** right side of the MoS₂ flake. Both measured at 10 K.

As a next step, the temperature dependence of the signal was measured in Sample A and B. As seen in Figure 5.12a, only the R_{NL}^{\uparrow} part of the antisymmetric Hanle curve was measured for sample A, so that a full analysis of the ISHE is not possible but the temperature dependence of the second contribution $\Delta \bar{R}_{SCC}$ can be extracted (see Table 1). It is only weakly affected by the change in temperature. However, the resulting SCC efficiencies change more drastically. At 300 K, a Rashba-Edelstein efficiency of $\alpha_{REE} \approx 3\%$ would be needed, while the spin Hall angle of MoS₂ would only change to $\theta_{SH}^{MoS_2} \approx 2.2\%$. Such a weak temperature variation in the spin Hall angle is expected for a bulk material, which is the case for this thick MoS₂ flake (see Figure 5.2d). Although no scenario can be fully ruled out, the temperature dependence of the in-plane SCC suggests that spin absorption and subsequent ISHE in the TMDC is a more plausible option. However, the third option of both effects occurring at the same time with varying degrees, depending on the temperature, is also possible.

In sample B, the in-plane contribution was not observed, but a full set of antisymmetric Hanle curves was recorded, so that the temperature dependence of the extracted θ_{SH}^{eff} can be plotted in Figure 5.12b. It shows an excellent agreement with the value at 10 K of sample A as well as a reduction in θ_{SH}^{eff} for increasing temperature. This trend is in line with a change in the proximity effect due to thermal broadening leading to smearing out of the hybridization. In the analysis, the temperature dependence of the electrical

properties of the heterostructure has to be considered, such as the two-point resistance of the two LSVs shown in Figure 5.13a. It shows that the resistance also decreases with increasing temperature, a feature reported in graphene when the Fermi level is near the Dirac point [256]. According to the theoretical calculations, this could mean that the device is not at the optimal Fermi level for SCC and the signals could be improved by measuring the gate dependence [32, 98].

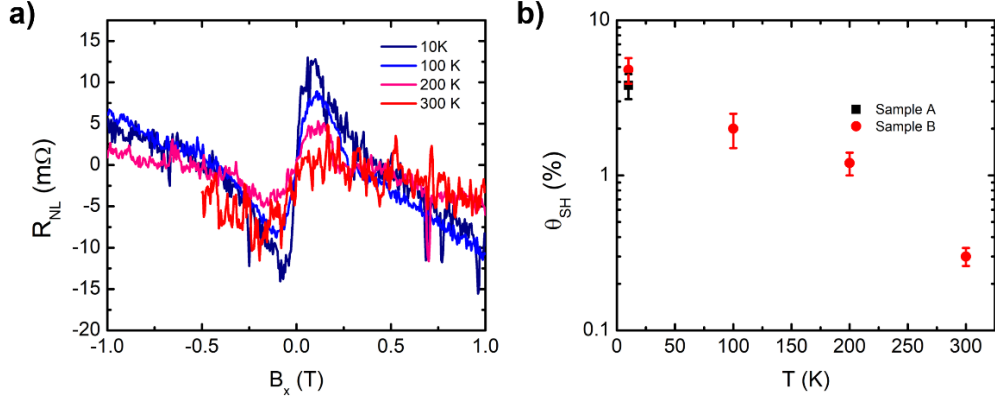


Figure 5.12: Temperature dependence of the SHE. **a)** The R_{NL}^{\uparrow} part of the antisymmetric Hanle curves measured at different temperatures in sample A. **b)** Temperature dependence of the spin Hall angle θ_{SH} for the two samples.

As final control experiment, the SCC voltage across the pristine graphene Hall bar was measured and the results are shown in Figure 5.13b. As expected, no ISHE or IREE signal can be observed, since pristine graphene has negligible SOC and therefore no SCC should occur. The linear background is similar to the one shown with linear fits in Figure 5.10c. As it is linear and antisymmetric in field, it probably stems from ordinary Hall effect contribution in graphene that can be large, especially near the CNP (see Figure 3.2c). The underlying origin, a component of the magnetic field parallel to z , probably comes from a slight out-of-plane misalignment of the sample.

Table 1 and 2 list the spin transport and SCC parameters of the two samples and, where possible, their temperature dependence. The spin diffusion length for the pristine graphene LSV λ_s^{gr} achieved here is, compared to the state-of-the-art values listed in Section 3.1.2, rather short, but typical for bare samples exposed to multiple fabrication steps. As already explained, the main advantage of using graphene as a spin transport channel material is the temperature independence of λ_s^{gr} that even reaches its largest value in both samples at room temperature. The spin transport parameters of the proximitized graphene show the effect of the adjacent TMDC: Not surprisingly, τ_s^{eff} is reduced down to roughly a third or fourth of its pristine value as the induced SOC leads to a SOF that relaxes the spin via the DP mechanism. D_s^{eff} is even more decreased, in one case to 10% of its original size.

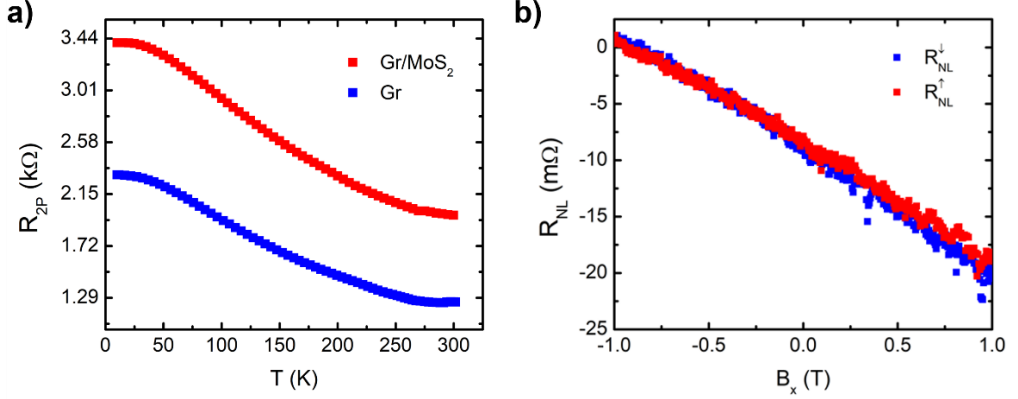


Figure 5.13: Reference data of sample A. a) Temperature dependence of the two-point resistance R_{2P} for the pristine and the proximitized graphene Hall bar. b) SCC measurement across the pristine graphene Hall bar showing no signal above the linear background. Measured at 10 K.

The SCC conversion parameters exceed the prior theoretical calculations [98]. Looking at the spin Hall angle, θ_{SH}^{eff} is an order of magnitude larger than the predicted 0.1%, with 4.8% at 10 K and still 0.33% at room temperature. To get a better comparison with the values shown in Figure 5.1, the tables also give the spin Hall conductivity. $\sigma_{xy}^{gr/TMDC}$ is in the range of $10^{-5} \Omega^{-1}$ and hence two orders of magnitude larger than the maximum theoretical value calculated for no disorder, in-line with the results of the spin Hall angle. One should however note that those calculations have been limited to a phenomenological description of disorder using intrinsic broadening of the electronic states and also did not include any extrinsic effects that could play a role here.

Additionally, the figure of merit $\theta_{SH}^{eff} \lambda_s^{eff}$ has its largest value at 10 K with 16 nm and still reaches 1.5 nm at room temperature, rather large values even when considering the potential of the vdW heterostructure, combining the advantages of graphene (long spin diffusion length) and TMDC (large SOC). In the next chapter, these values will be outperformed and a thorough comparison to other SCC systems will be given.

Finally, it should be noted that even though the SCC due to ISHE in proximitized graphene could be observed reliably in two samples, some experiments could not be conducted: First of all, the direct SHE could not be measured. Secondly, due to a leaking back gate dielectric, no gate dependence was recorded. Thirdly, as already mentioned, the anisotropic transport across the TMDC flake could not be observed. All those three shortcomings could, fortunately, be realized in the experiments presented in the next chapter.

Table 1: Extracted spin transport and SCC parameters for sample A. R_{sq}^{gr} and $R_{sq}^{gr/TMDC}$ are calculated from the four-point resistance between the respective electrode pairs and the length and width of the channel from the scanning electron microscopy image. D_s^{gr} , τ_s^{gr} , and P are extracted from fits to the symmetric Hanle precession data, D_s^{eff} , τ_s^{eff} , and θ_{SH}^{eff} are extracted from fits to the antisymmetric Hanle precession data, and $\Delta\bar{R}_{SCC}$ is extracted from fits to the S-shaped background of the antisymmetric Hanle precession data.

Sample A	10 K	100 K	300 K
R_{sq}^{gr} (Ω)	543	454	295
$R_{sq}^{gr/TMDC}$ (Ω)	497	430	288
D_s^{gr} ($10^{-3} m^2/s$)	5.7 ± 0.5	8.8 ± 0.5	20 ± 4
τ_s^{gr} (ps)	300 ± 20	221 ± 8	152 ± 6
λ_s^{gr} (μm)	1.3 ± 0.1	1.4 ± 0.1	1.7 ± 0.3
P (%)	2.9 ± 0.2	2.9 ± 0.1	4.8 ± 0.2
D_s^{eff} ($10^{-3} m^2/s$)	1.2 ± 0.1		
τ_s^{eff} (ps)	72 ± 7		
λ_s^{eff} (nm)	300 ± 30		
θ_{SH}^{eff} (%)	4.5 ± 0.6		
$\Delta\bar{R}_{SCC}$ (m Ω)	11.5 ± 0.4	12.0 ± 0.5	7.4 ± 0.4
$\sigma_{xy}^{gr/TMDC}$ ($10^{-5} \Omega^{-1}$)	9 ± 1		
$\theta_{SH}^{eff} \lambda_s^{eff}$ (nm)	13 ± 1.5		

Table 2: Extracted spin transport and SCC parameters for sample B. $R_{sq}^{gr/TMDC}$, D_s^{gr} , τ_s^{gr} , P , D_s^{eff} , τ_s^{eff} and θ_{SH}^{eff} as for Table 1. R_{sq}^{gr} was not measured for this sample and $\Delta\bar{R}_{SCC}$ not observed above the baseline of the noise level. At 10 K the SCC parameters for the right and left electrodes are listed separately.

Sample B	10 K	10 K (left)	100 K	200 K	300 K
$R_{sq}^{gr/TMDC}$ (Ω)	282		266	231	215
D_s^{gr} ($10^{-3} m^2/s$)	7.0 ± 0.3		11 ± 1	15 ± 2	16 ± 3
τ_s^{gr} (ps)	252 ± 8		146 ± 14	139 ± 2	114 ± 1
λ_s^{gr} (μm)	1.3 ± 0.1		1.3 ± 0.1	1.4 ± 0.1	1.4 ± 0.2
P (%)	2.4 ± 0.1		7.2 ± 0.1	7.7 ± 0.1	6.9 ± 0.1
D_s^{eff} ($10^{-3} m^2/s$)	1.5 ± 0.1	2.1 ± 0.1	1.6 ± 0.1	1.4 ± 0.1	2.8 ± 0.4
τ_s^{eff} (ps)	70 ± 9	73 ± 6	49 ± 3	44 ± 3	72 ± 16
λ_s^{eff} (nm)	320 ± 30	390 ± 30	300 ± 30	250 ± 20	450 ± 80
θ_{SH}^{eff} (%)	4.8 ± 0.9	1.5 ± 0.2	2.0 ± 0.5	1.2 ± 0.2	0.33 ± 0.04
$\sigma_{xy}^{gr/TMDC}$ ($10^{-5} \Omega^{-1}$)	17 ± 3	5.3 ± 0.7	7.5 ± 2	5.2 ± 0.9	1.5 ± 0.2
$\theta_{SH}^{eff} \lambda_s^{eff}$ (nm)	16 ± 2	5.9 ± 0.6	5 ± 1	3 ± 0.4	1.5 ± 0.2

6 Record spin-to-charge conversion efficiency by electrical control in graphene proximitized with WSe₂

6.1 Theoretical prediction of Fermi energy dependence

In the previous chapter, it has been shown that the proximity effect in graphene-based vdW heterostructures can lead to an efficient SCC. Combining the long spin diffusion length of graphene with the strong SOC of a TMDC leads to efficiencies that easily outperform other typical SCC systems like heavy metals. However, one aspect of the theoretical predictions that preceded these experiments has been neglected so far. Due to the tunable Fermi level in the linear band structure of graphene, also the SCC should show a dependence on applied back gate voltage [98]. By exploiting this behavior, it should be possible to optimize the efficiency of this 2D material system even further.

Figure 6.1a shows the energy dependence of the previously mentioned spin Hall conductivity for out-of-plane spins σ_{xy}^z on the Fermi energy for different TMDCs. This measure gives an indication of the ability of the system to convert charge currents into spin currents via the SHE. In all four cases, a tuning of its size is calculated and, for the TMDCs made up of W as transition metal, even a switching of the sign is predicted. This behavior stems from the change in the proximitized band structure and the difference in the local Berry phase. A maximum value for σ_{xy}^z in graphene is computed when proximitized with WS₂ when looking at the hole regime and with WSe₂ when electrons are the majority carriers. In both cases, the peak of the amplitude is found energetically close to the Dirac point. This gives a first indication of which TMDC to choose for the vdW heterostructure when optimizing for large SCC outputs. It should be noted, however, that these calculations were done for monolayer TMDC on monolayer graphene and without considering any disorder in the heterostructure [98].

The in-plane spin density n_s^{\parallel} in Figure 6.1b accounts for the second SCC mechanism, the REE. Similar to σ_{xy}^z , it is maximum for WS₂ and WSe₂ on the hole and electron side, respectively. However, opposite to the behavior of the SHE, it is non-zero even for energies far away from the Dirac point, which should make it more stable against

unwanted doping of the graphene flake. Interestingly, the inset shows that the main ingredient for REE is the existence of Rashba SOC in the system. For the out-of-plane SCC, the inset in Figure 6.1a shows a more complex dependence on the different SOC that have been introduced in Section 2.1. Importantly, VZ SOC is the main ingredient but will alone not lead to a sizeable SHE.

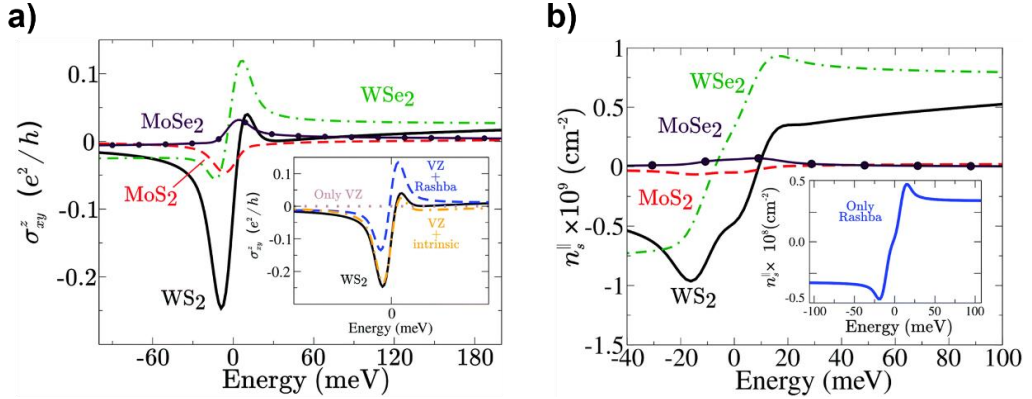


Figure 6.1: SCC effects in graphene proximitized with different TMDCs. a) Spin Hall conductivity for out-of-plane spins σ_{xy}^z as a function of the Fermi energy. The inset shows the results for WS₂ in the case of only considering VZ SOC, VZ and intrinsic SOC, or VZ and Rashba SOC. **b)** In-plane spin density n_s^{\parallel} of the spin accumulation due to the REE as a function of Fermi energy. The inset shows the results for WS₂ in the case of only considering Rashba SOC. Images taken from Ref. [32].

In regards to the SOC, another theoretical study that used fully relativistic first-principles calculations based on density functional theory concluded that WSe₂ has the largest spin-splitting of the 2H TMDC group of up to 456 meV [138] and therefore has the largest capability to transfer SOC into graphene. Indeed, a similar calculation for 2H TMDCs on graphene came to the result that WSe₂ imprints the largest SOC into graphene, even leading to band inversion [33].

These predictions lead to the choice of WSe₂ as TMDC for the proximity with graphene and the results of this study are published in the second paper of this thesis [257] and are presented in the following section. However, in the one year that chronologically lies between the results of this chapter and the previous one, other reports have shown similar results.

Ghiasi et al. from the van Wees group in Groningen used a similar graphene-based heterostructure but chose WS₂ as TMDC to demonstrate REE and SHE [198]. In their presentation, they focused on the REE as they could modulate the amplitude with an applied back gate voltage in the electron regime of graphene. The signal also showed a strong temperature dependence, being reduced to 15% between 4.2 K and room

temperature. They additionally observed a SHE component in the charge-to-spin conversion signal but were not able to quantify the efficiencies reliably.

Also using a graphene/WS₂ device, Benitez et al. from the Valenzuela group in Barcelona measured the electrical tuning of ISHE and IREE over a wide temperature range [199]. Quantifying the anisotropic spin transport across the proximitized LSV allowed them to give exact and exceptionally large efficiencies for both effects. The values are part of the comparison in Table 5 under graphene-based LSVs. They also achieved a sign change for both effects when crossing the Dirac point of graphene by applying a back gate voltage.

Khokhriakov et al. in the Dash group in Gothenburg used a topological insulator from the BiSbTe family to demonstrate a large IREE at room temperature [258]. Opposite to the two earlier results, the SCC stems here not from the proximitized graphene but from the surface states of the topological insulator. Using an effective spin diffusion length λ_s^{eff} , they estimated the efficiency of the effect. Additionally, they observed a sign change of the signal on applying V_g but the value for the axis intercept in regard to the CNP varied strongly between the three devices and no reproducibility for the trend of the amplitude away from the Dirac point was shown.

Noticeably, these previous reports never observe only SHE, while the results in the next section on graphene/WSe₂ show SCC solely because of ISHE and no IREE contribution. However, both effects can be compared via the efficiencies defined in Section 2.5 and a wide variety of systems is listed in the last section of this chapter.

6.2 Device characterization, spin transport, and spin-charge interconversion

The fabrication process follows the recipe given in Section 5.2 so that it is not repeated here. The resulting device can be seen in Figure 6.2a in a scanning electron microscope and in Figure 6.2b in an atomic force microscope image. The lateral dimensions are similar to the previous devices. However, the height profile in Figure 6.2c shows that the graphene flake is noticeably thinner. The number of layers was determined by Raman spectroscopy to be three. As in the case of MoS₂, the TMDC flake is bulk according to the thickness measurement in Figure 6.2d.

To electrically characterize the device before the non-local measurements, the four-point resistance of the graphene channel between the electrodes of the reference graphene LSV and of the graphene/WSe₂ LSV was measured and the corresponding square resistance R_{sq} was calculated. The temperature dependence of R_{sq} for the two regions is shown in Figure 6.3a. The TMDC not only enhances the SOC by proximity effect but also dopes the graphene. Figure 6.3b shows the gate dependence of R_{sq} for both regions at 100 K and how the different doping moves the CNP from higher positive gate voltages to between 5 and 6 V. Due to a larger leakage current (> 1 nA) it was not possible to apply

higher gate voltages so that a full analysis of the charge transport measurements was unachievable. One reason for this could be damage to the SiO₂ from the wire bonding.

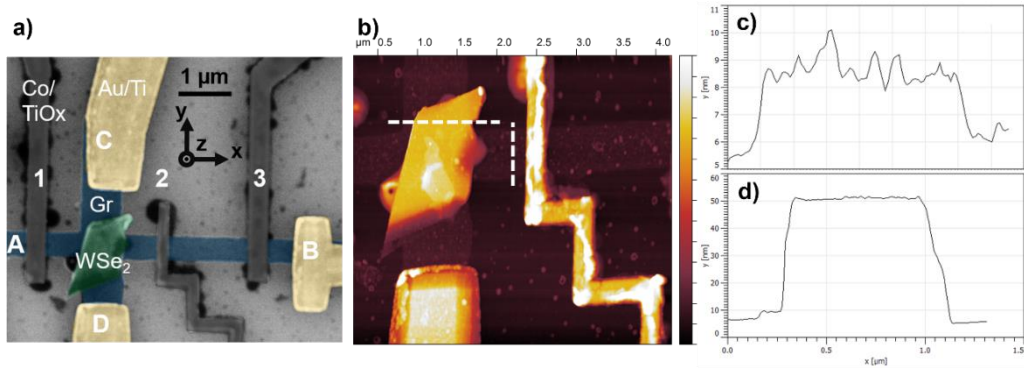


Figure 6.2: Device characterization. **a)** False-colored scanning electron microscopy image of the device after the electrical measurements. The oxidation of the Co electrodes is visible as well as some contamination. The width of the graphene channel was measured as 495 nm, the width of the graphene Hall bar arms is 810 nm. The center-to-center distance between the Co electrodes is 1.84 μm for the reference LSV on the right (electrodes 2 and 3) and 2.48 μm for the graphene/WSe₂ LSV in the middle (electrodes 1 and 2). **b)** Atomic force microscopy characterization of the device after the electrical measurements. **c)** Line profile taken along the marked line across the graphene and **d)** WSe₂ flake. The thickness of the graphene was measured as 3 nm and for the WSe₂ flake as 45 nm.

Similar to the previous chapter, the spin transport of graphene was thoroughly characterized. For the sake of brevity, this will not be explained in detail, but Figure 6.4 shows an exemplary analysis for 100 K.

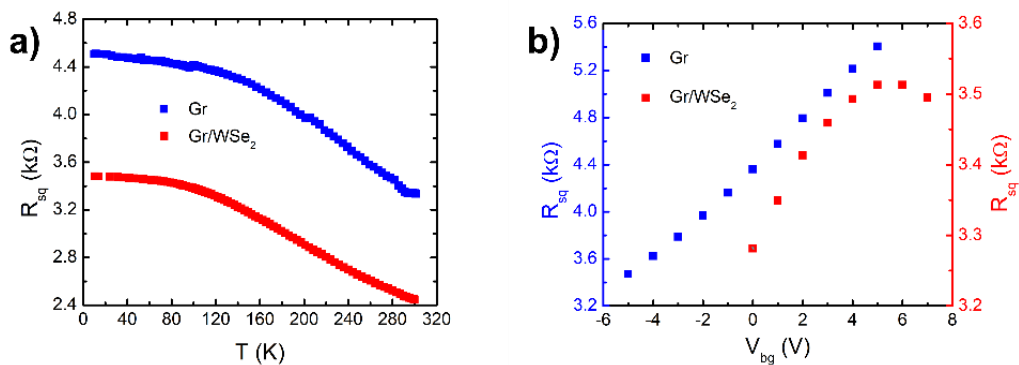


Figure 6.3: Temperature and gate dependence of the resistance. **a)** Square resistance R_{sq} for the reference and proximitized LSV as a function of temperature at $V_{bg} = 0$ V and **b)** of back gate voltage at 100 K.

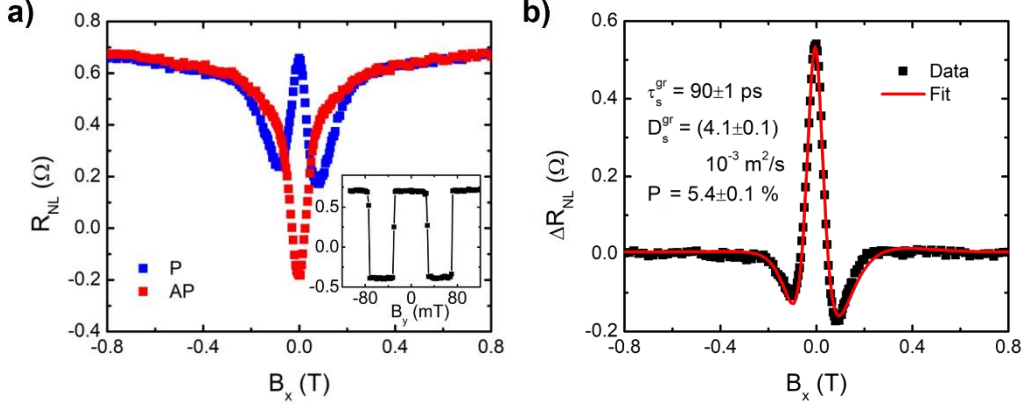


Figure 6.4: Analysis of the symmetric Hanle curve of the reference LSV. a) Raw data at 100 K. The blue and red curves indicate the initial state of the injector and detector magnetizations, parallel and antiparallel. Inset: LSV signal for applying B_y . b) Fit of the data in a) to Equation 20 with the spin transport parameters of the fit given.

The reference LSV between FM electrodes 2 and 3 (see Figure 6.2a) was used and the dependence of the non-local resistance on B_x and B_y is shown in Figure 6.4a and in the inset, respectively. ΔR_{NL} at zero field is larger by more than a factor of ten compared to the graphene/MoS₂ device. The reason for this, as seen in Equation 20 in Section 2.4, is the ten times larger square resistance R_{sq}^{gr} .

Figure 6.4b shows the difference between parallel and antiparallel curves, the pure spin precession data, from where the spin transport parameters at 100 K are extracted. It can be seen that the spin diffusion length λ_s^{gr} is roughly half of the values of the devices of the previous chapter while the polarization of the spin injection P could be doubled.

One of the missing measurements in the previous chapter was the anisotropic spin transport across the graphene/TMDC region. However, such a measurement was realized in this graphene/WSe₂ device (using electrodes 1 and 2 in Figure 6.2a) and is shown in Figure 6.5.

Surprisingly, the LSV signal ΔR_{NL} in Figure 6.5a shows an opposite sign than expected. Complementarily, Figure 6.5b shows the Hanle precession: As theoretically predicted [185] and already experimentally observed [71, 188], the enhanced SOC by proximity effect leads not only to an enhanced spin relaxation compared to the pristine graphene but also to a large anisotropy between the in- and out-of-plane spin lifetimes ($\tau_{\parallel}^{gr/TMDC}$ and $\tau_{\perp}^{gr/TMDC}$, respectively). This shows up in the curves as a suppression of the spin signal at low fields when the spins are polarized in plane. As the magnetic field increases, the injected spins precess out of the sample plane and acquire a lifetime, which is a combination of $\tau_{\parallel}^{gr/TMDC}$ and $\tau_{\perp}^{gr/TMDC}$. This leads to a sign change in ΔR_{NL} and the

observation of enhanced shoulders when compared with the zero-field value (see Figure 2.6b). This typically allows the determination of the two spin lifetimes from the experimental data by fitting it to the solution of the anisotropic Bloch equation [71, 185, 188]. However, the data here, while clearly showing all the other signatures of anisotropic spin transport, miss the characteristic crossing of R_{NL}^P and R_{NL}^{AP} at low fields (see the inset in Figure 6.5b), preventing the determination of $\tau_{\parallel}^{gr/TMDC}$ and $\tau_{\perp}^{gr/TMDC}$. This negative sign of the spin signal at zero field matches the result in Figure 6.5a. The missing crossing is a surprising result that is not expected as the enhanced shoulders are already a consequence of the out-of-plane precession, which should lead to the reversal of the in-plane spin precession in this field range. Whereas the shoulders show that the out-of-plane spin signal is enhanced ($\Delta R_{NL} \approx -0.2 \Omega$) and much larger than the in-plane one ($\Delta R_{NL} \approx -10 \text{ m}\Omega$), it is still smaller than that in the pristine graphene LSV, where $\Delta R_{NL} \approx 0.55 \Omega$ was obtained.

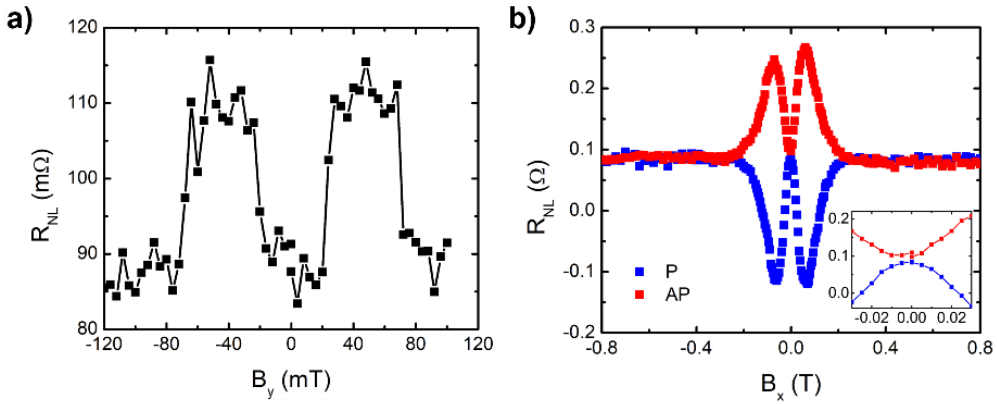


Figure 6.5: Analysis of the symmetric Hanle curve of the graphene/WSe₂ LSV1. **a)** LSV signal for applying B_y . **b)** Raw data for B_x . The blue and red curves indicate the initial state of the injector and detector magnetizations, parallel and antiparallel. Inset: Zoomed-in image of the measurement at a low magnetic field. Both measurements were taken at 100 K.

Some factors can influence the measurement of the non-local resistance shown in the Hanle precession measurement. Firstly, it should be noted that this missing zero-field crossing cannot be a background-related effect as both curves overlap within the noise level when the magnetizations have saturated. Secondly, an out-of-alignment mounting of the sample in the rotational sample holder should not affect the measurements as it does not change the orientation of the electrodes to each other in regard to the magnetic field. Furthermore, such a misalignment must be small in these measurements, as otherwise, it would lead to premature switching of the contact magnetizations when B_x is applied but this is not visible in the data: The saturation field $B_{sat} \approx 250 \text{ mT}$ as in previous measurements. A slight out-of-plane misalignment between the two FM electrodes due to inhomogeneous magnetic domain formation could lead to a shift of the

Hanle curves. However, this effect would shift the Hanle precession data with respect to B_x and would not impede the crossing of both curves at low field. Nevertheless, the interpretation of the data could be more complex due to local invariances of the strength of the SOC, as the proximity effect can depend on the distance between the two flakes and could vary due to wrinkles or strain after the stamping, which would have to persist after annealing. However, this cannot affect the sign of the spin signal itself unless the Landé factors would change sign, leading to complex precession processes. Hence, the reason for the missing crossing of R_{NL}^P and R_{NL}^{AP} in Figure 6.5b could not be determined with the set of experiments in this chapter. Fortunately, the next chapter will study this phenomenon further and give a conclusive answer to this open question.

The observed spin lifetime anisotropy in the symmetric Hanle curves is a fingerprint of the induced SOC in graphene by proximity with WSe₂. Such a spin-orbit proximity in the graphene/WSe₂ region is also expected to lead to a sizable SHE, even though the intervalley scattering leading to anisotropy has been predicted to be detrimental to the SHE [32]. The next set of experiments, therefore, moves to the SCC configuration using electrode 1 (see Figure 6.2a) for spin injection and the Au contacts C and D for voltage detection. The resulting antisymmetric Hanle precession curves for the non-local resistance can be seen in Figure 6.6a for a measurement at 100 K. For the two cases of initial magnetization of the Co electrode along the y -direction (R_{NL}^\uparrow for positive and R_{NL}^\downarrow for negative magnetization along the easy axis) the antisymmetric Hanle curve is reversed, as expected from the precession of spins with opposite polarization.

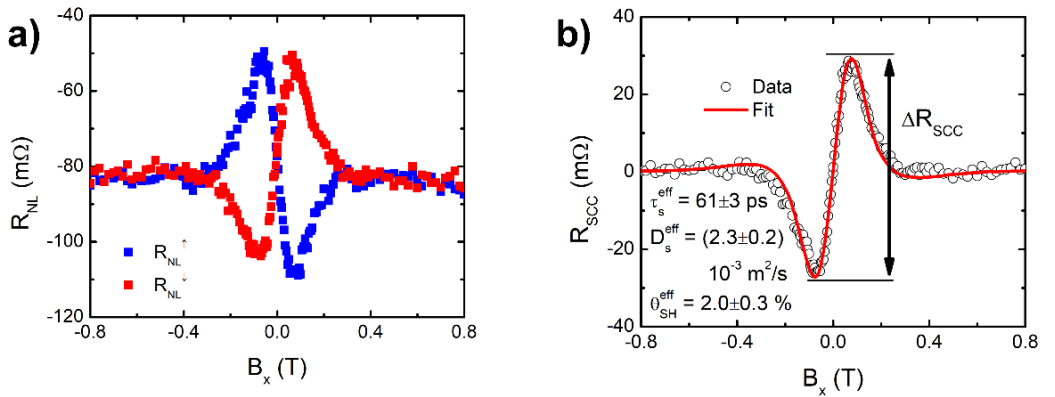


Figure 6.6: Analysis of the antisymmetric Hanle curve. a) Raw data R_{NL} for the SCC measurement at 100 K. b) Fit of the data $R_{SCC} = (R_{NL}^\uparrow - R_{NL}^\downarrow)/2$ from panel a) to Equation 25 with the SCC parameters of the fit given.

Similar to the symmetric Hanle curves, the difference between the two antisymmetric Hanle precession curves, $R_{SCC} = (R_{NL}^\uparrow - R_{NL}^\downarrow)/2$, gives the net signal that can be fitted to the solution of the Bloch equation, as shown in Figure 6.6b for the case of 100 K alongside the fitted parameters: An effective spin lifetime (τ_s^{eff}), an effective spin

diffusion constant (D_s^{eff}) and an effective spin polarization (P^{eff}). As the spin current is now detected via the SCC in the proximitized graphene/WSe₂ region and not with an FM electrode, P_d of the detector is replaced by the spin Hall angle θ_{SH}^{eff} and thus $P^{eff} = \sqrt{P_i \theta_{SH}^{eff}}$. Assuming the same $P_i = P$ for the injector as the one obtained from the electrode pair of the reference LSV ($P = \sqrt{P_i P_d}$), the value of θ_{SH}^{eff} can be calculated. However, because the sign of P is not known, the sign of θ_{SH}^{eff} cannot be determined either.

The results in Figure 6.6b also confirm that no IREE is present in the SCC signal, as the background does not switch between positive and negative high fields when the applied magnetic field pulls and saturates the magnetization of the FM electrode along the x -axis and the injected spins are thus polarized in this direction.

Like in the previous chapter, the control experiment for injecting the spin current from both sides of the graphene/WSe₂ region was performed. The antisymmetric Hanle curve for injection with electrode 2 from the right side can be seen in Figure 6.7a. The $R_{NL}^{\uparrow(\downarrow)}$ curve changes sign with reversing the spin current direction, which further confirms the proximity-induced ISHE in graphene as the source of the SCC. The measurement has a similar signal amplitude to the one from the left side but larger noise and a linear background due to drift. Therefore, all the following measurements were performed with electrode 1.

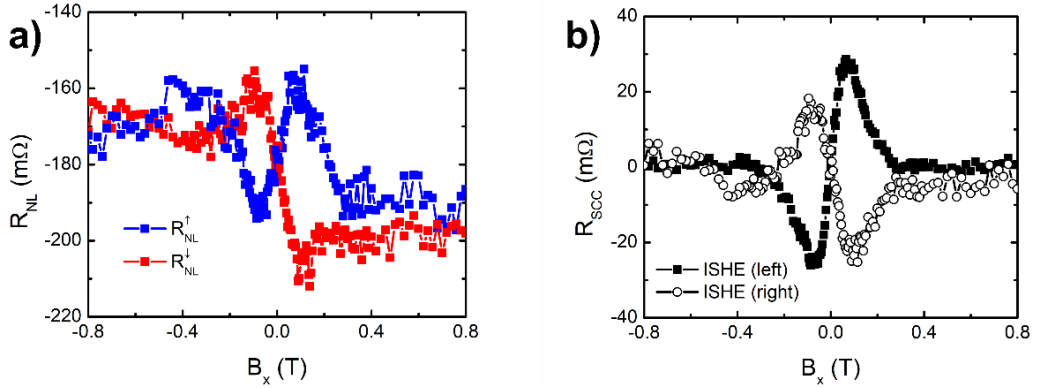


Figure 6.7: Antisymmetric Hanle curves for both sides. a) Raw data R_{NL} for using the electrode 2 on the right side of the WSe₂ flake measured at 100 K. **b)** Comparison of $R_{SCC} = (R_{NL}^{\uparrow} - R_{NL}^{\downarrow})/2$ of the ISHE with spin injection from the right and the left.

Figure 6.7b compares R_{SCC} for the ISHE measurements injecting spin current from the left and the right side of the graphene/WSe₂ region. Again, the opposite precession in the antisymmetric Hanle curve is expected for injecting a spin current from the opposite

direction into the graphene/WSe₂ region and is, therefore, another robust evidence for ISHE due to the proximity effect in this device.

The Onsager reciprocity, where a charge current through the graphene/WSe₂ region (along y) gives rise to a transverse spin current (along x) due to the direct SHE, is also confirmed in this device – something that was missing as a control experiment from the study in the previous chapter. Swapping the contact pairs of the SCC measurement enables the direct observation of the SHE. In this case, the charge current is applied across the graphene/WSe₂ region with Au contacts C and D. Due to the proximity-induced SHE, a spin current diffuses along the graphene channel (along x) with out-of-plane spins. An in-plane magnetic field applied along the x -axis (B_x) precesses the spins towards the y -axis, which can then be detected with the FM electrode. The measurement is shown in Figure 6.8a.

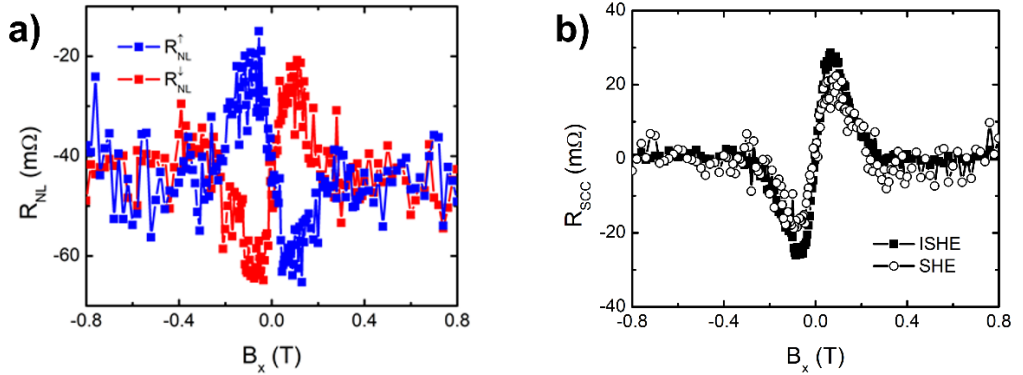


Figure 6.8: Antisymmetric Hanle curves for direct and inverse SHE. **a)** Raw data for interchanging voltage and current leads for the SCC measurement at 100 K. **b)** Comparison of $R_{SCC} = (R_{NL}^{\uparrow} - R_{NL}^{\downarrow})/2$ for the ISHE and SHE.

Figure 6.8b compares R_{SCC} for the SHE and ISHE measurement. As the definition for the direction of the magnetic field and the magnetization of the FM did not change, the two antisymmetric Hanle curves have the same sign (following $R_{NL(12,34)}(H, M) = R_{NL(34,12)}(H, M)$ [81]), which is therefore another strong evidence for SHE due to the proximity effect in this device. The charge-to-spin conversion signal is only slightly smaller than its Onsager reciprocal, but the measurement is noisier as it uses the FM electrode for detection that has a higher contact resistance due to the TiO_x tunnel barrier than the Au/Ti contacts. Therefore, all the following measurements were performed in the ISHE setup.

6.3 Temperature and gate dependence of the spin-to-charge conversion in graphene/WSe₂

In a next step, the temperature dependence of the symmetric (spin transport) and antisymmetric (SCC) Hanle curves were measured between 10 K and 300 K. The spin transport measurements at different temperatures are shown in Figure 6.9a. The non-local spin signal in the reference graphene LSV between electrodes 2 and 3 decreases for lower temperatures as seen in the smaller peak amplitudes (see Table 3 for a list of the fitted parameters at all temperatures).

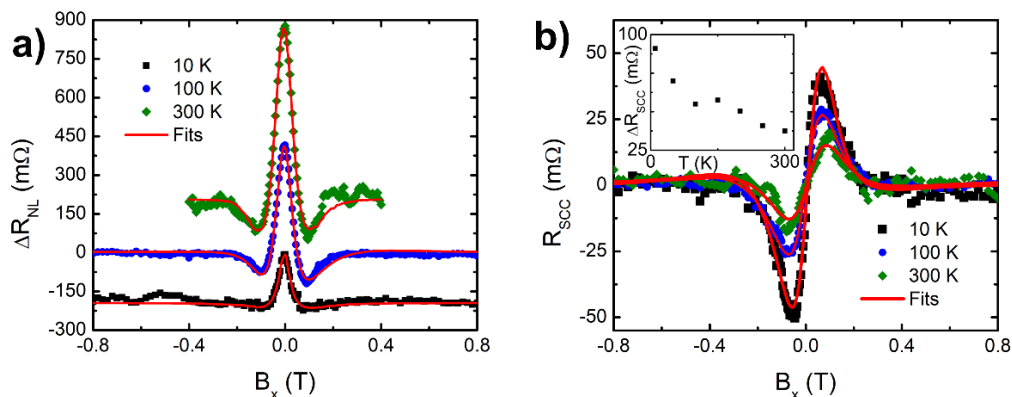


Figure 6.9: Analysis of the symmetric and asymmetric Hanle curves for different temperatures at $V_{bg} = 0$ V. a) ΔR_{NL} across the pristine graphene LSV for different temperatures. b) ISHE data for the same temperatures and the fits for the SCC parameters, respectively. Inset: Temperature dependence of the amplitude $\Delta R_{SCC} = (R_{SCC}^{max} - R_{SCC}^{min})$.

The ISHE measurements at different representative temperatures with the corresponding fits are plotted in Figure 6.9b. It should be noted that the SCC signal, ΔR_{SCC} , defined as the difference between the minimum and maximum of R_{SCC} , increases with decreasing temperature (inset in Figure 6.9b). One contributing factor for this trend is the increasing square resistance of the graphene channel, which increases roughly by 40% from 300 K to 10 K (see Figure 6.3a). Also, λ_s^{eff} and θ_{SH}^{eff} are slightly increasing with decreasing temperature, which leads to more spin current reaching the proximitized area under the WSe₂ flake and being converted there more efficiently at lower temperatures (see Table 3).

As a final experimental characterization step, the back gate voltage, V_{bg} , dependence of the symmetric and antisymmetric Hanle curves was measured at 100 K. For the reference LSV, the symmetric Hanle curves and fits can be seen in Figure 6.10a. For the ISHE measurement, the resulting data together with the fits are plotted in Figure 6.10b. The back gated measurements show that the SCC signal can be increased by 400% by

applying -5 V and completely suppressed for 5 V gate voltage (see inset in Figure 6.10b). This gate voltage range translates into charge carrier density values from $7.2 \times 10^{11} \text{ cm}^{-2}$ to the CNP.

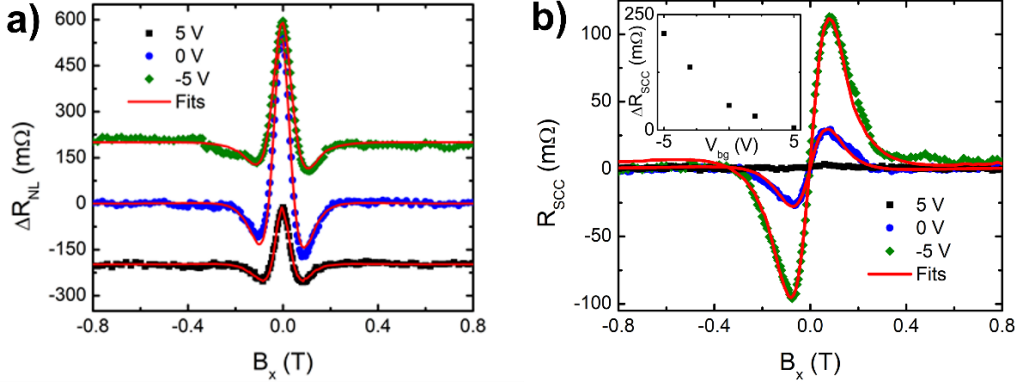


Figure 6.10: Analysis of the symmetric and asymmetric Hanle curves for different back gate voltages at 100 K. a) ΔR_{NL} across the pristine graphene LSV for different back gate voltages. **b)** ISHE data for the same back gate voltages and the fits for the SCC parameters, respectively. Inset: Back gate voltage dependence of the amplitude $\Delta R_{SCC} = (R_{SCC}^{max} - R_{SCC}^{min})$.

The strong variation of the SCC signal cannot be explained by the change in resistance of the graphene channel, as it decreases for negative gate voltages (see Figure 6.3b) or by the effective spin diffusion length, which varies only slightly when applying positive gate voltages (see Table 4 for a list of the fitted parameters at all gate voltages). However, the estimated θ_{SH}^{eff} scales with the SCC signal and increases to 8.4% for -5 V gate voltage, while at 5 V it decreases below 0.2%, which is estimated as an upper limit due to the noise level. Therefore, the conclusion is that the gate voltage directly controls the SCC.

The gate tunability of the SHE in graphene proximitized by a TMDC has been theoretically predicted, where a sign change is expected around the Dirac point [98]. The gate voltage range limitation (due to a leakage current through the gate dielectric) prevented a crossing of the CNP to observe the sign change. Because of this, it cannot be ruled out that the suppression (amplification) of the SCC signal arises from an increased (decreased) spin absorption into the WSe₂ flake if the applied back gate voltage strongly modifies the resistance of WSe₂ in this range. In this scenario, the largest estimated θ_{SH}^{eff} (8.4% at -5 V) would be a lower limit for the ISHE in proximitized graphene. In either case, though, a large tunability of the SCC signal is achieved with a back gate voltage, an extra functionality that opens new possibilities in spin-orbit-based logic or memory.

Finally, it is also worth noting that, even though the SCC signal at 300 K is smaller than at low temperatures, the modulation due to the gate voltage could amplify it immensely as it is stronger than the temperature dependence of the signal (see Figure 6.11). Applying

higher negative gate voltages could also lead to giant ISHE signals at room temperature as we see from the charge transport measurements that the saturation region far away from the Dirac point is not reached yet.

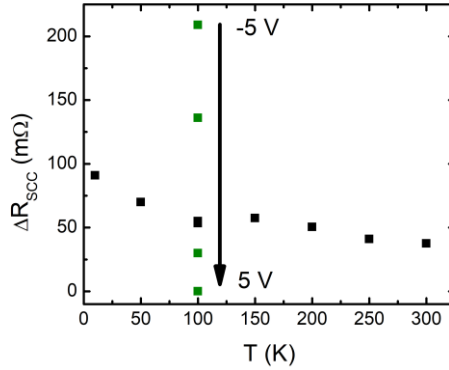


Figure 6.11: Comparison of the ISHE signals from the insets of Figure 6.10. The gate dependence of ΔR_{SCC} indicated by the black arrow and green scatter points was measured at 100 K.

In agreement with other experimental studies of the proximity effect of TMDCs in graphene [198, 199, 253], the measured θ_{SH}^{eff} is larger than the theoretical calculation by tight-binding models [98], from which a maximum value of 1.1% is extracted in the hole-doped regime, assuming the experimentally characterized resistance, suggesting that extrinsic sources of spin-dependent scattering such as vacancies or impurities might also be relevant in these heterostructures [248, 259]. It should be noted that the theoretical calculation is done for ideal monolayer graphene/monolayer TMDC systems and discrepancies could therefore occur in thicker samples. However, as the proximity effect will strongly decay over distance, the SCC will mainly occur in the graphene layer adjacent to the TMDC and the theoretical model should be a good approximation. As there is no control of the crystallographic alignment of the graphene and TMDC flake in the transfer process, the twist angle between the two could also lead to a deviation from the theoretical model, which assumes a quasi-commensurate structure [98].

In contrast to the previous measurements with MoS₂ discussed in chapter 5, the SCC signal here is solely due to ISHE, as no IREE was observed at any temperature or gate voltage that would be visible as an S-shaped background in the antisymmetric Hanle measurements [198, 199, 253]. From the noise level of the background, an estimation for the IREE efficiency α_{REE} gives $< 0.05\%$. The results suggest that the VZ SOC induced in graphene, main responsible of the SHE, dominates over the Rashba SOC, which generates the REE. Experimentally, the same has been found in weak antilocalization measurements of graphene/WSe₂ and WS₂ [191, 193, 196]. The VZ term originates in the broken sublattice symmetry of the TMD, which is imprinted into the graphene by proximity and spin polarizes the bands out of the plane with opposite orientation in the K and K' valleys [32, 33, 182]. This causes an out-of-plane tilt of the spin texture and

should, in principle, reduce the in-plane component induced by the Rashba term [32, 260], which arises from the perpendicular electric field at the interface due to broken inversion symmetry.

The spin transport parameters relevant to determine θ_{SH} in the device have been obtained using a 1-region model given in Equation 25. It assumes that the spin transport parameters of the pristine graphene region between electrode and Hall bar arms are the same as those of the graphene/WSe₂ region, equivalent to the fitting procedure of the previous chapter. This approximation was necessary to perform the quantitative analysis, as it was not possible to extract the in-plane and out-of-plane spin lifetimes of the proximitized graphene/WSe₂ region from the symmetric Hanle curves. Unfortunately, it is known that this assumption leads to uncertainties. In particular, it leads to the extraction of a spin lifetime (τ_s^{eff}), which is an average of the spin lifetime of the pristine graphene (τ_s^{gr}) and the graphene/TMDC region ($\tau_s^{gr/TMDC}$). Although this spin lifetime is anisotropic and $\tau_{\perp}^{gr/TMDC} > \tau_{\parallel}^{gr/TMDC}$, $\tau_{\perp}^{gr/TMDC}$ is typically shorter than τ_s^{gr} . Hence, the use of τ_s^{eff} leads to the overestimation of $\tau_{\perp}^{gr/TMDC}$ and the extracted θ_{SH}^{eff} is underestimated by this model.

However, due to the complexity of the system, the actual magnitude of the underestimation cannot be obtained from simple considerations. To disentangle it, a new modeled geometry accounts for the different spin transport properties of the TMDC-covered and the pristine graphene regions by dividing the channel into four different regions (see inset of Figure 6.12a). Region 1 is at the left side of the spin injector and is semi-infinite, region 2 connects the spin injector and the TMDC-proximitized graphene region, which is region 3. Finally, a pristine graphene region (region 4) is added, which is placed at the right side of region 3. The spin accumulations in the device can then be modeled by accounting for the spin propagation using the Bloch equations given in Section 2.2. Together with the boundary conditions given by spin injection and spin transport ($\mu_s(x)$ is continuous everywhere and $\mu_s(x) \rightarrow 0$ when $x \rightarrow \pm\infty$), antisymmetric Hanle curves can be simulated for a wide range of $\tau_{\perp}^{gr/TMDC}$. The data can then be fitted with the 1-region model and the assumed values compared with the resulting effective ones. Figure 6.12a shows exemplary that the physics of the 4-region model can fully be expressed by the approximation of the effective spin transport parameters. This operation has been performed for $\tau_{\perp}^{gr/TMDC}$ ranging from 1 ps to 1 ns. λ_s^{eff} and θ_{SH}^{eff} extracted from the fits are plotted in Figure 6.12b normalized by the input $\lambda_{\perp}^{gr/TMDC}$ and $\theta_{SH}^{gr/TMDC}$. From this plot, it can be observed that in the low $\tau_{\perp}^{gr/TMDC}$ range, despite the factor 9 overestimation in λ_s^{eff} , the $\theta_{SH}^{eff} \lambda_s^{eff}$ product is only overestimated by a factor 2.

It should finally be noted that the 4-region model does not account for spin diffusion into the top and bottom arms of the TMDC-covered region used for the Hall measurements. Hence, because the spins propagating along y do not contribute to the SCC voltage along

γ , θ_{SH} is underestimated by both models, which again would decrease the correction factor calculated in this section. With this caveat on the quantification of the efficiency of the ISHE, the next section will compare a wide range of SCC materials.

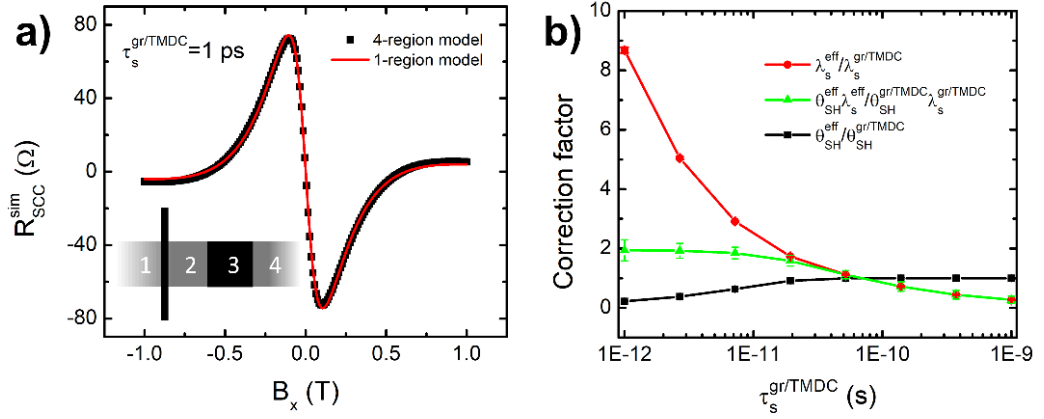


Figure 6.12: Parameter uncertainties induced by the 1-region model approximation. **a)** Antisymmetric Hanle curve (R_{SCC}) simulated using the 4-region model, with $\tau_{\perp}^{gr/TMDC} = 1$ ps, $\tau_s^{gr} = 60$ ps and an arbitrary injection polarization $P_i = 1$ (black squares). This simulation is fitted to Equation 25 of the 1-region model (red line). The inset at the bottom left corner is the 4-region model schematic, where the grey regions (1,2,4) are pristine graphene, the TMDC-covered region (3) is black, and the FM electrode used for injection is represented by the black vertical bar. **b)** Correction factor between $\lambda_{\perp}^{gr/TMDC}$ and λ_s^{eff} (red circles), $\theta_{SH}^{gr/TMDC}$ and θ_{SH}^{eff} (black squares) and their products (blue triangles), extracted with the procedure shown in panel a) for different values of $\tau_{\perp}^{gr/TMDC}$. Note that, when $\tau_{\perp}^{gr/TMDC} = \tau_s^{gr}$, the correction factors are 1. The lines are a guide to the eye.

Table 3: Charge and spin transport parameters for the temperature range from 10 K to room temperature. R_{sq}^{gr} and $R_{sq}^{gr/TMDC}$ are calculated from the four-point resistance between the respective electrode pairs and the length and width of the channel from the scanning electron microscopy image. D_s^{gr} , τ_s^{gr} and P_i are extracted from the fits to the symmetric Hanle precession curves, D_s^{eff} , τ_s^{eff} and P_i^{eff} from the antisymmetric ones. They enable the calculation of λ_s^{gr} , λ_s^{eff} and θ_{SH}^{eff} . ΔR_{SCC} is the spin-to-charge conversion signal and $\theta_{SH}^{eff} \lambda_s^{eff}$ the figure of merit for the conversion.

	10 K	50 K	100 K	150 K	200 K	250 K	300 K
R_{sq}^{gr} (Ω)	4508	4467	4361	4260	3973	3641	3338
$R_{sq}^{gr/TMDC}$ (Ω)	3482	3461	3281	3181	2905	2638	2445
D_s^{gr} ($10^{-3}\text{m}^2/\text{s}$)	4.5 ± 0.3	4.3 ± 0.1	4.1 ± 0.1	5.5 ± 0.1	8.4 ± 0.2	4.8 ± 0.1	6.0 ± 0.2
τ_s^{gr} (ps)	127 ± 6	125 ± 2	90 ± 1	100 ± 2	108 ± 3	84 ± 2	92 ± 2
λ_s^{gr} (nm)	760 ± 90	730 ± 30	610 ± 20	740 ± 30	950 ± 50	635 ± 30	740 ± 40
P (%)	2.6 ± 0.1	3.5 ± 0.1	5.4 ± 0.1	4.1 ± 0.1	3.4 ± 0.1	8.5 ± 0.3	5.8 ± 0.2
D_s^{eff} ($10^{-3}\text{m}^2/\text{s}$)	2.1 ± 0.1	2.2 ± 0.1	2.3 ± 0.2	2.3 ± 0.1	2.4 ± 0.1	1.9 ± 0.1	2.0 ± 0.1
τ_s^{eff} (ps)	81 ± 5	64 ± 6	61 ± 3	54 ± 1	42 ± 2	44 ± 2	44 ± 2
P^{eff} (%)	2.7 ± 0.1	2.7 ± 0.1	3.3 ± 0.2	2.9 ± 0.1	3.4 ± 0.1	3.7 ± 0.2	3.1 ± 0.3
λ_s^{eff} (nm)	410 ± 50	380 ± 35	380 ± 50	350 ± 17	320 ± 28	290 ± 11	295 ± 14
θ_{SH}^{eff} (%)	2.8 ± 0.3	2.0 ± 0.2	2.0 ± 0.3	2.1 ± 0.2	3.4 ± 0.2	1.6 ± 0.2	1.7 ± 0.2
ΔR_{SCC} (m Ω)	90 ± 3	70 ± 2	55 ± 1	58 ± 1	51 ± 2	41 ± 1	38 ± 2
$\theta_{SH}^{eff} \lambda_s^{eff}$ (nm)	12 ± 2	7.5 ± 0.9	7.6 ± 0.7	7.2 ± 0.4	11 ± 0.9	4.6 ± 0.5	4.9 ± 0.7

Table 4: Charge and spin transport parameters for different gate voltages at 100 K. All parameters as for Table 3. The values of $R_{sq}^{gr/TMD}$ for -3 V and -5 V are determined by a linear fit to the data left of the CNP shown in Figure 6.3b.

	-5 V	-3 V	0 V	2 V	5 V
R_{sq}^{gr} (Ω)	3470	3788	4361	4794	5405
$R_{sq}^{gr/TMD}$ (Ω)	(2574)	(2810)	3281	3413	3513
D_s^{gr} ($10^{-3}\text{m}^2/\text{s}$)	7.1 ± 0.1	4.9 ± 0.1	4.1 ± 0.1	4.0 ± 0.1	3.6 ± 0.1
τ_s^{gr} (ps)	100 ± 2	88 ± 1	90 ± 1	103 ± 2	106 ± 2
λ_s^{gr} (nm)	840 ± 30	660 ± 20	610 ± 20	640 ± 30	620 ± 30
P (%)	2.9 ± 0.1	4.6 ± 0.2	5.4 ± 0.1	5.9 ± 0.2	3.4 ± 0.1
D_s^{eff} ($10^{-3}\text{m}^2/\text{s}$)	3.5 ± 0.1	3.5 ± 0.2	2.3 ± 0.2	2.1 ± 0.1	-
τ_s^{eff} (ps)	67 ± 4	45 ± 5	61 ± 3	68 ± 2	-
λ_s^{eff} (nm)	480 ± 40	400 ± 60	380 ± 50	280 ± 25	-
P^{eff} (%)	4.9 ± 0.1	4.2 ± 0.2	3.3 ± 0.2	2.8 ± 0.1	-
θ_{SH}^{eff} (%)	8.4 ± 0.2	3.8 ± 0.2	2.0 ± 0.3	1.3 ± 0.1	<0.2 %
ΔR_{SCC} (m Ω)	209 ± 1	136 ± 1	55 ± 1	30 ± 1	0 ± 2
$\theta_{SH}^{eff} \lambda_s^{eff}$ (nm)	41 ± 3	15 ± 2	7.6 ± 0.7	3.7 ± 0.3	-

6.4 Comparison to other spin-to-charge conversion systems

Even though the calculated θ_{SH}^{eff} for graphene proximitized with WSe₂ of 1.3% up to 8.4% at 100 K and 1.7% at 300 K is smaller than in transition metals as Pt [80] or Ta [97] that are prototypical SCC materials and have been used for spin-orbit torque magnetization switching [261], the maximum output signal ΔR_{SCC} of 209 m Ω at 100 K (38 m Ω at 300 K) is orders of magnitude larger than for Cu/Pt [80] or Cu/Ta [97] LSVs or three times the maximum non-local ISHE signal reported for a graphene/Pt device (11 m Ω at 300 K [262]). One major difference between the SCC in spin-orbit proximitized graphene and other devices is that transport of the spin current and conversion into a charge current happen in the same material, in the graphene channel itself, and no losses due to spin absorption across an interface or shunting occur. Nevertheless, even when compared to the output of the very similar graphene/MoS₂ device (25 m Ω at 10 K), graphene/WS₂ (10 m Ω at 100 K [199]) or graphene/topological insulator devices (15 m Ω at 300 K [258]), the values achieved here are still an order of magnitude till 200% larger. Only at lower temperatures and applied back gate voltage, the REE in a graphene/WS₂ device can compete (300 m Ω at 4.2 K and -10 V [198]).

However, as mentioned before, ΔR_{SCC} is not a good figure of merit if one needs to compare efficiencies in the achievable output voltage across different materials and geometries in SCC devices. If interested in the output current efficiency (for instance in the case of spin-orbit torques for magnetic switching), the $\theta_{SH}\lambda_s$ product is the proper figure of merit [95], which has units of length and compares straightforwardly with λ_{IREE} that quantifies the efficiency of the IREE [94].

Table 5 lists those efficiencies for a wide range of SCC materials and experiments, starting with mainly metallic LSVs, to graphene-based LSVs, and finally spin pumping experiments that are especially important for IREE. Not just for metallic systems such as Pt, the vast swathe of works cannot be mentioned here due to space limitations and repetition. Many of them also do not disentangle efficiency and spin diffusion length or take values reported in the literature [263] and, therefore, make a comparison cumbersome. Additionally, some works only focus on a large θ_{SH} and do not report the efficiency [264]. Especially for graphene-based LSVs, a complete analysis requires a thorough, critical determination of all parameters involved in the SCC (P , D_s , τ_s , ...), which is often out of the scope of first reports on SCC for new material combinations [198, 256, 262, 265–268]. Furthermore, some experiments rely on the faulty double H-bar design [269–271] discussed in Section 5.1 or have other design flaws and therefore leave reason to doubt the exceptionally large values claimed [272, 273]. Finally, no spin-orbit torque experiments have been listed as it is complex to compare them to the experiments of this thesis and assess the figures of merit like spin-orbit torque efficiency and spin Hall angle. An overview is given in the recent review in Ref. [274].

The SCC length of 12 nm at 10 K obtained here is more than 40 times larger than the values for metallic LSVs (< 0.3 nm), mainly using Cu as their spin channel. Therefore, they are also mostly limited to measurements at low temperatures as λ_s of Cu is strongly reduced with increasing temperature. While the LSVs experiments of those heavy metals show low efficiencies at room temperature (< 0.1 nm), some spin pumping experiments, for example, on Pt can reproduce low-temperature efficiencies of LSVs at room temperature, achieving similar values as typical IREE interfaces like Ag/Bi, that are still an order of magnitude smaller than in graphene/WSe₂ (4.9 nm, or ≈ 2.45 nm if corrected for a maximum overestimation of a factor of 2, as discussed in the previous section). Additionally, at the lowest temperatures, spin transport is also possible in high-mobility semiconducting channels such as GaAs, where the large intrinsic Dresselhaus SOC also achieves comparable SCC efficiencies that are however limited to this temperature range.

Other exceptional spin pumping experiments at room temperature use topological insulators such as α -Sn or HgTe, where the conversion happens in topologically protected surface states. However, they often do not reach the values of the graphene-based LSVs combined with other 2D materials. Interestingly, the largest efficiencies are also reported for graphene/topological insulators but the estimation of λ_s for these surface states is difficult. Equating it with the spin diffusion length of the channel is probably a massive overestimation, so that the values have to be evaluated carefully. Direct measurements of LSVs made up of the topological insulator as the channel with different lengths would be needed to extract robust values [275]. Additionally, the combination of metallic TMDCs in the 1T-phase (such as MoTe₂ or WTe₂) with graphene allows the observation of highly efficient, unconventional SCCs that do not follow the symmetry requirements of neither ISHE nor IREE.

The largest SCC efficiencies so far have been achieved in 2DEGs in oxides, prominently SrTiO₃, where the amplitude and sign can also be controlled by applying a gate voltage. However, these large values are limited to liquid He temperatures and only if they could be repeated at room temperature, where so far only small values have been reported, they would be interesting for future applications, especially because reports suggest long λ_s even at 300 K [276]. Improved samples could, for example, introduce controlled strain in the crystal structure [277].

In summary, the comparison shows the potential of 2D materials for spintronic applications. The high efficiencies and the electrical control of the SCC could pave the way for a new generation of spintronic devices as a beyond-CMOS technology [100]. The next chapter will further study the spin transport across proximitized graphene and show the electrical control of spin precession, another interesting spin phenomenon that could be used in future devices.

Table 5: Comparison of SCC efficiencies in different material systems. Listing the material of spin transport channel and the SOC material in the case of ISHE and the materials forming the Rashba interface in case of IREE, the SCC effect (ISHE or IREE), the absolute value of θ_{SH} or α_{REE} , the spin diffusion length λ_s (λ_s^\perp for ISHE, λ_s^\parallel for IREE), the temperature, and the SCC efficiency ($\theta_{SH}\lambda_s$ or λ_{IREE}), that are reported or calculated from the values in the given references. More full or partial data sets for (I)SHE experiments can be found in the reviews in Ref. [278] and, especially for graphene-based systems, in Ref. [279]. SCC* as effect stands for an unconventional SCC whose origin is unclear, effective λ_s means an isotropic averaging over the whole LSV as discussed in the previous section. Exceptional values are emphasized in bold, the results of this thesis are italicized.

Material	Effect	θ_{SH} or α_{REE} [%]	λ_s [nm]	Temp. [K]	$\theta_{SH}\lambda_s$ or λ_{IREE} [nm]	Ref.
LSVs with spin absorption						
Ag/IrO ₂	ISHE	4.0	3.8	RT	0.15	[280]
Al	ISHE	(1.6–3.2) 10 ⁻³	705 – 455	4.2	0.011 – 0.015	[84]
GaAs	ISHE	0.15	2187	4.2	3.28	[281]
	ISHE	0.08	8500	4.2	6.8	[282]
Cu/Au	IREE	-	-	10 RT	0.15 0.025	[91]
Cu/AuW	ISHE	14	1.3	RT	0.18	[283]
Cu/Bi	IREE	-	-	10 RT	0.001 0.01	[89]
Cu/Bi ₂ O ₃	IREE	-	-	10	0.16	[90]
Cu/CuBi	ISHE	11	45	10	4.95	[284]
Cu/CuIr	ISHE	2.5	10	10	0.25	[285]
Cu/Mo	ISHE	0.8	8.6	10	0.07	[286]
Cu/Nb	ISHE	0.87	5.9	10	0.05	[286]
Cu/Pd	ISHE	1.2	13	10	0.16	[286]
Cu/Pt	ISHE	2.1	10.1	10	0.21	[80]
	ISHE	2.1	11	10	0.23	[286]
Cu/Ta	ISHE	35 – 5	0.8 – 2.4	10	0.28 – 0.12	[97]
	ISHE	0.37	2.7	10	0.01	[286]
Graphene-based LSVs						
Bi ₂ O ₃	ISHE	0.6	583	10	3.5	[287]
		0.1	435	RT	0.4	
(Bi _{0.15} Sb _{0.85}) ₂ Te ₃	IREE	0.17 – 4.8	1210 – 3500 (eff.)	RT	6 – 75	[258]
TaTe ₂	ISHE	≥ 20	-	RT	≥ 6	[288]

MoS ₂	ISHE	4.8 0.33	320 (eff.) 450 (eff.)	10 RT	16 1.5	[253]
MoTe ₂	ISHE SCC*	≥ 21 ≥ 10	- -	RT	≥ 1.15 ≥ 0.5	[289]
WS ₂	ISHE IREE	0.3 0.1	1250 420	RT	3.75 0.42	[199]
WSe ₂	ISHE	2.8 8.4 1.7	410 (eff.) 480 (eff.) 295 (eff.)	10 100 RT	12 41 4.9	[257]
WTe ₂	ISHE	-	-	RT	0.1	[290]
	IREE	-	-	RT	1.0	[291]
	SCC*	-	-	RT	0.72	[292]
Spin pumping experiments						
Al/KTaO ₃	IREE	-	-	10	3.5	[293]
AlO _x / SrTiO ₃	IREE	-	-	15 RT	-16 – 28 0.5	[294]
	IREE	-	-	7	60	[295]
Ag/ α -Sn	IREE	-	-	RT	2.1	[92]
Ag/Bi	IREE	-	-	RT	0.17 – 0.32	[22]
	IREE	-	-	40 – RT	≈ 0.4	[296]
	IREE	-	-	RT	0.11	[297]
Ag/Sb	IREE	-	-	RT	0.01	[297]
AuTa	ISHE	30	2	RT	0.6	[283]
AuW	ISHE	-	-	RT	0.2	[283]
Bi	ISHE	2	8	RT	0.16	[298]
	ISHE	1.6	15.4	RT	0.25	[299]
(Bi _{0.22} Sb _{0.78}) ₂ Te ₃	IREE	-	-	RT	0.08	[300]
Bi ₂ Se ₃	ISHE	0.9	6.2	RT	0.06	[301]
	IREE	-	-	RT	0.04	[302]
	IREE	-	-	RT	0.11	[303]
(Bi,Sb) ₂ Te ₃	IREE	-	-	RT	0.02	[302]
Cu/Bi ₂ O ₃	IREE	-	-	RT	0.6	[304]
HgCdTe/ HgTe	IREE	-	-	RT	2.0	[305]
ITO	ISHE	0.65	30	RT	0.195	[306]
LaAlO ₃ / SrTiO ₃	IREE	-	-	7	6.4	[93]
Pt	ISHE	8	3.7	RT	0.3	[307]
	ISHE	5.6	3.4	RT	0.19	[308]
	ISHE	10	7.3	RT	0.73	[309]

Ta	ISHE	2	1.8	RT	0.04	[310]
	ISHE	7.1	1.9	RT	0.13	[309]
W	ISHE	14	2.1	RT	0.29	[309]

7 Coherent spin precession in graphene proximitized with WSe₂

7.1 Spin polarization in the strong spin-orbit coupling regime

An open question of the last chapter was the interpretation of the anisotropic spin transport data across graphene proximitized by a TMDC. This topic has been theoretically studied in different reports and Figure 7.1 shows exemplary two similar results.

In the first report, a tight-binding model with a Hamiltonian equivalent to the one given in Section 2.1 was used to calculate the effect of the intervalley scattering and the SOC imprinted by the TMDC [185]. The results for strong intervalley scattering can be seen in Figure 7.1a. The spin lifetimes for polarizations along x and z are strongly anisotropic due to the direction of the effective magnetic field of the VZ SOC ($\vec{B}_{VZ} \parallel z$). It will stabilize spins pointing out-of-plane as for them intravalley scattering with a shorter scattering time will not lead to spin relaxation. Spins with polarization in plane will relax faster than the out-of-plane ones and the ratio between the two can reach values up to 100. This large anisotropy was also the focus of the experimental studies so far [71, 188]. The difference can be seen in the Hanle precession as a suppression of the spin signal at low fields, when the spins are polarized in plane, and enhanced shoulders for the mid-field range, when the spins are polarized out of plane (as discussed in Section 2.4 and 6.2).

Interestingly, Figure 7.1b shows that, for weak intervalley scattering, the spins along x do not relax but dephase and an oscillatory behavior can be observed for the in-plane spin polarization. This can be understood in the picture of spin relaxation by the DP mechanism in the strong SOC regime as shown in Figure 2.4c, where between scattering events the spins precess coherently around the SOF. Intuitively, this implies a strong SOC with large SOF and a short in-plane spin precession period τ_{VZ} around the out-of-plane VZ SOF so that it is in the range of the intervalley scattering time τ_{iv} . This set of conditions is appropriately named strong SOC regime.

Ref. [259] uses a microscopic theory with a time-dependent perturbative treatment to study the same phenomenon for different τ_{iv} and strong or weak VZ or Rashba SOC. The

results demonstrate the different effects of the two SOFs, as it has been shown in Figure 2.2: In Figure 7.1c, the VZ SOC leads to a highly anisotropic transport, where the out-of-plane spin lifetime is enhanced and the in-plane spin precesses coherently as before. Additionally, in Figure 7.1d, the Rashba SOC leads to a spin precession of the spin polarization in the x - z -plane, due to the direction of the effective magnetic field ($\vec{B}_R \parallel y$).

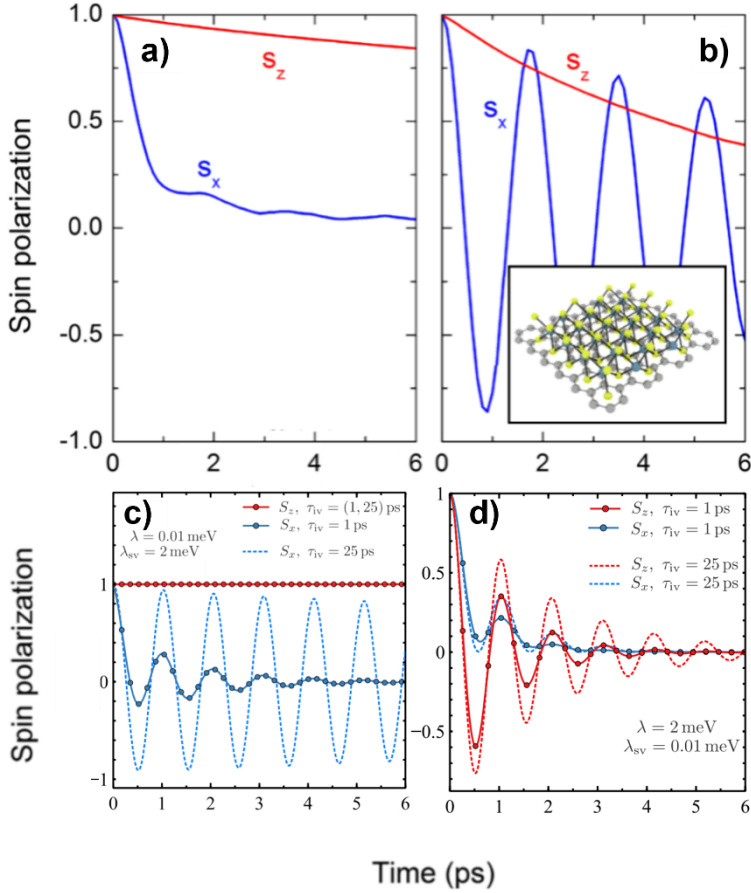


Figure 7.1: Spin dynamics in a graphene/TMDC heterostructure.

a) Spin polarization for in-plane (along x) and out-of-plane (along z) spins for strong and **b)** weak intervalley scattering. Images adapted from Ref. [185]. **c)** Same plot with both cases (short and long intervalley scattering time τ_{iv}) but for strong Rashba SOC (2 meV) and weak VZ SOC (0.01 meV) and **d)** vice versa. Images adapted from Ref. [259].

While these two reports capture the spin dynamics in the strong SOC regime, they focus in their conclusion mainly on the anisotropic spin transport. Other theoretical works that describe the damped oscillatory behavior of spin polarization in this regime are limited to 2DEGs in semiconductors and the interplay of Rashba and Dresselhaus SOC [38]. Here, the momentum scattering time τ_p stops the coherent spin precession and achieving

favorable conditions experimentally to demonstrate the precession would be limited to low temperatures.

To illustrate the special situation of in-plane spins in a graphene/TMDC heterostructure, Figure 7.2a sketches the precession due to the VZ SOF for the two different valleys. As discussed in Section 2.1, the VZ SOC has opposite sign for K and K' valleys and spins, therefore, precess clockwise and anticlockwise, respectively. A scattering event that transfers the electron from one valley to the other thus restarts the spin precession. Unlike in conventional materials, the spin-valley locking present in graphene/TMDC heterostructures might enable the strong SOC regime if τ_{VZ} would become comparable to τ_{iv} . Such a condition may even be achieved in the diffusive regime due to the valley polarization of the TMDC prolonging τ_{iv} and the strong VZ SOC leading to short τ_{VZ} . Experiments probing the spin precession due to the strong SOC regime could therefore be possible at room temperature.

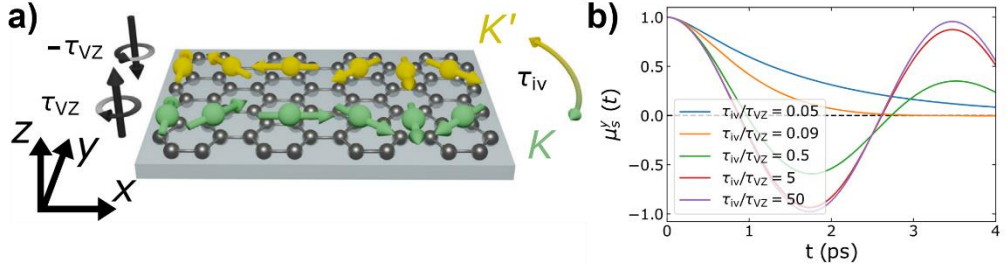


Figure 7.2: Spin precession in graphene/TMDC. **a)** Sketch of the heterostructure. Out-of-plane VZ SOF (black arrows) with opposite sign for the K and K' valleys induce in-plane spin precession with a period τ_{VZ} . Spins can scatter between the valleys via intervalley scattering (τ_{iv}). The shorter intravalley scattering time τ_{intra} plays no role for the precession. **b)** Time dependence of the spin accumulation μ_s^y for different τ_{iv} values. μ_s^y undergoes net precession for $\tau_{iv} \geq 0.5 \tau_{VZ}$.

Figure 7.2b shows the time dependence of the total in-plane spin accumulation μ_s^y for different τ_{iv}/τ_{VZ} values. The calculation uses the diffusion and precession equations of Section 2.4 for each valley separately:

$$D_s \frac{\partial^2 \vec{\mu}_s^K}{\partial x^2} - \frac{\vec{\mu}_s^K}{\tau_s} - v_d \frac{\partial \vec{\mu}_s^K}{\partial x} + \vec{\omega}_{VZ} \times \vec{\mu}_s^K - \frac{\vec{\mu}_s^K - \vec{\mu}_s^{K'}}{2\tau_{iv}} = 0 \quad (28)$$

$$D_s \frac{\partial^2 \vec{\mu}_s^{K'}}{\partial x^2} - \frac{\vec{\mu}_s^{K'}}{\tau_s} - v_d \frac{\partial \vec{\mu}_s^{K'}}{\partial x} + \vec{\omega}_{VZ} \times \vec{\mu}_s^{K'} - \frac{\vec{\mu}_s^{K'} - \vec{\mu}_s^K}{2\tau_{iv}} = 0 \quad (29)$$

where $\vec{\omega}_{VZ}$ only considers the spin precession due to the VZ SOF. The last term accounts for the intervalley scattering between K and K' valley. While the expected exponential decay due to spin relaxation is observable for all curves, μ_s^y undergoes net precession for

$\tau_{iv} \geq 0.5\tau_{VZ}$ leading to spin dephasing. This gives a lower limit for achieving the strong SOC in graphene/TMDC heterostructures.

The following sections will present the results of the third main paper of this thesis [311], which reports the observation of coherent spin precession in the strong SOC regime in a bilayer graphene/WSe₂ heterostructure up to room temperature. The next section will present the anisotropic spin transport in an LSV with proximitized graphene, similar to the results of the last chapter. Then the gate and current control of the spin diffusion and, consequently, spin precession will be demonstrated. These effects persist up to room temperature and are a realization of the Datta-Das spin field-effect transistor, a concept that will be discussed in more detail in the last section.

7.2 Gate-controlled anisotropic spin transport in graphene/WSe₂

The LSV used in this chapter is similar to the devices used for the SCC measurements in the previous two chapters. However, as only the spin transport across the proximitized region is studied, the structuring of the graphene flake into a Hall bar shape is not necessary. Therefore, the reactive ion etching step in the fabrication can be skipped. All other steps – exfoliation, transfer, annealing, and electrical contacting – remain the same. The graphene flake was determined to be bilayer and the WSe₂ is multilayer and can be assumed to be bulk as in earlier samples. Figure 7.3a shows an optical microscope image of the final device with the five FM electrodes for spin injection and detection (number 2 to 6) and the Ti/Au contacts at each end of the graphene channel (number 1 and 7). As previously, this allows the measurement across multiple LSVs including a reference of pristine graphene (between electrode 4 and 5) and one with proximitized graphene (between electrode 3 and 4). In a first step, the spin transport in the reference LSV was thoroughly characterized and then compared to the anisotropic transport across the graphene/WSe₂. In both cases, this includes the dependence on an applied back gate voltage. Figure 7.3b shows a picture of the measurement setup, where, as before, the non-local resistance due to spin transport in the pristine or proximitized graphene channel is measured in an applied magnetic field (either B_y or B_x). The spin precession due to the proximity-enhanced SOC in the case of a TMDC flake on top is sketched as well.

Figure 7.4a shows the standard LSV measurement for the pristine graphene reference at 50 K. As before, the two FM contact configurations (parallel and antiparallel as indicated by the arrow pairs) are clearly visible in the non-local resistance when sweeping B_y . The amplitude of the spin signal $\Delta R_{NL} \approx 1 \Omega$ is similar to the one in the SCC graphene/WSe₂ devices. The accompanying symmetric Hanle curve for sweeping B_x is shown in Figure 7.4b. Repeating the previous analyses, the difference ΔR_{NL} between the two – parallel and antiparallel – curves can be extracted and fitted to the diffusion equation of Section 2.4. The results can be seen in Figure 7.4c. These measurements were repeated for a back gate voltage range from -50 to 50 V and the resulting fit parameters are plotted in Figure 7.4d.

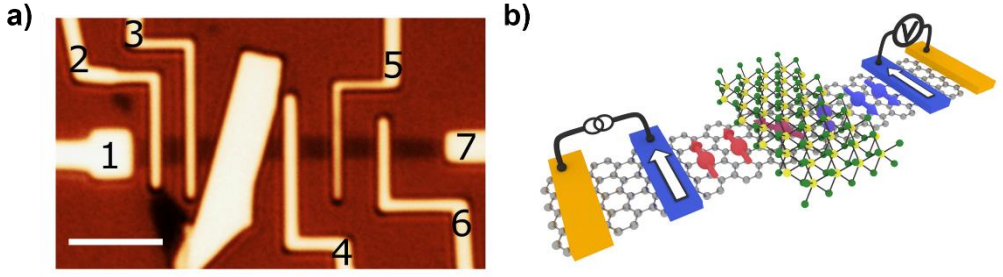


Figure 7.3: Device overview. **a)** Optical microscope image of the device with the corresponding contact numbering. The dark horizontal channel is exfoliated graphene, the bright vertical flake is dry-transferred WSe₂. The white scale bar is 4 μm. **b)** Sketch of the LSV measurement with a TMDC flake in the middle.

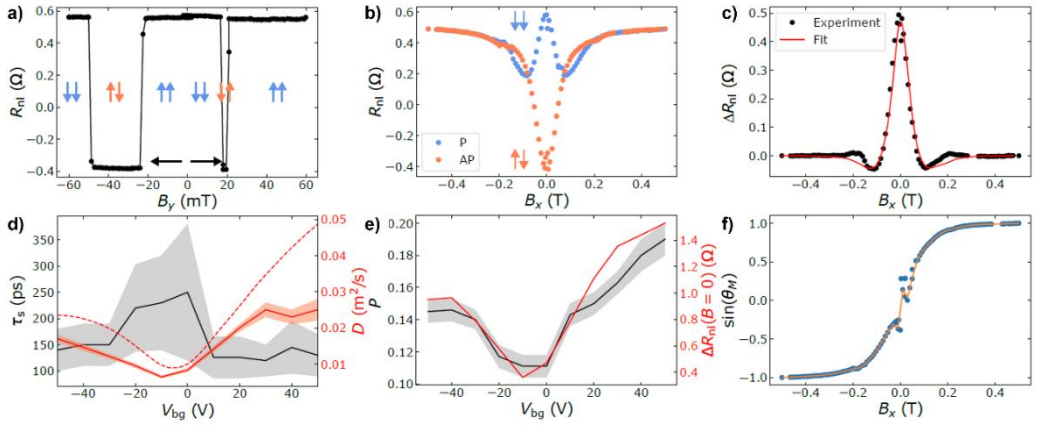


Figure 7.4: Spin transport in the reference LSV at 50 K. **a)** Non-local LSV measurement, plotting R_{NL} as a function of B_y . **b)** Non-local spin precession around B_x for the parallel (P) and antiparallel (AP) initial FM contact configuration (R_{NL}^P and R_{NL}^{AP} , respectively). **c)** Pure spin transport data with $\Delta R_{NL} = (R_{NL}^P - R_{NL}^{AP})/2$ obtained from the data in panel b) (black solid circles) with the corresponding fit to Equation 20 (red line). **d)** Spin lifetime (τ_s , black line) and spin (D_s , red solid line) and charge (D_c , red dashed line) diffusivity as a function of back gate voltage V_{bg} . **e)** Spin polarization of the FM electrodes $P = \sqrt{P_i P_d}$ together with the amplitude of the spin signal $\Delta R_{NL}(B = 0)$. **f)** Sine of the angle between the magnetization of the FM electrode and the applied magnetic field obtained from the data in panel b) (blue solid circles). The orange line is a guide to the eye.

The spin relaxation time τ_s is modulated in an interval between 150 and 250 ps and the D_s ranges from 0.01 to 0.03 m²/s. However, as the trend of the two parameters is opposite, the spin diffusion lengths $\lambda_s = \sqrt{\tau_s D_s}$ shows only a minor change with V_{bg} . Interestingly, the charge diffusivity D_c , extracted from the gate dependence of the square resistance of

this LSV, follows the trend of D_s . It is, therefore, appropriate to speak only of one diffusivity in these experiments [46].

The third fitting parameter, the spin polarization P of the FM electrodes, is compared in Figure 7.4e to the spin signal ΔR_{NL} . The correlation shows clearly that the tuning of ΔR_{NL} is related to the change in P . Additionally, it should also be noted that the spin signal is positive for all the V_{bg} values, ranging from 0.4 up to 1.5 V. Finally, Figure 7.4f shows $\sin(\beta)$, effectively, the pulling of the magnetization of the FM electrode towards the applied magnetic field. The saturation field $B_{sat} \approx 200$ mT is similar to the values obtained in the other devices of this thesis, as it is expected from the identical material, width, and thickness of the electrodes.

The anisotropic transport across the LSV with graphene proximitized by the TMDC flake will strongly depend on the interplay of B_x and the direction of the spin magnetic moment as sketched in Figure 7.5. In Figure 7.5a, the precession from in-plane to out-of-plane polarization and so forth is shown for the spins that increase in “size” while pointing along z as τ_s^\perp is expected to be larger than. Figure 7.5b shows the pulling of the magnetization of the FM electrode for a magnetic field larger than B_{sat} and the injecting of spins polarized along x , where then the spin precession around the SOF plays again the determining role.

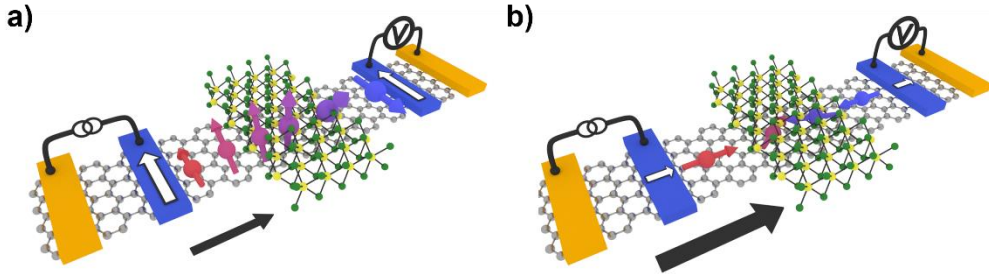


Figure 7.5: Schematic of the anisotropic Hanle measurement. a) Magnetic field-induced precession leads to out-of-plane spins with increased lifetimes. **b)** Pulling of the magnetization direction of the FM electrodes for higher fields leads to in-plane spin injection and SOF-induced precession.

The realization of these measurements for different back gate voltages is shown in Figure 7.6, where, in the two columns, LSV and Hanle measurements are shown in pairs. As in the previous chapter, the LSV signal now has a negative sign, meaning that $R_{NL}^{AP} > R_{NL}^P$. The same fact can be seen at the zero-field values of the Hanle measurements that are shown in more detail in the insets. This can now be understood by the rotation of the spin polarization by $\sim 180^\circ$ due to coherent spin precession around the SOF as theoretically predicted in Figure 7.1 and illustrated graphically in Figure 7.3b. As before, the enhanced shoulders for the mid-field range are due to the spin lifetime anisotropy $\tau_s^\perp > \tau_s^\parallel$, that is illustrated in Figure 7.5a. For fields larger than $B_{sat} \approx 200$ mT, both Hanle curves for parallel and antiparallel FM configuration saturate at a resistance value that is equal to

the zero-field R_{NL} in the parallel state. The reason for this is the combination of the pulling of the magnetization of the FM electrode and the coherent spin precession around the proximity-induced SOF as shown in Figure 7.5b.

Additionally, closer to the Dirac point at -10 V, the LSV signal is suppressed, shown exemplarily in the plot for $V_{bg} = -30$ V. As shown in Figure 7.4d, the diffusivity is tuned strongly by the applied back gate voltage. Figure 7.7 shows the correlation between ΔR_{NL} and D_c making the diffusivity the most likely responsible for the measured V_{bg} dependence. However, the electron-hole asymmetry in ΔR_{NL} indicates that other factors such as spin absorption by the WSe₂ [147, 148] may also play a role. Note that a sign change of the signal below the noise level near the CNP cannot be disregarded.

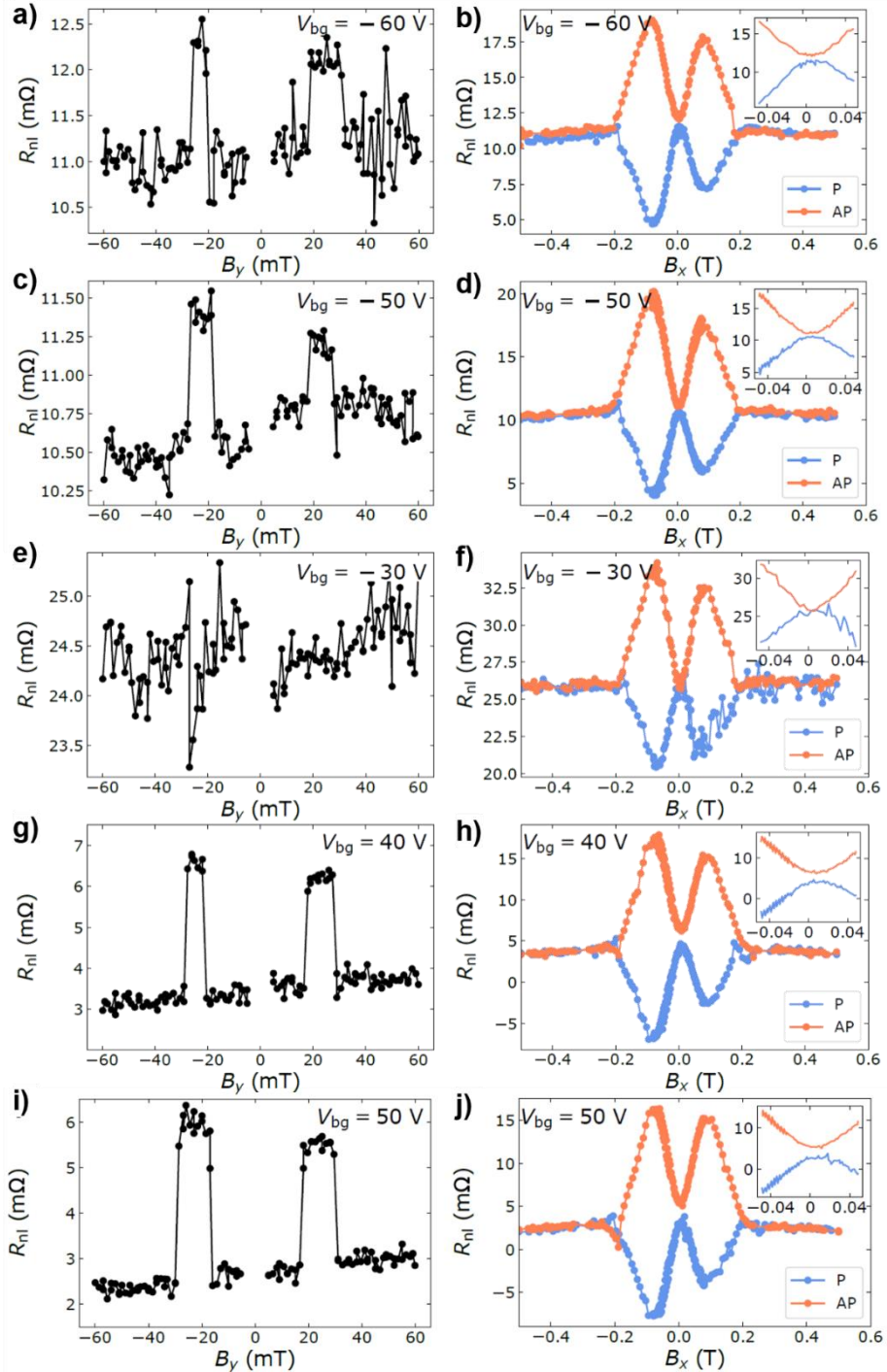


Figure 7.6: Non-local spin transport across the WSe₂-covered graphene region at 50 K. a), c), e), g) and i) LSV measurements and b), d), f), h) and j) Hanle spin precession measurements performed at $V_{bg} = -60$ V, -50 V, -30 V, 40 V, and 50 V. The insets are a zoom of the data at low B_x range.

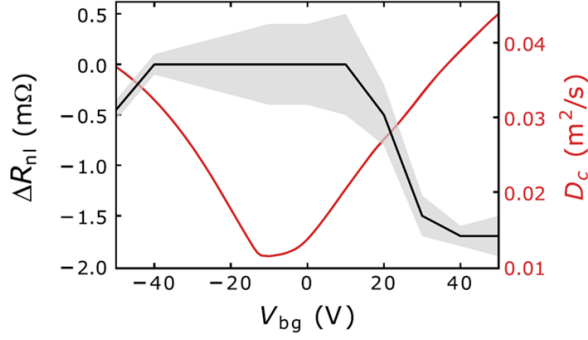


Figure 7.7: Spin signal as a function of back gate voltage at 50 K for proximitized graphene. Spin signal ΔR_{NL} (black line) and charge diffusivity D_c (red line) as a function of V_{bg} showing a clear correlation.

This behavior can be understood when looking at the spin polarization plotted in Figure 7.2b for $\tau_{iv}/\tau_{VZ} = 0.09$. A sign change that corresponds to a spin precession of more than 90° can be observed after 3 ps. In a diffusion experiment, this time can be translated via D_s into a lateral distance as shown in Figure 7.8a, where the local minima in the absolute amplitude of μ_s^y are the points of sign change. Intuitively, the tuning of the diffusivity with an applied V_{bg} will also modulate the amplitude of the spin polarization and, in certain cases, the sign, when the minima point passes the detector electrode. The effect of the change in diffusivity is shown for the interval of D_s experimentally extracted above and the resulting difference in x of ~ 500 nm lies in an accessible range for the electrode width in this device.

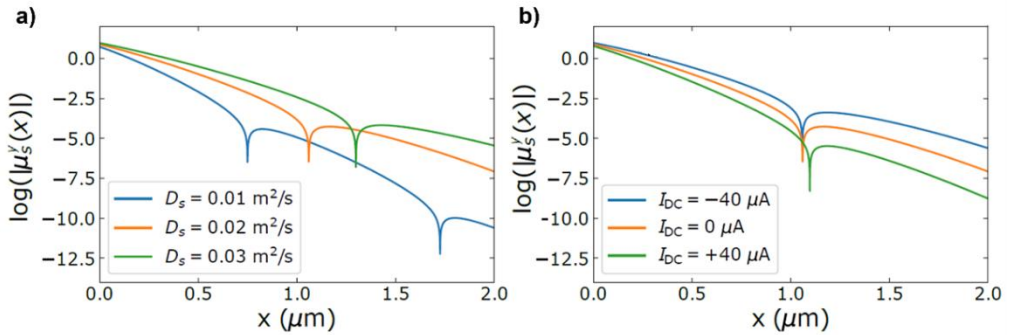


Figure 7.8: Effect of changing diffusivity and drift current on μ_s^y . a) Lateral evolution of μ_s^y for $D_s = 0.01, 0.02$ and 0.03 m^2/s and b) for $I_{DC} = -40$ μA , 0 and 40 μA at $D_s = 0.02$ m^2/s . $\tau_{iv}/\tau_{VZ} = 0.09$ for both panels.

However, the experimentally achieved spin signal is small and noisy around the CNP, where the largest modulation of D_s is expected. It can, therefore, not be concluded whether, for the lower diffusivities around there, a sign change of the spin signal was

achieved. This would be a proof that the spin polarization reversed sign due to coherent spin precession. Fortunately, Figure 7.8b shows that an additional dc current as drift current applied along the channel will also modulate the spin polarization and the sign change point. The experimental realization of this prediction is shown in the next section.

7.3 Drift-current-guided anisotropic spin transport in graphene/WSe₂

As discussed in Section 2.4, adding a dc current to the electrical setup will lead to electron drift, an experimental method that already has been used to guide spin currents in pristine graphene [73]. Figure 7.9a shows the electrical configuration in that case. The spin is injected with the same dc current reversal technique (also known as delta mode) as before, the non-local resistance is calculated from the voltage probed by the detector. The only difference is the added dc current I_{DC} , applied with an electrode between injector and detector. The advantage of the delta mode is the filtering of any possible dc spin current injected by the I_{DC} electrode.

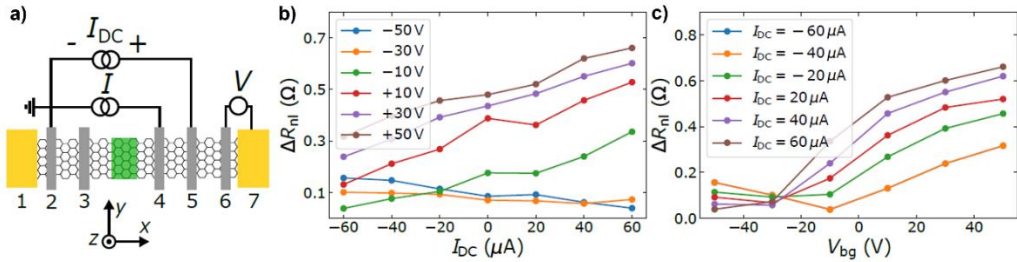


Figure 7.9: Room temperature spin drift experiments in the pristine graphene region. a) Sketch of the measurement configuration, where the TMDC flake in the LSV (green shape) is not present for the pristine graphene case. b) I_{DC} -dependence of ΔR_{NL} at different V_{bg} values. c) V_{bg} -dependence of ΔR_{NL} at different I_{DC} values.

The effect of the resulting electron drift on the LSV signal can be seen in Figure 7.9b, where it is plotted for different back gate voltages. For $V_{bg} > V_{Dirac} \approx -20$ V, so for electrons as majority carriers, ΔR_{NL} increases for positive drift current and decreases for $I_{DC} < 0$. The modulation of the signal is more or less linear and roughly 50% for the applied range. This is in line with the acceleration and deceleration of electrons by the electric field of the dc current. On the other hand, the effect of I_{DC} is reversed for holes, when applying -50 and -30 V back gate voltage as the charge and therefore the drift direction changes sign.

Additionally, Figure 7.9c shows that the effect of V_{bg} on the LSV signal is independent of the applied dc current. This means that a modulation of the diffusivity with the back

gate voltage is possible even for the electron drift configuration. It should be noted that, for all these data points of pristine graphene, the sign of ΔR_{NL} is always positive.

The same set of experiments has been conducted for the LSV with proximitized graphene and Figure 7.10 shows a summary of the results. In panel a), the control of the spin signal by the applied dc current is demonstrated. ΔR_{NL} is suppressed for no drift and a positive sign of the spin signal is recovered for negative dc current and vice versa. This can be understood as well through the acceleration or deceleration of the carriers by the external electric field. For a negative I_{DC} , the charge carriers will have less time precessing when passing the area of proximitized graphene underneath the TMDC flake. This corresponds to the second column in x direction in Figure 7.2a. The sum of the two spins will therefore have a component along the direction of injector and detector (y). The suppression of the LSV signal for no drift can then be explained by the compensation of opposite spins in K and K' valley due to a rotation of roughly 90° as illustrated by the third pair of spins. Finally, applying a positive dc current will then slow down the carriers even more and increase the available time for spin precession leading to a longer rotation, similar to the signal measured above in the standard LSV configuration across WSe₂ without drift. This case of coherent spin precession is seen in the fourth column of the spins in Figure 7.2a. The drift, therefore, controls the spin precession (or rather the precession time) and can be exploited to modulate ΔR_{NL} . Figure 7.10b shows the resulting continuous tuning of the spin signal by I_{DC} for three different back gate voltages.

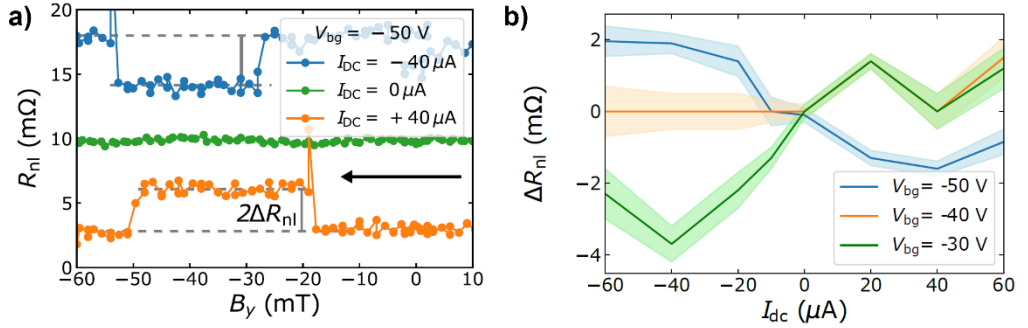


Figure 7.10: LSV measurement with drift current and back gate voltage at 50 K. **a)** R_{NL} as a function of B_y for $V_{bg} = -50$ V at $I_{DC} = -40$ μ A, 0 and 40 μ A. The curves have been shifted for clarity. **b)** ΔR_{NL} as a function of I_{DC} at $V_{bg} = -50$ V, -40 V and -30 V.

The difference between the three curves can be understood by the separate tuning of the diffusivity by V_{bg} as demonstrated in Figure 7.9c. Especially for negative I_{DC} , the three different slopes of the curves can easily be equated to the distinct possibilities in the illustration in Figure 7.2a: The standard LSV signal is observed for $V_{bg} = -50$ V due to a precession of less than 90° in both valleys, that is suppressed when the spins precess more and compensate each other in the two valleys (-40 V). If the back gate voltage is increased, and the diffusivity decreases even more closer to the CNP, the negative ΔR_{NL} due to coherent spin precession in the strong SOC regime can be observed (-30 V). As

expected, the slope of the three curves is similar for positive dc currents (as in Figure 7.9b), but ΔR_{NL} changes sign. However, particularly for the gate voltages closer to the CNP (-30 V and -40 V), the difference in spin signal is less clear. It seems that, for the smaller diffusivities there, the acceleration by I_{DC} flattens out most of differences.

Finally, spin precession measurements were conducted for some of these I_{DC} and V_{bg} values. Eight of them are plotted in Figure 7.11. They prove that the applied drift current not only controls ΔR_{NL} but really the time for spin precession around the SOF and therefore the anisotropy of the transport, seen in the different shapes of the Hanle curves.

The transition for applying increasingly larger negative dc currents at $V_{bg} = -50$ V can be followed in panels a) to d). For $0 \mu\text{A}$, an anisotropic Hanle curve with the characteristic $R_{NL}^{AP} > R_{NL}^P$ of the strong SOC regime and its induced spin precession around the SOF is observed (Figure 7.11a). Applying a negative I_{DC} speeds up the diffusion of the electrons and reduces the precession time. Therefore, the spins do not precess more than 90° now and the zero-field gap closes and both curves overlap, analog to a positive LSV signal (Figure 7.11b). Increasing the amplitude of the current leads to a reduction of the anisotropy of the curve or, more precisely, a smaller enhancement of the signal in the mid-field B_x range compared to the one at zero field (Figure 7.11c). This can also be understood by the faster diffusion, as the spins will spend less time in the graphene area under the TMDC flake and therefore the difference in spin relaxation times $\tau_s^\perp > \tau_s^\parallel$ will have less effect over the isotropic transport in the rest of the pristine graphene channel. For even larger I_{DC} , the shoulders of the Hanle curves disappear. The shape is now very similar to the isotropic case as the fast electrons pick up almost no signature of the SOC during their short time in the proximitized graphene, while in general the spin signal is increased by the accelerated spin transport (Figure 7.11d).

Applying a smaller back gate voltage of -30 V reduces the diffusivity in the bilayer graphene channel. Therefore, in Figure 7.11e for no dc current, the spin signal is reduced below the noise level. Accelerating the electrons with $I_{DC} = -10 \mu\text{A}$ makes first the shoulders of the Hanle curves visible as the out-of-plane spins with longer lifetime reach the detector (Figure 7.11f). Only stronger drift leads to the recovery of the anisotropic Hanle curve of the strong SOC regime (Figure 7.11g) as now also in-plane spins are fast enough to cross the whole channel. A maximum negative zero-field signal is finally observed for even more drift in Figure 7.11h, almost covering the shoulders of the Hanle curve. Also, the spin signal has a maximum for this back gate voltage and dc current in Figure 7.10b. Increasing I_{DC} then leads to a reduction of ΔR_{NL} and indicates an oscillatory behavior as predicted theoretically. For the evolution of the Hanle curves, this points to a transition from an anisotropic towards an isotropic shape, similar to the one starting in Figure 7.11a and ending in Figure 7.11d.

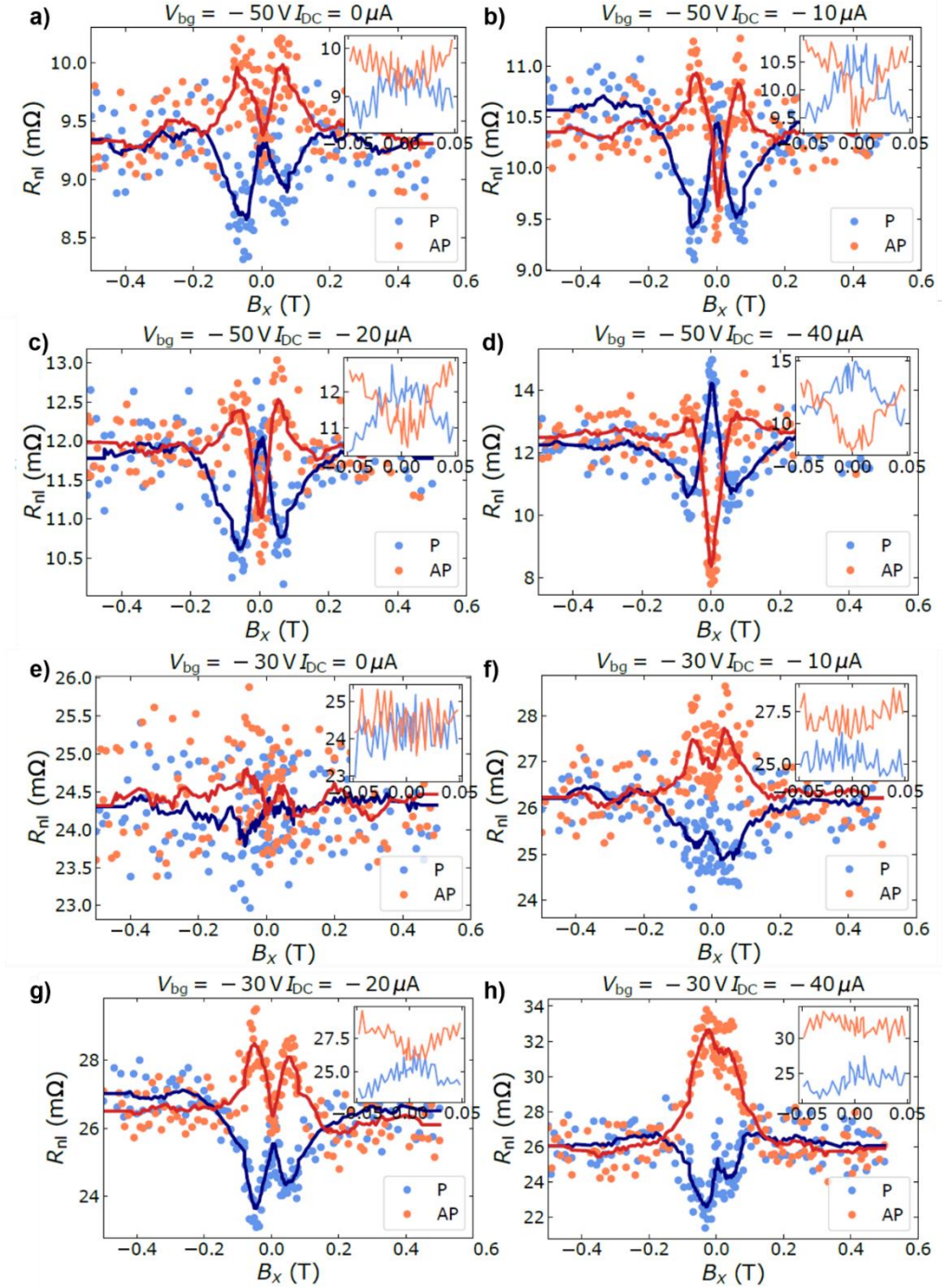


Figure 7.11: Full data for the Hanle measurements at 50 K. a), b), c) and d) Spin precession measurements at $V_{bg} = -50$ V and different I_{DC} values (0 to $-40 \mu\text{A}$). e), f), g) and h) Same measurements but at $V_{bg} = -30$ V and the same dc currents. The insets correspond to the low B_x range and the solid lines have been obtained averaging a window of eleven points.

7.4 Magnetic-field-free control of spin polarization in graphene/WSe₂ at room temperature

So far, all spin precession measurements have been conducted at 50 K. But, as for the SCC measurements, the strength of the graphene/TMDC system is the favorable properties up to room temperature that make the material also interesting for spintronic applications. Two factors play a key role in the persistence of the strong SOC regime at higher temperatures: the proximity effect that transfers the properties of the TMDC, mainly spin-valley locking, into graphene and its intrinsic long spin diffusion length.

As a consequence, the coherent spin precession around the SOF and its electrical control can also be observed at 300 K. Figure 7.12 shows the LSV signal as a function of back gate voltage for two different dc currents as a summary of those measurements.

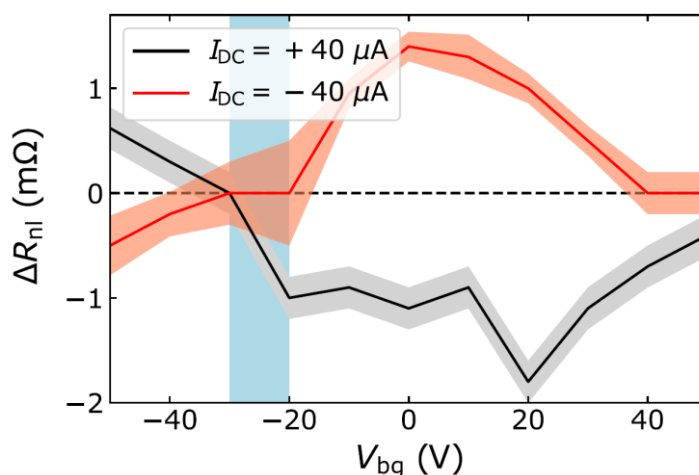


Figure 7.12: Summary of the LSV measurements at room temperature. ΔR_{NL} as a function of V_{bg} for $I_{DC} = 40 \mu A$ and $-40 \mu A$. The blue vertical strip represents the CNP of the TMDC-covered region.

These results are very similar to those at 50 K, demonstrating that the device is in the strong SOC regime up to room temperature and the spin orientation can be controlled using both I_{DC} and V_{bg} . At fixed I_{DC} , ΔR_{NL} changes sign once, at $V_{bg} = -30$ V, and decreases again at $V_{bg} = 50$ V, indicating that there might be another sign change for $V_{bg} > 50$ V. This would be in line with the oscillatory behavior of the spin precession shown in Section 7.1. Furthermore, ΔR_{NL} is reversed at every gate voltage by changing the sign of I_{DC} , as at 50 K.

In addition to the device reported until this point, a second sample was prepared using the same recipe and very similar results were obtained, showing the robustness of the findings in bilayer graphene/WSe₂ vdW heterostructures. The optical microscope image of the device after fabrication can be seen in Figure 7.13a. The only difference to the

previous ones of this thesis is the obvious capping with an h-BN flake, prominently visible as a yellow flake.

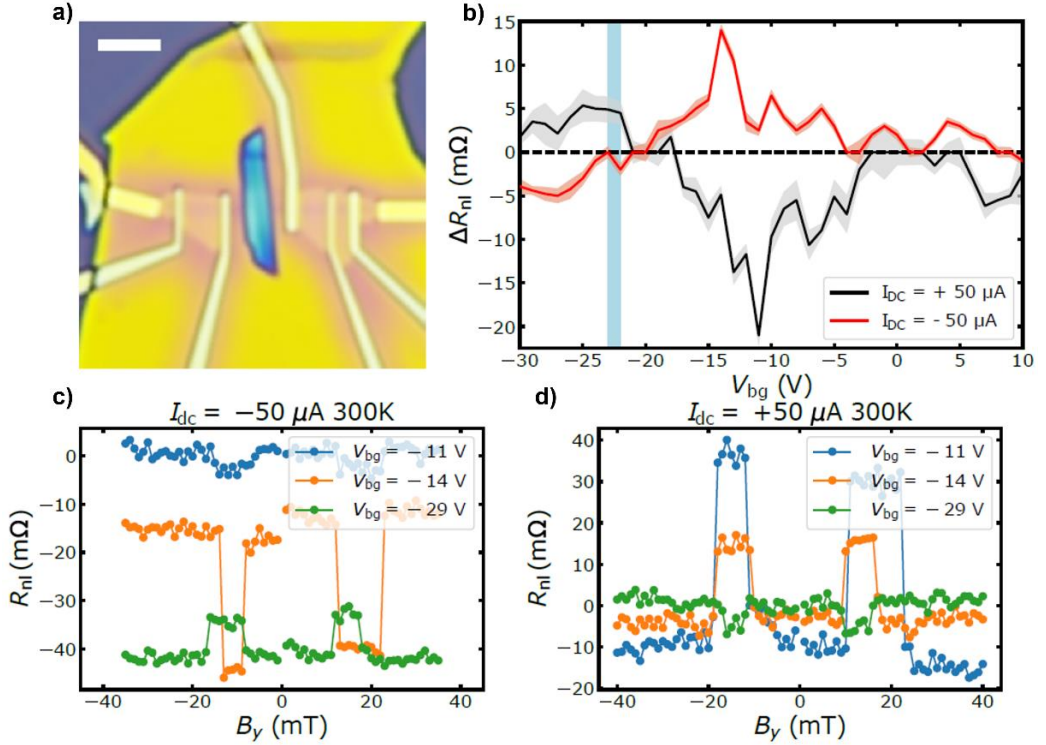


Figure 7.13: Spin drift experiments in the second sample. a) Optical image of the second device. The vertical WSe₂ flake (blue) and Co electrodes (light grey) are visible below the h-BN flake (yellow) used to cap the device. The horizontal bilayer graphene flake is barely visible as a darker strip underneath the electrodes and the TMDC flake. The scale bar is 3 μm. For the spin drift measurements, an identical configuration as in Figure 7.9a was used. **b)** V_{bg} -dependence of ΔR_{NL} for $I_{DC} = 50 \mu\text{A}$ and $-50 \mu\text{A}$ at 100 K. The blue vertical strip represents the CNP of the TMDC-covered region. **c)** and **d)** Room-temperature LSV measurements at $I_{DC} = -50 \mu\text{A}$ and $50 \mu\text{A}$, respectively and at $V_{bg} = -11 \text{ V}$, -14 V and -29 V .

Not to repeat the raw data of all measurements again, Figure 7.13b plots the V_{bg} -dependence of ΔR_{NL} for two different I_{DC} values as summary. As in Figure 7.7 and Figure 7.12 for the first sample, sweeping V_{bg} controls the amplitude of ΔR_{NL} and the spin signal reverses sign close to the CNP of the graphene proximitized with WSe₂. Due to the width of the WSe₂-covered graphene region being 1.4 μm (narrower than in the first sample with 2 μm), the amplitude of the spin signal is roughly ten times larger and the signal-to-noise ratio of ΔR_{NL} is higher.

As shown theoretically in Figure 7.8b and experimentally for the first sample in Figure 7.10b, when the width of the WSe₂ flake is designed so that the position where μ_s^y changes sign lies within the proximitized region, the sign of ΔR_{NL} can be controlled by the applied I_{DC} . Indeed, for the full range of V_{bg} values, reversing the sign of I_{DC} reverses the sign of the spin signal. This shows the achievement of the electrical control of spin reversal in two independent electrical ways without the need for a magnetic field in two different bilayer graphene/TMDC heterostructures. As in the first sample, both effects persist up to room temperature as exemplarily shown in Figure 7.13c and 7.13d.

In conclusion, the data of both devices show the VZ SOC induced magnetic-field free control of spin precession in a bilayer graphene/WSe₂ vdW heterostructure at the strong SOC regime. By tuning the diffusivity using V_{bg} and the spin transport time using I_{DC} , the spin polarization can be controlled up to room temperature, making the devices operate as a spin field-effect transistor. It is the first realization of a Datta-Das type transistor at room temperature since its initial proposal over 30 years ago [39]. This achievement has prospects for future spin-based logic applications and the next section will discuss it in the context of other similarly working devices.

7.5 Spin field-effect transistor and Datta-Das proposal

Spin transistors combine the working principle of the ordinary transistor and the fundamental property of spin [312]. They are an important part of the initiative to use spintronic principles not just in memory but also in logic applications or even combine these two fundamental functions [96, 313, 314]. The existing spin-logic proposals had to find a way around the current limitations of spin transport in metallic or semiconducting channels, solving it, for example, via cascading of multiple devices [313], using a SOC material for SCC making electrical connections accessible [96] or discussing graphene's long spin diffusion length [314]. They also use different schemes for the control of the FM parts that are needed for programming the logic operations or storing the memory bits. Two ways, for example, are either via magnetoelectric switching [96] or spin-transfer torque [313, 314].

On a device design level, a spin transistor requires the electrical control of spin currents. The 1990 proposal by Datta-Das (the original drawing shown in Figure 7.14) relied on the tuning of the Rashba SOC in a 2DEG by an externally applied electrical field leading to the controlled rotation of spin polarization [39]. However, this requires spin coherence in the full channel, making, especially for the proposed semiconducting channels, ballistic transport at low temperatures necessary. Updated proposals were more tolerant against spin-independent scattering but required complicated fine-tuning of the involved SOC's (Rashba and Dresselhaus) to achieve this [315] or involved the use of external magnetic fields that seems unrealizable outside of single devices in the laboratory [316].

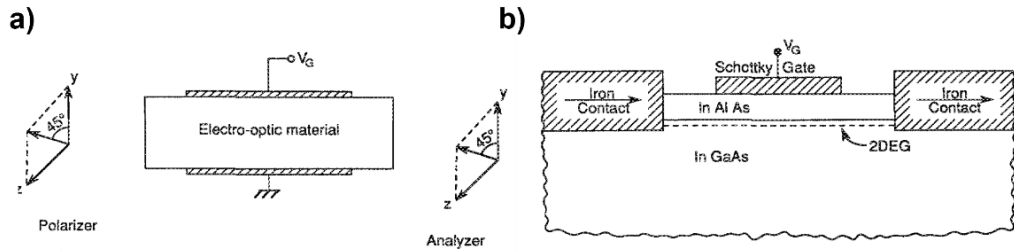


Figure 7.14: Analogy of the Datta-Das proposal. a) Opto-electronic manipulator, where a gate voltage controls the properties of the optically active material. b) Proposal for a spin field-effect transistor after the same principle with a 2DEG. Images taken from Ref. [39].

Hence, the first experimental realization of a spin field-effect transistor was measured at 1.8 K, close to the limit of He temperatures, in a device consisting of a 2DEG in a semiconducting heterostructure, two FM electrodes for injection and detection, and an electrical top-gate to control the SOC, following the design proposal by Datta and Das [317]. The non-local resistance in this standard LSV could be periodically modulated for a gate voltage range of 3 V and was observed to a certain extent up to 40 K. This temperature range is, however, still not feasible for realistic applications.

Just one year later, a similar semiconducting device with a 2DEG was reported that used the ISHE instead of an FM electrode to detect the spin current [318]. However, it relies on the optical injection of spins, which in other reports has been extended up to 240 K [319], but is impossible in integrated circuits. However, the FM injection of spin currents in such semiconducting channels is possible and a similar device based on the ISHE has been demonstrated but required an additional electrical drift current and, again, liquid He temperatures [281]. At those temperatures, Choi et al. have shown that it is possible to modulate the signal at the ISHE detector by applying a gate voltage as it changes the Rashba SOC in the 2DEG precessing the spin [320]. As a next step, the same group replaced the spin injection from the FM electrode with the SHE in a second Hall bar, realizing an FM-free, all-electrical Datta-Das based on spin-charge interconversion, but again limited to 1.8 K [321]. A similar design had been presented before that replaced the FM electrodes with quantum point contacts instead and realized spin injection and detection through the spin-split one-dimensional conduction [322]. Here the effect was observed up to slightly higher temperatures (11 K) that could be improved by optimizing the fabrication of the quantum point contacts.

Not surprisingly, graphene seemed a likely candidate to accomplish the electrical control of spin polarization at higher temperatures up to 300 K. However, due to the absence of Rashba SOC, the field-effect tuning of the spin precession required a new working principle. Theoretical proposals focused on the electrical tuning of the properties of bilayer graphene proximitized by another material. One idea is to place a ferromagnetic oxide on top that induces spin precession via the proximity exchange interaction [323]. The conduction is now either through the upper or lower layer of graphene depending on

the external, vertical electric field. As the proximity effect mainly occurs in the top layer, this essentially turns the spin precession on and off. Another proposal suggests a bilayer graphene/TMDC heterostructure, similar to the one used in this thesis [324]. Here, the proximity effect introduces SOC that leads to fast spin relaxation. However, the calculated band structure shows that the resulting spin-splitting is larger in holes than electrons as the carriers of the valence band are mainly localized in the top graphene layer. Changing the carrier type through an applied gate voltage would therefore turn the spin transport on and off.

In both cases, the design does not fulfill the characteristics of a spin field-effect transistor but resembles a spin field-effect switch. Such a design has been realized in graphene proximitized by a TMDC flake at low temperatures and up to 200 K [147], but also up to room temperature [148]. Here, the spin transport through the channel can be suppressed by the spin absorption into the semiconducting TMDC, whose conductivity is electrically tuned.

Finally, other LSV experiments have reported a similar sign change of ΔR_{NL} as shown in this chapter, using a fully encapsulated, pristine graphene channel and one-dimensional FM contacts. However, the applied gate voltage there only changes the spin polarization of the injection and does not tune any properties of the channel [325].

In summary, the results of this chapter show for the first time the realization of the Datta-Das transistor at room temperature, passing a long-standing barrier of similar experiments with semiconducting 2DEGs. They also go further than similar spin-switches that have been realized in graphene-based LSVs by controlling the properties of the spin transport and realizing an oscillatory tuning of the spin signal. Optimistically, they can pave the way for the use of 2D materials to realize future spintronic ideas.

As a cautionary tale, the next chapter will discuss some of the obstacles when transferring the results from a single device in a laboratory environment to a more applied design. The idea is the application of the highly efficient SCC in proximitized graphene that was presented in detail in Chapters 5 and 6 in a spintronic logic device proposal by Intel.

8 Local device as a step towards spintronic application

8.1 Introduction to the device proposal by Intel

This thesis set out to study 2D materials and their heterostructures as a possible material system for a spin-based beyond-CMOS technology. But what are some of the current ideas for the future generation of spintronic devices? A group of researchers from the Intel corporation proposed a spintronic logic based on a magnetoelectric spin-orbit (MESO) device in 2019 [96]. It promises low energy consumption, a low operating voltage, and a high device density. The general structure can be seen in Figure 8.1, where the position of the different constituting materials is shown.

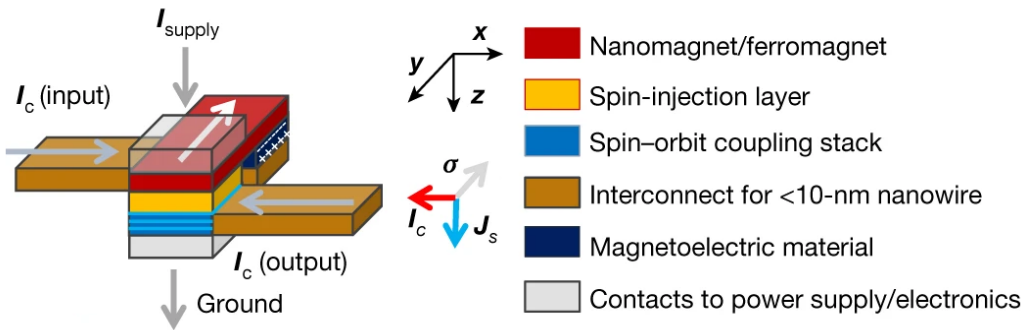


Figure 8.1: Material stack of the MESO device’s writing and reading blocks. In the foreground, the stack for reading the magnetization of the FM can be seen, where a supply charge current (I_{supply}) leads to the injection of a spin-polarized current, that is converted in the SOC material to an output charge current. In the background, the writing block is shown, where an input current is used to build up an electric field across the magnetoelectric material to electrically switch the magnetization of the FM. In a cascading operation, the output current after the reading will be fed as the input current for the next FM element to be switched.

Instead of tuning the channel resistance with an applied gate voltage like in a standard field-effect transistor, the central working principle is based on the magnetization direction of an FM element. This is favorable for the miniaturization of the device as the

FM is more stable on the nanometer-scale when compared to the conduction of electrons, which inherently leads to leakage currents. Via the magnetization direction as switchable property, it is possible to realize a logic, but, due to its non-volatility, information can also be stored with it for memory use. The different building blocks are connected via charge conductors and input and output are charge currents, which makes integration into existing electronic systems easy.

The magnetization direction is read out by detecting the spin polarization after a supply current is passed through the FM. The spins are converted in the SOC layer via an SCC mechanism into an output charge current (and output voltage), whose sign is sensitive to the spin polarization and therefore magnetization direction. In the cascading mode of the proposed circuit, the output of one device will be used as an input for the next device to switch the respective FM there. While large output currents will enable fast switching, the main limit is reaching output voltages that are sufficient to in turn be used for writing the next FM element via magnetoelectric coupling. Current metallic systems undercut the anticipated minimum switching voltage of 100 mV by three orders of magnitude [95, 96]. Therefore, an efficient SCC is sought after – this is where the results of this thesis can contribute to a solution for a current technological problem.

As shown in Section 6.4, proximitized graphene is a very competitive material system to generate sizeable SCC outputs. And while the large-scale CVD production of such graphene/TMDC heterostructures is still under development, a single device proof of concept to extract benchmark values is possible, similar to the realization of the prototype of a single spin transistor in the previous chapter.

The main difference between the proposed device design and the spin transport and interconversion studies conducted in this thesis is the local transport configuration in the MESO device. Both charge and spin current flow through the SOC material, while in the LSVs so far, they were separated by the graphene channel. The following section will show the problems that can result from this change in measurement scheme as one example of the hurdles that have to be taken when transitioning from the laboratory to application.

8.2 2D material local SCC device

The reading block of the MESO device can be realized with a mostly 2D material stack that is shown in Figure 8.2a. A graphene/TMDC heterostructure (in this chapter MoS₂ was chosen but others are possible as well) is used for the SOC material, which is placed on the standard SiO₂/Si substrate that allows the application of a back gate voltage. As before, Co is used as an FM and a thin TiO_x barrier is inserted to enhance spin injection. A full 2D material stack could be realized by using 2D FMs and a thin layer of h-BN here. The electrical contacts to the graphene and the FM are done with Au, for which Ti or Cr were used as a wetting layer.

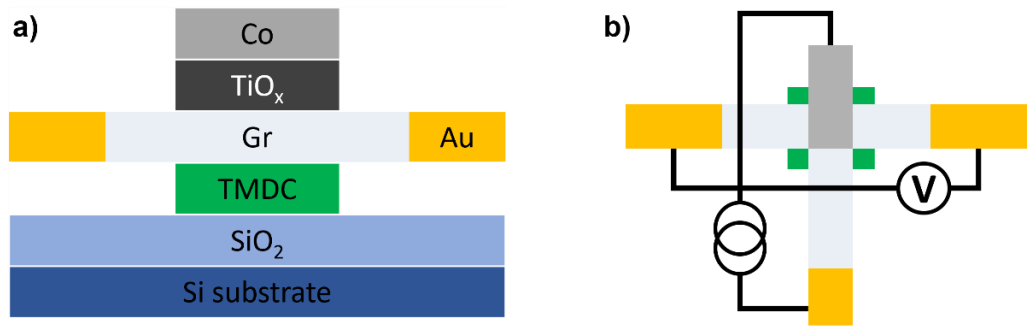


Figure 8.2: Initial design for the local device. a) Side-view of the 2D material stack for the reading block of the MESO device. b) Top-view of the T-shaped device with the ISHE measurement configuration.

The fabrication process is similar to the ones in the previous chapters; however, one significant change is the stacking order of the 2D materials. Here, the TMDC flake is directly exfoliated on the Si substrate and the graphene flake has to be transferred on top. This requires the PC method described in Section 4.1, where a PC membrane on PDMS attached to a glass slide is used to pick up the graphene from a Si substrate after exfoliation and transfer it onto the TMDC flake. Afterwards, the steps of etching, annealing, and patterning electrical contacts are done following the same recipe as before. The final sample following the initial design can be seen in Figure 8.3 after fabrication.

The electrical measurements are conducted in the same setup as the other spin-charge interconversion experiments in this thesis, applying a delta mode dc current and measuring the resulting voltage. The magnetic field is swept along the in-plane easy axis of the FM electrodes, as before this axis is defined as y . In contrast to R_{NL} , the local resistance will show a large background due to the charge current flowing through the device. However, the spin signal is also expected to be larger as the spins are injected directly into the SOC material. Therefore, a clear jump in the resistance should be visible when the magnetization of the FM switches direction as an oppositely polarized spin current will lead to a sign change in the SCC voltage. The switching field should correlate with the ones observed in the LSV measurement for electrodes with similar widths and change sign when reversing the sweeping direction of the magnetic field saturating the initial magnetization in opposite directions. Figure 8.4 shows the results of the measurements at 10 K.

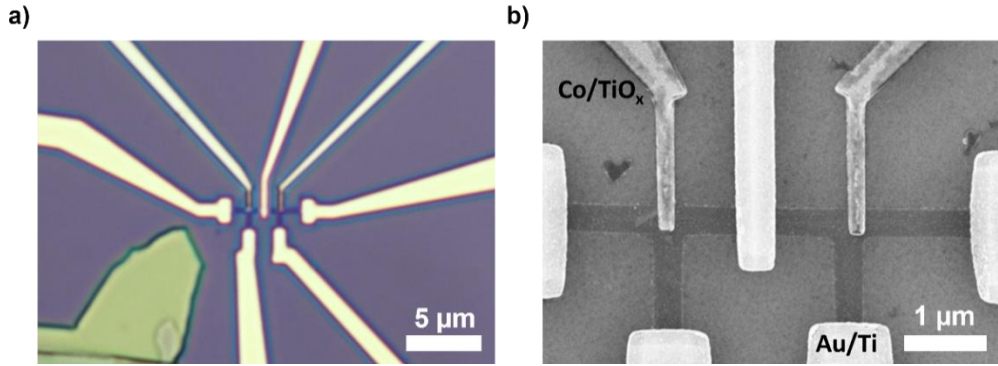


Figure 8.3: Images of the initial local devices after fabrication. a) Optical microscope image showing the two FM electrodes and five Au contacts forming two devices. **b)** Scanning electron microscope image zoomed in on the devices. The MoS₂ flake underneath the left Co electrode is barely visible. There is also a slight misalignment in the reference device with pristine graphene on the right.

In panels a) and b) a large signal ($\Delta R \approx 1 \Omega$) can be observed for the graphene/TMDC device in IREE and REE configuration, which could indicate an efficient interconversion. However, this initial excitement was dampened when looking at the same measurements for the pristine graphene reference. Nominally the same configurations, the stack lacks a MoS₂ flake and therefore no SOC should be imprinted into the graphene. Any signal observed will therefore not be due to spin-charge interconversion as no IREE will occur. However, Figure 8.4c shows a similar resistance change in the IREE configuration as for the graphene/TMDC part but with opposite sign. The same can be observed for the REE configuration in Figure 8.4d. Observing a signal with a similar amplitude in both devices can only lead to the conclusion that the steps in resistance are spin-unrelated.

Nevertheless, as the steps occur for the two configurations at the same fields, which correspond to the ones seen in the LSV measurements, they are related to the switching of the magnetization of the FM. Two effects could play a role here: One possible mechanism explaining the results is the stray field-induced ordinary Hall effect in graphene [326, 327], which is caused by an out-of-plane magnetic field. As the Co magnetization is aligned along the y direction, an out-of-plane stray field generated at the edges of the Co electrode through the graphene channel will linearly increase and saturate with sweeping B_y . In combination with the current from the FM electrode, this could lead to a sizeable Hall voltage in graphene resulting in a linearly varying and saturating R as a function of B_y as observed in Figure 8.4. The sign of the detected Hall voltage would change when the magnetization rotates, leading to the observed jumps.

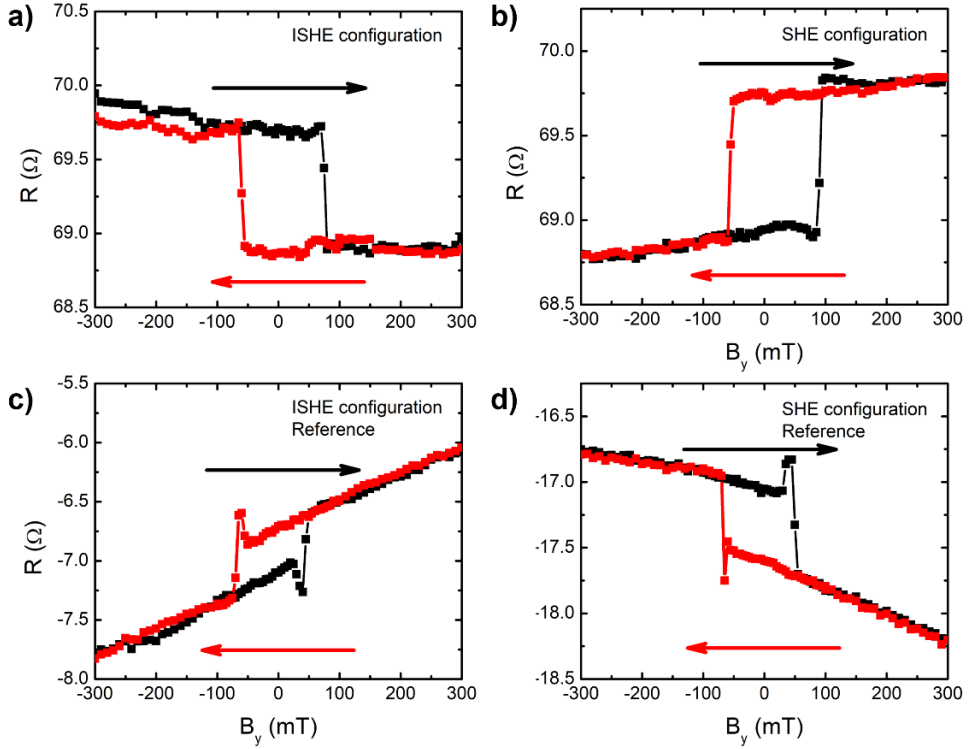


Figure 8.4: Spin-charge interconversion measurements for the local device at 10 K. a) and c) ISHE configuration as in Figure 8.2b. b) and d) SHE configuration with current and voltage leads interchanged. Data in c) in d) is measured in the pristine graphene device. The red and black arrows indicate the magnetic field sweep direction.

Secondly, due to the anomalous Hall effect in the FM electrode [95, 326, 327], a voltage along the in-plane x direction could build up in Co with magnetization along y , when a current is applied along z . If the underlying graphene Hall bar probes this voltage, a step-shaped R vs. B_y curve could be obtained as the sign of the anomalous Hall effect depends on the direction of the magnetization as well.

While the anomalous Hall angle of Co is relatively small (around 1% [328]), the Hall coefficient in graphene can be quite large, especially near the CNP (see Figure 3.2c). Therefore, it seems likely that the jump in resistance stems from the stray fields of the FM electrode and multiple device iterations to reduce it will be shown in the next section.

8.3 Device design iterations

It is known that the stray fields of an FM electrode are largest at the faces perpendicular to the easy axis [254, 329]. The initial design for the local device shown in Figure 8.2a has the fundamental problem that this face is located directly over the measurement

region. Figure 8.5 shows multiple ways of trying to fix this fact without hindering the basic working principle of the MESO device block.

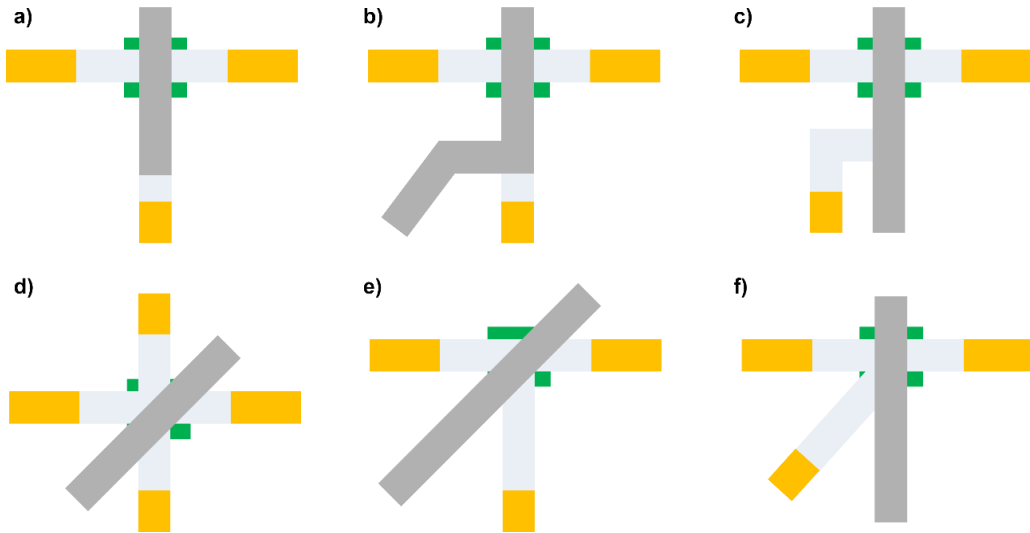


Figure 8.5: Design changes of the T-shaped device to reduce stray fields. **a)** Extending the FM electrode. **b)** Further extension of the FM electrode by introducing a bend. **c)** Further but straight extension and angling the graphene channel. **d)** 45° rotation of the extended, straight FM electrode on a graphene cross. **e)** Rotated FM electrode on a straight or **f)** on an angled graphene T.

The basic idea is to extend the length of the electrode to spatially separate the main source of the stray fields from the T-shaped graphene area as shown in Figure 8.5a. The drawback is the reduced current density flowing through the interface of the FM with the proximitized graphene area. Fewer spins will be injected directly into the SOC material and more into the pristine graphene forming the base of the T. They are subsequently not converted into charge, lowering the output voltage of the device. This effect can be mitigated by adding a bend to the FM electrode (Figure 8.5b) or to the graphene channel (Figure 8.5c).

A sample incorporating all four device designs discussed so far was fabricated out of only pristine graphene without TMDC. The resistance signal was measured for the first three designs, the fourth unfortunately oxidized before the measurement. Despite separating the end of the bend in the electrode 5 μm from the graphene T-junction, a sizeable jump in resistance was observed for low temperatures, however, smaller than in the initial local device design. Furthermore, due to a working back gate in this sample, the gate-dependence of the signal could be recorded to determine the origin.

The control experiment consists of measuring the signal for the hole and electron-doped regimes in graphene, which can be obtained by applying V_{bg} . Opposite signs are expected for the ordinary Hall effect and a corresponding sign change should be observed for the B_y -dependence of R . Importantly, the sign of the anomalous Hall effect is expected to be

independent of V_{bg} as it originates directly in the FM. Figure 8.6 shows the results of these tests.

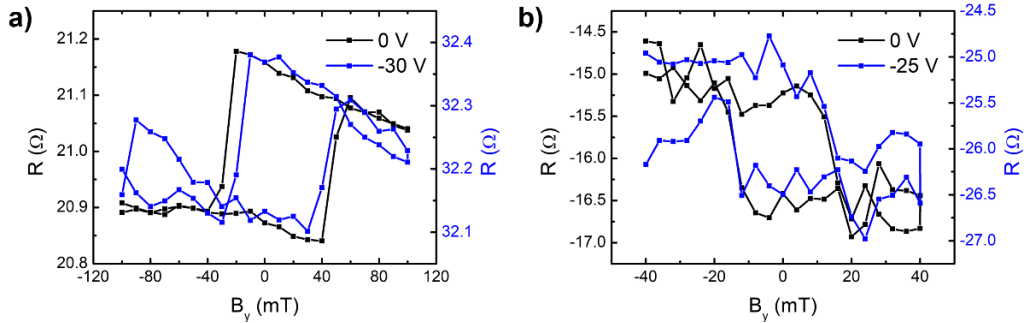


Figure 8.6: Gated spin-charge interconversion measurement in a local device at 10 K. a) ISHE measurement in a device with a bent electrode design as in Figure 8.5b. **b)** SHE measurement in a device with the initial electrode design as in Figure 8.2b. Both devices were fabricated on the same graphene flake without TMDC underneath and the Dirac point was observed at -15 V in this sample.

It can be observed for the ISHE and SHE measurement configuration that the sign of the signal is the same for gate voltages that coincide with the hole and electron regime of the pristine graphene region. This points to the anomalous Hall effect as the source of the steps in resistance. However, the effect of the Co electrode on top of the graphene cannot be neglected.

To investigate this, an additional test sample of pristine graphene was fabricated following the design in Figure 8.5d. Here, the electrode is extended 15 μm and tilted 45° to reduce unwanted spin injection outside of the hypothetically proximitized region, which also allows adding a fourth graphene arm to this area. The final device can be seen in Figure 8.7a. Due to the cross shape of the graphene channel, the Hall resistance can directly be measured as a function of an out-of-plane magnetic field B_z for different values of V_{bg} and the results are shown in Figure 8.7b. It can be observed that, even though the CNP can be detected in the longitudinal resistance (Figure 8.7c), the carrier density only changes marginally as it is sensed primarily in the area directly under the Co electrode. Here, the Fermi level is probably pinned due to the direct contact with the metallic FM. Therefore, the ordinary Hall effect due to stray fields could still be the main source of the signal, even though it does not change with sweeping V_{bg} .

Figure 8.7d shows the IREE measurement of the same device. For the first time in this series of experiments, a device design shows a linear background without steps even at low temperatures as expected for pristine graphene. This is a clear indication that the spatial separation of the electrode end from the graphene channel can suppress any unwanted ordinary Hall effect contribution, even though the noise level could be improved. However, the additional arm that is used for the Hall characterization would prevent a spin accumulation in the device due to the SHE as the spins can equally diffuse

in both directions. Hence, the designs in Figure 8.5e and Figure 8.5f could be possible improvements for the local device. Unfortunately, the realization of these devices was not achieved during the experimental work of this thesis.

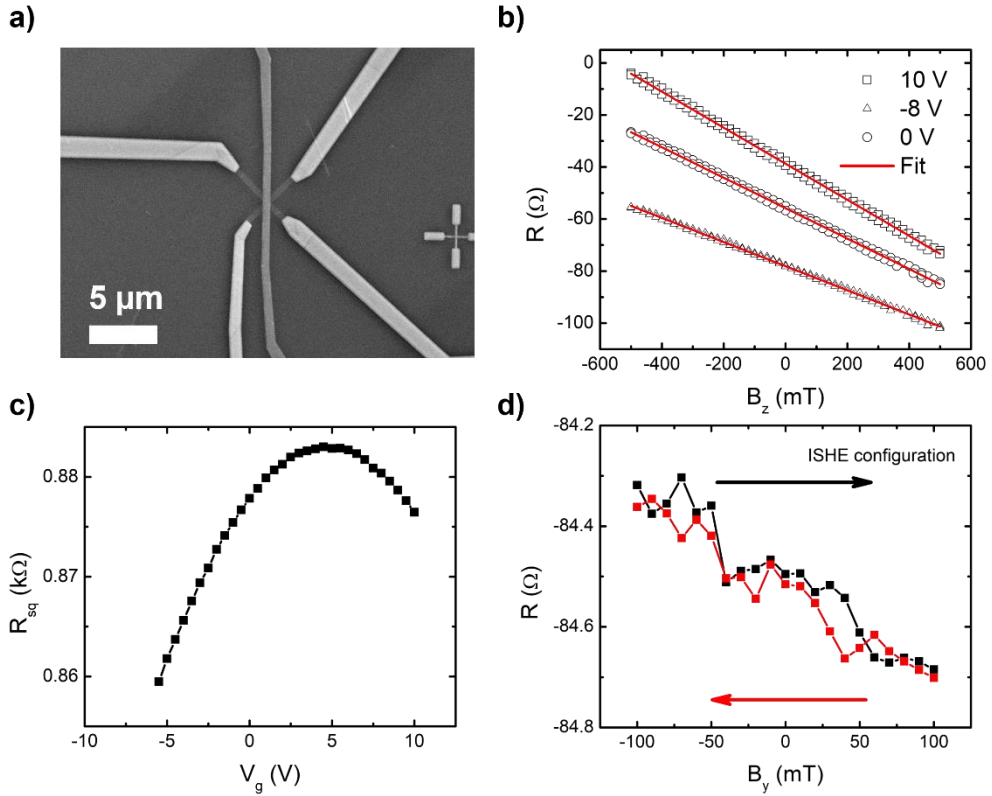


Figure 8.7: Hall cross design for the local device, fabricated without TMDC flake. **a)** Scanning electron microscopy image of the device. **b)** Hall measurements for out-of-plane magnetic field at 300 K at different back gate voltages and the accompanying fits giving $9 \times 10^{12} < n_c < 1.3 \times 10^{13} \text{ cm}^{-2}$. **c)** Two-point resistance of the graphene channel at 300 K, showing the CNP at 4.5 V. **d)** ISHE measurement at 10 K. It should be noted that the configuration in this device leaves one graphene arm connected to ground.

It should finally be noted that similar signals have been observed in local measurements and attributed to the ordinary Hall effect stemming from the roughness of the oxide tunnel barrier on graphene [330]. This will strongly depend on the growth conditions and the surface properties of the graphene flake so that extreme care has to be taken to control for it in future experiments.

9 Conclusion and outlook

The ongoing Corona pandemic, during which also this thesis was written, showed the dependence of today's society on readily available and powerful information technology – from video calls to supply chain management. And while the computing power of integrated circuits has found its way into every aspect of modern life, the total energy consumption of these devices and their infrastructure is growing steadily. This problem has to be solved or else it will propel the ongoing climate catastrophe, whose consequences – from wildfires to flooding – could not even be overshadowed by this worldwide once-in-a-lifetime event in the last two years.

The various proposals that exist to replace the common transistor with a more efficient spin-based device promise low-power consumption for spin logic as well as a smaller footprint and additional functionality like on-chip memory. However, to realize them, multiple steps in technological development are needed. Long-range spin transport, electrical spin manipulation, and efficient spin-charge interconversion are obstacles that conventional materials cannot overcome at room temperature at the moment.

Graphene and other 2D materials, that were introduced in Chapter 3, could be the basis to tackle these challenges. As detailed there, previous reports have shown spin diffusion lengths of more than $10\ \mu\text{m}$ at 300 K in graphene even for CVD-grown samples, but, due to the low SOC, means to control or convert spins were lacking. Fortunately, TMDCs, another member of the family of 2D materials, could fill this functional gap. Their strong SOC can be imprinted into graphene by the proximity effect in vdW heterostructures. Conducting spin-based experiments in this new materials system of proximitized graphene was the goal of this thesis. It required extensive nanofabrication and multiple experimental techniques, which were summarized in Chapter 4. The fine-tuning of the growth of the tunnel barrier necessary for spin injection proved to be the crux for a lot of devices. While here a working recipe was completed, the delicate electrical Ohmic contacts to graphene showed little reproducibility until the end of this thesis and beyond.

In Chapter 5, a new device concept was realized, an LSV of FM electrodes on a graphene channel with an additional cross-shaped Hall bar that is proximitized by MoS_2 . With it, an unprecedented and unambiguous experimental demonstration of the proximity-induced ISHE in graphene has been found together with a manifestation of another SCC phenomenon either due to a proximity-induced IREE in graphene or an ISHE in MoS_2 . Due to the measurement protocol of Hanle precessions, the spin transport and the SCC parameters could be quantified, and an exceptional SCC efficiency has been obtained.

While the observation of ISHE up to room temperature is an exciting result, other interesting experiments were missing: Measuring the direct SHE signal, anisotropic spin transport across the proximitized graphene region, and the electrical control of the SCC.

With a similar device, using for the first time WSe₂ as TDMC on top, these gaps could be filled with the results shown in Chapter 6. Again, the temperature dependence of the spin transport and SCC parameters were quantified, showing a robust performance up to room temperature. Interestingly, the ISHE appears as the only SCC mechanism without an accompanying IREE, suggesting the dominance of the VZ term over the Rashba term in the proximity-induced SOC. Additionally, the direct gate control of the SCC signal was realized, tuning it from an off state up to 209 mΩ, while increasing the conversion efficiency. This leads to a very large $\theta_{SH}\lambda_S$ product of around 40 nm in the best scenario (at 100 K and -5 V), with a remarkable 2.5 nm at room temperature and zero gate voltage. These results demonstrate graphene/TMDCs as a superior SCC material system as shown in the comparison of the final section in this chapter.

In Chapter 8, preliminary steps were sketched to transition these results from the non-local devices of the laboratory to the local configuration in the MESO proposal by Intel. The first excitement over a large voltage output was dampened by the probable origin of these signals: stray field-induced ordinary Hall effect. Several design iterations were tested, and finally a successful reference sample was fabricated. In the future, the improved design could be used to measure the SCC effects. However, more improvements will probably be needed to reach the required SCC voltage output necessary to cascade multiple devices.

Fortunately, the non-local Hall bar device concept can also be extended to study SCC in a variety of other material combinations of graphene: with heavy metals, oxides, different TMDCs, topological insulators [331], or other topological materials with low symmetry [332]. More efficient SCC could be found, as well as other novel spin phenomena. It could also be a platform to answer the question of what happens when combining multiple proximity effects from different materials in graphene. Finally, it should also be possible to use the deterministic transfer methods to fabricate non-local and later local devices fully out of 2D materials using the recently discovered 2D FMs.

Also, the exploration of more basic research questions is possible in 2D materials, such as the interplay of the different SOC terms and their accompanying SCCs and SOFs that have been introduced in Chapter 2. The results of Chapter 7 show how pursuing such a fundamental idea as the strong SOC regime can, at the same time, still be used to realize applied concepts. There, the VZ SOC-induced magnetic-field free control of spin precession in a graphene/WSe₂ vdW heterostructure is presented. By tuning the carrier density via an applied back gate voltage and guiding the spins with an additional drift current, the spin polarization can be controlled up to room temperature. The LSV device, therefore, operates as a spin field-effect transistor, a long-awaited milestone in spintronics.

And while it should be noted that one critical requirement is the further development of the CVD growth of these materials, these achievements show that 2D materials have the prospect for spin-based logic applications such as non-volatile and reconfigurable logic. Hopefully, the findings of this thesis are helpful for the realization of future 2D material-based spintronic devices that solve some of the challenges facing society today.

Appendix A Contact pulling in Hanle precession measurements

Applying a magnetic field along the channel of a LSV leads in first order to the precession of the injected spins. For larger magnetic fields, it will also pull the effective magnetization of the FM electrodes away from the easy axis towards B_x by an angle $\beta(B_x)$ as shown in the inset of Figure A.1a.

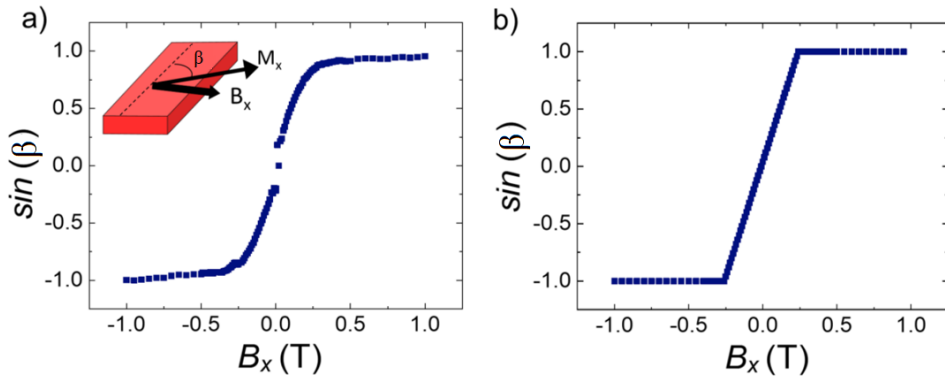


Figure A.1: Angle of the effective magnetization. a) $\sin(\beta)$ as a function of B_x obtained from Hanle measurements across a graphene LSV by using Equation 32. Inset: Sketch that defines the angle β between the easy axis of the FM electrode and the effective magnetization M_x that is pulled towards B_x . b) $\sin(\beta)$ as a function of B_x using the Stoner-Wohlfarth model.

The magnetization of both electrodes – injector and detector – will be shifted by this angle β and, hence, the amount of spins that precess will be reduced until it is zero, when all spins point along x parallel to the magnetic field, effectively reducing the spin signal. As shown in Equation 20 the spin precession data is therefore proportional to $\cos^2(\beta)$

$$\Delta R_{NL} = \frac{R_{NL}^P - R_{NL}^{AP}}{2} \sim \cos^2(\beta) \quad (30)$$

where the proportionality factor is the magnetic-field dependent spin signal that is used to extract the spin transport parameter. However, due to this field-dependence, β cannot be extracted from that curve and, additionally, it has to be included in the fitting to extract correct parameters.

Nevertheless, as mentioned in Section 2.4 and 5.2, the addition of both curves gives

$$\bar{R}_{NL} = \frac{R_{NL}^P + R_{NL}^{AP}}{2} = R_{\parallel} \sin^2(\theta_M) \quad (31)$$

where R_{\parallel} is the spin signal at $B_x = 0$ that is constant due to the parallelism of injector and detector. Following Equation 31, $\sin(\beta)$ can now be calculated by

$$\sin(\beta) = \text{sign}(B_x) \sqrt{\frac{\bar{R}_{NL} - \min(\bar{R}_{NL})}{\max(\bar{R}_{NL}) - \min(\bar{R}_{NL})}} \quad (32)$$

using the maximum and minimum values of \bar{R}_{NL} for fields larger than B_{sat} to normalize the values of the sine between 1 and -1. Figure A.1a shows exemplary the behavior of $\sin(\beta)$ for one LSV.

Another approach to extract β is the Stoner-Wohlfarth model [333] for FM electrodes under a perpendicular magnetic field. Here, the assumption is that the magnetization moves linear with the applied magnetic field between the two saturation fields B_{sat} . This case is plotted in Figure A.1b. The dependence is similar and avoids complicated calculations and noise or jumps in the experimental data.

Appendix B Fitting of the Hanle precession data in Python

All of the fitting of the experimental data in this thesis was done in Python running in a Jupyter notebook. This chapter will give a quick overview of this process through (incomplete) code snippets. The packages numpy and scipy were used for mathematical functions, arrays, fitting module and physical constants.

```
import numpy as np
from scipy.optimize import curve_fit
from scipy import constants
```

Equation 20 (and separately Equation 25) was realized as a function with the magnetic field (B_x), the different spin transport parameters (τ_s , D_s , P), device parameters (R_{sq} , L , w) and fit constants to allow for small offsets (R_0 , B_0) as input, returning the values for the non-local resistance ΔR_{NL} . beta is a self-defined function returning the interpolated data of the pulling calculation described in Appendix A.

```
def sym_fit_pull(B, tau, D, P, R0, B0, Rsq, L, W):
    g = 2
    muB = constants.physical_constants["Bohr magneton"][0]
    hbar = constants.hbar
    w = g*muB*B/hbar
    w0 = g*muB*B0/hbar
    return (1-(beta(B)**2)*P**2*Rsq*D/(2*W)*np.real(np.exp(-
        L*np.sqrt((D*tau)**(-1)-1j*(w-w0)/D))/(np.sqrt(D/tau-1j*(w-w0)*D)))+R0
```

The fitting can then be realized by providing the experimental data, the bounds and starting values for the fitting parameters in the curve_fit module. The printed values are the spin transport parameters in practical units and their uncertainties.

```
popt, pcov = curve_fit(lambda x, tau, D, P, B0: sym_fit_pull(x, tau, D, P, R0, B0,
Rsq, L, W), data[:,0], data[:,1], bounds=([0,0,0,-0.01,-0.01], [1E-
9,0.05,1,0.01,0.01]),
                                p0=[100*10**-12,5*10**-3,0.1,0,0])

print(np.round(popt[0]*10**12,1),np.round(popt[1]*10**3,1),np.round(popt[2]*100,1))

sigma = np.sqrt(np.diag(pcov))

print(np.round(sigma[0]*10**12,1),np.round(sigma[1]*10**3,1),np.round(sigma[2]*100,
1))
```

Including a finite contact resistance or using a four-region model requires an algebraic solution to the diffusion equations in Section 2.4 and 2.5 that, due to its length, is not shown here.

Bibliography

1. Brinkman, W. F., Haggan, D. E. & Troutman, W. W. A history of the invention of the transistor and where it will lead us. *IEEE Journal of Solid-State Circuits* **32**, 1858–1865 (1997).
2. Bardeen, J. & Brattain, W. H. The Transistor, A Semi-Conductor Triode. *Physical Review* **74**, 230–231 (1948).
3. Williams, R. S. What's Next? [The end of Moore's law]. *Computing in Science Engineering* **19**, 7–13 (2017).
4. Dayarathna, M., Wen, Y. & Fan, R. Data Center Energy Consumption Modeling: A Survey. *IEEE Communications Surveys Tutorials* **18**, 732–794 (2016).
5. Andrae, A. S. G. & Edler, T. On Global Electricity Usage of Communication Technology: Trends to 2030. *Challenges* **6**, 117–157 (2015).
6. Binasch, G., Grünberg, P., Saurenbach, F. & Zinn, W. Enhanced magnetoresistance in layered magnetic structures with antiferromagnetic interlayer exchange. *Physical Review B* **39**, 4828–4830 (1989).
7. Baibich, M. N., Broto, J. M., Fert, A., Van Dau, F. N., Petroff, F., Etienne, P., Creuzet, G., Friederich, A. & Chazelas, J. Giant Magnetoresistance of (001)Fe/(001)Cr Magnetic Superlattices. *Physical Review Letters* **61**, 2472–2475 (1988).
8. Forschungszentrum Jülich - Press releases - Nobel Prize for Prof. Peter Grünberg from Research Centre Jülich (https://www.fz-juelich.de/SharedDocs/Pressemitteilungen/UK/EN/2007/index12b7_hm.html).
9. Global Hard Disk Market Report 2021-2027 (<https://www.prnewswire.com/news-releases/global-hard-disk-market-report-2021-2027-market-is-expected-to-surge-significantly-due-to-the-requirement-for-data-storage-booming-laptop-market-and-digitalization-301255924.html>).
10. Moodera, J. S., Kinder, L. R., Wong, T. M. & Meservey, R. Large Magnetoresistance at Room Temperature in Ferromagnetic Thin Film Tunnel Junctions. *Physical Review Letters* **74**, 3273–3276 (1995).
11. Dieny, B., Prejbeanu, I. L., Garello, K., Gambardella, P., Freitas, P., Lehdorff, R., Raberg, W., Ebels, U., Demokritov, S. O., Akerman, J., Deac, A., Pirro, P., Adelman, C., Anane, A., Chumak, A. V., Hirohata, A., Mangin, S., Valenzuela, S. O., Onbaşlı, M. C., d'Aquino, M., Prenat, G., Finocchio, G., Lopez-Diaz, L., Chantrell, R., Chubykalo-Fesenko, O. & Bortolotti, P. Opportunities and challenges for spintronics in the microelectronics industry. *Nature Electronics* **3**, 446–459 (2020).
12. Berry, M. V. & Geim, A. K. Of flying frogs and levitrons. *European Journal of Physics* **18**, 307–313 (1997).

13. Novoselov, K. S., Geim, A. K., Morozov, S. V., Jiang, D., Zhang, Y., Dubonos, S. V., Grigorieva, I. V. & Firsov, A. A. Electric Field Effect in Atomically Thin Carbon Films. *Science* **306**, 666–669 (2004).
14. Novoselov, K. S., Geim, A. K., Morozov, S. V., Jiang, D., Katsnelson, M. I., Grigorieva, I. V., Dubonos, S. V. & Firsov, A. A. Two-dimensional gas of massless Dirac fermions in graphene. *Nature* **438**, 197–200 (2005).
15. Mas-Ballesté, R., Gómez-Navarro, C., Gómez-Herrero, J. & Zamora, F. 2D materials: to graphene and beyond. *Nanoscale* **3**, 20–30 (2011).
16. Novoselov, K. S., Mishchenko, A., Carvalho, A. & Neto, A. H. C. 2D materials and van der Waals heterostructures. *Science* **353**, aac9439 (2016).
17. Han, W., Kawakami, R. K., Gmitra, M. & Fabian, J. Graphene spintronics. *Nature Nanotechnology* **9**, 794–807 (2014).
18. Lin, X., Yang, W., Wang, K. L. & Zhao, W. Two-dimensional spintronics for low-power electronics. *Nature Electronics* **2**, 274 (2019).
19. Blundell, S. *Magnetism in Condensed Matter*. (Oxford University Press, 2001).
20. Xiao, D., Yao, W. & Niu, Q. Valley-Contrasting Physics in Graphene: Magnetic Moment and Topological Transport. *Physical Review Letters* **99**, 236809 (2007).
21. Sierra, J. F., Fabian, J., Kawakami, R. K., Roche, S. & Valenzuela, S. O. Van der Waals heterostructures for spintronics and opto-spintronics. *Nature Nanotechnology* 1–13 (2021).
22. Rojas-Sánchez, J. C., Vila, L., Desfonds, G., Gambarelli, S., Attané, J. P., Teresa, J. M. D., Magén, C. & Fert, A. Spin-to-charge conversion using Rashba coupling at the interface between non-magnetic materials. *Nature Communications* **4**, 2944 (2013).
23. Luo, Y. K., Xu, J., Zhu, T., Wu, G., McCormick, E. J., Zhan, W., Neupane, M. R. & Kawakami, R. K. Opto-Valleytronic Spin Injection in Monolayer MoS₂/Few-Layer Graphene Hybrid Spin Valves. *Nano Letters* **17**, 3877–3883 (2017).
24. Xiao, D., Liu, G.-B., Feng, W., Xu, X. & Yao, W. Coupled Spin and Valley Physics in Monolayers of MoS₂ and Other Group-VI Dichalcogenides. *Physical Review Letters* **108**, 196802 (2012).
25. Xu, X., Yao, W., Xiao, D. & Heinz, T. F. Spin and pseudospins in layered transition metal dichalcogenides. *Nature Physics* **10**, 343–350 (2014).
26. Cao, T., Wang, G., Han, W., Ye, H., Zhu, C., Shi, J., Niu, Q., Tan, P., Wang, E., Liu, B. & Feng, J. Valley-selective circular dichroism of monolayer molybdenum disulfide. *Nature Communications* **3**, 887 (2012).
27. Zeng, H., Dai, J., Yao, W., Xiao, D. & Cui, X. Valley polarization in MoS₂ monolayers by optical pumping. *Nature Nanotechnology* **7**, 490–493 (2012).
28. Mak, K. F., He, K., Shan, J. & Heinz, T. F. Control of valley polarization in monolayer MoS₂ by optical helicity. *Nature Nanotechnology* **7**, 494–498 (2012).
29. Yuan, H., Wang, X., Lian, B., Zhang, H., Fang, X., Shen, B., Xu, G., Xu, Y., Zhang, S.-C., Hwang, H. Y. & Cui, Y. Generation and electric control of spin-valley-coupled circular photogalvanic current in WSe₂. *Nature Nanotechnology* **9**, 851–857 (2014).

30. Allain, A., Kang, J., Banerjee, K. & Kis, A. Electrical contacts to two-dimensional semiconductors. *Nature Materials* **14**, 1195–1205 (2015).
31. Gmitra, M., Kochan, D. & Fabian, J. Spin-Orbit Coupling in Hydrogenated Graphene. *Physical Review Letters* **110**, 246602 (2013).
32. Garcia, J. H., Vila, M., Cummings, A. W. & Roche, S. Spin transport in graphene/transition metal dichalcogenide heterostructures. *Chemical Society Reviews* **47**, 3359–3379 (2018).
33. Gmitra, M., Kochan, D., Högl, P. & Fabian, J. Trivial and inverted Dirac bands and the emergence of quantum spin Hall states in graphene on transition-metal dichalcogenides. *Physical Review B* **93**, 155104 (2016).
34. Mott, N. F. & Fowler, R. H. The electrical conductivity of transition metals. *Proceedings of the Royal Society of London. Series A - Mathematical and Physical Sciences* **153**, 699–717 (1936).
35. Yafet, Y. g Factors and Spin-Lattice Relaxation of Conduction Electrons. in *Solid State Physics* (eds. Seitz, F. & Turnbull, D.) **14**, 1–98 (Academic Press, 1963).
36. Elliott, R. J. Theory of the Effect of Spin-Orbit Coupling on Magnetic Resonance in Some Semiconductors. *Physical Review* **96**, 266–279 (1954).
37. Dyakonov, M. I. & Perel, V. I. Spin relaxation of conduction electrons in noncentrosymmetric semiconductors. *Soviet Physics Solid State* **13**, 3023–3026 (1972).
38. Liu, X., Liu, X.-J. & Sinova, J. Spin dynamics in the strong spin-orbit coupling regime. *Physical Review B* **84**, 035318 (2011).
39. Datta, S. & Das, B. Electronic analog of the electro-optic modulator. *Applied Physics Letters* **56**, 665–667 (1990).
40. Huertas-Hernando, D., Guinea, F. & Brataas, A. Spin-Orbit-Mediated Spin Relaxation in Graphene. *Physical Review Letters* **103**, 146801 (2009).
41. Ochoa, H., Castro Neto, A. H. & Guinea, F. Elliot-Yafet Mechanism in Graphene. *Physical Review Letters* **108**, 206808 (2012).
42. Tombros, N., Tanabe, S., Veligura, A., Jozsa, C., Popinciuc, M., Jonkman, H. T. & van Wees, B. J. Anisotropic Spin Relaxation in Graphene. *Physical Review Letters* **101**, 046601 (2008).
43. Han, W. & Kawakami, R. K. Spin Relaxation in Single-Layer and Bilayer Graphene. *Physical Review Letters* **107**, 047207 (2011).
44. Yang, T.-Y., Balakrishnan, J., Volmer, F., Avsar, A., Jaiswal, M., Samm, J., Ali, S. R., Pachoud, A., Zeng, M., Popinciuc, M., Güntherodt, G., Beschoten, B. & Özyilmaz, B. Observation of Long Spin-Relaxation Times in Bilayer Graphene at Room Temperature. *Physical Review Letters* **107**, 047206 (2011).
45. Khokhriakov, D., Karpiak, B., Hoque, A. Md., Zhao, B., Parui, S. & Dash, S. P. Robust Spin Interconnect with Isotropic Spin Dynamics in Chemical Vapor Deposited Graphene Layers and Boundaries. *ACS Nano* **14**, 15864–15873 (2020).
46. Maassen, T., Dejene, F. K., Guimarães, M. H. D., Józsa, C. & van Wees, B. J. Comparison between charge and spin transport in few-layer graphene. *Physical Review B* **83**, 115410 (2011).

47. Zomer, P. J., Guimarães, M. H. D., Tombros, N. & van Wees, B. J. Long-distance spin transport in high-mobility graphene on hexagonal boron nitride. *Physical Review B* **86**, 161416 (2012).
48. Heisenberg, W. Zur Theorie des Ferromagnetismus. *Zeitschrift für Physik* **49**, 619–636 (1928).
49. Crooker, S. A., Furis, M., Lou, X., Adelman, C., Smith, D. L., Palmstrøm, C. J. & Crowell, P. A. Imaging Spin Transport in Lateral Ferromagnet/Semiconductor Structures. *Science* **309**, 2191–2195 (2005).
50. Jedema, F. J. *Electrical spin injection in metallic mesoscopic spin valves*. (Materials Science Centre, 2002).
51. Jedema, F. J., Heersche, H. B., Filip, A. T., Baselmans, J. J. A. & van Wees, B. J. Electrical detection of spin precession in a metallic mesoscopic spin valve. *Nature* **416**, 713–716 (2002).
52. Johnson, M. & Silsbee, R. H. Calculation of nonlocal baseline resistance in a quasi-one-dimensional wire. *Physical Review B* **76**, 153107 (2007).
53. Bakker, F. L., Slachter, A., Adam, J.-P. & van Wees, B. J. Interplay of Peltier and Seebeck Effects in Nanoscale Nonlocal Spin Valves. *Physical Review Letters* **105**, 136601 (2010).
54. Volmer, F., Drögeler, M., Pohlmann, T., Güntherodt, G., Stampfer, C. & Beschoten, B. Contact-induced charge contributions to non-local spin transport measurements in Co/MgO/graphene devices. *2D Materials* **2**, 024001 (2015).
55. Jedema, F. J., Filip, A. T. & van Wees, B. J. Electrical spin injection and accumulation at room temperature in an all-metal mesoscopic spin valve. *Nature* **410**, 345–348 (2001).
56. Aronov, A. G. Spin injection in metals and polarization of nuclei. *Pis'ma Zh. Eksp. Teor. Fiz.* **24**, 37 (1976).
57. Johnson, M. & Silsbee, R. H. Interfacial charge-spin coupling: Injection and detection of spin magnetization in metals. *Physical Review Letters* **55**, 1790–1793 (1985).
58. Bass, J. & Pratt, W. P. Spin-diffusion lengths in metals and alloys, and spin-flipping at metal/metal interfaces: an experimentalist's critical review. *Journal of Physics: Condensed Matter* **19**, 183201 (2007).
59. Hill, E. W., Geim, A. K., Novoselov, K., Schedin, F. & Blake, P. Graphene Spin Valve Devices. *IEEE Transactions on Magnetics* **42**, 2694–2696 (2006).
60. Tombros, N., Jozsa, C., Popinciuc, M., Jonkman, H. T. & van Wees, B. J. Electronic spin transport and spin precession in single graphene layers at room temperature. *Nature* **448**, 571–574 (2007).
61. Han, W., Pi, K., McCreary, K. M., Li, Y., Wong, J. J. I., Swartz, A. G. & Kawakami, R. K. Tunneling Spin Injection into Single Layer Graphene. *Physical Review Letters* **105**, 167202 (2010).
62. Rashba, E. I. Theory of electrical spin injection: Tunnel contacts as a solution of the conductivity mismatch problem. *Physical Review B* **62**, R16267–R16270 (2000).

63. Schmidt, G., Ferrand, D., Molenkamp, L. W., Filip, A. T. & van Wees, B. J. Fundamental obstacle for electrical spin injection from a ferromagnetic metal into a diffusive semiconductor. *Physical Review B* **62**, R4790–R4793 (2000).
64. Drögeler, M., Volmer, F., Wolter, M., Terrés, B., Watanabe, K., Taniguchi, T., Güntherodt, G., Stampfer, C. & Beschoten, B. Nanosecond Spin Lifetimes in Single- and Few-Layer Graphene–hBN Heterostructures at Room Temperature. *Nano Letters* **14**, 6050–6055 (2014).
65. Gurram, M., Omar, S. & van Wees, B. J. Bias induced up to 100% spin-injection and detection polarizations in ferromagnet/bilayer-hBN/graphene/hBN heterostructures. *Nature Communications* **8**, (2017).
66. Singh, S., Katoch, J., Zhu, T., Wu, R. J., Ahmed, A. S., Amamou, W., Wang, D., Mkhoyan, K. A. & Kawakami, R. K. Strontium Oxide Tunnel Barriers for High Quality Spin Transport and Large Spin Accumulation in Graphene. *Nano Letters* **17**, 7578–7585 (2017).
67. Slachter, A., Bakker, F. L., Adam, J.-P. & van Wees, B. J. Thermally driven spin injection from a ferromagnet into a non-magnetic metal. *Nature Physics* **6**, 879–882 (2010).
68. Flipse, J., Bakker, F. L., Slachter, A., Dejene, F. K. & van Wees, B. J. Direct observation of the spin-dependent Peltier effect. *Nature Nanotechnology* **7**, 166–168 (2012).
69. Ando, K. Dynamical generation of spin currents. *Semiconductor Science and Technology* **29**, 043002 (2014).
70. Ralph, D. C. & Stiles, M. D. Spin transfer torques. *Journal of Magnetism and Magnetic Materials* **320**, 1190–1216 (2008).
71. Ghiasi, T. S., Ingla-Aynés, J., Kaverzin, A. A. & van Wees, B. J. Large Proximity-Induced Spin Lifetime Anisotropy in Transition-Metal Dichalcogenide/Graphene Heterostructures. *Nano Letters* **17**, 7528–7532 (2017).
72. Villamor, E., Hueso, L. E. & Casanova, F. Effect of the interface resistance in non-local Hanle measurements. *Journal of Applied Physics* **117**, 223911 (2015).
73. Ingla-Aynés, J., Meijerink, R. J. & Wees, B. J. van. Eighty-Eight Percent Directional Guiding of Spin Currents with 90 μm Relaxation Length in Bilayer Graphene Using Carrier Drift. *Nano Letters* **16**, 4825–4830 (2016).
74. Sierra, J. F., Neumann, I., Cuppens, J., Raes, B., Costache, M. V. & Valenzuela, S. O. Thermoelectric spin voltage in graphene. *Nature Nanotechnology* **13**, 107–111 (2018).
75. Hall, E. H. On a new action of the magnet on electric currents. *American Journal of Science* **s3-19**, 200–205 (1880).
76. Karplus, R. & Luttinger, J. M. Hall Effect in Ferromagnetics. *Physical Review* **95**, 1154–1160 (1954).
77. Dyakonov, M. I. & Perel, V. I. Current-induced spin orientation of electrons in semiconductors. *Physics Letters A* **35**, 459–460 (1971).
78. Hirsch, J. E. Spin Hall Effect. *Physical Review Letters* **83**, 1834–1837 (1999).

79. Berry, M. V. Quantal phase factors accompanying adiabatic changes. *Proceedings of the Royal Society of London. A. Mathematical and Physical Sciences* **392**, 45–57 (1984).
80. Sagasta, E., Omori, Y., Isasa, M., Gradhand, M., Hueso, L. E., Niimi, Y., Otani, Y. & Casanova, F. Tuning the spin Hall effect of Pt from the moderately dirty to the superclean regime. *Physical Review B* **94**, 060412 (2016).
81. Büttiker, M. Symmetry of electrical conduction. *IBM Journal of Research and Development* **32**, 317–334 (1988).
82. Kato, Y. K., Myers, R. C., Gossard, A. C. & Awschalom, D. D. Observation of the Spin Hall Effect in Semiconductors. *Science* **306**, 1910–1913 (2004).
83. Saitoh, E., Ueda, M., Miyajima, H. & Tataru, G. Conversion of spin current into charge current at room temperature: Inverse spin-Hall effect. *Applied Physics Letters* **88**, 182509 (2006).
84. Valenzuela, S. O. & Tinkham, M. Direct electronic measurement of the spin Hall effect. *Nature* **442**, 176–179 (2006).
85. Bychkov, Yu. A. & Rashba, E. I. Properties of a 2D electron gas with lifted spectrum degeneracy. *JETP Lett.* **39**, 78 (1984).
86. Edelstein, V. M. Spin polarization of conduction electrons induced by electric current in two-dimensional asymmetric electron systems. *Solid State Communications* **73**, 233–235 (1990).
87. Ganichev, S. D., Ivchenko, E. L., Bel'kov, V. V., Tarasenko, S. A., Sollinger, M., Weiss, D., Wegscheider, W. & Prettl, W. Spin-galvanic effect. *Nature* **417**, 153–156 (2002).
88. Silov, A. Yu., Blajnov, P. A., Wolter, J. H., Hey, R., Ploog, K. H. & Averkiev, N. S. Current-induced spin polarization at a single heterojunction. *Applied Physics Letters* **85**, 5929–5931 (2004).
89. Isasa, M., Martínez-Velarte, M. C., Villamor, E., Magén, C., Morellón, L., De Teresa, J. M., Ibarra, M. R., Vignale, G., Chulkov, E. V., Krasovskii, E. E., Hueso, L. E. & Casanova, F. Origin of inverse Rashba-Edelstein effect detected at the Cu/Bi interface using lateral spin valves. *Physical Review B* **93**, 014420 (2016).
90. Sanz-Fernández, C., Pham, V. T., Sagasta, E., Hueso, L. E., Tokatly, I. V., Casanova, F. & Bergeret, F. S. Quantification of interfacial spin-charge conversion in hybrid devices with a metal/insulator interface. *Applied Physics Letters* **117**, 142405 (2020).
91. Pham, V. T., Yang, H., Choi, W. Y., Marty, A., Groen, I., Chuvilin, A., Bergeret, F. S., Hueso, L. E., Tokatly, I. V. & Casanova, F. Large spin-charge interconversion induced by interfacial spin-orbit coupling in a highly conducting all-metallic system. *Physical Review B* **104**, 184410 (2021).
92. Rojas-Sánchez, J.-C., Oyarzún, S., Fu, Y., Marty, A., Vergnaud, C., Gambarelli, S., Vila, L., Jamet, M., Ohtsubo, Y., Taleb-Ibrahimi, A., Le Fèvre, P., Bertran, F., Reyren, N., George, J.-M. & Fert, A. Spin to Charge Conversion at Room Temperature by Spin Pumping into a New Type of Topological Insulator: α -Sn Films. *Physical Review Letters* **116**, 096602 (2016).

93. Lesne, E., Fu, Y., Oyarzun, S., Rojas-Sánchez, J. C., Vaz, D. C., Naganuma, H., Sicoli, G., Attané, J.-P., Jamet, M., Jacquet, E., George, J.-M., Barthélémy, A., Jaffrès, H., Fert, A., Bibes, M. & Vila, L. Highly efficient and tunable spin-to-charge conversion through Rashba coupling at oxide interfaces. *Nature Materials* **15**, 1261–1266 (2016).
94. Rojas-Sánchez, J.-C. & Fert, A. Compared Efficiencies of Conversions between Charge and Spin Current by Spin-Orbit Interactions in Two- and Three-Dimensional Systems. *Physical Review Applied* **11**, 054049 (2019).
95. Pham, V. T., Groen, I., Manipatruni, S., Choi, W. Y., Nikonov, D. E., Sagasta, E., Lin, C.-C., Gosavi, T. A., Marty, A., Hueso, L. E., Young, I. A. & Casanova, F. Spin-orbit magnetic state readout in scaled ferromagnetic/heavy metal nanostructures. *Nature Electronics* **3**, 309–315 (2020).
96. Manipatruni, S., Nikonov, D. E., Lin, C.-C., Gosavi, T. A., Liu, H., Prasad, B., Huang, Y.-L., Bonturim, E., Ramesh, R. & Young, I. A. Scalable energy-efficient magnetoelectric spin-orbit logic. *Nature* **565**, 35–42 (2019).
97. Sagasta, E., Omori, Y., Vélez, S., Llopis, R., Tollan, C., Chuvilin, A., Hueso, L. E., Gradhand, M., Otani, Y. & Casanova, F. Unveiling the mechanisms of the spin Hall effect in Ta. *Physical Review B* **98**, 060410 (2018).
98. Garcia, J. H., Cummings, A. W. & Roche, S. Spin Hall Effect and Weak Antilocalization in Graphene/Transition Metal Dichalcogenide Heterostructures. *Nano Letters* **17**, 5078–5083 (2017).
99. Offidani, M., Milletari, M., Raimondi, R. & Ferreira, A. Optimal Charge-to-Spin Conversion in Graphene on Transition-Metal Dichalcogenides. *Physical Review Letters* **119**, 196801 (2017).
100. Manipatruni, S., Nikonov, D. E. & Young, I. A. Beyond CMOS computing with spin and polarization. *Nature Physics* **14**, 338–343 (2018).
101. Harris, P. J. F. Transmission Electron Microscopy of Carbon: A Brief History. *C - Journal of Carbon Research* **4**, 4 (2018).
102. Lloyd-Hughes, J. & Jeon, T.-I. A Review of the Terahertz Conductivity of Bulk and Nano-Materials. *Journal of Infrared, Millimeter, and Terahertz Waves* **33**, 871–925 (2012).
103. Dresselhaus, G. & Dresselhaus, M. S. Spin-Orbit Interaction in Graphite. *Physical Review* **140**, A401–A412 (1965).
104. Mermin, N. D. Crystalline Order in Two Dimensions. *Physical Review* **176**, 250–254 (1968).
105. Semenov, G. W. Condensed-Matter Simulation of a Three-Dimensional Anomaly. *Physical Review Letters* **53**, 2449–2452 (1984).
106. Geim, A. K. & Novoselov, K. S. The rise of graphene. *Nature Materials* **6**, 183–191 (2007).
107. Zhang, Y., Tang, T.-T., Girit, C., Hao, Z., Martin, M. C., Zettl, A., Crommie, M. F., Shen, Y. R. & Wang, F. Direct observation of a widely tunable bandgap in bilayer graphene. *Nature* **459**, 820–823 (2009).

108. Castro Neto, A. H., Guinea, F., Peres, N. M. R., Novoselov, K. S. & Geim, A. K. The electronic properties of graphene. *Reviews of Modern Physics* **81**, 109–162 (2009).
109. Zhan, B., Li, C., Yang, J., Jenkins, G., Huang, W. & Dong, X. Graphene Field-Effect Transistor and Its Application for Electronic Sensing. *Small* **10**, 4042–4065 (2014).
110. Novoselov, K. S., Jiang, Z., Zhang, Y., Morozov, S. V., Stormer, H. L., Zeitler, U., Maan, J. C., Boebinger, G. S., Kim, P. & Geim, A. K. Room-Temperature Quantum Hall Effect in Graphene. *Science* **315**, 1379–1379 (2007).
111. Chen, J.-H., Jang, C., Xiao, S., Ishigami, M. & Fuhrer, M. S. Intrinsic and extrinsic performance limits of graphene devices on SiO₂. *Nature Nanotechnology* **3**, 206–209 (2008).
112. Meyer, J. C., Geim, A. K., Katsnelson, M. I., Novoselov, K. S., Booth, T. J. & Roth, S. The structure of suspended graphene sheets. *Nature* **446**, 60–63 (2007).
113. Du, X., Skachko, I., Barker, A. & Andrei, E. Y. Approaching ballistic transport in suspended graphene. *Nature Nanotechnology* **3**, 491–495 (2008).
114. Bolotin, K. I., Sikes, K. J., Jiang, Z., Klima, M., Fudenberg, G., Hone, J., Kim, P. & Stormer, H. L. Ultrahigh electron mobility in suspended graphene. *Solid State Communications* **146**, 351–355 (2008).
115. Dean, C. R., Young, A. F., Meric, I., Lee, C., Wang, L., Sorgenfrei, S., Watanabe, K., Taniguchi, T., Kim, P., Shepard, K. L. & Hone, J. Boron nitride substrates for high-quality graphene electronics. *Nature Nanotechnology* **5**, 722–726 (2010).
116. Zomer, P. J., Guimarães, M. H. D., Brant, J. C., Tombros, N. & van Wees, B. J. Fast pick up technique for high quality heterostructures of bilayer graphene and hexagonal boron nitride. *Applied Physics Letters* **105**, 013101 (2014).
117. Kretinin, A. V., Cao, Y., Tu, J. S., Yu, G. L., Jalil, R., Novoselov, K. S., Haigh, S. J., Gholinia, A., Mishchenko, A., Lozada, M., Georgiou, T., Woods, C. R., Withers, F., Blake, P., Eda, G., Wirsig, A., Hucho, C., Watanabe, K., Taniguchi, T., Geim, A. K. & Gorbachev, R. V. Electronic Properties of Graphene Encapsulated with Different Two-Dimensional Atomic Crystals. *Nano Letters* **14**, 3270–3276 (2014).
118. Haigh, S. J., Gholinia, A., Jalil, R., Romani, S., Britnell, L., Elias, D. C., Novoselov, K. S., Ponomarenko, L. A., Geim, A. K. & Gorbachev, R. Cross-sectional imaging of individual layers and buried interfaces of graphene-based heterostructures and superlattices. *Nature Materials* **11**, 764–767 (2012).
119. Wang, L., Meric, I., Huang, P. Y., Gao, Q., Gao, Y., Tran, H., Taniguchi, T., Watanabe, K., Campos, L. M., Muller, D. A., Guo, J., Kim, P., Hone, J., Shepard, K. L. & Dean, C. R. One-Dimensional Electrical Contact to a Two-Dimensional Material. *Science* **342**, 614–617 (2013).
120. Son, J., Kwon, J., Kim, S., Lv, Y., Yu, J., Lee, J.-Y., Ryu, H., Watanabe, K., Taniguchi, T., Garrido-Menacho, R., Mason, N., Ertekin, E., Huang, P. Y., Lee, G.-H. & M. van der Zande, A. Atomically precise graphene etch stops for three

- dimensional integrated systems from two dimensional material heterostructures. *Nature Communications* **9**, (2018).
121. Guimarães, M. H. D., Zomer, P. J., Ingla-Aynés, J., Brant, J. C., Tombros, N. & van Wees, B. J. Controlling Spin Relaxation in Hexagonal BN-Encapsulated Graphene with a Transverse Electric Field. *Physical Review Letters* **113**, 086602 (2014).
 122. Ingla-Aynés, J., Guimarães, M. H. D., Meijerink, R. J., Zomer, P. J. & van Wees, B. J. 24 μm spin relaxation length in boron nitride encapsulated bilayer graphene. *Physical Review B* **92**, 201410 (2015).
 123. Drögeler, M., Franzen, C., Volmer, F., Pohlmann, T., Banszerus, L., Wolter, M., Watanabe, K., Taniguchi, T., Stampfer, C. & Beschoten, B. Spin Lifetimes Exceeding 12 ns in Graphene Nonlocal Spin Valve Devices. *Nano Letters* **16**, 3533–3539 (2016).
 124. Gebeyehu, Z. M., Parui, S., Sierra, J. F., Timmermans, M., Esplandiu, M. J., Brems, S., Huyghebaert, C., Garello, K., Costache, M. V. & Valenzuela, S. O. Spin communication over 30 μm long channels of chemical vapor deposited graphene on SiO_2 . *2D Materials* **6**, 034003 (2019).
 125. Panda, J., Ramu, M., Karis, O., Sarkar, T. & Kamalakar, M. V. Ultimate Spin Currents in Commercial Chemical Vapor Deposited Graphene. *ACS Nano* **14**, 12771–12780 (2020).
 126. Li, X., Cai, W., An, J., Kim, S., Nah, J., Yang, D., Piner, R., Velamakanni, A., Jung, I., Tutuc, E., Banerjee, S. K., Colombo, L. & Ruoff, R. S. Large-Area Synthesis of High-Quality and Uniform Graphene Films on Copper Foils. *Science* **324**, 1312–1314 (2009).
 127. Petrone, N., Dean, C. R., Meric, I., van der Zande, A. M., Huang, P. Y., Wang, L., Muller, D., Shepard, K. L. & Hone, J. Chemical Vapor Deposition-Derived Graphene with Electrical Performance of Exfoliated Graphene. *Nano Letters* **12**, 2751–2756 (2012).
 128. Banszerus, L., Schmitz, M., Engels, S., Dauber, J., Oellers, M., Haupt, F., Watanabe, K., Taniguchi, T., Beschoten, B. & Stampfer, C. Ultrahigh-mobility graphene devices from chemical vapor deposition on reusable copper. *Science Advances* **1**, e1500222 (2015).
 129. Khokhriakov, D., Karpiak, B., Hoque, A. Md. & Dash, S. P. Two-dimensional spintronic circuit architectures on large scale graphene. *Carbon* **161**, 892–899 (2020).
 130. Cummings, A. W., Dubois, S. M.-M., Charlier, J.-C. & Roche, S. Universal Spin Diffusion Length in Polycrystalline Graphene. *Nano Letters* **19**, 7418–7426 (2019).
 131. Bae, S., Kim, H., Lee, Y., Xu, X., Park, J.-S., Zheng, Y., Balakrishnan, J., Lei, T., Ri Kim, H., Song, Y. I., Kim, Y.-J., Kim, K. S., Özyilmaz, B., Ahn, J.-H., Hong, B. H. & Iijima, S. Roll-to-roll production of 30-inch graphene films for transparent electrodes. *Nature Nanotechnology* **5**, 574–578 (2010).

132. Hirsch, A. The Graphene Flagship—A Giant European Research Project. *Angewandte Chemie International Edition* **54**, 9132–9133 (2015).
133. Berger, C., Song, Z., Li, X., Wu, X., Brown, N., Naud, C., Mayou, D., Li, T., Hass, J., Marchenkov, A. N., Conrad, E. H., First, P. N. & Heer, W. A. de. Electronic Confinement and Coherence in Patterned Epitaxial Graphene. *Science* **312**, 1191–1196 (2006).
134. Dlubak, B., Martin, M.-B., Deranlot, C., Servet, B., Xavier, S., Mattana, R., Sprinkle, M., Berger, C., De Heer, W. A., Petroff, F., Anane, A., Seneor, P. & Fert, A. Highly efficient spin transport in epitaxial graphene on SiC. *Nature Physics* **8**, 557–561 (2012).
135. Chaves, A., Azadani, J. G., Alsalman, H., da Costa, D. R., Frisenda, R., Chaves, A. J., Song, S. H., Kim, Y. D., He, D., Zhou, J., Castellanos-Gomez, A., Peeters, F. M., Liu, Z., Hinkle, C. L., Oh, S.-H., Ye, P. D., Koester, S. J., Lee, Y. H., Avouris, P., Wang, X. & Low, T. Bandgap engineering of two-dimensional semiconductor materials. *npj 2D Materials and Applications* **4**, 29 (2020).
136. Jariwala, D., Sangwan, V. K., Lauhon, L. J., Marks, T. J. & Hersam, M. C. Emerging Device Applications for Semiconducting Two-Dimensional Transition Metal Dichalcogenides. *ACS Nano* **8**, 1102–1120 (2014).
137. Kośmider, K., González, J. W. & Fernández-Rossier, J. Large spin splitting in the conduction band of transition metal dichalcogenide monolayers. *Physical Review B* **88**, 245436 (2013).
138. Zhu, Z. Y., Cheng, Y. C. & Schwingenschlögl, U. Giant spin-orbit-induced spin splitting in two-dimensional transition-metal dichalcogenide semiconductors. *Physical Review B* **84**, 153402 (2011).
139. Latzke, D. W., Zhang, W., Suslu, A., Chang, T.-R., Lin, H., Jeng, H.-T., Tongay, S., Wu, J., Bansil, A. & Lanzara, A. Electronic structure, spin-orbit coupling, and interlayer interaction in bulk MoS₂ and WS₂. *Physical Review B* **91**, 235202 (2015).
140. Le, D., Barinov, A., Preciado, E., Isarraraz, M., Tanabe, I., Komesu, T., Troha, C., Bartels, L., Rahman, T. S. & Dowben, P. A. Spin–orbit coupling in the band structure of monolayer WSe₂. *Journal of Physics: Condensed Matter* **27**, 182201 (2015).
141. Mak, K. F., McGill, K. L., Park, J. & McEuen, P. L. The valley Hall effect in MoS₂ transistors. *Science* **344**, 1489–1492 (2014).
142. Lee, J., Wang, Z., Xie, H., Mak, K. F. & Shan, J. Valley magnetoelectricity in single-layer MoS₂. *Nature Materials* **16**, 887–891 (2017).
143. Han, G. H., Duong, D. L., Keum, D. H., Yun, S. J. & Lee, Y. H. van der Waals Metallic Transition Metal Dichalcogenides. *Chemical Reviews* **118**, 6297–6336 (2018).
144. Frindt, R. F. Superconductivity in Ultrathin NbSe₂ Layers. *Physical Review Letters* **28**, 299–301 (1972).

145. Xi, X., Wang, Z., Zhao, W., Park, J.-H., Law, K. T., Berger, H., Forró, L., Shan, J. & Mak, K. F. Ising pairing in superconducting NbSe₂ atomic layers. *Nature Physics* **12**, 139–143 (2016).
146. Yabuki, N., Moriya, R., Arai, M., Sata, Y., Morikawa, S., Masubuchi, S. & Machida, T. Supercurrent in van der Waals Josephson junction. *Nature Communications* **7**, 10616 (2016).
147. Yan, W., Txoperena, O., Llopis, R., Dery, H., Hueso, L. E. & Casanova, F. A two-dimensional spin field-effect switch. *Nature Communications* **7**, 13372 (2016).
148. Dankert, A. & Dash, S. P. Electrical gate control of spin current in van der Waals heterostructures at room temperature. *Nature Communications* **8**, 16093 (2017).
149. Debashis, P., Hung, T. Y. T. & Chen, Z. Monolayer WSe₂ induced giant enhancement in the spin Hall efficiency of Tantalum. *npj 2D Materials and Applications* **4**, 18 (2020).
150. Shao, Q., Yu, G., Lan, Y.-W., Shi, Y., Li, M.-Y., Zheng, C., Zhu, X., Li, L.-J., Amiri, P. K. & Wang, K. L. Strong Rashba-Edelstein Effect-Induced Spin–Orbit Torques in Monolayer Transition Metal Dichalcogenide/Ferromagnet Bilayers. *Nano Letters* **16**, 7514–7520 (2016).
151. MacNeill, D., Stiehl, G. M., Guimaraes, M. H. D., Buhrman, R. A., Park, J. & Ralph, D. C. Control of spin–orbit torques through crystal symmetry in WTe₂/ferromagnet bilayers. *Nature Physics* **13**, 300–305 (2017).
152. Xie, Q., Lin, W., Sarkar, S., Shu, X., Chen, S., Liu, L., Zhao, T., Zhou, C., Wang, H., Zhou, J., Gradečak, S. & Chen, J. Field-free magnetization switching induced by the unconventional spin–orbit torque from WTe₂. *APL Materials* **9**, 051114 (2021).
153. Culcer, D. & Winkler, R. Generation of Spin Currents and Spin Densities in Systems with Reduced Symmetry. *Physical Review Letters* **99**, 226601 (2007).
154. Roy, A., Guimarães, M. H. D. & Ślawińska, J. Unconventional spin Hall effects in nonmagnetic solids. *arXiv:2110.09242 [cond-mat]* (2021).
155. Ochoa, H. & Roldán, R. Spin-orbit-mediated spin relaxation in monolayer MoS₂. *Physical Review B* **87**, 245421 (2013).
156. Song, Y. & Dery, H. Transport Theory of Monolayer Transition-Metal Dichalcogenides through Symmetry. *Physical Review Letters* **111**, 026601 (2013).
157. Yang, L., Sinitsyn, N. A., Chen, W., Yuan, J., Zhang, J., Lou, J. & Crooker, S. A. Long-lived nanosecond spin relaxation and spin coherence of electrons in monolayer MoS₂ and WS₂. *Nature Physics* **11**, 830–834 (2015).
158. Chen, P., Zhang, Z., Duan, X. & Duan, X. Chemical synthesis of two-dimensional atomic crystals, heterostructures and superlattices. *Chemical Society Reviews* **47**, 3129–3151 (2018).
159. Shim, J., Bae, S.-H., Kong, W., Lee, D., Qiao, K., Nezich, D., Park, Y. J., Zhao, R., Sundaram, S., Li, X., Yeon, H., Choi, C., Kum, H., Yue, R., Zhou, G., Ou, Y., Lee, K., Moodera, J., Zhao, X., Ahn, J.-H., Hinkle, C., Ougazzaden, A. & Kim, J. Controlled crack propagation for atomic precision handling of wafer-scale two-dimensional materials. *Science* **362**, 665–670 (2018).

160. Cui, X., Lee, G.-H., Kim, Y. D., Arefe, G., Huang, P. Y., Lee, C.-H., Chenet, D. A., Zhang, X., Wang, L., Ye, F., Pizzocchero, F., Jessen, B. S., Watanabe, K., Taniguchi, T., Muller, D. A., Low, T., Kim, P. & Hone, J. Multi-terminal transport measurements of MoS₂ using a van der Waals heterostructure device platform. *Nature Nanotechnology* **10**, 534–540 (2015).
161. Pacilé, D., Meyer, J. C., Girit, Ç. Ö. & Zettl, A. The two-dimensional phase of boron nitride: Few-atomic-layer sheets and suspended membranes. *Applied Physics Letters* **92**, 133107 (2008).
162. Scavuzzo, A., Mangel, S., Park, J.-H., Lee, S., Loc Duong, D., Strelow, C., Mews, A., Burghard, M. & Kern, K. Electrically tunable quantum emitters in an ultrathin graphene–hexagonal boron nitride van der Waals heterostructure. *Applied Physics Letters* **114**, 062104 (2019).
163. Li, L., Yu, Y., Ye, G. J., Ge, Q., Ou, X., Wu, H., Feng, D., Chen, X. H. & Zhang, Y. Black phosphorus field-effect transistors. *Nature Nanotechnology* **9**, 372–377 (2014).
164. Li, L., Ye, G. J., Tran, V., Fei, R., Chen, G., Wang, H., Wang, J., Watanabe, K., Taniguchi, T., Yang, L., Chen, X. H. & Zhang, Y. Quantum oscillations in a two-dimensional electron gas in black phosphorus thin films. *Nature Nanotechnology* **10**, 608–613 (2015).
165. Avsar, A., Tan, J. Y., Kurpas, M., Gmitra, M., Watanabe, K., Taniguchi, T., Fabian, J. & Özyilmaz, B. Gate-tunable black phosphorus spin valve with nanosecond spin lifetimes. *Nature Physics* **13**, 888–893 (2017).
166. Mak, K. F., Shan, J. & Ralph, D. C. Probing and controlling magnetic states in 2D layered magnetic materials. *Nature Reviews Physics* **1**, 646–661 (2019).
167. Fei, Z., Huang, B., Malinowski, P., Wang, W., Song, T., Sanchez, J., Yao, W., Xiao, D., Zhu, X., May, A. F., Wu, W., Cobden, D. H., Chu, J.-H. & Xu, X. Two-dimensional itinerant ferromagnetism in atomically thin Fe₃GeTe₂. *Nature Materials* **17**, 778–782 (2018).
168. Gong, C., Li, L., Li, Z., Ji, H., Stern, A., Xia, Y., Cao, T., Bao, W., Wang, C., Wang, Y., Qiu, Z. Q., Cava, R. J., Louie, S. G., Xia, J. & Zhang, X. Discovery of intrinsic ferromagnetism in two-dimensional van der Waals crystals. *Nature* **546**, 265–269 (2017).
169. Huang, B., Clark, G., Navarro-Moratalla, E., Klein, D. R., Cheng, R., Seyler, K. L., Zhong, D., Schmidgall, E., McGuire, M. A., Cobden, D. H., Yao, W., Xiao, D., Jarillo-Herrero, P. & Xu, X. Layer-dependent ferromagnetism in a van der Waals crystal down to the monolayer limit. *Nature* **546**, 270–273 (2017).
170. Li, H., Ruan, S. & Zeng, Y.-J. Intrinsic Van Der Waals Magnetic Materials from Bulk to the 2D Limit: New Frontiers of Spintronics. *Advanced Materials* **31**, 1900065 (2019).
171. Huang, B., McGuire, M. A., May, A. F., Xiao, D., Jarillo-Herrero, P. & Xu, X. Emergent phenomena and proximity effects in two-dimensional magnets and heterostructures. *Nature Materials* **19**, 1276–1289 (2020).

172. Dolui, K., Petrović, M. D., Zollner, K., Plecháč, P., Fabian, J. & Nikolić, B. K. Proximity Spin–Orbit Torque on a Two-Dimensional Magnet within van der Waals Heterostructure: Current-Driven Antiferromagnet-to-Ferromagnet Reversible Nonequilibrium Phase Transition in Bilayer CrI₃. *Nano Letters* **20**, 2288–2295 (2020).
173. Shin, I., Cho, W. J., An, E.-S., Park, S., Jeong, H.-W., Baek, W. J., Park, S. Y., Yang, D.-H., Seo, J. H., Ali, M. N., Choi, S.-Y., Lee, H.-W., Kim, J. S., Kim, S. & Lee, G.-H. Spin-orbit Torque Switching in an All-Van der Waals Heterostructure. *arXiv:2102.09300 [cond-mat]* (2021).
174. Kao, I.-H., Muzzio, R., Zhang, H., Zhu, M., Gobbo, J., Weber, D., Rao, R., Li, J., Edgar, J. H., Goldberger, J. E., Yan, J., Mandrus, D. G., Hwang, J., Cheng, R., Katoch, J. & Singh, S. Field-free deterministic switching of a perpendicularly polarized magnet using unconventional spin-orbit torques in WTe₂. *arXiv:2012.12388 [cond-mat]* (2020).
175. Zhao, B., Ngaley, R., Hoque, A. M., Karpiak, B., Khokhriakov, D. & Dash, S. P. Van der Waals Magnet based Spin-Valve Devices at Room Temperature. *arXiv:2107.00310 [cond-mat]* (2021).
176. Li, D., Chen, M., Sun, Z., Yu, P., Liu, Z., Ajayan, P. M. & Zhang, Z. Two-dimensional non-volatile programmable p–n junctions. *Nature Nanotechnology* **12**, 901–906 (2017).
177. Withers, F., Del Pozo-Zamudio, O., Mishchenko, A., Rooney, A. P., Gholinia, A., Watanabe, K., Taniguchi, T., Haigh, S. J., Geim, A. K., Tartakovskii, A. I. & Novoselov, K. S. Light-emitting diodes by band-structure engineering in van der Waals heterostructures. *Nature Materials* **14**, 301–306 (2015).
178. Liang, S.-J., Cheng, B., Cui, X. & Miao, F. Van der Waals Heterostructures for High-Performance Device Applications: Challenges and Opportunities. *Advanced Materials* **32**, 1903800 (2020).
179. Žutić, I., Matos-Abiague, A., Scharf, B., Dery, H. & Belashchenko, K. Proximitized materials. *Materials Today* (2018).
180. McMillan, W. L. Tunneling Model of the Superconducting Proximity Effect. *Physical Review* **175**, 537–542 (1968).
181. Titov, M. & Beenakker, C. W. J. Josephson effect in ballistic graphene. *Physical Review B* **74**, 041401 (2006).
182. Gmitra, M. & Fabian, J. Graphene on transition-metal dichalcogenides: A platform for proximity spin-orbit physics and optospintronics. *Physical Review B* **92**, 155403 (2015).
183. Frank, T., Högl, P., Gmitra, M., Kochan, D. & Fabian, J. Protected Pseudohelical Edge States in Z₂-Trivial Proximitized Graphene. *Physical Review Letters* **120**, 156402 (2018).
184. Island, J. O., Cui, X., Lewandowski, C., Khoo, J. Y., Spanton, E. M., Zhou, H., Rhodes, D., Hone, J. C., Taniguchi, T., Watanabe, K., Levitov, L. S., Zaletel, M. P. & Young, A. F. Spin–orbit-driven band inversion in bilayer graphene by the van der Waals proximity effect. *Nature* **571**, 85 (2019).

185. Cummings, A. W., Garcia, J. H., Fabian, J. & Roche, S. Giant Spin Lifetime Anisotropy in Graphene Induced by Proximity Effects. *Physical Review Letters* **119**, 206601 (2017).
186. Raes, B., Scheerder, J. E., Costache, M. V., Bonell, F., Sierra, J. F., Cuppens, J., Vondel, J. V. de & Valenzuela, S. O. Determination of the spin-lifetime anisotropy in graphene using oblique spin precession. *Nature Communications* **7**, 11444 (2016).
187. Leutenantsmeyer, J. C., Ingla-Aynés, J., Fabian, J. & van Wees, B. J. Observation of Spin-Valley-Coupling-Induced Large Spin-Lifetime Anisotropy in Bilayer Graphene. *Physical Review Letters* **121**, 127702 (2018).
188. Benítez, L. A., Sierra, J. F., Saverio Torres, W., Arrighi, A., Bonell, F., Costache, M. V. & Valenzuela, S. O. Strongly anisotropic spin relaxation in graphene–transition metal dichalcogenide heterostructures at room temperature. *Nature Physics* **14**, 303–308 (2018).
189. Wang, Z., Ki, D.-K., Khoo, J. Y., Mauro, D., Berger, H., Levitov, L. S. & Morpurgo, A. F. Origin and Magnitude of ‘Designer’ Spin-Orbit Interaction in Graphene on Semiconducting Transition Metal Dichalcogenides. *Physical Review X* **6**, 041020 (2016).
190. Yang, B., Lohmann, M., Barroso, D., Liao, I., Lin, Z., Liu, Y., Bartels, L., Watanabe, K., Taniguchi, T. & Shi, J. Strong electron-hole symmetric Rashba spin-orbit coupling in graphene/monolayer transition metal dichalcogenide heterostructures. *Physical Review B* **96**, 041409 (2017).
191. Wakamura, T., Reale, F., Palczynski, P., Zhao, M. Q., Johnson, A. T. C., Guéron, S., Mattevi, C., Ouerghi, A. & Bouchiat, H. Spin-orbit interaction induced in graphene by transition metal dichalcogenides. *Physical Review B* **99**, 245402 (2019).
192. Völkl, T., Rockinger, T., Drienovsky, M., Watanabe, K., Taniguchi, T., Weiss, D. & Eroms, J. Magnetotransport in heterostructures of transition metal dichalcogenides and graphene. *Physical Review B* **96**, 125405 (2017).
193. Zihlmann, S., Cummings, A. W., Garcia, J. H., Kedves, M., Watanabe, K., Taniguchi, T., Schönenberger, C. & Makk, P. Large spin relaxation anisotropy and valley-Zeeman spin-orbit coupling in WSe₂/graphene/h-BN heterostructures. *Physical Review B* **97**, 075434 (2018).
194. Wang, Z., Ki, D.-K., Chen, H., Berger, H., MacDonald, A. H. & Morpurgo, A. F. Strong interface-induced spin–orbit interaction in graphene on WS₂. *Nature Communications* **6**, 8339 (2015).
195. Yang, B., Tu, M.-F., Kim, J., Wu, Y., Wang, H., Alicea, J., Wu, R., Bockrath, M. & Shi, J. Tunable spin–orbit coupling and symmetry-protected edge states in graphene/WS₂. *2D Materials* **3**, 031012 (2016).
196. Wakamura, T., Reale, F., Palczynski, P., Guéron, S., Mattevi, C. & Bouchiat, H. Strong Anisotropic Spin-Orbit Interaction Induced in Graphene by Monolayer WS₂. *Physical Review Letters* **120**, 106802 (2018).

197. Milletari, M., Offidani, M., Ferreira, A. & Raimondi, R. Covariant Conservation Laws and the Spin Hall Effect in Dirac-Rashba Systems. *Physical Review Letters* **119**, 246801 (2017).
198. Ghiasi, T. S., Kaverzin, A. A., Blah, P. J. & van Wees, B. J. Charge-to-Spin Conversion by the Rashba–Edelstein Effect in Two-Dimensional van der Waals Heterostructures up to Room Temperature. *Nano Letters* **19**, 5959–5966 (2019).
199. Benítez, L. A., Savero Torres, W., Sierra, J. F., Timmermans, M., Garcia, J. H., Roche, S., Costache, M. V. & Valenzuela, S. O. Tunable room-temperature spin galvanic and spin Hall effects in van der Waals heterostructures. *Nature Materials* **19**, 170–175 (2020).
200. Lazić, P., Belashchenko, K. D. & Žutić, I. Effective gating and tunable magnetic proximity effects in two-dimensional heterostructures. *Physical Review B* **93**, 241401 (2016).
201. Zollner, K., Gmitra, M., Frank, T. & Fabian, J. Theory of proximity-induced exchange coupling in graphene on hBN/(Co, Ni). *Physical Review B* **94**, 155441 (2016).
202. Mendes, J. B. S., Alves Santos, O., Meireles, L. M., Lacerda, R. G., Vilela-Leão, L. H., Machado, F. L. A., Rodríguez-Suárez, R. L., Azevedo, A. & Rezende, S. M. Spin-Current to Charge-Current Conversion and Magnetoresistance in a Hybrid Structure of Graphene and Yttrium Iron Garnet. *Physical Review Letters* **115**, 226601 (2015).
203. Wang, Z., Tang, C., Sachs, R., Barlas, Y. & Shi, J. Proximity-Induced Ferromagnetism in Graphene Revealed by the Anomalous Hall Effect. *Physical Review Letters* **114**, 016603 (2015).
204. Wei, P., Lee, S., Lemaitre, F., Pinel, L., Cutaia, D., Cha, W., Katmis, F., Zhu, Y., Heiman, D., Hone, J., Moodera, J. S. & Chen, C.-T. Strong interfacial exchange field in the graphene/EuS heterostructure. *Nature Materials* **15**, 711–716 (2016).
205. Leutenantsmeyer, J. C., Kaverzin, A. A., Wojtaszek, M. & Wees, B. J. van. Proximity induced room temperature ferromagnetism in graphene probed with spin currents. *2D Materials* **4**, 014001 (2017).
206. Wu, Y., Yin, G., Pan, L., Grutter, A. J., Pan, Q., Lee, A., Gilbert, D. A., Borchers, J. A., Ratcliff, W., Li, A., Han, X. & Wang, K. L. Large exchange splitting in monolayer graphene magnetized by an antiferromagnet. *Nature Electronics* **3**, 604–611 (2020).
207. Ghiasi, T. S., Kaverzin, A. A., Dismukes, A. H., de Wal, D. K., Roy, X. & van Wees, B. J. Electrical and thermal generation of spin currents by magnetic bilayer graphene. *Nature Nanotechnology* **16**, 788–794 (2021).
208. Zhao, C., Norden, T., Zhang, P., Zhao, P., Cheng, Y., Sun, F., Parry, J. P., Taheri, P., Wang, J., Yang, Y., Scrace, T., Kang, K., Yang, S., Miao, G., Sabirianov, R., Kioseoglou, G., Huang, W., Petrou, A. & Zeng, H. Enhanced valley splitting in monolayer WSe₂ due to magnetic exchange field. *Nature Nanotechnology* **12**, 757–762 (2017).

209. Zhong, D., Seyler, K. L., Linpeng, X., Cheng, R., Sivadas, N., Huang, B., Schmidgall, E., Taniguchi, T., Watanabe, K., McGuire, M. A., Yao, W., Xiao, D., Fu, K.-M. C. & Xu, X. Van der Waals engineering of ferromagnetic semiconductor heterostructures for spin and valleytronics. *Science Advances* **3**, e1603113 (2017).
210. Lohmann, M., Su, T., Niu, B., Hou, Y., Alghamdi, M., Aldosary, M., Xing, W., Zhong, J., Jia, S., Han, W., Wu, R., Cui, Y.-T. & Shi, J. Probing Magnetism in Insulating $\text{Cr}_2\text{Ge}_2\text{Te}_6$ by Induced Anomalous Hall Effect in Pt. *Nano Letters* **19**, 2397–2403 (2019).
211. Cao, Y., Fatemi, V., Fang, S., Watanabe, K., Taniguchi, T., Kaxiras, E. & Jarillo-Herrero, P. Unconventional superconductivity in magic-angle graphene superlattices. *Nature* **556**, 43–50 (2018).
212. Park, J. M., Cao, Y., Watanabe, K., Taniguchi, T. & Jarillo-Herrero, P. Tunable strongly coupled superconductivity in magic-angle twisted trilayer graphene. *Nature* **590**, 249–255 (2021).
213. David, A., Rakyta, P., Kormányos, A. & Burkard, G. Induced spin-orbit coupling in twisted graphene–transition metal dichalcogenide heterobilayers: Twistronics meets spintronics. *Physical Review B* **100**, 085412 (2019).
214. Li, Y. & Koshino, M. Twist-angle dependence of the proximity spin-orbit coupling in graphene on transition-metal dichalcogenides. *Physical Review B* **99**, 075438 (2019).
215. Pezo, A., Zanolli, Z., Wittemeier, N., Fazzio, A., Roche, S. & Garcia, J. H. A Twist for Tuning the Spin-orbit Coupling in Graphene/Transition Metal Dichalcogenide Heterobilayers. *arXiv:2011.06714v1 [cond-mat]* (2020).
216. Naimer, T., Zollner, K., Gmitra, M. & Fabian, J. Twist-angle dependent proximity induced spin-orbit coupling in graphene/transition-metal dichalcogenide heterostructures. *arXiv:2108.06126 [cond-mat]* (2021).
217. Alsharari, A. M., Asmar, M. M. & Ulloa, S. E. Topological phases and twisting of graphene on a dichalcogenide monolayer. *Physical Review B* **98**, 195129 (2018).
218. Pezo, A., Zanolli, Z., Wittemeier, N., Ordejon, P., Fazzio, A., Roche, S. & Garcia, J. H. Manipulation of spin transport in graphene/transition metal dichalcogenide heterobilayers upon twisting. *2D Materials* (2021).
219. Andrei, E. Y., Efetov, D. K., Jarillo-Herrero, P., MacDonald, A. H., Mak, K. F., Senthil, T., Tutuc, E., Yazdani, A. & Young, A. F. The marvels of moiré materials. *Nature Reviews Materials* **6**, 201–206 (2021).
220. Zollner, K., Gmitra, M. & Fabian, J. Swapping Exchange and Spin-Orbit Coupling in 2D van der Waals Heterostructures. *Physical Review Letters* **125**, 196402 (2020).
221. Fülöp, B., Márffy, A., Zihlmann, S., Gmitra, M., Tóvári, E., Szentpéteri, B., Kedves, M., Watanabe, K., Taniguchi, T., Fabian, J., Schönenberger, C., Makk, P. & Csonka, S. Boosting proximity spin orbit coupling in graphene/ WSe_2 heterostructures via hydrostatic pressure. *arXiv:2103.13325 [cond-mat]* (2021).
222. Miao, F., Liang, S.-J. & Cheng, B. Straintronics with van der Waals materials. *npj Quantum Materials* **6**, 59 (2021).

223. Masubuchi, S., Morimoto, M., Morikawa, S., Onodera, M., Asakawa, Y., Watanabe, K., Taniguchi, T. & Machida, T. Autonomous robotic searching and assembly of two-dimensional crystals to build van der Waals superlattices. *Nature Communications* **9**, 1413 (2018).
224. Han, B., Lin, Y., Yang, Y., Mao, N., Li, W., Wang, H., Yasuda, K., Wang, X., Fatemi, V., Zhou, L., Wang, J. I.-J., Ma, Q., Cao, Y., Rodan-Legrain, D., Bie, Y.-Q., Navarro-Moratalla, E., Klein, D., MacNeill, D., Wu, S., Kitadai, H., Ling, X., Jarillo-Herrero, P., Kong, J., Yin, J. & Palacios, T. Deep-Learning-Enabled Fast Optical Identification and Characterization of 2D Materials. *Advanced Materials* **32**, 2000953 (2020).
225. Masubuchi, S., Watanabe, E., Seo, Y., Okazaki, S., Sasagawa, T., Watanabe, K., Taniguchi, T. & Machida, T. Deep-learning-based image segmentation integrated with optical microscopy for automatically searching for two-dimensional materials. *npj 2D Materials and Applications* **4**, 3 (2020).
226. Liu, F., Wu, W., Bai, Y., Chae, S. H., Li, Q., Wang, J., Hone, J. & Zhu, X.-Y. Disassembling 2D van der Waals crystals into macroscopic monolayers and reassembling into artificial lattices. *Science* **367**, 903–906 (2020).
227. Roddaro, S., Pingue, P., Piazza, V., Pellegrini, V. & Beltram, F. The Optical Visibility of Graphene: Interference Colors of Ultrathin Graphite on SiO₂. *Nano Letters* **7**, 2707–2710 (2007).
228. Blake, P., Hill, E. W., Castro Neto, A. H., Novoselov, K. S., Jiang, D., Yang, R., Booth, T. J. & Geim, A. K. Making graphene visible. *Applied Physics Letters* **91**, 063124 (2007).
229. Castellanos-Gomez, A., Buscema, M., Molenaar, R., Singh, V., Janssen, L., van der Zant, H. S. J. & Steele, G. A. Deterministic transfer of two-dimensional materials by all-dry viscoelastic stamping. *2D Materials* **1**, 011002 (2014).
230. Schneider, G. F., Calado, V. E., Zandbergen, H., Vandersypen, L. M. K. & Dekker, C. Wedging Transfer of Nanostructures. *Nano Letters* **10**, 1912–1916 (2010).
231. Cao, Y., Wang, X., Lin, X., Yang, W., Lv, C., Lu, Y., Zhang, Y. & Zhao, W. Movable-Type Transfer and Stacking of van der Waals Heterostructures for Spintronics. *IEEE Access* **8**, 70488–70495 (2020).
232. Uwanno, T., Hattori, Y., Taniguchi, T., Watanabe, K. & Nagashio, K. Fully dry PMMA transfer of graphene on h-BN using a heating/cooling system. *2D Materials* **2**, 041002 (2015).
233. Frisenda, R., Navarro-Moratalla, E., Gant, P., Pérez De Lara, D., Jarillo-Herrero, P., Gorbachev, R. V. & Castellanos-Gomez, A. Recent progress in the assembly of nanodevices and van der Waals heterostructures by deterministic placement of 2D materials. *Chemical Society Reviews* **47**, 53–68 (2018).
234. Rooney, Aidan. P., Kozikov, A., Rudenko, A. N., Prestat, E., Hamer, M. J., Withers, F., Cao, Y., Novoselov, K. S., Katsnelson, M. I., Gorbachev, R. & Haigh, S. J. Observing Imperfection in Atomic Interfaces for van der Waals Heterostructures. *Nano Letters* **17**, 5222–5228 (2017).

235. Goossens, A. M., Calado, V. E., Barreiro, A., Watanabe, K., Taniguchi, T. & Vandersypen, L. M. K. Mechanical cleaning of graphene. *Applied Physics Letters* **100**, 073110 (2012).
236. Mohammad, M. A., Muhammad, M., Dew, S. K. & Stepanova, M. Fundamentals of Electron Beam Exposure and Development. in *Nanofabrication: Techniques and Principles* (eds. Stepanova, M. & Dew, S.) 11–41 (Springer, 2012).
237. Sugawara, M. *Plasma Etching: Fundamentals and Applications*. (OUP Oxford, 1998).
238. Ci, L., Xu, Z., Wang, L., Gao, W., Ding, F., Kelly, K. F., Yakobson, B. I. & Ajayan, P. M. Controlled nanocutting of graphene. *Nano Research* **1**, 116–122 (2008).
239. Liu, X., Howell, S. T., Conde-Rubio, A., Boero, G. & Brugger, J. Thermomechanical Nanocutting of 2D Materials. *Advanced Materials* **32**, 2001232 (2020).
240. Binnig, G., Quate, C. F. & Gerber, Ch. Atomic Force Microscope. *Physical Review Letters* **56**, 930–933 (1986).
241. Malard, L. M., Pimenta, M. A., Dresselhaus, G. & Dresselhaus, M. S. Raman spectroscopy in graphene. *Physics Reports* **473**, 51–87 (2009).
242. Ferrari, A. C., Meyer, J. C., Scardaci, V., Casiraghi, C., Lazzeri, M., Mauri, F., Piscanec, S., Jiang, D., Novoselov, K. S., Roth, S. & Geim, A. K. Raman Spectrum of Graphene and Graphene Layers. *Physical Review Letters* **97**, 187401 (2006).
243. Parker, M. Measuring boron nitride films from thick to thin. *Nature Electronics* **3**, 133–133 (2020).
244. Daire, A., Goeke, W. & Tupta, M. A. New Instruments Can Lock Out Lock-ins. *Keithley Instruments White Paper* 14 (2004).
245. Balakrishnan, J., Kok Wai Koon, G., Jaiswal, M., Castro Neto, A. H. & Özyilmaz, B. Colossal enhancement of spin–orbit coupling in weakly hydrogenated graphene. *Nature Physics* **9**, 284–287 (2013).
246. Balakrishnan, J., Koon, G. K. W., Avsar, A., Ho, Y., Lee, J. H., Jaiswal, M., Baek, S.-J., Ahn, J.-H., Ferreira, A., Casalilla, M. A., Neto, A. H. C. & Özyilmaz, B. Giant spin Hall effect in graphene grown by chemical vapour deposition. *Nature Communications* **5**, 4748 (2014).
247. Avsar, A., Tan, J. Y., Taychatanapat, T., Balakrishnan, J., Koon, G. K. W., Yeo, Y., Lahiri, J., Carvalho, A., Rodin, A. S., O’Farrell, E. C. T., Eda, G., Neto, A. H. C. & Özyilmaz, B. Spin–orbit proximity effect in graphene. *Nature Communications* **5**, 4875 (2014).
248. Ferreira, A., Rappoport, T. G., Casalilla, M. A. & Castro Neto, A. H. Extrinsic Spin Hall Effect Induced by Resonant Skew Scattering in Graphene. *Physical Review Letters* **112**, 066601 (2014).
249. Cresti, A., Nikolic, B., Garcia, J. H. & Roche, S. Charge, spin and valley Hall effects in disordered graphene. *La Rivista del Nuovo Cimento* **39**, 587–667 (2016).
250. Van Tuan, D., Marmolejo-Tejada, J. M., Waintal, X., Nikolić, B. K., Valenzuela, S. O. & Roche, S. Spin Hall Effect and Origins of Nonlocal Resistance in Adatom-Decorated Graphene. *Physical Review Letters* **117**, 176602 (2016).

251. Völkl, T., Kochan, D., Ebnet, T., Ringer, S., Schiermeier, D., Nagler, P., Korn, T., Schüller, C., Fabian, J., Weiss, D. & Eroms, J. Absence of a giant spin Hall effect in plasma-hydrogenated graphene. *Physical Review B* **99**, 085401 (2019).
252. Pierucci, D., Henck, H., Avila, J., Balan, A., Naylor, C. H., Patriarche, G., Dappe, Y. J., Silly, M. G., Sirotti, F., Johnson, A. T. C., Asensio, M. C. & Ouerghi, A. Band Alignment and Minigaps in Monolayer MoS₂-Graphene van der Waals Heterostructures. *Nano Letters* **16**, 4054–4061 (2016).
253. Safeer, C. K., Ingla-Aynés, J., Herling, F., Garcia, J. H., Vila, M., Ontoso, N., Calvo, M. R., Roche, S., Hueso, L. E. & Casanova, F. Room-Temperature Spin Hall Effect in Graphene/MoS₂ van der Waals Heterostructures. *Nano Letters* **19**, 1074–1082 (2019).
254. Berger, A. J., Page, M. R., Wen, H., McCreary, K. M., Bhallamudi, V. P., Kawakami, R. K. & Chris Hammel, P. Correlating spin transport and electrode magnetization in a graphene spin valve: Simultaneous magnetic microscopy and non-local measurements. *Applied Physics Letters* **107**, 142406 (2015).
255. Feng, W., Yao, Y., Zhu, W., Zhou, J., Yao, W. & Xiao, D. Intrinsic spin Hall effect in monolayers of group-VI dichalcogenides: A first-principles study. *Physical Review B* **86**, 165108 (2012).
256. Torres, W. S., Sierra, J. F., Benítez, L. A., Bonell, F., Costache, M. V. & Valenzuela, S. O. Spin precession and spin Hall effect in monolayer graphene/Pt nanostructures. *2D Materials* **4**, 041008 (2017).
257. Herling, F., Safeer, C. K., Ingla-Aynés, J., Ontoso, N., Hueso, L. E. & Casanova, F. Gate tunability of highly efficient spin-to-charge conversion by spin Hall effect in graphene proximitized with WSe₂. *APL Materials* **8**, 071103 (2020).
258. Khokhriakov, D., Hoque, A. M., Karpiak, B. & Dash, S. P. Gate-tunable spin-galvanic effect in graphene-topological insulator van der Waals heterostructures at room temperature. *Nature Communications* **11**, 3657 (2020).
259. Offidani, M. & Ferreira, A. Microscopic theory of spin relaxation anisotropy in graphene with proximity-induced spin-orbit coupling. *Physical Review B* **98**, 245408 (2018).
260. Offidani, M., Milletari, M., Raimondi, R. & Ferreira, A. Optimal Charge-to-Spin Conversion in Graphene on Transition-Metal Dichalcogenides. *Physical Review Letters* **119**, 196801 (2017).
261. Liu, L., Pai, C.-F., Li, Y., Tseng, H. W., Ralph, D. C. & Buhrman, R. A. Spin-Torque Switching with the Giant Spin Hall Effect of Tantalum. *Science* **336**, 555–558 (2012).
262. Yan, W., Sagasta, E., Ribeiro, M., Niimi, Y., Hueso, L. E. & Casanova, F. Large room temperature spin-to-charge conversion signals in a few-layer graphene/Pt lateral heterostructure. *Nature Communications* **8**, 661 (2017).
263. Mosendz, O., Pearson, J. E., Fradin, F. Y., Bauer, G. E. W., Bader, S. D. & Hoffmann, A. Quantifying Spin Hall Angles from Spin Pumping: Experiments and Theory. *Physical Review Letters* **104**, 046601 (2010).

264. Jamali, M., Lee, J. S., Jeong, J. S., Mahfouzi, F., Lv, Y., Zhao, Z., Nikolić, B. K., Mkhoyan, K. A., Samarth, N. & Wang, J.-P. Giant Spin Pumping and Inverse Spin Hall Effect in the Presence of Surface and Bulk Spin–Orbit Coupling of Topological Insulator Bi₂Se₃. *Nano Letters* **15**, 7126–7132 (2015).
265. Li, L., Zhang, J., Myeong, G., Shin, W., Lim, H., Kim, B., Kim, S., Jin, T., Cavill, S., Kim, B. S., Kim, C., Lischner, J., Ferreira, A. & Cho, S. Gate-Tunable Reversible Rashba–Edelstein Effect in a Few-Layer Graphene/2H-TaS₂ Heterostructure at Room Temperature. *ACS Nano* **14**, 5251–5259 (2020).
266. Hoque, A. M., Khokhriakov, D., Zollner, K., Zhao, B., Karpiak, B., Fabian, J. & Dash, S. P. All-electrical creation and control of spin-galvanic signal in graphene and molybdenum ditelluride heterostructures at room temperature. *Communications Physics* **4**, 1–9 (2021).
267. Kovács-Krausz, Z., Hoque, A. M., Makk, P., Szentpéteri, B., Kocsis, M., Fülöp, B., Yakushev, M. V., Kuznetsova, T. V., Tereshchenko, O. E., Kokh, K. A., Lukács, I. E., Taniguchi, T., Watanabe, K., Dash, S. P. & Csonka, S. Electrically Controlled Spin Injection from Giant Rashba Spin–Orbit Conductor BiTeBr. *Nano Letters* **20**, 4782–4791 (2020).
268. Vaklinova, K., Hoyer, A., Burghard, M. & Kern, K. Current-Induced Spin Polarization in Topological Insulator–Graphene Heterostructures. *Nano Letters* **16**, 2595–2602 (2016).
269. Stephen, G. M., Vail, O. A., DeMell, J. E., Hanbicki, A. T., Taylor, P. J. & Friedman, A. L. Nonlocal Measurement as a Probe of the Spin Hall Effect in Topological Insulators. *Physical Review Applied* **16**, 034007 (2021).
270. Trier, F., Vaz, D. C., Bruneel, P., Noël, P., Fert, A., Vila, L., Attané, J.-P., Barthélémy, A., Gabay, M., Jaffrès, H. & Bibes, M. Electric-Field Control of Spin Current Generation and Detection in Ferromagnet-Free SrTiO₃-Based Nanodevices. *Nano Letters* **20**, 395–401 (2020).
271. Jin, M.-J., Moon, S. Y., Park, J., Modepalli, V., Jo, J., Kim, S.-I., Koo, H. C., Min, B.-C., Lee, H.-W., Baek, S.-H. & Yoo, J.-W. Nonlocal Spin Diffusion Driven by Giant Spin Hall Effect at Oxide Heterointerfaces. *Nano Letters* **17**, 36–43 (2017).
272. Song, P., Hsu, C.-H., Vignale, G., Zhao, M., Liu, J., Deng, Y., Fu, W., Liu, Y., Zhang, Y., Lin, H., Pereira, V. M. & Loh, K. P. Coexistence of large conventional and planar spin Hall effect with long spin diffusion length in a low-symmetry semimetal at room temperature. *Nature Materials* **19**, 292–298 (2020).
273. Seki, T., Hasegawa, Y., Mitani, S., Takahashi, S., Imamura, H., Maekawa, S., Nitta, J. & Takanashi, K. Giant spin Hall effect in perpendicularly spin-polarized FePt/Au devices. *Nature Materials* **7**, 125–129 (2008).
274. Manchon, A., Železný, J., Miron, I. M., Jungwirth, T., Sinova, J., Thiaville, A., Garello, K. & Gambardella, P. Current-induced spin-orbit torques in ferromagnetic and antiferromagnetic systems. *Reviews of Modern Physics* **91**, 035004 (2019).
275. Vaklinova, K., Polyudov, K., Burghard, M. & Kern, K. Spin filter effect of hBN/Co detector electrodes in a 3D topological insulator spin valve. *Journal of Physics: Condensed Matter* **30**, 105302 (2018).

276. Ohshima, R., Ando, Y., Matsuzaki, K., Susaki, T., Weiler, M., Klingler, S., Huebl, H., Shikoh, E., Shinjo, T., Goennenwein, S. T. B. & Shiraishi, M. Strong evidence for d-electron spin transport at room temperature at a LaAlO₃/SrTiO₃ interface. *Nature Materials* **16**, 609–614 (2017).
277. Haeni, J. H., Irvin, P., Chang, W., Uecker, R., Reiche, P., Li, Y. L., Choudhury, S., Tian, W., Hawley, M. E., Craigo, B., Tagantsev, A. K., Pan, X. Q., Streiffer, S. K., Chen, L. Q., Kirchoefer, S. W., Levy, J. & Schlom, D. G. Room-temperature ferroelectricity in strained SrTiO₃. *Nature* **430**, 758–761 (2004).
278. Sinova, J., Valenzuela, S. O., Wunderlich, J., Back, C. H. & Jungwirth, T. Spin Hall effects. *Reviews of Modern Physics* **87**, 1213–1260 (2015).
279. Galceran, R., Tian, B., Li, J., Bonell, F., Jamet, M., Vergnaud, C., Marty, A., García, J. H., Sierra, J. F., Costache, M. V., Roche, S., Valenzuela, S. O., Manchon, A., Zhang, X. & Schwingenschlögl, U. Control of spin–charge conversion in van der Waals heterostructures. *APL Materials* **9**, 100901 (2021).
280. Fujiwara, K., Fukuma, Y., Matsuno, J., Idzuchi, H., Niimi, Y., Otani, Y. & Takagi, H. 5d iridium oxide as a material for spin-current detection. *Nature Communications* **4**, 2893 (2013).
281. Olejník, K., Wunderlich, J., Irvine, A. C., Campion, R. P., Amin, V. P., Sinova, J. & Jungwirth, T. Detection of Electrically Modulated Inverse Spin Hall Effect in an Fe/GaAs Microdevice. *Physical Review Letters* **109**, 076601 (2012).
282. Ehlert, M., Song, C., Ciorga, M., Utz, M., Schuh, D., Bougeard, D. & Weiss, D. All-electrical measurements of direct spin Hall effect in GaAs with Esaki diode electrodes. *Physical Review B* **86**, 205204 (2012).
283. Laczkowski, P., Fu, Y., Yang, H., Rojas-Sánchez, J.-C., Noel, P., Pham, V. T., Zahnd, G., Deranlot, C., Collin, S., Bouard, C., Warin, P., Maurel, V., Chshiev, M., Marty, A., Attané, J.-P., Fert, A., Jaffrès, H., Vila, L. & George, J.-M. Large enhancement of the spin Hall effect in Au by side-jump scattering on Ta impurities. *Physical Review B* **96**, 140405 (2017).
284. Niimi, Y., Kawanishi, Y., Wei, D. H., Deranlot, C., Yang, H. X., Chshiev, M., Valet, T., Fert, A. & Otani, Y. Giant Spin Hall Effect Induced by Skew Scattering from Bismuth Impurities inside Thin Film CuBi Alloys. *Physical Review Letters* **109**, 156602 (2012).
285. Niimi, Y., Morota, M., Wei, D. H., Deranlot, C., Basletic, M., Hamzic, A., Fert, A. & Otani, Y. Extrinsic Spin Hall Effect Induced by Iridium Impurities in Copper. *Physical Review Letters* **106**, 126601 (2011).
286. Morota, M., Niimi, Y., Ohnishi, K., Wei, D. H., Tanaka, T., Kontani, H., Kimura, T. & Otani, Y. Indication of intrinsic spin Hall effect in 4d and 5d transition metals. *Physical Review B* **83**, (2011).
287. Safeer, C. K., Ingla-Aynés, J., Ontoso, N., Herling, F., Yan, W., Hueso, L. E. & Casanova, F. Spin Hall Effect in Bilayer Graphene Combined with an Insulator up to Room Temperature. *Nano Letters* **20**, 4573–4579 (2020).

288. Hoque, A. Md., Khokhriakov, D., Karpiak, B. & Dash, S. P. Charge-spin conversion in layered semimetal TaTe₂ and spin injection in van der Waals heterostructures. *Physical Review Research* **2**, 033204 (2020).
289. Safer, C. K., Ontoso, N., Ingla-Aynés, J., Herling, F., Pham, V. T., Kurzmann, A., Ensslin, K., Chuvilin, A., Robredo, I., Vergniory, M. G., de Juan, F., Hueso, L. E., Calvo, M. R. & Casanova, F. Large Multidirectional Spin-to-Charge Conversion in Low-Symmetry Semimetal MoTe₂ at Room Temperature. *Nano Letters* **19**, 8758–8766 (2019).
290. Zhao, B., Khokhriakov, D., Zhang, Y., Fu, H., Karpiak, B., Hoque, A. Md., Xu, X., Jiang, Y., Yan, B. & Dash, S. P. Observation of charge to spin conversion in Weyl semimetal WTe₂ at room temperature. *Physical Review Research* **2**, 013286 (2020).
291. Zhao, B., Hoque, A. Md., Khokhriakov, D., Karpiak, B. & Dash, S. P. Charge-spin conversion signal in WTe₂ van der Waals hybrid devices with a geometrical design. *Applied Physics Letters* **117**, 242401 (2020).
292. Zhao, B., Karpiak, B., Khokhriakov, D., Johansson, A., Hoque, A. Md., Xu, X., Jiang, Y., Mertig, I. & Dash, S. P. Unconventional Charge–Spin Conversion in Weyl-Semimetal WTe₂. *Advanced Materials* **32**, 2000818 (2020).
293. Vicente-Arche, L. M., Bréhin, J., Varotto, S., Cosset-Cheneau, M., Mallik, S., Salazar, R., Noël, P., Vaz, D. C., Trier, F., Bhattacharya, S., Sander, A., Le Fèvre, P., Bertran, F., Saiz, G., Ménard, G., Bergeal, N., Barthélémy, A., Li, H., Lin, C.-C., Nikonov, D. E., Young, I. A., Rault, J. E., Vila, L., Attané, J.-P. & Bibes, M. Spin–Charge Interconversion in KTaO₃ 2D Electron Gases. *Advanced Materials* **33**, 2102102 (2021).
294. Vaz, D. C., Noël, P., Johansson, A., Göbel, B., Bruno, F. Y., Singh, G., McKeown-Walker, S., Trier, F., Vicente-Arche, L. M., Sander, A., Valencia, S., Bruneel, P., Vivek, M., Gabay, M., Bergeal, N., Baumberger, F., Okuno, H., Barthélémy, A., Fert, A., Vila, L., Mertig, I., Attané, J.-P. & Bibes, M. Mapping spin–charge conversion to the band structure in a topological oxide two-dimensional electron gas. *Nature Materials* **18**, 1187–1193 (2019).
295. Noël, P., Trier, F., Vicente Arche, L. M., Bréhin, J., Vaz, D. C., Garcia, V., Fusil, S., Barthélémy, A., Vila, L., Bibes, M. & Attané, J.-P. Non-volatile electric control of spin–charge conversion in a SrTiO₃ Rashba system. *Nature* **580**, 483–486 (2020).
296. Nomura, A., Tashiro, T., Nakayama, H. & Ando, K. Temperature dependence of inverse Rashba-Edelstein effect at metallic interface. *Applied Physics Letters* **106**, 212403 (2015).
297. Zhang, W., Jungfleisch, M. B., Jiang, W., Pearson, J. E. & Hoffmann, A. Spin pumping and inverse Rashba-Edelstein effect in NiFe/Ag/Bi and NiFe/Ag/Sb. *Journal of Applied Physics* **117**, 17C727 (2015).
298. Emoto, H., Ando, Y., Shikoh, E., Fuseya, Y., Shinjo, T. & Shiraishi, M. Conversion of pure spin current to charge current in amorphous bismuth. *Journal of Applied Physics* **115**, 17C507 (2014).

299. Sangiao, S., De Teresa, J. M., Morellon, L., Lucas, I., Martinez-Velarte, M. C. & Viret, M. Control of the spin to charge conversion using the inverse Rashba-Edelstein effect. *Applied Physics Letters* **106**, 172403 (2015).
300. Mendes, J. B. S., Alves Santos, O., Holanda, J., Loreto, R. P., de Araujo, C. I. L., Chang, C.-Z., Moodera, J. S., Azevedo, A. & Rezende, S. M. Dirac-surface-state-dominated spin to charge current conversion in the topological insulator $(\text{Bi}_{0.22}\text{Sb}_{0.78})_2\text{Te}_3$ films at room temperature. *Physical Review B* **96**, 180415 (2017).
301. Deorani, P., Son, J., Banerjee, K., Koirala, N., Brahlek, M., Oh, S. & Yang, H. Observation of inverse spin Hall effect in bismuth selenide. *Physical Review B* **90**, 094403 (2014).
302. Wang, H., Kally, J., Lee, J. S., Liu, T., Chang, H., Hickey, D. R., Mkhoyan, K. A., Wu, M., Richardella, A. & Samarth, N. Surface-State-Dominated Spin-Charge Current Conversion in Topological-Insulator--Ferromagnetic-Insulator Heterostructures. *Physical Review Letters* **117**, 076601 (2016).
303. DC, M., Liu, T., Chen, J.-Y., Peterson, T., Sahu, P., Li, H., Zhao, Z., Wu, M. & Wang, J.-P. Room-temperature spin-to-charge conversion in sputtered bismuth selenide thin films via spin pumping from yttrium iron garnet. *Applied Physics Letters* **114**, 102401 (2019).
304. Karube, S., Kondou, K. & Otani, Y. Experimental observation of spin-to-charge current conversion at non-magnetic metal/ Bi_2O_3 interfaces. *Applied Physics Express* **9**, 033001 (2016).
305. Noel, P., Thomas, C., Fu, Y., Vila, L., Haas, B., Jouneau, P.-H., Gambarelli, S., Meunier, T., Ballet, P. & Attané, J. P. Highly Efficient Spin-to-Charge Current Conversion in Strained HgTe Surface States Protected by a HgCdTe Layer. *Physical Review Letters* **120**, 167201 (2018).
306. Qiu, Z., An, T., Uchida, K., Hou, D., Shiomi, Y., Fujikawa, Y. & Saitoh, E. Experimental investigation of spin Hall effect in indium tin oxide thin film. *Applied Physics Letters* **103**, 182404 (2013).
307. Azevedo, A., Vilela-Leão, L. H., Rodríguez-Suárez, R. L., Lacerda Santos, A. F. & Rezende, S. M. Spin pumping and anisotropic magnetoresistance voltages in magnetic bilayers: Theory and experiment. *Physical Review B* **83**, (2011).
308. Rojas-Sánchez, J.-C., Reyren, N., Laczkowski, P., Savero, W., Attané, J.-P., Deranlot, C., Jamet, M., George, J.-M., Vila, L. & Jaffrès, H. Spin Pumping and Inverse Spin Hall Effect in Platinum: The Essential Role of Spin-Memory Loss at Metallic Interfaces. *Physical Review Letters* **112**, 106602 (2014).
309. Wang, H. L., Du, C. H., Pu, Y., Adur, R., Hammel, P. C. & Yang, F. Y. Scaling of Spin Hall Angle in 3d, 4d, and 5d Metals from $\text{Y}_3\text{Fe}_5\text{O}_{12}$ /Metal Spin Pumping. *Physical Review Letters* **112**, 197201 (2014).
310. Hahn, C., de Loubens, G., Klein, O., Viret, M., Naletov, V. V. & Ben Youssef, J. Comparative measurements of inverse spin Hall effects and magnetoresistance in YIG/Pt and YIG/Ta. *Physical Review B* **87**, 174417 (2013).

311. Ingla-Aynés, J., Herling, F., Fabian, J., Hueso, L. E. & Casanova, F. Electrical Control of Valley-Zeeman Spin-Orbit-Coupling--Induced Spin Precession at Room Temperature. *Physical Review Letters* **127**, 047202 (2021).
312. Sugahara, S. & Nitta, J. Spin-Transistor Electronics: An Overview and Outlook. *Proceedings of the IEEE* **98**, 2124–2154 (2010).
313. Dery, H., Dalal, P., Cywiński, Ł. & Sham, L. J. Spin-based logic in semiconductors for reconfigurable large-scale circuits. *Nature* **447**, 573–576 (2007).
314. Behin-Aein, B., Datta, D., Salahuddin, S. & Datta, S. Proposal for an all-spin logic device with built-in memory. *Nature Nanotechnology* **5**, 266–270 (2010).
315. Schliemann, J., Egues, J. C. & Loss, D. Nonballistic Spin-Field-Effect Transistor. *Physical Review Letters* **90**, 146801 (2003).
316. Betthausen, C., Dollinger, T., Saarikoski, H., Kolkovsky, V., Karczewski, G., Wojtowicz, T., Richter, K. & Weiss, D. Spin-Transistor Action via Tunable Landau-Zener Transitions. *Science* **337**, 324–327 (2012).
317. Koo, H. C., Kwon, J. H., Eom, J., Chang, J., Han, S. H. & Johnson, M. Control of Spin Precession in a Spin-Injected Field Effect Transistor. *Science* **325**, 1515–1518 (2009).
318. Wunderlich, J., Park, B.-G., Irvine, A. C., Zárbo, L. P., Rozkotová, E., Nemeč, P., Novák, V., Sinova, J. & Jungwirth, T. Spin Hall Effect Transistor. *Science* **330**, 1801–1804 (2010).
319. Wunderlich, J., Irvine, A. C., Sinova, J., Park, B. G., Zárbo, L. P., Xu, X. L., Kaestner, B., Novák, V. & Jungwirth, T. Spin-injection Hall effect in a planar photovoltaic cell. *Nature Physics* **5**, 675–681 (2009).
320. Choi, W. Y., Kim, H., Chang, J., Han, S. H., Koo, H. C. & Johnson, M. Electrical detection of coherent spin precession using the ballistic intrinsic spin Hall effect. *Nature Nanotechnology* **10**, 666–670 (2015).
321. Choi, W. Y., Kim, H., Chang, J., Han, S. H., About, A., Saidaoui, H. B. M., Manchon, A., Lee, K.-J. & Koo, H. C. Ferromagnet-Free All-Electric Spin Hall Transistors. *Nano Letters* **18**, 7998–8002 (2018).
322. Chuang, P., Ho, S.-C., Smith, L. W., Sfigakis, F., Pepper, M., Chen, C.-H., Fan, J.-C., Griffiths, J. P., Farrer, I., Beere, H. E., Jones, G. a. C., Ritchie, D. A. & Chen, T.-M. All-electric all-semiconductor spin field-effect transistors. *Nature Nanotechnology* **10**, 35–39 (2015).
323. Michetti, P., Recher, P. & Iannaccone, G. Electric Field Control of Spin Rotation in Bilayer Graphene. *Nano Letters* **10**, 4463–4469 (2010).
324. Gmitra, M. & Fabian, J. Proximity Effects in Bilayer Graphene on Monolayer WSe₂: Field-Effect Spin Valley Locking, Spin-Orbit Valve, and Spin Transistor. *Physical Review Letters* **119**, 146401 (2017).
325. Xu, J., Singh, S., Katoch, J., Wu, G., Zhu, T., Žutić, I. & Kawakami, R. K. Spin inversion in graphene spin valves by gate-tunable magnetic proximity effect at one-dimensional contacts. *Nature Communications* **9**, 2869 (2018).

326. Groen, I., Pham, V. T., Leo, N., Marty, A., Hueso, L. E. & Casanova, F. Disentangling Spin, Anomalous, and Planar Hall Effects in Ferromagnet--Heavy-Metal Nanostructures. *Physical Review Applied* **15**, 044010 (2021).
327. Safeer, C. K., Herling, F., Choi, W. Y., Ontoso, N., Ingla-Aynés, J., Hueso, L. E. & Casanova, F. Reliability of spin-to-charge conversion measurements in graphene-based lateral spin valves. *2D Materials* **9**, 015024 (2021).
328. Sagasta, E., Borge, J., Esteban, L., Omori, Y., Gradhand, M., Otani, Y., Hueso, L. E. & Casanova, F. Interfacial mechanism in the anomalous Hall effect of Co/Bi₂O₃ bilayers. *Physical Review B* **100**, 100407 (2019).
329. Volmer, F., Bisswanger, T., Schmidt, A., Stampfer, C. & Beschoten, B. Charge-induced artifacts in non-local spin transport measurements: How to prevent spurious voltage signals. *arXiv:2112.02047 [cond-mat]* (2021).
330. Muduli, P. K., Barzola-Quiquia, J., Dusari, S., Ballestar, A., Bern, F., Böhlmann, W. & Esquinazi, P. Large local Hall effect in pin-hole dominated multigraphene spin-valves. *Nanotechnology* **24**, 015703 (2012).
331. Han, W., Otani, Y. & Maekawa, S. Quantum materials for spin and charge conversion. *npj Quantum Materials* **3**, 27 (2018).
332. Vila, M., Hsu, C.-H., Garcia, J. H., Benítez, L. A., Waintal, X., Valenzuela, S. O., Pereira, V. M. & Roche, S. Low-symmetry topological materials for large charge-to-spin interconversion: The case of transition metal dichalcogenide monolayers. *Physical Review Research* **3**, 043230 (2021).
333. Stoner, E. C. & Wohlfarth, E. P. A mechanism of magnetic hysteresis in heterogeneous alloys. *Philosophical Transactions of the Royal Society of London. Series A, Mathematical and Physical Sciences* **240**, 599–642 (1948).

List of publications

This thesis is based on the following publications:

- Room temperature spin Hall effect in graphene/MoS₂ van der Waals heterostructures, Safeer, C. K.[‡], Ingla-Aynés, J.[‡], Herling, F.[‡], Garcia, J. H., Vila, M., Ontoso, N., Reyes Calvo, M., Roche, S., Hueso, L. E. & Casanova, F., *Nano Letters* **19**, 1074–1082 (2019).
- Gate tunability of highly efficient spin-to-charge conversion by spin Hall effect in graphene proximitized with WSe₂, Herling, F., Safeer, C. K., Ingla-Aynés, J., Ontoso, N., Hueso, L. E. & Casanova, F., *APL Materials* **8**, 071103 (2020).
- Electrical control of valley-Zeeman spin-orbit coupling-induced spin precession at room temperature, Ingla-Aynés, J., Herling, F., Fabian, J., Hueso, L. E. & Casanova, F., *Physical Review Letters* **127**, 047202 (2021).

Beyond the scope of this thesis, the author contributed to the following publications:

- Large multi-directional spin-to-charge conversion in low symmetry semimetal MoTe₂ at room temperature, Safeer, C. K.[‡], Ontoso, N.[‡], Ingla-Aynés, J., Herling, F., Pham, V. T., Kurzman, A., Ensslin, K., Chuvilin, A., Robredo, I., Vergniory, M. G., de Juan, F., Hueso, L. E., Calvo, M. R. & Casanova, F., *Nano Letters* **19**, 8758–8766 (2019).
- Spin Hall Effect in Bilayer Graphene Combined with an Insulator up to Room Temperature, Safeer, C. K., Ingla-Aynés, J., Ontoso, N., Herling, F., Yan, W., Hueso, L. E. & Casanova, F., *Nano Letters* **20**, 4573–4579 (2020).
- Reliability of spin-to-charge conversion measurements in graphene-based lateral spin valves, Safeer, C. K., Herling, F., Choi, W. Y., Ontoso, N., Ingla-Aynés, J., Hueso, L. E. & Casanova, F., *2D Materials* **9**, 015024 (2021).
- Omnidirectional spin-to-charge conversion in graphene/NbSe₂ van der Waals heterostructures, Ingla-Aynés, J., Groen, I., Herling, F., Ontoso, N., Safeer, C. K., de Juan, F., Hueso, L. E., Gobbi, M. & Casanova, F., submitted to *Nano Letters* (2021).

[‡] Equal contribution

List of acronyms and symbols

2D	two-dimensional
2DEG	two-dimensional electron gas
CMOS	complementary metal–oxide–semiconductor
CNP	charge neutrality point
CVD	chemical vapor deposition
DP	Dyakonov-Perel after Mikhail Dyakonov (1940) and Wladimir Perel (1928-07)
EY	Elliott-Yafet after Roger Elliott (1928-2018) and Yako Yafet (1923)
FM	ferromagnet
h-BN	hexagonal boron nitride
IREE	inverse Rashba-Edelstein effect
ISHE	inverse spin Hall effect
LSV	lateral spin valve
MESO	magnetoelectric spin-orbit
PC	polycarbonate
PMMA	poly(methyl methacrylate)
REE	Rashba-Edelstein effect after Emmanuel Rashba (1927) and Viktor Edelstein
SCC	spin-to-charge conversion
SHE	spin Hall effect after Edwin Hall (1855-1938)
SOC	spin-orbit coupling
SOF	spin-orbit fields
TMDC	transition metal dichalcogenides
vdW	van der Waals after Johannes van der Waals (1837-1923)
VZ	valley-Zeeman after Pieter Zeeman (1865-1943)

Symbols used in equations:

α_{REE}	efficiency of the Rashba-Edelstein effect
\vec{B}	magnetic field
β	angle between effective magnetization and easy axis of the FM electrode
$D_{c/s}$	spin or charge diffusion constant
\vec{E}	electric field
E	energy
E_F	Fermi energy after Enrico Fermi (1901-1954)
e	charge of the electron
g	Landé factor after Alfred Landé (1888-1976)
\hbar	reduced Planck constant after Max Planck (1858-1947)
I_{DC}	dc current for drift experiment
$\overrightarrow{I_{s/c}}$	spin or charge current
\vec{k}	momentum vector
L	length or distance
λ_S	spin diffusion length
$\lambda_{IR EE}$	spin-to-charge conversion efficiency of the inverse Rashba-Edelstein effect
m_B	Bohr magneton after Niels Bohr (1885-1962)
m_e	mass of the electron
m_s	spin magnetic moment
$n_{s/c}$	spin or charge carrier density
ν	density of states
$P_{i/d}$	spin polarization of the FM interface of the injector or detector electrode
$R_{NL}^{(A)P}$	(anti-)parallel non-local resistance
R_{sq}	square resistance
R_{SCC}	non-local spin-to-charge resistance calculated by $(R_{NL}^P - R_{NL}^{AP})/2$
\vec{s}	Pauli spin operator after Wolfgang Pauli (1900-1958)

$\vec{\sigma}$	pseudospin Pauli spin operator
$\sigma_{xx/xy}$	longitudinal and spin Hall conductivity
τ_{iv}	intervalley scattering time
τ_s	spin relaxation time
τ_p	momentum scattering time
τ_{VZ}	time period of the spin precession due to the valley-Zeemann spin-orbit field
θ_{SH}	spin Hall angle
$\vec{\mu}_s$	spin chemical potential
$\mu_{\uparrow/\downarrow}$	chemical potential for spin up or down
V_{bg}	back gate voltage
v_D	drift velocity
v_F	Fermi velocity
w	width
ω	Larmor frequency after Joseph Larmor (1857-1942)

Acknowledgments

Whoever thinks that you can achieve anything meaningful in life alone and on your own is gravely and profoundly mistaken. Therefore, I would like to finish this thesis by thanking all the people who have supported me along the way and made it in one way or another possible to finish the presented work.

First of all, I am grateful to my supervisors Felix and Luis, who four years ago gave me the opportunity to join the Nanodevices group and the QuESTech ITN. They placed a lot of trust in me by letting me work freely on my projects but always made time to discuss any problems or questions I struggled with. They not only taught me a great deal in physics but also about science and research itself. Secondly, I also want to thank Safer, Pep, and Haozhe that as postdocs – weathered science veterans – showed me pretty much everything I know now about experimental techniques and measurements in the cleanroom and the lab. Last but not least, I thank Nerea as head of the graphene lovers, the three musketeers of AK9 for all the late-nights discussions and for being the best colleagues/flat mates/friends in personal union and all the members of the nanodevices group and nanoGUNE that made the time in San Sebastian the best I ever had. So many people, I had the privilege to work side by side with, also became friends outside of the bunker that it is impossible to name everybody here. Finally, I want to mention Roger and Ralph as the good spirits in the background, without whom no experiment would work.

As part of my Ph.D., I had the pleasure to be part of an EU Innovative Training Network and I want to state how much I enjoyed this experience. Thanks to Erika for all the organization, Willy, Alex, and Guido for the Christmassy stay in Dortmund, Arun, Emily, Edmund, and Chris for the return to Leeds, Ananthu, Naveen, and Thilo for surviving the start of the pandemic together in Gothenburg, Elias and Amaia for the insights into Graphenea and all the other ESRs and PIs for the meetings and trainings together. I hope we can stay in touch!

As probably every Ph.D. student knows, you can only stay sane six days a week in the lab if your seventh day makes up for it, a strategy that even God practiced. Thankfully, I met great people who taught me how to (almost) play beach volleyball and paddle tennis, how not to speak Euskera, went climbing and on bike tours with me, showed up to ultimate frisbee games on the beach and guitar jam sessions, or just provided an excuse

to share a beer in the sun or a pintxo in the rain. I appreciate every moment we could spend together, and I hope I was able to give a little bit back as well.

Moving to Spain was a big step for me personally and therefore I am really happy that my friends from home were there for me whenever they could, be it with regular hangout sessions even all the way from Russia or, worse, Käbschütztal, with a bed to sleep in when traveling or being quarantined or with constant visits and job offers. Also, they made sure that at least my chess skills did not suffer from the pandemic.

The biggest thanks of course go to my family who never stopped supporting me on my way and who are thrilled for every small achievement along the way. I hope that in the coming time we will be able to see each other more in person and not just on a screen and that, ultimately, I made you proud.

Eskerrik asko y Danke schön!

Franz, Donostia, January 2022.